1-1-2016

Development Of Novel Radiotracers For Pet Imaging Of Hdac-Mediated Epigenetic Regulation

Robin Edwards Bonomi
Wayne State University,

DEVELOPMENT OF NOVEL RADIOTRACERS FOR PET IMAGING OF HDAC-MEDIATED EPIGENETIC REGULATION

by

ROBIN E. BONOMI

DISSERTATION

Submitted to the Graduate School

of Wayne State University,

Detroit, Michigan

in partial fulfillment of the requirements

for the degree of

DOCTOR OF PHILOSOPHY

2016

MAJOR: BIOMEDICAL ENGINEERING

Approved By:

Advisor: Juri G. Gelovani, M.D., Ph.D.	Date
Zhifeng Kou, Ph.D.	Date
Anthony Shields, M.D. Ph.D,	Date
Matthew Allen, Ph.D.	Date

ACKNOWLEDGEMENTS

I would like to express immense gratitude and appreciation to my advisor, Dr. Juri Gelovani, for his mentorship and continuous commitment to helping me become a better scientist. I would like to thank my committee members, Dr. Anthony Shields, Dr. Zhifeng Kou, and Dr. Matthew Allen for their insights and opinions in imaging and chemistry.

I would also like to thank the entire Gelovani Group for their support and participation in this work, including Dr. Aleksandr Shavrin, Dr. Vadim Popov, Jay Llaniguez, Swatabdi Kamal, and Maxwell Laws, as well as past members, Dr. Nashaat Turkman (Stony Brook University), Philip Alther, and Dr. Uday Mukhopadhyay, Dr. Hsien-Hsien Yeh, Dr. Anjoy Majhi. Additionally, Dr. Thomas Mangner, Dr. Xin Lu, and Dr. Otto Muzik have been instrumental in providing resources and insights for this work. This work has been funded primarily by NIH and NCI, and I thank these groups for the support. Lastly, I am incredibly grateful for the continued love, support and encouragement from my dear husband, Brian Bonomi, through all of my endeavors; without which, many of them would not be possible.

TABLE OF CONTENTS

ACKNOWLEDGEMENTS ii

LIST OF FIGURES v

CHAPTER 1 INTRODUCTION AND SIGNIFICANCE 1

1a: Need for HDACs-Specific PET Imaging Agents 1

1b: Overview of HDACs 2

1C. HDAC Class III Biological Implications 6

CHAPTER 2 HDAC CLASS III SUBSTRATE SPECIFICITY 17

CHAPTER 3 DEVELOPMENT OF NOVEL HDAC CLASS IIa IMAGING AGENTS 26

3a: Novel Histone Deacetylase Class IIa Selective Substrate Radiotracer for PET Imaging of Epigenetic Regulation in the Brain 26

3b. Continuing work 54

CHAPTER 4 DEVELOPMENT OF NOVEL PET IMAGING SUBSTRATES FOR SIRT2 58

4a. A novel substrate radiotracer for molecular imaging of SIRT2 expression and activity with positron emission tomography 58

4b. Continuing work 87

CHAPTER 5 DEVELOPMENT OF NOVEL PET IMAGING SUBSTRATES FOR SIRT1 90

5a. Development of a novel substrate-type radiotracer, 2-[^{18}F]PhAHA, for PET imaging of SIRT1-mediated epigenetic regulation 90

5b. Continuing work 129

CHAPTER 6 CONCLUSIONS AND FUTURE DIRECTIONS 147

REFERENCES 149

ABSTRACT 178

AUTOBIOGRAPHICAL STATEMENT 180

LIST OF FIGURES

Figure 1: Pictorial description of epigenetic regulation by acetylation and deacetylation of histone core proteins……3

Figure 2: The mechanism of cleavage for sirtuin enzymes…….18

Figure 3: The entrapment mechanism of a sample sirtuin substrate leaving group within a cell through attachment of the leaving group to the adenine dinucleotide. ……..20

Figure 4: Synthesis of DFAHA and TFAHA……..29

Figure 5: Synthesis of DFAHA and TFAHA precursors…….....30

Figure 6: Synthesis of [^{18}F]DFAHA and [^{18}F]TFAHA……..31

Figure 7: QC for [^{18}F]DFAHA and [^{18}F]TFAHA……..33

Figure 8: Substrate affinity of FAHA, DFAHA, and TFAHA to different recombinant HDACs in vitro…...…….34

Figure 9: Description of the three components to the HDAC substrates……35

Figure 10: Table demonstrating molecular modeling scores for HDAC class IIa substrates……..35

Figure 11: Mechanism of deactylation of TFAHA by HDAC8……..36

Figure 12: Proposed mechanism of action of HDAC4 (inability to deacetylate)……..37

Figure 13: Proposed mechanism of de-trifluoroacetylation by HDAC4……38

Figure 14: PET/CT images for [^{18}F]FAHA, [^{18}F]DFAHA and [^{18}F]TFAHA and corresponding time activity curves……....41

Figure 15: The corresponding map and brain image for co-localization and ROI identification…51

Figure 16: Quantification for ROI's within the brain for each of the fluorinated compounds, FAHA, DFAHA, and TFAHA……..52

Figure 17: Logan plot quantification for FAHA, DFAHA and TFAHA cerebellum using the cortex as reference tissue. ……53

Figure 18: Autoradiography for axial slices of the brain 20 min post i.v. injection of ^{18}F-TFAHA.53

Figure 19: PET/CT imaging with ^{18}F-TFAHA before and after administration of SAHA (100mg/kg)…….54

Figure 20: ^{18}F-TFAHA-derived radioactivity in a 9L tumor-bearing rat, with PET/CT images overlaid on MR……...56

Figure 21: ^{18}F-TFAHA-derived radioactivity in a U87 tumor-bearing rat, with PET/CT images overlaid on MR……..57

Figure 12**:** Overview image of Boc-lys(myr)-AMC docking in SIRT2 with the mechanism for SIRT2-mediated cleavage of myristoylated lysine……60

Figure 23: The focused library of compounds synthesized with fluroalkyl chain derivatized lysines compounds **5-10**…….61

Figure 24: Synthesis of Cbz-lys-lys(myr)-AMC (**11**)……62

Figure 25: Biochemical assay data from fluorogenic (*Fluor de Lys*®) assay for compounds **5-11** and standard, BPS1…….63

Figure 26: Catalytic rate comparison between compounds **8, 9, 11** with different cap groups and either 12 or 14 carbon chain leaving group with a panel of recombinant SIRT enzymes.……...64

Figure 27: IC_{50} curve using increasing concentrations of AGK2 in a competitive inhibition assay with SIRT2 and substrate compound **8** at its apparent k_m……..64

Figure 28: Molecular modeling of **8** in interaction with SIRT2 catalytic site as well as a table docking scores for varying substrates and SIRT2……..65

Figure 29: Illustration of both backbones used, one for *in vitro* and the analogous peptide mimetic for *in vivo* radiotracer development. ……66

Figure 30: Synthesis of compounds **12, 13, 14, 15**……66

Figure 31: The quality control chromatogram of the 12-[^{18}F]DDAHA (**15**) radiotracer……67

Figure 32: Cellular uptake studies with 12-[^{18}F]DDAHA……68

Figure 33: PET/CT images from a rat bearing a 9L brain tumor using 12[^{18}F]-DDAHA……87

Figure 34: Possible schemes for synthesis of alternative SIRT2-selective radiotracers……..89

Figure 35: The unique SIRT1 mechanism for cleavage of a benzyl moiety (highlighted in red) from a lysine residue of a protein using NAD^+ as a cofactor……93

Figure 36: Synthesis of control compound **17,** Cbz-Lys(ac)-AMC……93

Figure 37: Synthesis of the focused library of SIRT1 substrates……94

Figure 38: Synthesis of 4-fluorophenylaminohexanoic anilide (**28**)……94

Figure 39: Synthesis of compounds **29-34**……..95

Figure 40**:** Synthesis of compounds **35-37…**……96

Figure 41: The catalytic efficiencies (k_{cat}) for the library of compounds synthesized assayed against a panel of recombinant SIRT enzymes……..97

Figure 42: Evaluation of phenyl ring fluorine substituent positioning on both the phenyl and benzyl leaving groups on SIRT1 catalytic efficiency, as determined by fluorogenic (*Fluor de Lys*®) assay……..99

Figure 43: The catalytic efficiency for the lead compound Cbz-Lys(2FPh)-AMC (19) was assessed in a panel of recombinant HDACs for relative selectivity for SIRT1……100

Figure 44: IC_{50} curve for SIRT1 with **19** at its apparent *km* value obtained by competition assay with known potent SIRT1 selective inhibitor, EX-527 at increasing concentrations on the log scale……101

Figure 45: HPLC analysis for catalytic rates of cleavage of 4-FPhAHA (**28**) with a panel of recombinant HDAC enzymes (HDACs 1-11 and SIRT1-5) demonstrating selective cleavage by SIRT1…….....101

Figure 46: Dynamic PET/CT images and quantification for the images demonstrated as time activity curves and logan plots of ROI with brainstem as reference tissue……102

Figure 47: Representative PET/CT images using 2-[^{18}F]PhAHA aligned with rat brain atlas maps……103

Figure 48: IHC results demonstrating increased SIRT1-expression in the rat……104

Figure 49: Autoradiography (left) aligned with corresponding PET/CT/MR image (right) for 2-[^{18}F]PhAHA……104

Figure 50. Fluorescence microscopy of SIRT1 expression (green) counterstained with DAPI nuclear marker (blue) in the *n. accumbens* region of a rat at 10x magnification, with inset at 20x magnification……...…106

Figure 51. Fluorescence microscopy of SIRT1 expression (green) counterstained with DAPI nuclear marker (blue) in the *hippocampal* region of a rat at 10x magnification……..107

Figure 52. Fluorescence microscopy of SIRT1 expression (green) counterstained with DAPI nuclear marker (blue) in the *CA2* region of a rat, 20x magnification……...107

Figure 53: PET/CT images acquired with 2-[^{18}F]PhAHA and corresponding quantification with and without administration of SIRT1-selective inhibitor, EX-527……..109

Figure 54: Dynamic PET/CT images with compounds **30** and **31** imaged in a mouse brain and overlaid onto one another to highlight similarities and differences between the two radiotracers.....110

Figure 55: Dynamic PET/CT images using compounds **30** and **31** mapped to corresponding regions in mouse brain……..111

Figure 56: Comparison between PET/CT images acquired post i.v. administration of three tracers, the parent compound 2-[^{18}F]PhAHA (**37**), and two possible metabolites: 2-[^{18}F]benzaldehyde (**34**) and 2-[^{18}F]Ethylbenzoate (**30**) metabolized to 2-[^{18}F]benzoic acid (**31**)……...112

Figure 57: In vitro cellular uptake studies to determine cell lines with increased levels of SIRT1 expression as dictated by uptake of SIRT1-selective radiotracer 2-[^{18}F]PhAHA derived radioactivity…….……133

Figure 58: IHC results for SIRT1 staining in different types of medulloblastoma cells. (Ma et al., 2013)..……..134

Figure 59: H&E staining of axial section from brain of 9L tumor bearing rat aligned with corresponding PET/CT image at 30 min post administration of 2-[^{18}F]PhAHA……..134

Figure 60: Coronal slices from dynamic PET/CT/MRI images of 9L tumor bearing rat at 30 min post 2-[^{18}F]PhAHA……..135

Figure 61: Coronal slices from dynamic PET/CT/MRI images of U87 tumor bearing rat at 30 min post 2-[^{18}F]PhAHA administration centered at bregma……136

Figure 62: Bioluminescence imaging of U87TdRLuc tumor in a rat demonstrating tumor localization within the brain…….136

Figure 63: Coronal slices of each tracer separately and overlay both tracers to visualize expression-activity of HDACs class IIA and SIRT1 in a 9L bearing animal…….137

Figure 64: Coronal slices of each tracer separately and overlay both tracers to visualize expression-activity of HDACs class IIA and SIRT1 in a U87 bearing animal……..138

Figure 65: Quantification of 2-[^{18}F]PhAHA-derived accumulation in tumor tissue in both U87 and 9L glioma models with brainstem as reference tissue for the Logan plot analysis……139

Figure 66: Logan plot quantification for areas of the brain with high SIRT1 expression-activity, including tumor lesions for animals bearing 9L tumors……...141

Figure 67**:** Coronal and axial sections in 1 mm steps through tumor of an animal at two different time points (7d and 15d) post i.c. 9L tumor cell injection…….142

Figure 68: An inhibitor study using EX-527 demonstrating significant decreases in 2-[^{18}F]PhAHA –dervied accumulation before and after administration of inhibitor….....143

CHAPTER 1 INTRODUCTION AND SIGNIFICANCE

1a: Need for HDACs-Specific PET Imaging Agents

Over the past two decades, epigenetic regulation has become a rapidly growing, highly innovative and influential field of biology and medicine. One of the key epigenetic regulatory mechanisms involves the acetylation and deacetylation of lysine residues on histone core proteins and other critical proteins involved regulation of gene expression and protein function. Protein acetylation and deacetylation is mediated by histone acetylase transferases (HATs) and histone deacetylases (HDACs), respectively. The important roles of some of the HDACs in normal cellular physiology and the pathophysiology of different diseases have been recognized for more than a decade. Several HDAC inhibitors have been developed by the pharmaceutical industry and academia and some of them have been approved by the FDA for treatment of certain diseases (i.e., Vorinostat® for treatment of cutaneous T-cell lymphoma). However, many of the existing HDACs inhibitors lack enzyme isoform specificity and/or are unable to pass through the BBB (Hendricks et al., 2011a; Hooker et al., 2009) and are unsuitable for treatment of many CNS diseases.

The vast majority of studies on epigenetic regulation were conducted in cell cultures and tissue samples using conventional methodologies of molecular and cellular biology. However, these methods have several limitations for monitoring the efficacy of HDACs-targeted inhibitory therapies, because they require invasive biopsies of tissues, which, except for cancer, are prohibitive in most types of diseases involving vital organs (i.e., diseases of heart and brain). Therefore, there is a growing need for novel, advanced methodologies that allow for non-invasive detection and monitoring of HDAC–mediated epigenetic regulatory processes in different organs and tissues, to improve our understanding of their roles in epigenetic pathophysiology of different diseases and to aid the development and clinical translation of novel inhibitors of HDACs. One

such methodology is molecular imaging with positron emission tomography (PET), which allows for non-invasive visualization and quantification of spatial and temporal dynamics of expression-activity of various receptors and enzymes in different organs and tissues in norm and disease.

The availability of selective substrates to individual classes and isoforms of HDACs would enable the development of radiolabeled imaging agents for non-invasive *in vivo* PET imaging. The advantages of enzyme substrate based vs. inhibitor based imaging agents include the ability to measure enzyme expression-activity product rather than the presence and level of expression in tissues, and provide the means for non-invasive monitoring of pharmacodynamics of HDACs inhibitors at the target level. Therefore, the aim of this work was to develop class- and/or isoform-selective radiolabeled substrates of HDACs, with particular emphasis on class III (sirtuins, SIRTs), as will be discussed further.

1b: Overview of HDACs

The modification of DNA and corresponding histone core proteins to alter the transcriptional availability of chromatin is referred to as epigenetic regulation. The primary methods of epigenetic regulation include DNA methylation, nucleosomal remodeling and covalent histone modifications. These epigenetic modifications, carried out by a variety of enzymes, act as either activators or repressors of DNA transcription through alteration of surface charges on DNA or histone protein and subsequent changes in interactions between the two. One of the primary epigenetic regulations, includes the addition or subsequent removal of an acetyl moiety to a lysine residue in the tail of a histone core protein (Wolffe, 1996). The addition of an acetyl moiety to a lysine amino acid on a histone tail causes the tail to “loosen” its coil of the DNA thereby opening the core nucleosome structure and allowing RNA polymerase to bind, thus forming the open reading frame structure. The enzymes responsible for the transfer of an acetyl moiety to the lysine residue, and subsequent

transcriptional activation, are so called histone acetyl transferases (HATs) (Nishina et al.) (Brownell and Allis, 1996). Consequently, the enzymes responsible for the removal of the acetyl groups from these lysine residues, and subsequent transcriptional silencing, are referred to as histone deacetylases (HDACs) (**Fig. 1**). While, the processes of acetylation and deacetylation were first discovered in 1968 , the first HAT and HDAC enzymes were not known until the mid-1990's (Yang and Seto, 2007).

Since the 1990's the number and type of distinct HDACs has grown considerably. To date, 18 HDAC enzymes have been identified in humans and are typically divided into four major classes (Haberland et al., 2009). To date, 18 HDAC enzymes have been identified in humans and are typically divided into four major classes (Haberland et al., 2009). Class I HDACs includes: HDAC1, HDAC2, HDAC3, and HDAC8, which have significant domain and sequence similarity. HDAC's in this class have typically a nuclear localization (Park et al., 2004) and are involved in the regulation of cellular proliferative activity (de Ruijter et al., 2003; Khochbin et al., 2001). Class II HDACs, including HDAC4, HDAC5, HDAC6, HDAC7, HDAC9, and HDAC10, shuttle between the cytoplasm and nucleus. Class II is divided further into Class IIa (HDACs 4, 5, 7, 9) and Class IIb (HDACs 6, 10), with the primary difference in the central domain of class IIb, containing a zinc finger motif, while class IIa contains

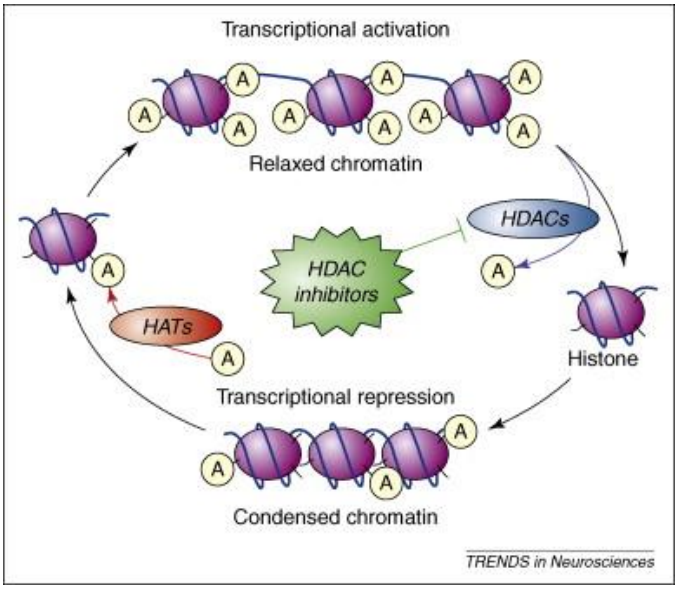

Figure 1. Histone acetylation and deacetylation causing transcriptional activation and repression of associated DNA. Figure from (Chuang et al., 2009)

a structural regulatory zinc-binding domain (Bottomley et al., 2008; Yang and Grégoire, 2005). Class IIa is able to shuttle more readily between the nucleus and the cytoplasm, whereas class IIb is primarily localized in the cytoplasm. In studying brain activity and pathophysiology, class IIa HDACs are more relevant over class IIb due to their increased expression in certain structures of the brain. HDAC enzymes in classes I, II, and IV are dependent on Zn^{2+} for enzymatic activity. Class III is comprised of HDAC enzymes termed "silent information regulators" or "sirtuins" (SIRTs), which represent a family of closely related deacetylases that are Zn^{2+}-independent but are dependent on NAD^{+}. Seven sub-types of SIRTs (SIRT 1-7) have been identified in humans (Haberland et al., 2009). SIRT enzymes are becoming increasingly scrutinized for their involvement in cancer, mental illness, and lifespan regulation. Class IV HDACs is comprised of a single HDAC protein, HDAC11, which is considered separate from classes I and II due to its biological actions (Gao et al., 2002; Gregoretti et al., 2004). The mechanisms of catalytic activity amongst different HDAC classes and unique structures of individual isoforms correspond to peptide sequence-specificity and types of post-translational modifications of their client proteins (i.e., acetylation, succinylation, myristoylation, etc.) (Yao and Yang, 2011). This allows for the development of class and isoform-specific inhibitors for treatment of various pathological conditions and diseases (Thomas, 2009).

HDACs class III is comprised of HDAC enzymes termed "silent information regulators" (sirtuins, SIRTs), representing a family of closely related deacetylases that are Zn^{2+}-independent but NAD^{+}-dependent. This family was first discovered as SIR2 (silent information regulator) gene in the murine mode (Michan and Sinclair, 2007) and thus far seven sub-types of SIRTs (SIRT 1-7) have been identified in humans (Haberland et al., 2009). Sirtuins are implicated in a variety of cellular processes including gene silencing, cell cycle regulation, metabolism, apoptosis, lifespan

extension and the effects of calorie restriction, as well as circadian rhythms (Pan et al., 2011a). Each of the SIRT isoforms plays a unique role in the regulation of cellular processes through SIRT-mediated epigenetics. Accordingly, the SIRT isoforms vary in their cellular localization, with SIRTs 1, 6, and 7 being primarily located in the nucleus, SIRTs 3, 4, and 5 located in mitochondria.

While SIRT enzymes cleave the acetyl moiety from a lysine residue, much like their other HDAC counterparts, it has recently been recognized that the SIRT isoforms are capable of cleaving many larger leaving groups than the acetyl (i.e., acetylation, succinylation, myristoylation, etc.) (Yao and Yang, 2011). Furthermore, these enzymes are reported to act on other client proteins outside of histone core proteins including TNF-a, FOXO, p53, a-tubulin and others (Jiang et al., 2013; Solomon et al., 2006).

The HDAC enzymes are implicated in an increasing number of pathologies including cancers and neurodegenerative disorders. A review on HDAC class IIa has been done very recently by Volmar and Wahlestedt describing the expression of HDAC Class IIa enzymes in the brain and their involvement with Alzheimer's, stress related disorders, Autism and addiction (Volmar and Wahlestedt, 2015). But these findings have not yet resulted in a substantial improvement to treatment due to the complexity of these interactions. Likewise, HDAC1 was originally linked to mSin3A expression in human cancers and a great rush ensued to produce inhibitors of HDAC1 for cancer treatment (Dhordain et al., 1998; Laherty et al., 1997). However, as more research has amassed and much data has been produced; the resulting evidence for either activating or inhibiting HDACs in disease has been inconclusive and conflicting (Lakshmaiah et al., 2014; Taunton, 1996). To confound this problem, many of the existing HDAC inhibitors lack selectivity to a single isoform or class thereby limiting the understanding of the true biological effects of these enzymes.

1C. HDAC Class III Biological Implications

Sirtuins play a variety of roles in the regulation of cellular metabolism and survival. Within the cell, the SIRT enzymes are tagged for nuclear, cytoplasmic, or mitochondrial localization in accordance with the primary function of the enzyme. SIRTs 1, 6 and 7 are primarily localized in the nucleus while SIRT2 retains the ability to shuttle between the nucleus and the cytoplasm and are believed to regulate histone core protein acetylation (North and Verdin, 2004). SIRTs 3, 4, and 5 are located in the mitochondria and primarily regulate metabolic processes (North and Verdin, 2004).

In particular, SIRT1 has been recognized for involvement in diabetes, cardiovascular disease and neurodegeneration (Haigis, 2010) through cleavage of an acetyl moiety from lysine residues of various proteins including PPARϒ, and NF-Kβ, and members of the p53 family. Through regulation of these client proteins, SIRT1 acts as both a suppressor and activator of disease in cancer and neurodegeneration.

Through deacetylation of lysine residues on histones H1, H3 and H4, namely H1K26, H3K9, H4K16, H4K56, (Vaquero et al., 2004b) SIRT1 induces hypoacetylation thus causing the formation of heterochromatin, which is generally associated with gene repression (Blander and Guarente, 2004; Michan and Sinclair, 2007; Taylor et al., 2008) (Imai et al., 2000; Vaquero et al., 2004a). Additionally, non-histone protein substrates, such as components of the core RNA polymerase I transcriptional machinery and the HAT p300/CBP (Bouras et al., 2005), are deacetylated by SIRT1 also contribute to the role of SIRT1 in reducing gene expression (Muth et al., 2001). Through this gene regulation, SIRT1 may play a anti-apoptotic function and thus promote cancer growth (Michan and Sinclair, 2007). SIRT1 can further promote cancer cell survival by deacetylating the DNA repair protein Ku70 thereby blocking mitochondrial

translocation of BAX to prevent apoptosis (Cohen et al., 2004). Additional key client proteins of SIRT1 include tumor suppressors p53 and p73, as well as other enzymes of the p53 family, PPARγ, and NF-Kβ (Rahman and Islam, 2011). SIRT1-mediated p53 deacetylation prevents p53 transcriptional activity preventing the usual apoptotic triggers in response to oxidative stress and DNA damage (Dai et al., 2007; Di Giovanni et al., 2006; Luo et al., 2001; Vaziri et al., 2001). SIRT1-mediated deacetylation of FOXO family transcription factors may also contribute a role to the anti-apoptotic nature of SIRT1 pathways (Michan and Sinclair, 2007; Wang et al., 2007; Wang and Tong, 2009).

However, SIRT1 has also been reported in some cases to act as a tumor suppressor through indirect regulation of cell cycle progression (Brooks and Gu, 2009). For example, SIRT1 deficiency in mice actually impairs the DNA damage response and leads to genomic instability (Wang et al., 2008). Whereas under in wild-type SIRT1 models, the introduction of double-stranded breaks causes SIRT1 to relocate as part of the transcription complex from more housekeeping gene promoters to the site of DNA damage and begin facilitating repair (Oberdoerffer et al., 2008).

SIRT1 catalytic activity is regulated by phosphorylation of key functional site residues (i.e. threonine, serine, tyrosine residues) on the enzyme surface. In SIRT1, the primary sites of regulation include S27, S47, T530, T540, T522, S434 and S682 (Protein Data Bank). One example of this regulation begins with the JNK1 mediated pathway. JNK1 phosphorylates S47 on hSIRT1 to increase SIRT1 activity upon increase in cellular glucose levels, which subsequently targets SIRT1 for ubiquination and degradation in response to increase in insulin levels (Gao et al., 2011). JNK2 also phosphorylates SIRT1 at S27 to stabilize SIRT1 and allow the enzyme to activate apoptotic pathways in cancer cells under damaged DNA conditions (Ford et al., 2008). Similarly,

DYRK1A and DYRK3 phosphorylate SIRT1 at T522 to prevent apoptotic pathways from occurring under conditions of damaged DNA, thereby acting as pro-survival enzymes through direct SIRT1 modulation (Guo et al., 2010). Other factors influencing the activity of SIRT1 include AMPK and cAMP/PKA. These enzymes primarily regulate SIRT1 activity in response to cellular glucose levels, especially in the liver. For example, cAMP regulates PKA which in turn phosphorylates S434 of SIRT1 to enhance deacetylase activity and promote fatty acid oxidation under conditions of glucagon receptor stimulation in the liver (Gerhart-Hines et al., 2011). The same pathway is also stimulated by oleic acid to activate SIRT1-PGC1α complex in skeletal muscles to increase rates of fatty acid oxidation (Lim et al., 2013).

Other measurements of cellular energy stores may influence SIRT1 catalytic activity. Because SIRT1 is dependent on NAD+ for catalytic activity, the ratio of NAD+ to NADH within a cell plays a part in the ability of SIRT1 to effectively deacetylate client proteins. Under energy depravation conditions, the ratio of NAD+ to NADH will increase, thus increasing the ability of SIRT1 to be active. This theory is supported by studies demonstrating activation of a *C. elegans* SIRT1 homologue as a result of calorie restriction, which may contribute to an increase in lifespan and longevity (Bordone and Guarente, 2005). This pathway is of particular interest for the treatment of obesity and Diabetes Type II resulting in exploratory clinical trials with SIRT1 activators for therapy (NCT01677611, NCT01031108, NCT01938521). Other hypotheses have included the use of Resveratrol (a small molecule SIRT1-activator) for therapeutic use in humans to increase lifespan (NCT01150955). Other clinical trials ongoing involve EX-527 (Selisistat, SEN0014196) a SIRT1 selective inhibitor, for tolerability and treatment of Huntington ’s disease (NCT01521585, NCT01485965). While these hold great promise for pharmacologic intervention

of these diseases through SIRT1-targeted therapies, conclusive results have not yet been determined.

Other indirect pathways for metabolic regulation include the SIRT1-mediated deacetylation of PPARGC1α and forkhead box o1 (FoXo1) to increase gluconeogenesis in low energy states under stimulation from glucagon and epinephrine (Schwer and Verdin, 2008). To promote fat mobilization from white adipocytes in the fasted state, SIRT1 interacts with SMRT to inhibit the transcription of PPARγ target genes (Picard et al., 2004). Additionally, SIRT1 is involved in regulation of cholesterol metabolism in the liver through deacetylation and activation of liver X receptor (LXR) causing the LXR to regulate the ATP-binding cassette transporter A1 (*aBCa1*) promoter (Li et al., 2007) dictating cholesterol efflux rate from peripheral tissues and subsequent formation of high-density lipoprotein particles (HDL).

In addition to the role SIRT1 plays in cancers and all of cellular metabolism on a larger scale, SIRT1 is implicated in the outcome of many neurodegenerative diseases. Both SIRT1 and SIRT2 have been implicated in many types of neuronal degeneration including amyotrophic lateral sclerosis (ALS), Parkinson's, Huntington's and Alzheimer's disease and models of induced axonal degeneration (i.e. Wallerian degeneration) (Dillin and Kelly, 2007; Outeiro et al., 2008; Tang and Chua, 2008; Taylor et al., 2008). Through SIRT1 interactions with p53 and p73, SIRT1 may indirectly influence neuronal cell migration, nerve fiber outgrowth, growth cone motility and axonal regeneration (Di Giovanni et al., 2006; Tedeschi and Di Giovanni, 2009; Zhang and Chen, 2007). For this reason, SIRT1 has generally been assigned neuroprotective functions, while SIRT2 has been implicated in more neurodegenerative functions. For instance, blocking SIRT2 function resulted in rescue of alpha synuclein toxicity in Parkinson's disease models (Outeiro et al., 2007) while the overexpression of SIRT2 prevented resistance of Wallerian axonal degeneration in a

mouse model (Suzuki and Koike, 2007). Other studies demonstrate that elevated SIRT2 level down-regulates neuronal motility (Pandithage et al., 2008).

The role of SIRT2 in the cell is primarily centered on cell cycle regulation through deacetylation of H4K16 and α-tubulin (Inoue et al., 2007a; Inoue et al., 2007c; Inoue et al., 2009). Through regulation of α-tubulin, SIRT2 is considered a primary mitotic exit regulator for the cell (Dryden et al., 2003) and relative expression of SIRT2 can be correlated with cell cycle progression. Therefore, the catalytic activity and expression of SIRT2 during cell cycle is also highly regulated. SIRT2 is regulated by phosphorylation at different site-specific residues on the surface of the enzyme. One example is inhibition of SIRT2 by CDK1-mediated phosphorylation on S368 to delay cell cycle progression during G1/M phase transition (North and Verdin, 2007b) (Pandithage et al., 2008). Similarly, phosphorylation of SIRT2 by CDC14B late in M/G2 transition (Dryden et al., 2003) may provoke mitotic exit through increasing SIRT2 targeted ubiquination and degradation. E-Cdk2 is another member of the cyclin family that may target SIRT2 for phosphorylation on S331 to inhibit SIRT2 function (Pandithage et al., 2008).

The role of SIRT2 in various cancers been explored in limited detail. Thus far, SIRT2 has been reported to act as to suppress glioma growth and colony formation in culture through inhibiting mitotic exit (Hiratsuka et al., 2003). The mitotic exit regulatory mechanisms of SIRT2 through deacetylation of α-tubulin may be particularly dependent on stress-induction within the cell, i.e. under normal, non-stressed conditions SIRT2 plays a much less significant role in cell cycle control (Pandithage et al., 2008). Whereas, under imposed stress conditions *in vitro* due to a microtubule poison, such as nocodazole, SIRT2 is overexpressed and delays mitotic exit (Dryden et al., 2003; Inoue et al., 2007c; Inoue et al., 2009).

Due to the pivotal role SIRT2 plays in cell cycle progression through its regulation of α-tubulin and ability to shuttle between the nucleus and cytoplasm, it follows that SIRT2 would be a key regulator cancer cell growth. *In* vitro studies have indicated an inverse relationship between colony colony growth in glioma (Claes et al., 2007) cell lines and SIRT2 expression, indicating that a decrease in SIRT2 expression may lead to a more severe grade of glioma . Furthermore, genomic analysis has confirmed that mutations causing deletion of the SIRT2 gene arise in many glioma cells as the cancer advances (Hiratsuka et al., 2003).

However, in some cases, the overexpression of SIRT2 is associated with an increase in cancer growth and progression. Through immunohistological staining, it has been demonstrated that SIRT2 is highly up regulated in breast cancer tissue (McGlynn et al., 2014). Previous studies demonstrated downregulation of SIRT2 expression in about 70% of gliomas (Hiratsuka et al., 2003; Inoue et al., 2007b). In contrast, studies that are more recent demonstrated that the labeling index of nuclear-localized SIRT2 is significantly higher in glioblastomas (grade IV), as compared to astrocytomas (grade II) and normal brain tissue and strongly correlated with malignant progression and the overall survival of patients with glioblastomas (Imaoka et al., 2012). Higher levels of expression and higher labeling index for SIRT2 is also associated with progression and poor prognosis in patients with non-small cell lung cancer (NSCLC) (Grbesa et al., 2015) and cervical carcinoma (Singh et al., 2015). Some tumors (i.e., melanomas), may harbor mutations in SIRT2 gene resulting in reduction of enzymatic activity by 80–90% compared to the wild-type protein, however consequences to tumor progression and overall prognosis are yet unknown (Lennerz et al., 2005).

The role of SIRT2 in tumor progression is attributed to the stabilization and lack of degradation of the Myc proteins, namely, C-Myc and N-Myc in pancreatic cancer and

neuroblastoma cells, respectively (Liu et al., 2013). Therefore, the use of SIRT2-selective inhibitors may provide therapy for Myc-induced malignancies. But, for most cancer strains it remains yet unknown, whether a patient's treatment would benefit most from inhibition or activation of SIRT2.

Unlike SIRTs 1 and 2, SIRT3 is localized in the mitochondria and acts primarily as a metabolic protein deacetylase rather than a true histone core protein deacetylase. SIRT3 is directly involved in regulation of TCA cycle and fatty acid synthesis through increasing pools of acetyl-coA molecules by deacetylation and subsequent activation of acetyl-CoA synthetase Lys-642 (ACS) (Jin et al., 2009). It is interesting to note that ACS may (has only been reported in yeast thus far) also facilitate the transfer of acetyl groups to the lysine residues of histone core protein tails, activating DNA transcription in a similar to the manner to HATs. Additionally, SIRT3 influences fatty acid oxidation and breakdown through regulation of the long-chain acyl-coA dehydrogenase (Bharathi et al., 2013). Due to the metabolic implications of SIRT3, clinical trials on undergoing intermittent fasting to affect aging and oxidative stress, as well as studies of vitamins C and E on SIRT activity are currently in progress with specific focus on SIRT3 and interactions with SIRT5 (NCT02132091, NCT02011906).

SIRT3 further plays a part in control of the TCA cycle through for deacetylation of alpha subunit of E1 on pyruvate dehydrogenase (PDH) and ICDH2 K75 and K241 (Mathias et al., 2014; Ozden et al., 2014; Schlicker et al., 2008b); while working in conjunction with SIRT4 to regulate the activity of PDH complex. In most cases, deacetylation of E1 by SIRT3 activates PDH and may contribute to the increase in metabolic activity of cancer cells. This may contribute to some of the metabolic reprogramming that occurs during the cancer cell transition phase, often referred to as the Warburg effect. SIRT3's integral role in cellular metabolism and glycolysis-

gluconeogenesis transition are still widely unknown and require further research to better understand the consequences of this enzyme in pathological conditions.

SIRT4 is also located in the mitochondria and functions primarily as a lipoamidase rather than a deacetylase (Mathias et al., 2014) and retains very little deacetylase activity. Primarily SIRT4 is responsible for catalyzing the removal of lipoyl and biotinyl moieties from lysine residues on metabolic client proteins (Mathias et al., 2014). Through delipoylation of pyruvate dehydrogenase E2 subunit, SIRT4 works in conjunction with SIRT3 to regulate PDH activity (Mathias et al., 2014) suggesting that PDH is regulated by other cofactors outside of E1 phosphorylation, as previously understood. Additionally, SIRT4 aids in cellular metabolism regulation by decreasing reactive oxygen production and increasing ATP production (Haigis et al., 2006). In cases of a SIRT4 knockout, the concentration of free fatty acids in the blood go to unhealthy levels indicating a direct link between SIRT4 regulation and regulation of FFA. Furthermore, circulating levels of SIRT4 may act as a biomarker for coronary artery disease due to its role of FFA regulation (Tarantino et al., 2014). SIRT4 may play pivotal roles in mitochondrial disease and aging though more research is currently needed to understand the cellular mechanisms at play.

SIRT5 is the third of the mitochondrial localized sirtuins and regulates proteins involved in oxidation/reduction reactions, fatty acid metabolism, aerobic respiration and TCA cycle (Tan et al., 2014). Similar to SIRT4, SIRT5 contains very little deacetylase activity and primarily cleaves succinyl and glutaryl moieties from lysine residues (Du et al., 2011). The cleavage of succinyl moiety from a lysine residue of client proteins by SIRT5 may play a role in directly regulating the succinyl-coA pool available for TCA cycle. SIRT5 also plays a critical role in mitochondrial and cellular health by controlling reactive oxygen species (ROS) through desuccinylation and

activation of superoxide disumutase 1 (SOD1) (Lin et al., 2013). Additionally, SIRT5 may work synergistically with SIRT1 to increase lifespan under conditions of calorie restriction (Geng et al., 2011). SIRT5 regulates the activity of carbamoyl phosphate synthetase I (CPSI) by desuccinylating specific lysine substrates (Du et al., 2011; Peng et al., 2011).

Through regulation of ROS, apoptosis and cellular metabolism, SIRT5 may alter the neuronal growth neuropathologies. In the rat model, immunohistochemical staining indicates SIRT5 is present in the neurons of the cerebral cortex and the cerebral medullary substance (Geng et al., 2011). Reportedly, SIRT5 knockout mice (KO) have minimal phenotypic differences from the WT under normal, non-pathological conditions, however when they are given a Parkinson's Disease-like state the KO become more severely affected than the WT with PD. Through this study the researchers believe that SIRT5 may be an important player in the protection of motor neurons in the brain after pathological state sets in (Lei Liu, 2015). These findings support the understanding that SIRT5 is a major player in the ROS pathway and neuronal mitochondria.

SIRT5 may also play a role in apoptosis and electron transport chain function through regulation of other mitochondrial client proteins, such as cytochrome C (Schlicker et al., 2008a). Reports have indicated that SIRT5 may be responsible for regulation, possible activation, of cytochrome C through deacetylation in the inner mitochondrial space (IMS) (Schlicker et al., 2008b). While the role of SIRT5 in many diseases has not been fully elucidated, the SIRT5-mediated regulation of many critical client proteins indicate that targeting SIRT5 for treatment of various pathologies may be beneficial. This work will need to be aided by the development of a non-invasive imaging agent that is specific for SIRT5. Development of this agent will allow for study of neuronal degenerative diseases such as ALS, Parkinson's, and Alzheimer's diseases to be

investigated further under the lens of SIRT5 activity. These findings will be important for the further discovery of treatments for these diseases.

SIRT6 is recognized for regulating cell cycle and cellular functions through control of client proteins, such as NF-KB, HIF-1α, and other genes involved in metabolism and ageing (Beauharnois et al., 2013). While SIRT6 does act as a deacetylase in vivo on endogenous client proteins, reports have demonstrated that this enzyme may contain demyristoylase activity as well. Though experimentally the ability of SIRT6 to cleave a myristoyl lysine from H3K9 or TNF-α K19-20 it has not been validated that these activities occur *in vivo* (Kokkonen et al., 2012). Pathologically, SIRT6 has been implicated in diseases such as type II diabetes (Huhtiniemi et al., 2011). SIRT6 has also demonstrated a protective role for the cell during ageing. It follows then, that using SIRT-6 targeted inhibitors or activators may be therapeutic for various pathological conditions (Kokkonen et al., 2014).

SIRT7, the most recently discovered sirtuin, is implicated in the cellular transformation from benign to malignant within cancer cells. SIRT7 localized to the nucleus and deacetylates both histones and other non-histone client proteins, though the primary target for SIRT7-mediated deacetylation is H3K18 (Paredes et al., 2014). SIRT7 plays a vital role to DNA transcription and protein translation through deacetylation of H3K18 and interactions with non-coding RNA's to regulate rRNA and tRNA synthesis. Additionally, SIRT7 has been found to deacetylate and play a role in regulation of p53 to aid in cellular regulation of DNA damage from oxidative stress (Paredes et al., 2014). Another role SIRT7 plays in cells under stress includes regulating MYC protein to facilitate the unfolded protein response (Paredes et al., 2014).

In cancer, the role of SIRT7 is likely both cancer suppressive and cancer supportive as its functionality may change with the phenotype of the cell. Reports have indicated inactivation of

SIRT7 in progressive cancers may halt the progression of cancer and even reverse the phenotype of the cancer cells to reduce tumor expression, *in vivo* (Barber et al., 2012; Paredes et al., 2014). However, it is also noted that SIRT7 plays a tumor suppressive and cellular protective role in pre-malignant, early stage cancer cells. One hypothesis for the change in cellular roles of SIRT7 is that enzyme regulation may come from free fatty acids in the cell, indicating a link between SIRT7 and cellular metabolic status (Paredes et al., 2014). While SIRT7 remains a promising target for therapy of cancers, more work is needed to understand the correct pharmacomodulation (i.e. activation or inhibition) most beneficial for a patient.

CHAPTER 2 HDAC CLASS III SUBSTRATE SPECIFICITY

The catalytic mechanism and active site structure varies slightly between each class of HDAC's. HDAC classes I and IV are very similar in both structure and function and have only very slight variations in the amino acid residues within their catalytic sites (Lombardi et al., 2011). These two classes vary more in their biological activity than their catalytic activity. HDAC class IIa has differences in the primary residues needed for catalysis within the active site, thereby altering the mechanism of action, which will be discussed further in chapter three.

Lastly, class III HDACs, the sirtuins, have the most unique catalytic structure and mechanism among the HDACs. These enzymes bind NAD^+, (generally prior to binding the substrate) which alters the state of the enzyme active site. Ultimately, the NAD^+ will be cleaved into two parts, the ADP-ribose ring and the nicotinamide during the catalyzed cleavage of a leaving group from a lysine residue on a client protein. During this cleavage reaction, the leaving group moiety will be transiently attached to the ADP-ribose ring (Sauve, 2010). Within the SIRT class, there are subclasses based on the mechanistic differences within this group. There are two primary catalytic functions among the sirtuins, which are defined as mono-ADP ribosyl transferase (ART) and NAD^+ dependent deacetylase (DAC) (Michan and Sinclair, 2007). Sirtuins can be subdivided into four classes, class I includes sirtuins 1, 2, and 3, which are able to do both ART and DAC and bind the substrate prior to the NAD^+ (Pan et al., 2011a). Classes II and III encompass sirtuins 4 and 5. While class IV includes sirtuins 6 and 7, which act as NAD^+ dependent allosteric activator enzymes, and act only as a DAC; this indicates that they rely on the binding of NAD^+ prior to the the substrate binding and are unable to act as an ART alone (Pan et al., 2011a). Unlike the rest of the HDACs, which primarily localize to the nucleus or cytoplasm, the sirtuins can also localize to

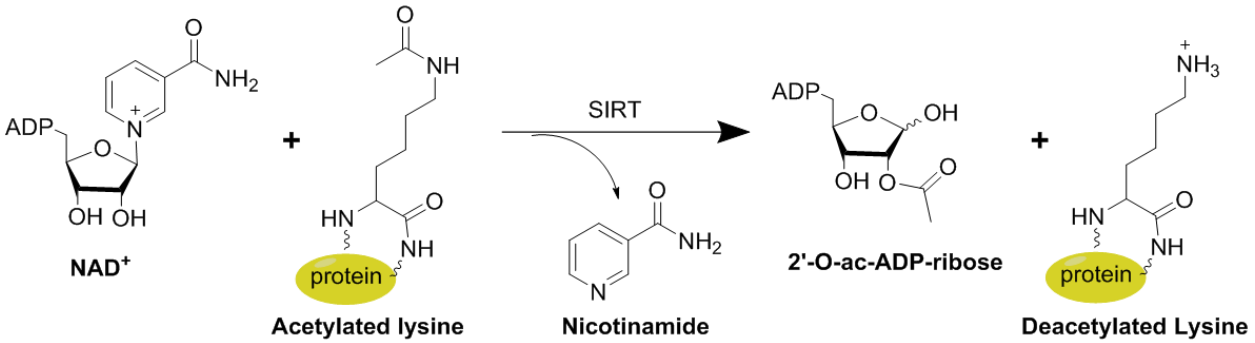

Figure 2. An illustration for deacetylation by SIRT of a lysine residue on a client protein using NAD^+ as a cofactor.

the mitochondria. Sirtuins, even more-so than other HDACs, deacetylate not only histone proteins but also many other client proteins with acetylated lysines. SIRTs also have the unique ability to cleave lysine moieties other than the typical acetyl susbtrate.

SIRT enzymes vary in cellular localization and core catalytic domain (Michan and Sinclair, 2007). As research continues, it becomes increasingly evident that sirtuins are capable of cleaving much larger leaving groups from lysine residues than the acetyl moiety. Recently, reports have indicated SIRT enzymes are responsible for acting as a desuccinylase, deglutarylase, delipoamidase or demirostoylase within the cell (Du et al., 2011; He et al., 2014; Hu et al., 2013; Tan et al., 2014). The SIRT substrates are wide ranging across many proteins outside of the histone core proteins and the even the nucleus. Due to this great variation in enzyme activity the catalytic residues and active site differ greatly in size and hydrophobicity within class III enzymes. HDAC class III is the most unique among the 18 HDAC proteins and has wide ranging impacts on norm and pathological states in the cell.

The primary mechanism for SIRT-mediated cleavage of lysine residue moieties using NAD^+ was published (Sauve, 2010) and is represented in **Fig. 2,** though there are distinct differences between the seven active sites allowing substrate specificity to be achieved. Towards an understanding of substrate specificity for each sirtuin enzyme and structure activity relationships (SAR) for these enzymes, an evaluation and comparison of the active site residues for each of the

seven sirtuins was performed. Another review of sirtuin substrate specificity has recently been published demonstrating some of the differences in pocket structure by molecular modeling (Bheda et al., 2016). All sirtuins contain a large Rossman fold (7 mostly parallel beta sheets connected by an alpha helix) encompassing the NAD^+ binding domain and a smaller, more variable, zinc ion binding domain. While SIRT enzymes have retained the Zn^{2+} binding domain from the other classes of HDACs this domain is not utilized as the primary coordination site for catalytic cleavage as it is in the other HDAC classes.

Activation of an acetylated lysine residue for SIRT-mediated amide bond cleavage occurs through interactions with water molecule and NAD^+. First, the acetylated lysine chain enters the active site from a channel opposite to the NAD^+, allowing for correct interaction between the two substrates at the active site. The overall mechanism for sirtuin deacetylation relies on the attachment of the lysine-leaving group to the adenine (Sauve et al., 2006). The nicotinamide leaves when the oxygen of the carbonyl carbon from the lysine acetyl group attacks the adenine sugar at the 1' position and this position has been activated by a histidine or tyrosine residue (Zhao et al., 2004). The 2'OH group is deprotonated by the histidine or tyrosine residue that is correctly positioned for this reaction to occur (Sauve, 2010). As the nicotinamide leaves, the lysine-acetyl moiety is transiently connected to the 1' position through an ester linkage. An oxocarbenium ring forms when the 2' hydroxyl oxygen attacks the double nitrogen amide bond. This oxocarbenium intermediate is stabilized by the presence of a highly conserved asparagine residue in all sirtuins (Zhao et al., 2004). As the oxocarbenium is opened the lysine leaves as $–NH_2$ while the acetyl (or other leaving group) moiety is transferred to the 2' position of adenine dinucleotide and connected via ester linkage. Two histidine residues facilitate this leaving group transition from the 1' position to the 2' position on the adenine ribose ring (Zhao et al., 2004). Therefore, the proof of a successful

synthetic sirtuin substrate composition comes through evidence of the leaving group attached to the adenine sugar ring.

This attachment of the leaving group to the 2' O-ADPR portion of NAD is instrumental in developing an imaging agent (**Fig. 3)**, because the entire molecule will be trapped inside the cell as it is too polar and large to be transferred back across the cell membrane. The ester linkage of the leaving group to the ADPR has been observed in cases of the long acyl chain leaving group as well as the small acetyl moiety (Feldman et al., 2013). The hydrophobic binding pocket containing the nicotinamide end of NAD^+ and the substrate leaving group is comprised of different residues in each of the sirtuins, thereby altering the substrate specificity.

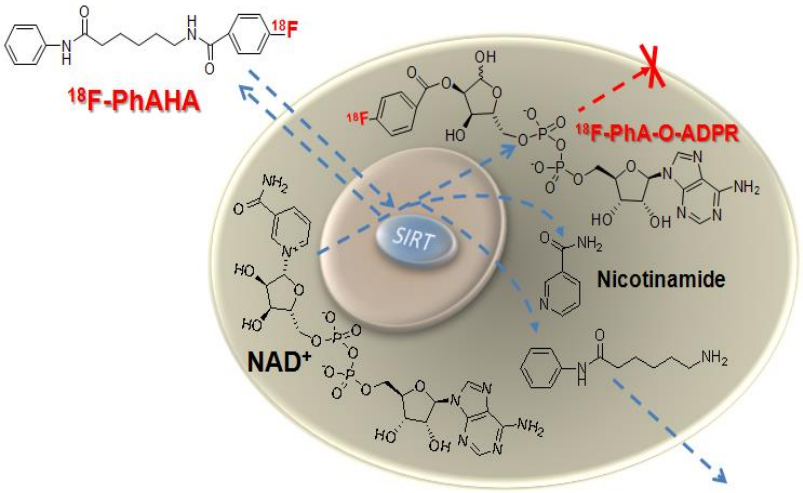

Figure 3. The entrapment mechanism of a sample sirtuin substrate leaving group within a cell through attachment of the leaving group to the adenine dinucleotide. From *Gelovani et al.*

Among sirtuins 1,2, and 5 there are a considerable number of conserved and semi-conserved residues surrounding the active site region (Cosgrove et al., 2006). Sirtuins have 4 active site loops within the large and small domains of the protein (Finnin et al., 2001). Finnin et al. gives an excellent description of each of the loops in the sirtuin enzyme structure and their functions for the enzymatic activity (Finnin et al., 2001). Due to such similarity, the ability to develop specific substrates for each sirtuin becomes increasingly difficult. The large groove residues, which include the NAD^+ binding site, remain identical across Sirt1, 2, 3, 4, 5, and 6 (Finnin et al., 2001). The

small domain, including alpha helices 5, 6, and 9, and loops 3 and 4 have some variations among the sirtuins. These helicies consist of primarily hydrophobic residues, containing both zinc binding sites and the substrate-binding site (Finnin et al., 2001). A number of these residues also encompass the catalytic site for the sirtuin, and in many cases amino acid mutations in this region will result in a complete loss of deacetylation activity.

To construct an isoform specific substrate, it is necessary to look closely at the residues within the two primary loops, L3 and L4, which contain the substrate binding and activating pocket. L3 is the active site containing the deprotonating residue for all sirtuins. This residue, generally a histidine, is responsible for activating the substrate allowing deacetylation to occur.

SIRT1 contains regions distinct from other sirtuins at both amino and carboxyl terminals; however, the catalytic core is highly conserved in all of the class III sirtuins. SIRT1 is an unordered protein due to a flexible loop involved in the active, C site, residues and forming about half of the total sequence (Autiero et al., 2009). While the core in all sirtuins is made from a Rossman fold, containing a channel terminating near the NAD+ ribose ring; SIRT1 active site contains five aromatic residues, Trp176, Tyr185, Phe187, Trp221 and Trp624 which contribute to pi-stacking interactions (Autiero et al., 2009). These aromatic residues line the hydrophobic pocket where the acetylated (or other moiety) lysine binds and could indicate that aromatic ring leaving groups with hydrophobic features would bind well in the pocket and contribute to the pi-pi stacking (Autiero et al., 2009). Therefore, it is understandable that an aromatic ring would work well as a leaving group on a substrate type radiotracer. Interesting to note, SIRT1 is unable to effectively cleave propionyl or butyryl groups, and functions at only ~28% and ~2%, respectively, of its deacetylase efficacy in these cases (Heltweg et al., 2004; Hirsch and Zheng, 2011). However, this study showed

that dephenylacetylation by SIRT1 had a catalytic reaction rate of about 56% of the deacetylation rate.

The distance between the alpha carbon and the side chain acetamido group plays a large role in the catalytic efficiency of SIRT1, thus the full lysine chain is necessary for activity (Hirsch and Zheng, 2011). The orientation of the lysine's center carbon (L-conformation) is also extremely important, as all catalytic activity is lost from the enzyme with the D-lysine isomer (Jamonnak et al., 2010).

Multiple X-ray crystal structures have been identified for SIRT2, allowing analysis of its substrates and catalytic site interaction (Finnin et al., 2001; Moniot et al., 2013). SIRT2 primarily regulate lysine residues on the tails of H3 (H3K9) and H4 (H4K16) (Imai et al., 2000). In contrast to Sir2-Af1 (the murine homologue of SIRT1) SIRT2 has a lower degree of flexibility in the binding loop leading to a very high level of substrate specificity even though it has a much wider channel than some of the other sirtuin homologues in other species (Finnin et al., 2001). Specifically, there are two residues that are necessary for deacetylase activity, Asn168 and Asp170, which activate the ribose ring to allow for a quicker enzymatic transfer (Finnin et al., 2001). It has also been proposed that it is Ser88 in SIRT2 performing the initial glycosidic attack on the NAD+, thereby allowing the nucleophilic attack on the carbonyl (Finnin et al., 2001). SIRT2 has a deeper catalytic pocket, though not wide enough to accommodate a benzene ring like SIRT1, SIRT2 has the ability to fit much longer chains. He et al. provide proof of SIRT2 cleaving the myristoyl moiety on a lysine chain of H3K9 and TNF-αK19-20 (He et al., 2014).

SIRT2 and SIRT3 share multiple residues in key positions, many of which are generally not conserved between all sirtuins. For example, the amino acid at the -2 position from the protonating residue is not conserved across all sirtuins, but both SIRT2 and SIRT3 share a tyrosine here.

Similarly, the two key residues in the L4 active site loop are shared between SIRT 2 and SIRT3 as they contain a valine at the +7 position from their respective FGEXL loops. Notably, the -1, -3 and -4 positions from this loop are also conserved between these two enzymes, yet not between any of the other sirtuins. This information is important to understand how to construct a substrate specific to one or the other.

Examining the surface residues for SIRT3 through *in silico* modeling demonstrates the cap residues more preferred by SIRT3. Investigation of many of the natural client proteins for SIRT3, the side chain and cap residues will provide valuable information for unique substrate synthesis for SIRT3 (Smith et al., 2011). According to this model study, SIRT3 prefers the positively charged and aromatic residues on both sides of the modulated lysine, namely, tyrosine, phenylalanine and tryptophan (Smith et al., 2011). This will explain why so many of the positive SIRT3 synthetic substrates are successful with the fluorescent compound amino-methylcoumarin (AMC) on one side of the lysine. Much of SIRT3's activity relies on the substrate's cap and its ability to fit well into SIRT3. Di-lysine cap groups also enhance SIRT3 catalytic activity regardless of changes in leaving group. However, the most selective leaving group for SIRT3 is the crotonyl moiety, as this sirtuin is the only one capable of successfully cleaving a crotonylated lysine moiety.

SIRT5 uses a histidine as the deprotonating residue, His158, which is common amongst the sirtuins, however SIRT5 has a unique arginine in the catalytic pocket (Du et al., 2011). The Tyr102 and Arg105 in the active site allow SIRT5 to cleave succinylated substrates (Du et al., 2011). SIRT5 has a further differentiated substrate-docking site due to its two arginine residues in the bottom of the binding pocket. Du *et al.,* demonstrated effectively that these two arginine residues form hydrogen bonding with the carboxylic acid present on the end of the succinyl moiety (Du et al., 2011). Because of this alteration in the active site, the substrate specification for SIRT5 is very

straightforward; this is the only enzyme that will easily cleave these terminal carboxylic acid chains. Tan et al. have also observed that SIRT5 is able to act as a deglutarylase on specific proteins with lysine-glutarylated residues (Tan et al., 2014). Literature reports have suggested that SIRT5 is the only sirtuin with the ability to act as a deglutarylase (Tan et al., 2014).

An interesting study demonstrated the corresponding changes in SIRT5 K_m and K_{cat} after the addition of various groups at the beta carbon of the succinyl and glutaryl substituents. The conclusion that the large changes in k_m did not necessarily reflect changes in k_{cat} demonstrates a fundamental difference in kinetic measurements of enzymatic activity (Roessler et al., 2014). It appears that for SIRT5 a lowered affinity to a substrate is not necessarily reflected in a decreased catalytic activity. In the development of synthetic substrates it is necessary to identify both strong K_m and K_{cat} values, but the K_{cat} is more indicative of the effectiveness for a particular substrate to be cleaved. Furthermore, they identified multiple different dicarbonic acyl groups, which are likely used as covalent lysine modifications for carbamoyl phosphate synthetase 1 (CPSI). Thus, it has been found that SIRT5 acts on many dicarbonic acyl chains of lengh 2 carbons to 8 carbons (Roessler et al., 2014). This finding was supported by the identification that Arg105 in SIRT5 is able to adopt different conformations allowing larger acyl residues to interact with the Tyr102 and Arg105 residues. This study also confirms the previous findings that SIRT5 is not an active deacetylase, as the K_{cat} and K_m for the deacetylase activity is extremely low. These findings are instrumental in our design of radiolabeled substrates for imaging of SIRT5 *in vivo.*

While all other sirtuins contain the FGE loop, named for the conserved FGEXL residues, SIRT6 contains instead a loop with WEDSL residues. Along with this, SIRT6 lacks the salt bridge that normally constrains the two loops used in binding NAD and substrate, in the Rossman fold. It has been documented in most sirtuins that the conserved FGEXL loop forms the hydrogen

bonding interactions with the substrate in the pocket (Jin et al., 2009). However, SIRT6 is the only enzyme without these conserved residues; instead it has a large gap in the protein sequence and corresponding cleft in the quaternary structure, followed by a WEDSL loop. These changes make the selectivity of the cap in SIRT6 much more important. This gives the enzyme more flexibility in its binding mechanism. It is implied in Hu et al. that the cap of the substrate plays a large role in the ability of an enzyme to cleave the lysine substrate (Hu et al., 2013). In their study they have tested three compounds with a myristoyl-lysine contained within. The H3K9 (myr)-AMC did not work at all while the TNF-alpha shortened analog works very well and SIRT6 is able to cleave the myristoylated lysine. Furthermore, the full chain length TNF-alpha protein with K20 myristoylated cuts the shortened peptide's Km in half (Hu et al., 2013). It has been shown that SIRT6 can catalyze demyristoylation *in vitro* for the TNF-α but it does not effectively cleave this moiety from the myristoylated lysine 9 in H3K9 (Hu et al., 2013). However, the same group has also published findings that SIRT2 can also cleave the myristoyl leaving group, but on H3K9, not TNF-α (He et al., 2014). Looking at the structures of the two amino acid sequences in the TNF protein and the histone protein there is one major difference. The TNF protein contains lysine-lysine moiety where the lysine is myristoylated, however the H3 protein contains only one lysine in the peptidic sequence. This leads us to believe that SIRT6 needs to have the Lys-Lys structure for cleavage to occur, which may be the reason for SIRT6's higher activity with a Lys-Lys substrate. These studies are important for differentiation of possibly substrates between SIRT2 and SIRT6 as they both fit many of the same leaving groups.

CHAPTER 3 DEVELOPMENT OF NOVEL HDAC CLASS IIa IMAGING AGENTS

Histone deacetylases (HDAC's) became increasingly important targets for therapy of various diseases, resulting in a pressing need to develop HDAC class- and isoform-selective inhibitors. Class IIa deacetylases possess only minimal deacetylase activity against acetylated histones, but have several other client proteins as substrates through which they participate in epigenetic regulation. Herein, we report the radiosyntheses of the second generation of HDAC class IIa–specific radiotracers: 6-(di-fluoroacetamido)-1-hexanoicanilide (DFAHA) and 6-(tri-fluoroacetamido)-1-hexanoicanilide ([^{18}F]-TFAHA). The selectivity of these radiotracer substrates to HDAC class IIa enzymes was assessed *in vitro,* in a panel of recombinant HDACs, and *in vivo* using PET/CT imaging in rats. [^{18}F]TFAHA showed significantly higher selectivity for HDAC class IIa enzymes, as compared to [^{18}F]DFAHA and previously reported [^{18}F]FAHA. PET imaging with [^{18}F]TFAHA can be used to visualize and quantify spatial distribution and magnitude of HDAC class IIa expression-activity in different organs and tissues *in vivo.* Furthermore, PET imaging with [^{18}F]TFAHA may advance the understanding of HDACs class IIa mediated epigenetic regulation of normal and pathophysiological processes, and facilitate the development of novel HDAC class IIa-specific inhibitors for therapy of different diseases.

3a: Novel Histone Deacetylase Class IIa Selective Substrate Radiotracer for PET Imaging of Epigenetic Regulation in the Brain

Portions of this chapter have been published by PLOS One (Bonomi et al., 2015)

Authors: Robin Bonomi, Uday Mukhopadhyay, Aleksander Shavrin, Hsien-Hsien Yeh, Anjoy Majhi, Sajeewa W. Dewage, Amer Najjar, Xin Lu, G. Andrés Cisneros, William P. Tong, Mian M. Alauddin, Ren-Shuan Liu, Thomas J. Mangner, Nashaat Turkman, Juri G. Gelovani,

Introduction:

There is an increasing demand for understanding the molecular pathophysiology of epigenetic regulation by histone deacetylases (HDACs). Longitudinal studies in experimental animal models and in humans, aimed to investigate different HDACs-mediated epigenetic mechanisms, could be greatly facilitated by the availability of agents for non-invasive, repetitive, and quantitative imaging of enzyme expression-activity *in vivo*. Previously, we demonstrated that Boc-Lys-trifluoroacetate (BLT) could be used for ^{19}F-NMR spectroscopic monitoring of HDAC activity *in vivo* (Sankaranarayanapillai et al., 2006; Sankaranarayanapillai et al., 2008). Also, our group developed the first radiotracer for PET imaging of HDAC expression and activity, the 6-([^{18}F]fluoroacetamido)-1-hexanoicanilide, termed [^{18}F]FAHA (Mukhopadhyay U, 2006a). We demonstrated that after intravenous injection, [^{18}F]FAHA rapidly accumulates in the brain in rats and in rhesus macaques, and that the rate of [^{18}F]FAHA accumulation in the brain is inhibited in a dose-dependent manner by HDAC inhibitor SAHA (vorinostat) (Nishii R, 2007; Sanabria S, 2008; Yeh et al., 2013a). Other investigators confirmed the results of our initial studies using PET imaging with [^{18}F]FAHA in mice (Tang et al., 2014) and baboons (Reid et al., 2009b; Seo et al., 2013) . These studies reproducibly demonstrated accumulation of [^{18}F]FAHA-derived radioactivity in the *n. accumbens*, *amygdala*, *hippocampus*, *periaqueductal grey matter* and in the *cerebellum*. These structures of the brain have selective upregulation of HDACs class IIa expression, as demonstrated by immunohistochemical staining methods in rhesus macaque (Nishii R, 2007; Sanabria S, 2008; Yeh et al., 2013a) and human brain (Yeh et al., 2013b). Furthermore, the importance of HDAC IIa enzymes in *n. accumbens*, such as HDAC4 and HDAC5, has been demonstrated in addiction, specifically in the development of drug-seeking behavior (Renthal et al., 2007) . Evidence from different laboratories using cell culture and in vivo model systems indicates that HDAC4 plays an essential role in the development of central nervous system (Morris

and Monteggia, 2013) and in maintenance of neuronal survival (Chen and Cepko, 2009; Majdzadeh et al., 2008). The HDAC4 null knockout mice, which die within 2 weeks of birth, display cerebellar degeneration (Price et al., 2013). Also, selective deletion of HDAC4 in the brain resulted in loss of learning and memory function (Kim, 2012), and haploinsufficiency of HDAC4 in humans is associated with brachydactyly mental retardation syndrome (Williams, 2010).

Considering the importance of HDAC class IIa in epigenetic regulatory mechanisms involved in brain development and function, we developed the second generation of HDAC class IIa–specific radiotracers: 6-(di-fluoroacetamido)-1-hexanoicanilide (DFAHA) and 6-(tri-fluoroacetamido)-1-hexanoicanilide ([^{18}F]-TFAHA) with improved selectivity and substrate efficiency to HDACs class IIa. The rationale for development of these radiotracers was based on previous reports that HDACs class IIa enzymes exhibit higher catalytic efficiency for Boc-L-Lys(ε-trifluoroacetyl)-AMC, as compared to Boc-L-Lys(ε-acetyl)- AMC. This is attributed to much higher electrophilicity of carbonyl carbon atom of the trifluoroacetyl moiety, as compared to acetyl moiety, despite the similarities in Van der Waals radii of acetyl and trifuloroacetyl moieties (28-30). However, Boc-L-Lys(ε-trifluoroacetyl)- AMC has demonstrated high substrate affinity also to HDAC8 (class I), which was discouraging in terms of its selectivity to HDACs class IIa. It is well established that the rim region in the active site of individual HDACs mediates the contact with capping groups of substrates (or inhibitors) and influences their affinity to individual HDACs (Riester et al., 2007). Therefore, in this study we tested the hypothesis that a smaller sized capping group, such as an aniline moiety, may preserve high substrate affinity of 6-(trifluoroacetamido)-1-hexanoicanilide to HDACs class IIa, while reducing its substrate affinity to HDAC8 and other HDACs class I enzymes. Also, we assessed whether the number of fluorine

atom substitutions in the acetyl moiety influences the substrate affinity and selectivity of mono-, di-, and tri- fluoroacetyl-hexanoicanilides to different HDACs.

Herein, we report the synthesis of DFAHA and TFAHA, as well as the radiosynthesis of [^{18}F]DFAHA and [^{18}F]TFAHA. We demonstrate that TFAHA exhibits significantly higher substrate affinity and selectivity to HDACs class IIa, especially to HDACs 4 and 5, as compared to FAHA and DFAHA. Although we have previously reported the results of ^{18}F-FAHA PET/MRI imaging studies in rhesus macaques (Yeh et al., 2013a), the results of PET imaging studies in rats comparing [^{18}F]FAHA, [^{18}F]DFAHA, and [^{18}F]TFAHA head-to-head are reported here for the first time.

Results and Discussion:

Several previously studied radiolabeled hydroxamite HDAC inhibitors, including [$^{125/131}$I]-SAHA

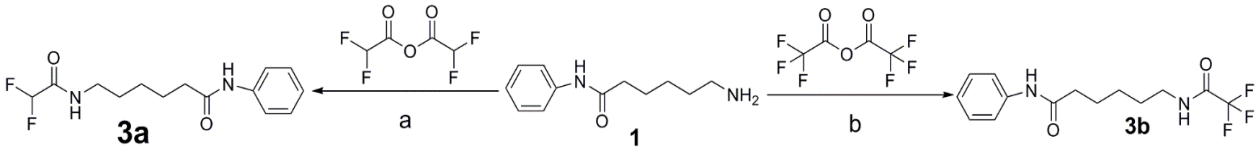

Figure 4. Synthesis of DFAHA and TFAHA. Reaction conditions are as follows: a) RT overnight; b) 2mL DCM, stirred overnight.

(Haberkorn U, 2007), [^{11}C]MS-275 (Hooker et al., 2009), [^{18}F]SAHA (Zeglis et al., 2011), [^{18}F]FESAHA (Hendricks et al., 2011b), and [^{64}Cu]CUDC-101 (Meng et al., 2013) demonstrated poor accumulation in the brain due to inability to efficiently cross the BBB. Other hydroxamite-based HDAC inhibitors containing more lipophilic capping groups, such as the adamantyl in [^{11}C]martinostat, demonstrated efficient cellular membrane and BBB penetration of this radiotracer, as well as efficient visualization and quantification of HDACs class I expression levels in the brain and other organs in non-human primates (Wang et al., 2014). Thus, PET imaging has been proven as an effective tool for image-guided optimization of potent BBB-permeable HDAC inhibitors (19, 35-37).

We focused on the development of class- and isoform- selective radiolabeled substrates instead of radiolabeled inhibitors, because of their ability to visualize not only the localization and magnitude of HDACs expression, but more importantly, their expression-activity product. In this paper, we report two novel radiolabeled substrate-based radiotracers [^{18}F]DFAHA and [^{18}F]TFAHA with enhanced enzyme selectivity for HDAC Class IIa, as compared to [^{18}F]FAHA (Nishii R, 2007; Yeh et al., 2013a). We demonstrate that increasing the number of fluorine atoms in the acetyl moiety from [^{18}F]FAHA to [^{18}F]DFAHA to [^{18}F]TFAHA increases not only the selectivity and catalytic efficiency of these substrates for HDACs class IIa, but also improves the metabolic entrapment of radiolabeled leaving groups ([^{18}F]difluoroacetate and [^{18}F]trifluoroacetate) in the brain. In contrast, previously reported studies with [^{11}C]6-acetamido-1-hexanoicanilide (^{11}C-AHA) demonstrated significantly lower uptake and more uniform distribution in the brain, as compared to ^{18}F-FAHA (Seo et al., 2013).

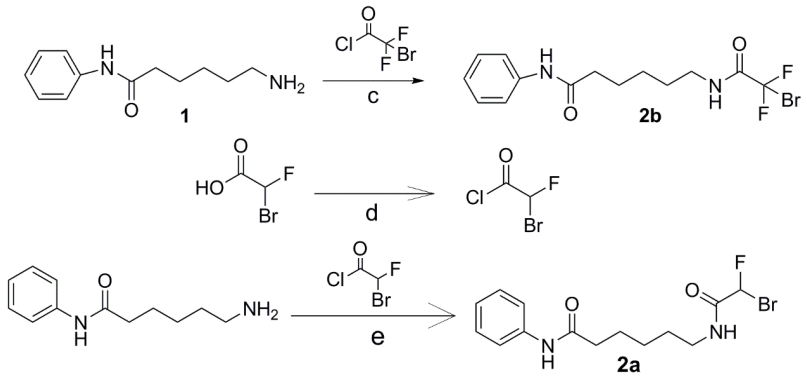

Figure 5. Synthesis of DFAHA and TFAHA precursors. Reaction conditions are as follows: c) pyridine, acetyl chloride added drop-wise at 0°C, stirred overnight at RT d) 0.9 eq. $SOCl_2$, 12 hr. stirred under argon at 40°C, catalytic DMF; e) DCM, triethylamine added drop-wise at 0°C, stirred 24 hr. under argon at RT.

The syntheses of DFAHA (**3a)** and TFAHA (**3b)** are shown in **Fig. 4**. Compound **1** was synthesized following a previously published method in 80% yield (Mukhopadhyay U, 2006b). Compound **1** was the key intermediate for the synthesis of the precursor compounds for both DFAHA (**3a**) and TFAHA (**3b**). Reaction of **1** with bromofluoro acetyl chloride (freshly prepared

by reacting bromofluoro acetic acid with thionyl chloride), and triethylamine in DCM at 0°C, produced compound **2a** in 15% yield. Due to the low boiling point of bromofluoro acetyl chloride, it was not possible to evaporate excess thionyl chloride prior to adding the compound **1**; for this reason, less than 1 equivalent of thionyl chloride was used in the reaction. Compound **2a** was obtained as a diastereoisomeric mixture and characterized by ^{1}H, ^{13}C and ^{19}F NMR spectroscopy and high-resolution mass spectroscopy. The ^{1}H NMR spectrum of compound **2a** showed 2 doublets corresponding to the fluorobromomethyl proton at 7.03 and 6.74 ppm with coupling constants of 49.45 Hz (typical for F-H coupling). Based on the relative integration of these two doublets the, diasteromeric mixture was obtained in an 80:20 ratio. The corresponding ^{19}F-NMR spectrum showed 2 doublet peaks at -147.34 and -143.52 ppm with coupling constants 50.35 Hz and 48.83 Hz respectively, and the same diasteromeric ratio of 80:20. Resolving the diastereomeric mixture was unnecessary, because the subsequent reaction (radio-fluorination) led to the formation of difluroacetyl amide, which is optically inactive. The yield of this reaction is quite low, only 15%. As an alternative, we performed this reaction using the isobutyl chloroformate as intermediary step to aid the coupling. Also, we tested N,N'-dicyclohexylcarbodiimide (DCC) as an alternative coupling agent with 4-dimethylaminopyridine (DMAP) as a catalyst. Although not yet tested, other alternative coupling agents such as hydroxybenzotriazole (HOBT) or (1-[Bis(dimethylamino)methylene]-1H-1,2,3-triazolo[4,5-b]pyridinium 3-oxid hexafluorophosphate) (HATU) can be explored with N,N-

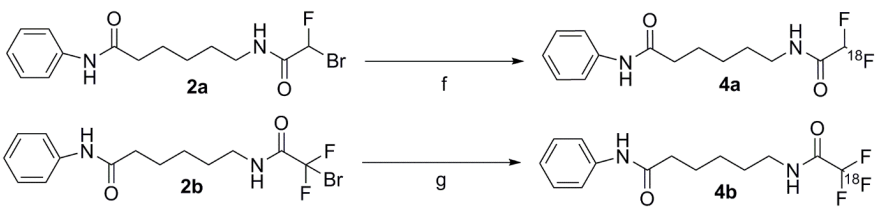

Figure 6. Synthesis of [^{18}F]DFAHA and [^{18}F]TFAHA. Reaction conditions are as follows: f) [^{18}F]KF, $K_{2,2,2}$; 0.4mL ACN, 105°C 25 min.; g)[^{18}F]KF, $K_{2,2,2}$; 0.4mL ACN, 105°C 25 min.

diisopropylethylamine (DIPEA) as catalyst. One possible reason for the consistently low yield is the bromine atoms ability to couple with the amine of compound **1.** The competition for coupling site between the bromine and the chlorine will inherently lower the correct product formation. Reaction of compound **1** with difluorobromo acetyl chloride in DCM in the presence of triethylamine (Mathias et al.) produced the precursor, compound **2b,** in 50% yield. Consistent with the structure of **2b**, a singlet at -60.07 ppm was observed in the ^{19}F NMR spectrum.

Compound **3a** was synthesized from **1** by reacting with difluoroacetic anhydride with no additional solvents in 42% yield. The ^{1}H NMR spectrum of **3a** in DMSO-d_6 was consistent with the structure and the geminal proton observed at 6.16 ppm as a doublet with a coupling constant of 53.8 Hz. The ^{19}F NMR spectrum showed a doublet at -125.65 ppm with coupling constant 54.93 Hz, matching the coupling seen in the ^{1}H NMR spectrum. Compound **3b** was obtained in 51% yield by reacting compound **1** with trifluoroacetic anhydride with only a small amount of DCM (~2 ml). A singlet fluorine peak was observed at -74.32 ppm in the ^{19}F NMR spectrum of **3b**, which is consistent with the structure of three fluorines in the trifluoroacetyl moiety. Compounds **3a** and **3b** were used as non-radioactive standards for HPLC analysis and biochemical assays (**Fig. 5)**. Compounds **4a** and **4b** were synthesized in radiochemical yields of 25% and 22%, respectively (**Fig. 6)**. The identity of the radioactive product was confirmed by co-elution with nonradioactive standard as it is not possible to test the purity of radiochemical compounds by NMR. The purity of the compounds was greater than 95%, as assessed by analytical radio-HPLC, and specific

activities ranging between 60 and 80 GBq/µmole. The quality control HPLC chromatograms taken for compounds **3a** and **3b** are shown in **Figs. 7a** and **7b** respectively.

Evaluation of substrate affinity of FAHA, DFAHA, and TFAHA in a panel of recombinant HDACs demonstrated the selectivity of these compounds for HDACs class IIa (HDACs 4, 5, 7, and 9), especially for HDACs 4 and 5. The k_{cat} values in HDACs class IIa were two orders of

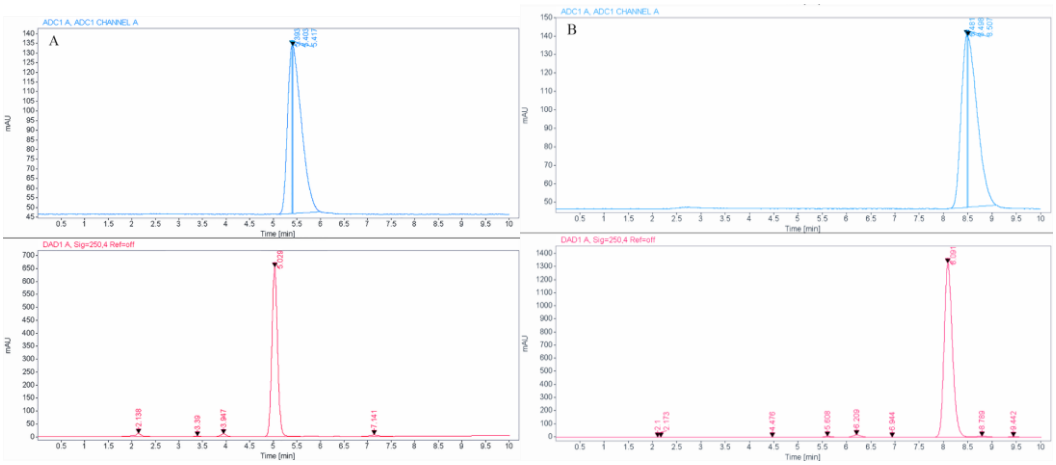

Figure 7. Quality control chromatograms for **4a and 4b. A)** Shows Compound **4a** in blue co-injected with compound **3a**, the cold standard, in red. **B**) Compound **4b** shown in blue with compound **3b**, the cold standard, shown in red. The blue shows the clean radioactive spectrum, of the pure compound. UV detection was done at 254nm.

magnitude higher than those for other classes of HDACs (**Fig. 8a**). The higher k_{cat} values of TFAHA, as compared to DFAHA and FAHA demonstrates the increasing ability of HDACs class IIa to cleave the trifluoro acetyl moiety, as compared to both difluoroacetyl and fluoroacetyl moieties. The HDAC class IIa enzymes also have lower k_m values and higher v_{max} values for TFAHA than the other HDACs enzymes (**Fig. 8b, 8c)**. There is a significant change in the v_{max} value of TFAHA from those of FAHA or DFAHA for HDAC8, demonstrating the decreased

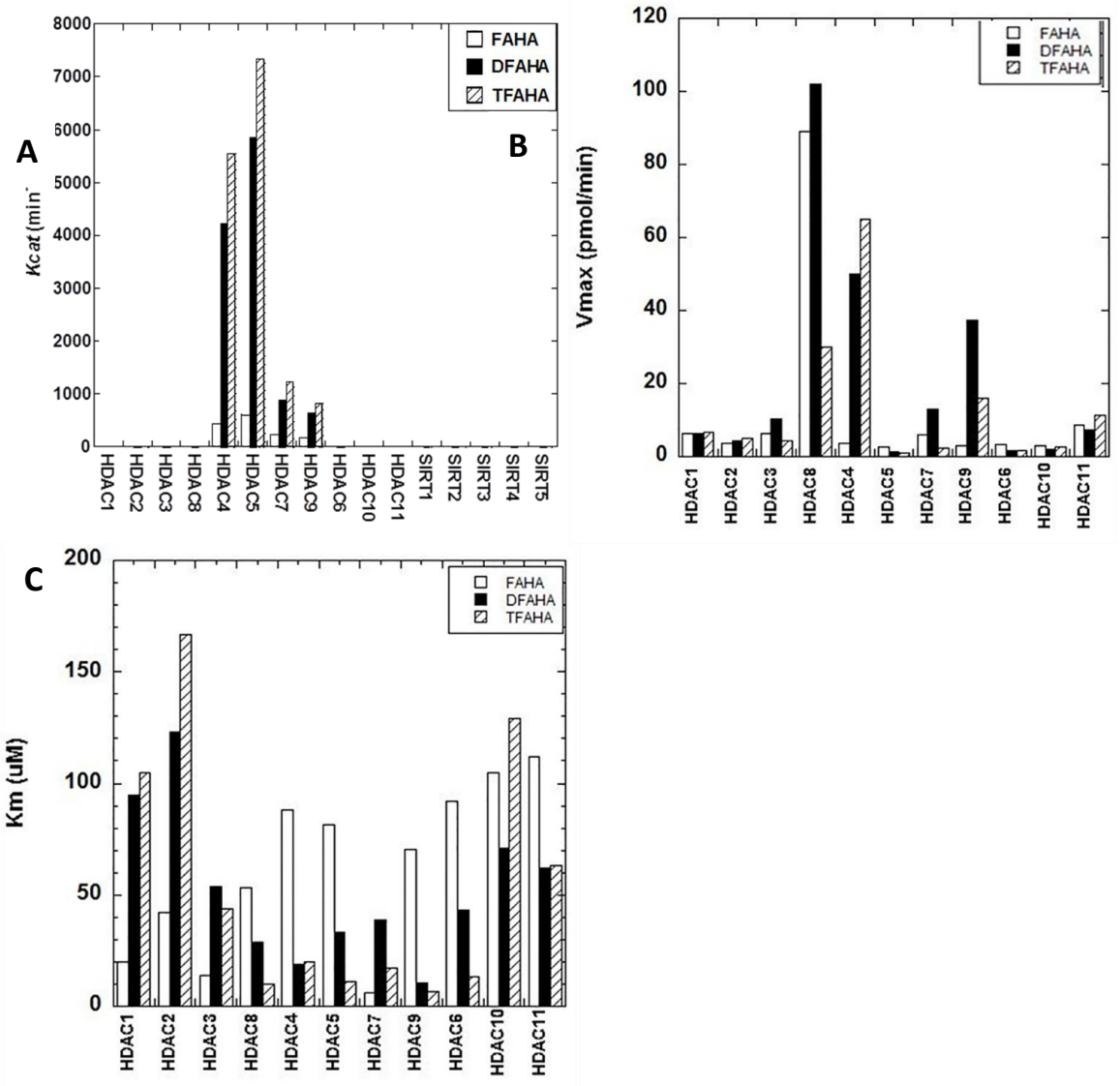

Figure 8. A) Substrate affinity of FAHA, DFAHA, and TFAHA to different recombinant HDACs *in vitro*. The substrate affinity is expressed as *Kcat*. **B**) Maximum catalytic rate of FAHA, DFAHA, and TFAHA for different recombinant HDACs *in vitro*, expressed as v_{max}. **C**) The concentration required for half of the maximal catalytic activity for all recombinant HDACs expressed as k_m.

cleavage efficiency of HDAC class I with the addition of fluorine atoms (**Fig. 8b**). Also, these results are consistent with previous reports demonstrating that HDACs class IIa enzymes exhibit higher catalytic efficiency for Boc-L-Lys(ε-trifluoroacetyl)- AMC, as compared to Boc-L-Lys(ε-acetyl)- AMC, which is not an efficient substrate to class IIa HDACs (Lahm et al., 2007). This explains, at least in part, why [^{11}C]6-acetamido-1-hexanoicanilide (^{11}C-AHA) demonstrated

significantly lower uptake and more uniform distribution in the brain in the regions of high accumulation of ^{18}F-FAHA (Seo et al., 2013).

It is important to note, that the entire structure of the substrate molecule plays a role in the selectivity for HDACs class IIa. The structure of HDAC substrates can be subdivided into three regions, which individually contribute to HDAC class and isoform selectivity: 1) the leaving group; 2) the linker; and 3) the capping moiety (**Fig. 9).** Previous studies demonstrated that trifluoroacetyl group can be cleaved by HDAC 8 when it is attached to a lysine residue flanked by Boc and AMC (Boc-Lys(TFA)- AMC) (Riester et al., 2004). In contrast, the phenyl capping group and lysine linker in DFAHA and TFAHA confer selectivity of these compounds only to HDAC Class IIa, with no significant affinity to HDAC8.

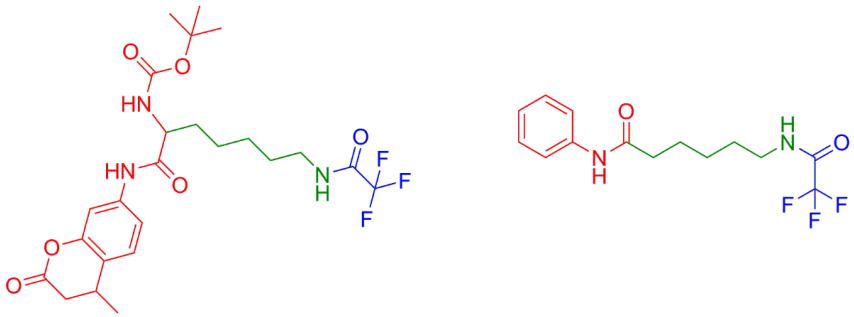

Fig 9. The three parts of a HDAC substrate, the cap (red), the linker (green), and the leaving group (blue).

Compound Name	Compound Structure	MW (g/mol)	HDAC 8 Score
AHA	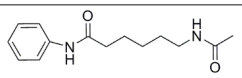	248	-24
FAHA	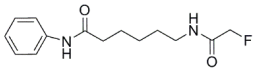	266	-20
DFAHA	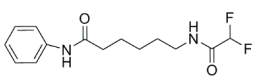	284	-20
TFAHA	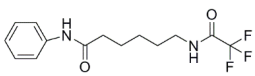	303	-17

Figure 10. The structures of compounds and docking scores with HDAC8, a HDAC Class I enzyme. A lower docking score indicates higher affinity.

Structural comparison of active sites of HDACs class I and IIa enzymes may explain the mechanism of selectivity of FAHA, DFAHA and TFAHA for HDACs class IIa. The major differences between HDACs class I (1, 2, 3 and 8) and HDACs class IIa (4, 5, 7 and 9) is the substitution of His976 (class IIa) for Tyr306 (class I) in the catalytic site. This change in amino acid residues in the catalytic site results in negligible intrinsic deacetylase activity but has two important structural consequences: the change in size of the active site, and the removal of a hydrogen bond donor site. Class I HDACs have a smaller catalytic cavity than class IIa enzymes, which explains why larger leaving groups do not fit in the catalytic site and are not cleaved by these enzymes. The docking results for HDAC 8 (class I) shown in **Fig. 10**, demonstrate that increasing the size of the leaving group (acetyl < trifluoroacetyl) increases the docking score, reflecting reduced ability of a molecule to fit inside the catalytic site of an enzyme. Indeed, previous studies have reported that larger leaving groups, such as propionyl, butyryl, (Z)-but-2-enyl, isobutyryl, 3-hydroxypropanyl, 3-methylbutanyl, 4-amino-4-

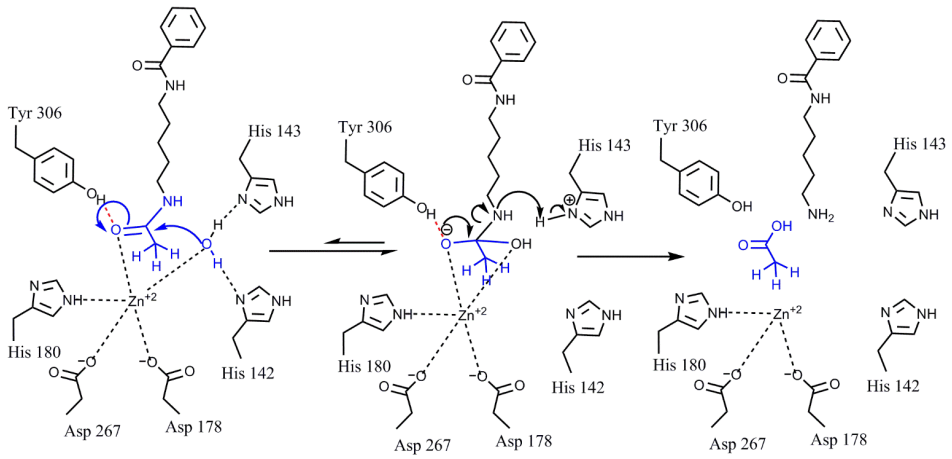

Figure 11. Mechanism of deactylation of AHA by HDAC8. In HDAC8 and other HDACs class I enzymes, the hydrogen bond forming between Tyr306 and the carbonyl oxygen of the acetyl moiety increases the electrophilicity of the carbonyl carbon, rendering it more susceptible to the nucleophilic attack by the activated water molecule, bound to His142 and His143. This leads to the formation of a tetrahedral oxyanion intermediate stabilized by Zn^{2+} ion and the hydroxyl group of Tyr306. Subsequently, the amide bond is cleaved and the acetyl moiety is released.

oxobutanyl, and several other similar compounds are poor substrates for class I HDACs (Jones et al., 2008).

HDAC class IIa enzymes lack a hydrogen bond donor that can bind to the carbonyl oxygen of the leaving acetyl group as a result of the substitution His976 (class IIa) for Tyr306 (class I), which renders the acetyl group inactive (**Figs. 11, 12)**. In HDAC class I, this hydrogen bond increases the electrophilicity of the carbonyl carbon in the acetyl group, which renders it more susceptible to the nucleophilic attack by the activated water molecule, bound to His142 and His143. This leads to the formation of a tetrahedral oxyanion intermediate stabilized by the Zn^{2+} ion and by the hydroxyl group of Tyr306 of HDAC8. Consecutive replacement of the hydrogen atoms in the methyl moiety of the leaving acetyl group by fluorine atoms reduces the enzymatic activity in HDACs class I. This suggests that increasing the electronegativity of the leaving group is not sufficient to overcome the size increase, which may force the carbonyl carbon to rotate away from the activated water molecule, adding additional distortion to the hydrogen bonding with Tyr306. Increasing the electronegativity should increase the reactivity of carbonyl

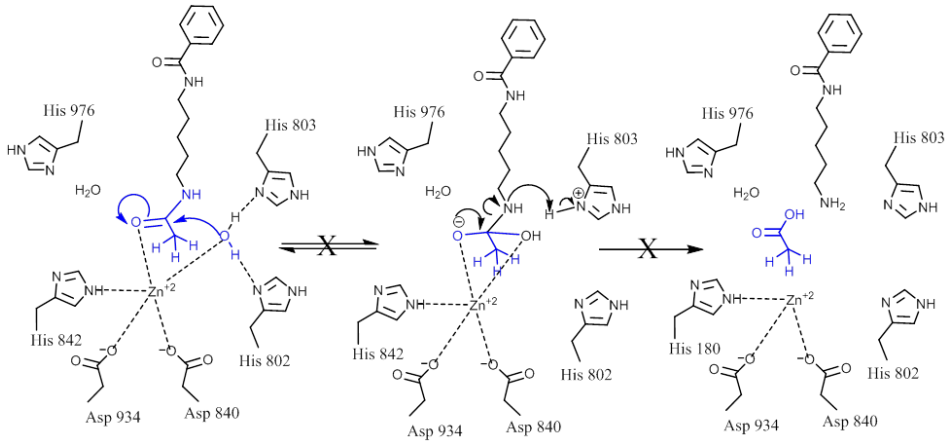

Figure 12. The mechanism of action of HDAC4. As compared to HDAC class I, HDAC class IIa enzymes exhibit significantly reduced ability to deacetylate. In class IIa enzymes the His976 located in the same position in the catalytic site as Tyr306 in class I HDACs does not serve as a hydrogen bond donor to bind to the carbonyl oxygen of the leaving acetyl group and thus reduces the susceptibility of carbonyl carbon to nucleophilic attack by the water, as in HDAC class I.

carbon, but since this is not the case, it is reasonable to assume that the relative increase in the effective size of the leaving group in TFAHA > DFAHA > FAHA may be a determining factor in the decreasing enzymatic activity. In contrast, increasing the number of fluorine atom substitutions in the methyl moiety of the acetyl leaving group increases the electrophilicity of the carbonyl carbon and restores the catalytic activity of HDACs class IIa by facilitating the nucleophilic attack on the carbonyl carbon of the acetyl moiety by activated water molecule bound to His802 and His803. As a result, the formation of the tetrahedral oxyanion is irreversible and releases trifluoroacetate as shown in **Fig. 13**.

The uptake, accumulation, and clearance of [^{18}F]FAHA, [^{18}F]DFAHA, and [^{18}F]TFAHA in various regions of the rat brain were studied using dynamic PET/CT imaging. Higher levels of accumulation of all three radiotracers were observed primarily in *n. accumbens*, *hippocampus*, *amygdala*, *periaqueductal grey*, and *cerebellum* (**Fig. 14**), where the HDACs 4 and 5 are abundantly expressed (Yeh et al., 2013a). The alignment of the PET/CT images with the digital rat brain atlas (Paxinos, 2006) was used to identify regions of interest (**Fig. 15**).

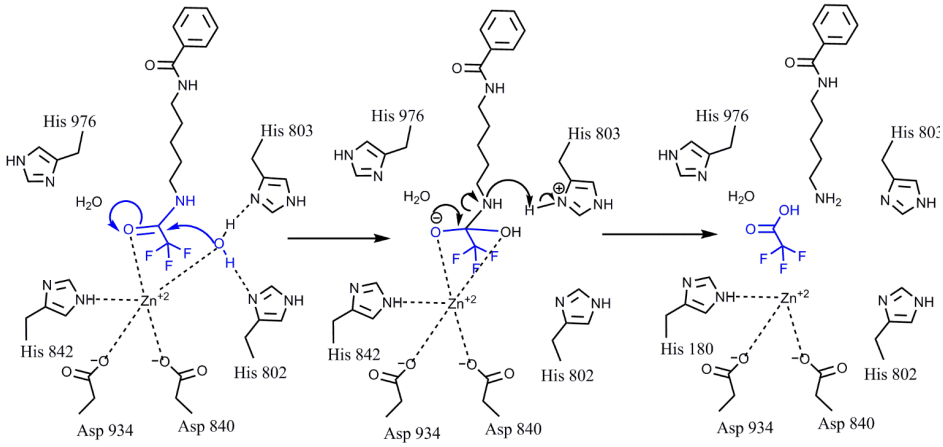

Figure 13. Proposed mechanism of de-trifluoroacetylation by HDAC4. Increased electronegativity of trifluoromethyl moiety of the trifluoroacetyl leaving group increases the susceptibility of the carbonyl carbon to the nucleophilic attack by the water molecule bound to His802 and His803 and enables the catalytic activity of HDACs class IIa. This results in formation of the tetrahedral oxyanion, which is irreversible, thereby releasing the trifluoroacetate.

Highly selective accumulation of [^{18}F]TFAHA-derived radioactivity was observed in the *cerebellum, n. accumbens, periaqueductal gray, and hippocampus* (dentate gyrus-CA1, CA3 region). The levels of [^{18}F]TFAHA-derived radioactivity accumulation in these brain structures were higher than those from either [^{18}F]DFAHA or [^{18}F]FAHA. While [^{18}F]FAHA exhibited moderate levels of radioactivity accumulation throughout the brain, including brain cortex, which is consistent with its higher substrate affinity to other HDAC classes, both [^{18}F]DFAHA and, especially [^{18}F]TFAHA, exhibited much lower accumulation in the cortex (**Fig. 16**). Logan graphical analysis of [^{18}F]FAHA, [^{18}F]DFAHA and [^{18}F]TFAHA accumulation in cerebellum using cortex as the reference tissue demonstrated that [^{18}F]TFAHA was more actively accumulated (had a steeper slope of the Logan plot) in the cerebellar nuclei than either [^{18}F]FAHA or [^{18}F]DFAHA (**Fig. 17**). Following PET/CT *in vivo* imaging with [^{18}F]TFAHA, quantitative autoradiography (QAR) was performed in selected animals to verify the results at higher resolution of images. **Fig. 18** demonstrates a high degree of correlation between the areas of ^{18}F-TFAHA-derived accumulation displayed by autoradiography and the PET images shown in **Fig. 18.** Higher levels of accumulation of [^{18}F]TFAHA were observed using QAR in *n. accumbens, hippocampus, periaqueductal grey*, and in cerebellar nuclei.

Furthermore, our preliminary imaging studies demonstrated the feasibility of PET/CT with [^{18}F]TFAHA for monitoring pharmacologic inhibition of HDACs class IIa with SAHA. A significant inhibition of [^{18}F]TFAHA-derived radioactivity accumulation in the brain was observed when SAHA (100 mg/kg) was administered i.p. 30 min prior to i.v. administration of [^{18}F]TFAHA (**Fig. 19**). These results demonstrate that [^{18}F]TFAHA is a much more selective and more efficient radiotracer for imaging expression-activity of HDAC class IIa enzymes in the brain, as compared to either [^{18}F]DFAHA or [^{18}F]FAHA.

In summary, current studies demonstrated that that [^{18}F]TFAHA is a more selective and effective substrate-based radiotracer for non-invasive PET imaging of class IIa HDACs expression-activity in the brain. This novel PET imaging radiotracer can be readily translated into the clinic and may aid in the fundamental understanding of epigenetic regulation by HDACs class IIa involved in brain development and function, as well as in the mechanisms of different diseases, including traumatic brain injury and post-traumatic stress disorders, depression, drug addiction, Alzheimer's, Huntington's, brain tumors and other diseases of the brain. Furthermore, PET imaging with [^{18}F]TFAHA should facilitate the development and clinical translation of novel HDACs class IIa selective inhibitors by enabling non-invasive quantification of their pharmacodynamics at the drug target level.

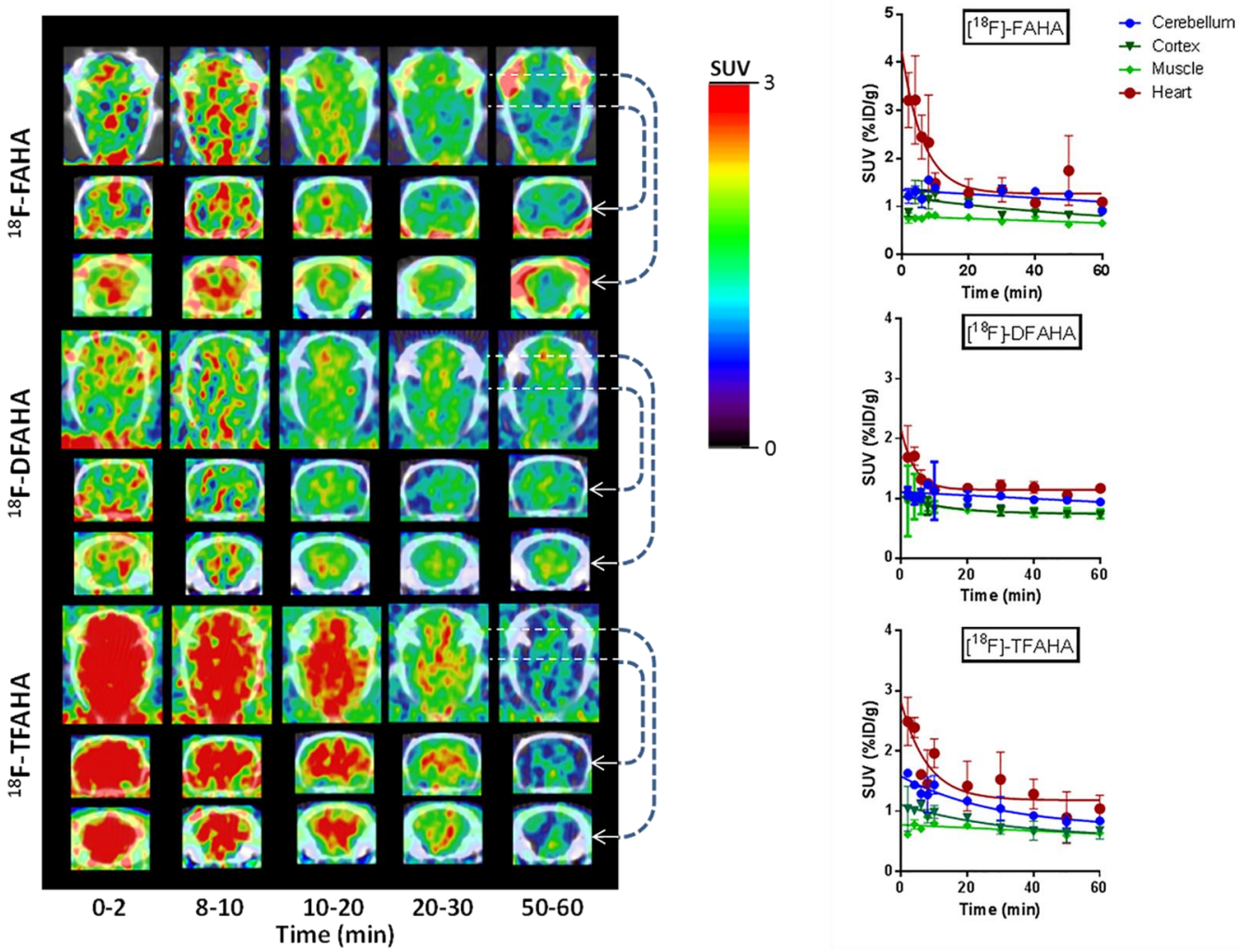

Figure 14. PET/CT images (**A**) of the spatial and temporal dynamics of influx, distribution, clearance and retention of each of the three radiotracers at different time intervals after intravenous administration: [^{18}F]FAHA (top panel), [^{18}F]DFAHA (middle panel), and [^{18}F]TFAHA (bottom panel). In each panel, PET/CT images are provided in three different planes: top row - axial images through the middle of the brain; middle row – coronal images through the middle of the brain; bottom row – coronal images through the cerebellum area. Images are color-coded to range of standard uptake values (SUV) shown in the color bar and cross-normalized to facilitate direct comparison of radioactivity distribution. Corresponding time-activity plots (**B**) of each radiotracer are provided on the right hand side for: cerebellum (blue diamonds), muscle (green triangles), cortex (red squares), and heart (grey crosshairs).

Materials and Methods:

All reagents and solvents were purchased from Aldrich Chemical Co. (Milwaukee, WI), and used without further purification. Preparation of 6-amino-1-hexanoicanilide ***(Mukhopadhyay et al., 2006)*** was done following a previously published method (Mukhopadhyay U, 2006b). Thin layer chromatography (TLC) was performed on pre-coated Dynamic Absorbance F-254 (Norcross, Georgia) silica gel, aluminum backed, plates. ^{1}H, ^{13}C and ^{19}F NMR spectra were recorded on Mercury and Varian 400 MHz spectrometers at Wayne State University. High-resolution mass spectra (HRMS) were obtained from a Waters LCT Premier/XE mass spectrometer at the Lumigen Imaging Center in the Department of Chemistry at Wayne State University using electrospray ionization (ESI) technique. High performance liquid chromatography (HPLC) was performed with an 1100 series pump from Agilent Technologies (Stuttgart, Germany), with a built-in UV detector operated at 254 nm and a radioactivity detector with a single channel analyzer model FC3200 (NaI/PMT) detector from Eckert and Ziegler Radiopharma, Inc. (Germany) with an Ascentis RP-Amide column (Supelco, 4.4x150mm) for analytical and quality control chromatography. Semi-preparative HPLC was conducted on a Knauer P4.1S pump 10ml/Ti, with a Azura UVD 2.1S Detector using Clarity Software (Berlin, Germany) pump with an Alltima C18 (Fisher Scientific, 250x10mm) column with a UV detector at 254 nm and a radio detector model FC-3500 from Eckert and Ziegler AG (Berlin, Germany).

Preparation of 6-(bromofluoroacetamido)-1-hexanoicanilide (2a): Bromofluoro acetic acid (530mg, 3.3 mmol) was added to a reaction flask with 0.9 equivalents of thionyl chloride (210 µl, 2.9 mmol). The reaction was stirred for 4 hours at 60°C. Subsequently, the reaction mixture was cooled to room temperature and a solution of compound **1** (280 mg, 1.37 mmol) in 12 mL of anhydrous dichloromethane was added and followed by trimethylamine (2 ml, 15 mmol). The

reaction was stirred under argon for 24 hours, after which, all of the solvent was evaporated and the compound was re-dissolved in dichloromethane and washed with aqueous saturated sodium bicarbonate solution. The organic layer was dried over sodium sulfate and evaporated. Flash column chromatography was used for purification of the compound with a gradient of solvent from 10% ethyl acetate in hexane to 50% ethyl acetate in hexane. Product **2a** (25 mg) was obtained in a 15% yield as an off-white solid.

Diastereomer 1: ^{1}H NMR (DMSO-d_6) δ: 9.83 (s, 1H, NH), 8.62 (s, 1H, NH), 7.56 (d, 2H, aromatic, *J* = 8.11 Hz), 7.26 (t, 2H, aromatic, *J* = 7.30 Hz), 6.99 (t, 1H, aromatic, *J* = 7.30 Hz), 7.03 (d, 1H, -CHFBr, J_{gem} = 49.45 Hz) 3.12 (q, 2H, CH_2, *J* = 6.49 Hz), 2.27 (t, 2H, CH_2, *J* = 7.34 Hz), 1.57 (m, 2H, CH_2), 1.46 (m, 2H, CH_2), 1.28 (m, 2H, CH_2). ^{13}C NMR (DMSO-d_6) δ: 189.88, 171.63, 164.66 (d, -C=O-CF, J = 22.13 Hz), 139.70, 128.97, 123.34, 119.58, 85.93 (d, -CHFBr, J = 262.46 Hz), 36.67, 28.89, 26.21, 25.13 ppm. ^{19}F NMR (DMSO-d_6) δ: -147.34 (d, *J* = 50.35 Hz), -143.52 (d, J = 48.83). HRMS (m / z): $[M + H]^+$ calculated for $C_{14}H_{20}FBrN_2O_2$, 367.0445; found 367.0433 (M+H).

Diastereomer 2: ^{1}H NMR (DMSO-d_6) δ: 9.83 (s, 1H, NH), 8.62 (s, 1H, NH), 7.56 (d, 2H, aromatic, *J* = 8.11 Hz), 7.26 (t, 2H, aromatic, *J* = 7.30 Hz), 6.99 (t, 1H, aromatic, *J* = 7.30 Hz), 7.03 6.74 (d, 1H, -CHFBr, J_{gem} = 49.45 Hz), 3.12 (q, 2H, CH_2, *J* = 6.49 Hz), 2.27 (t, 2H, CH_2, *J* = 7.34 Hz), 1.57 (m, 2H, CH_2), 1.46 (m, 2H, CH_2), 1.28 (m, 2H, CH_2). ^{13}C NMR (DMSO-d_6) δ: 189.88, 171.63, 164.66 (d, -C=O-CF, J = 22.13 Hz), 139.70, 128.97, 123.34, 119.58, 85.93 (d, -CHFBr, J = 262.46 Hz), 36.67, 28.89, 26.21, 25.13 ppm. ^{19}F NMR (DMSO-d_6) δ: -147.34 (d, *J* = 50.35 Hz), -143.52 (d, *J* = 48.83). HRMS (m / z): $[M + H]^+$ calculated for $C_{14}H_{19}FBrN_2O_2$, 367.0445; found 367.0433 (M+H).

Preparation of 6-(bromodifluoroacetamido)-1-hexanoicanilide (2b): Comound **1** (200 mg, 0.97 mmol) was dissolved in dimethylformamide (7.0 mL) with two equivalents of diisopropylethylamine and stirred at 0 °C. 2-bromodifluoro acetyl chloride (0.2 mL, 2.2 mmol) was added drop-wise to the mixture. The mixture was subsequently stirred at 0 °C for 1 hour then warmed to room temperature and stirred for an additional 3 hours under argon. After evaporation of solvent, the compound was purified using flash column chromatography with a gradient of 10-50% ethyl acetate/hexane as the eluent. Product **2b** (150 mg) was obtained after evaporation as a white solid with 50% yield. ^{1}H NMR (DMSO-d_6) δ: 9.83 (s, 1H, NH), 9.17 (s, 1H, NH), 7.54 (d, 2H, aromatic, *J* = 7.34 Hz), 7.34 (t, 2H, aromatic, *J* = 7.34 Hz), 6.99 (t, 1H, aromatic, *J* = 7.83 Hz), 3.15 (q, 2H, CH_2, *J* = 6.36 Hz), 2.27 (t, 2H, CH_2, *J* = 7.34 Hz), 1.58 (m, 2H, CH_2), 1.49 (m, 2H, CH_2), 1.28 (m, 2H, CH_2). ^{13}C NMR (DMSO-d_6) δ: 171.42, 159.95 (t, -CO-CF_2Br, *J* = 27.47 Hz), 139.71, 129.03, 123.21, 119.33, 112.21 (t, -CF_2Br, J = 315.10 Hz), 36.70, 28.58, 26.40, 25.21 ppm. ^{19}F NMR (DMSO-d_6) δ: -60.07 (s). HRMS (m/z): $[M+H]^+$ calculated for $C_{14}H_{17}N_2O_2F_2Br$ 363.0520, found 363.0515.

Preparation of 6-(difluoroacetamido)-1-hexanoicanilide (DFAHA 3a): Compound **1** (200 mg, 0.97mmol) was stirred in difluoroacetic anhydride at room temperature until fully dissolved. And then triethylamine (1 mL, 7.2 mmol) was added gradually until the pH of the solution reached a value close to 8. The reaction mixture stirred at room temperature overnight. The anhydride was removed under reduced pressure and the residue was purified by flash chromatography using 50% ethyl acetate in hexane. Product **3a** was obtained as a white powder in a 42% yield. ^{1}H NMR (DMSO-d_6) δ: 9.82 (s, 1H, NH), 8.75 (s, 1H, NH), 7.56 (d, 2H, aromatic, *J* = 7.83 Hz), 7.26 (t, 2H, aromatic, *J* = 7.34 Hz), 6.99 (t, 1H, aromatic, *J* = 7.34 Hz), 6.16 (t, 1H, -CHF_2, J_{gem} = 53.8 Hz), 3.12 (q, 2H, CH_2, *J* = 13.1, 6.7 Hz), 2.28 (t, 2H, CH_2, *J* = 7.34 Hz), 1.57

(m, 2H, CH_2), 1.46 (m, 2H, CH_2), 1.27 (m, 2H, CH_2). ^{13}C NMR (DMSO-d_6) δ: 171.42, 162.48 (t, -CO-CF2, J = 24.41 Hz), 139.71, 129.03, 123.21, 119.33, 108.98 (t, -CHF_2, J = 246.44 Hz), 36.83, 28.74, 26.47, 25.18 ppm. ^{19}F NMR (DMSO-d_6) δ: -125.65 (d, *J* = 54.93 Hz). HRMS (m / z): [M + H]$^+$ calculated for $C_{14}H_{19}F_2N_2O_2$, 307.1234; found 307.1226 (M+H).

Preparation of 6-(trifluoroacetamido)-1-hexanoicanilide (TFAHA 3b): Compound **1** (100 mg, 0.48 mmol) was dissolved in trifluoacetic anhydride (1.0 g, 4.76 mmol) and 2mL of dichloromethane at 0°C. The reaction mixture was stirred under argon for 20 min and then 2 hours at room temperature overnight. The solvent was evaporated and the crude compound was purified by flash column chromatography using 30% ethyl acetate in hexane. After evaporation of the solvent, the product **3b** was obtained as white solid in 51 % yield. ^{1}H NMR (DMSO-d_6) δ: 9.83 (s, 1H, NH), 9.4 (s, 1H, NH), 7.57 (d, 2H, aromatic, *J* = 8.8 Hz), 7.25 (t, 2H, aromatic, *J* = 7.83 Hz), 6.99 (t, 1H, aromatic, *J* = 6.85 Hz), 3.16 (q, 2H, CH_2, *J* = 13.1 Hz, *J* = 6.7), 2.28 (t, 2H, CH_2, *J* = 7.5 Hz), 1.57 (m, 2H, CH_2), 1.49 (m, 2H, CH_2), 1.27 (m, 2H, CH_2). ^{13}C NMR (DMSO-d_6) δ: 171.61, 156.51(q, -CO-CF3, *J* = 71.6, 35.86 Hz), 139.83, 129.18, 123.52, 119.42, 116.45 (q, -CF_3, *J* = 576.6, 288.40 Hz), 36.69, 28.47, 26.30, 25.09 ppm. ^{19}F NMR (DMSO-d_6) δ: -74.32 (s). HRMS (m / z): [M + H]$^+$ calculated for $C_{14}H_{18}F_3N_2O_2$, 303.1320; found 303.1312 (M+H).

Radiosynthesis of 6-([^{18}F]difluoroacetamido)-1-hexanoicanilide ([^{18}F]DFAHA 4a): A solution of K[^{18}F]/kryptofix in acetonitrile (1 ml) was received and transferred into a crimped V-vial. The acetonitrile removed under a stream of argon at 105°C. A solution of **2a** (6-7 mg) in dry acetonitrile (0.4 mL) was added to previously dried K^{18}F/kryptofix and the mixture was heated at 100°C for 20 minutes. The reaction was cooled and the mixture was passed through a silica gel cartridge (Alltech, 900 mg) and eluted with 30% methanol in dichloromethane (2.5 mL). After evaporation of the solvent under a stream of argon at 80°C, the mixture was re-dissolved in HPLC

solvent and purified by semi-preparative HPLC using 40% ACN/buffer solution. The compound eluted at 9.7 minutes. The solvent was evaporated under reduced pressure and the final product was re-dissolved in saline for animal injection. The product purity and identity was confirmed by co-injection with an authentic non-radiolabeled (**4a)** using an analytical HPLC. The compound was obtained in 25% decay corrected yield, with > 95% purity, and specific activity of 60-70 GBq/µmole.

Radiosynthesis of 6-([^{18}F]trifluoroacetamido)-1-hexanoicanilide ([^{18}F]TFAHA 4b)*:* A solution of kryptofix/ K[^{18}F] in acetonitrile (1 ml) was received and transferred into a crimped V-vial. The acetonitrile removed under a stream of argon at 105°C. A solution of **2b** (6-7 mg) in dry acetonitrile (0.4 mL) was added to previously dried K^{18}F/kryptofix and the mixture was heated at 100°C for 20 minutes. The mixture was heated and stirred at 110°C for 25 minutes. The reaction was cooled and the mixture was passed through a silica gel cartridge (Alltech, 900 mg) and eluted with 30% methanol in dichloromethane (2.5 mL). After evaporation of the solvent under a stream of argon at 80°C, the mixture was re-dissolved in HPLC solvent and purified by semi-preparative HPLC using 40% ACN/buffer solution. The compound was eluted at 20 minutes. The solvent was evaporated on a high vacuum pump and the desired product was re-dissolved in saline for animal injection. The solvent was evaporated under reduced pressure and the final product was re-dissolved in saline for animal injection. The product purity and identity was confirmed by co-injection with an authentic non-radiolabeled (**4b)** using an analytical HPLC. The product was obtained in a 22% decay corrected yield, with > 95% purity, and specific activity of 70-80 GBq/µmole.

In vitro HDAC enzyme affinity assay: *In vitro* enzyme assays were performed for a panel of Class I, II, III, and IV HDACs. 10 nmol solution of each test compound or 2 nmol of control

substrate 2A (BPS Bioscience, San Diego, CA) was incubated in 100 µl of the HDAC assay buffer (25 mM Tris-HCl, pH 8.0, 137 mM NaCl, 2.7 mM KCl, 1 mM $MgCl_2$) in the presence or absence of 1µg/ 100 µl of different HDAC enzymes (BPS Bioscience, San Diego, CA) at 37°C for 60 min. The reaction was quenched by heating the assay at 95°C for 3 min. Subsequently, 25 ul of the reaction mixture was analyzed by analytical HPLC (Agilent, Santa Clara, CA) equipped with Econosil C18 column (Altech Associates, Deefield, IL) using a mobile phase: 50% acetonitrile / 20 mM ammonium acetate, pH=8.5. Detection of reaction products was detected via UV detection at 240 nm. The area under the peak corresponding to hexanoic anilide reaction product were integrated and expressed as percent of the area under the peak of the parent compound and converted into mass (moles). The K_{cat} parameters were determined as described elsewhere (Leskovac, 2003) using software GraphPad Prism 4 (GraphPad Software, La Jolla, CA).

In silico modeling: The crystal structures 1T69 and 2VQJ were used for the docking studies of HDAC8 and HDAC4 respectively. For HDAC8 the missing residues 1-13 and 85-90 were added using MODELLER (UCSF, San Francisco, CA) (Sali and Blundell, 1993). The residues 85-90 are involved in the formation of a loop that is in close proximity to the inhibitor binding region of HDAC8. Due to this potential importance, the loop formed by these MODELLER-added residues was further refined using Chimera (UCSF, San Francisco, CA) (Pettersen et al., 2004). The two crystal structures were hydrogenated using MolProbity software (Duke University, Durham, NC) (Chen et al., 2009). Docking calculations were performed using the FlexX algorithm (Rarey et al., 1996) as implemented in the LeadIT software package (BioSolveIT GmbH, Germany) (BioSolveIT et al.). For both HDAC8 and HDAC4, native ligands in the crystal structure (namely SHH for HDAC8 and TFG for HDAC4) were used as reference ligands for the docking calculations. A grid volume that covered amino acids within 20Å from each reference ligand was

used. All the waters within the grid volume were taken as freely rotatable and displaceable. Pharmacophore rules based on the knowledge of ligand-receptor binding were used to guide the ligands towards the binding site. For both HDAC8 and HDAC4 docking was performed with the ligands AHA, FAHA, DFAHA, and TFAHA. Top 20 poses based on the docking score of each docking run were saved and the top 10 poses were used for binding affinity calculations using Hyde software (BioSolveIT GmbH, Germany) (Lange, 2010; Schneider et al., 2013).

PET Imaging Procedures in Animals: All studies involving animals were performed under a protocol (A 6-13-13) approved by the Institutional Animal Care and Use Committee of Wayne State University. Sprague-Dawley rats (200-250 g, N=3) were anesthetized with 3% isoflurane in oxygen and maintained at 2% isoflurane in oxygen throughout the imaging studies. The body temperature was maintained using electronically-controlled heating pad (M2M Imaging, Cleveland, OH) set at 37^{o}C. Anesthetized rats were placed in the microPET R4 scanner (Siemens, Knoxville, TN) in the supine position with the long axis of the animal parallel to the long axis of the scanner with the brain positioned in the center of the field of view. Each radiotracer (300-500 µCi/animal) was administered in saline via the tail-vein injection in a total volume ≤1.25 ml. Dynamic PET images were obtained over 60 minutes, followed by 2 overlapping frames (5 min each) acquired to obtain a whole body images of radiotracer biodistribution in other organs and tissues. After PET imaging, the positioning bed with the affixed anesthetized animal was transferred to the Inveon SPECT/CT scanner (Siemens, Knoxville, TN) and CT images and 4 overlapping frames (2 min each) were acquired covering the whole body using X-ray tube settings of 80 kV and 500 uA.

Quantitative Autoradiography: After PET imaging (or at certain time point after 300-500 µCi radiotracer injection i.v.), the animals were sacrificed, the brain was rapidly extracted, frozen,

and embedded in the mounting medium M1 (Shandon-Lipshaw, Pittsburg, PA). Serial 20 µm thick coronal sections of frozen brain tissue were obtained at -13°C using a cryomicrotome CM3050S (Leica, Germany). Tissue sections were thaw-mounted on poly-A lysine coated glass slides and heat-fixed for 5 min at 65°C on a slide warmer (Fischer Scientific, PA). For QAR, tissue sections were exposed to the phosphor plate (Fujifilm Life Science, Woodbridge, CT) along with set of 20 µm autoradiographic standards of known 18F radioactivity concentration, freshly prepared using calf liver homogenate. Knowing the radioactivity concentration in standards, the injected dose, and optical densities of each reference standard, a standard curve was developed, based on which the autoradiographic images were converted to color-coded parametric images of percent injected dose/g tissue (%ID/g) and/or standard uptake values (SUV) using software MCID 7.0 (Interfocus Imaging Ltd., Cambridge, UK).

Image Analysis and Quantification: PET images were reconstructed using ordered subset expectation–maximization (Guo et al.) method. PET image analysis was accomplished using the AMIDE software. Digital Rat Brain Atlas was used for alignment and identification of specific anatomical markers in the brain (Watson, 2006). GraphPad Prism 6 (Graph Pad Software La Jolla, CA) and Excel 2010 (Microsoft, Redmond, WA) were used for image data analysis. Levels of accumulation of individual radiotracers in tissues were expressed as standard uptake values (SUV) that were calculated for the regions of interest (Ron S. Broide and Floyd E. Bloom) using the AMIDE software. The SUV is defined as the ratio of the tissue radioactivity concentration C (e.g. expressed as Bq/g tissue) at given time point post injection T, and the injected dose (e.g. in Bq, decay-corrected to the same time T), and normalized by the body weight in grams. Formulas for calculations for Logan plot analysis are provided in the supplemental materials (Logan J, 1996).

Acknowledgements

This work was supported by the NCI CCSG Core Grant CA 016672 and RC2 DA028912-01 (NIH/NIDA) to JG. The Microscopy, Imaging and Cytometry Resources Core is supported, in part, by NIH Center grant P30 CA022453 to the Karmanos Cancer Institute at Wayne State University, and the Perinatology Research Branch of the National Institutes of Child Health and Development at Wayne State University.

Supporting Information

Quantification of dynamic PET imaging by multi-graphical analysis

To locate the exact ROI's the Rat Brain Atlas was referenced and the corresponding maps to PET images are shown in **Fig. 15**. While exact co-localization was difficult because the animal was not perfectly planar, these images show a very close representation of the sites for metabolite accumulation of the radiotracer. While the primary ROI of this paper is the cerebellum, the other regions of specific uptake are quantified and shown in **Fig. 16.**

$$\frac{\int_0^T C_t(t)dt}{C_t(T)} = DVR \times \frac{\int_0^T C_r(t)dt}{C_t(T)} + C$$

BP=DVR-1

We used the heart-derived blood time-activity curve (TAC) as an input function between 0 and 30 min, because a previous study showed that blood radioactivity

during the first 30 min post-i.v. injection of [^{18}F]FAHA is predominantly caused by the parent un-metabolized compound.

The dynamic PET imaging data were analyzed using Logan graphical analysis (25) to determine whether [^{18}F]TFAHA PET/CT imaging could have highest substrate affinity for HDAC 4 and 5. The ratio of integrated radioactivity concentration in ROIs over time normalized by the radioactivity concentration at a given time point in tumor radioactivity concentration was set as the y-axis. The ratio of integrated reference tissue radioactivity concentration over time normalized by tumor radioactivity concentration was set as the x-axis of a Logan plot. The cortex was used as reference tissue, because relatively it has low HDAC4 and 5 activity or expression in

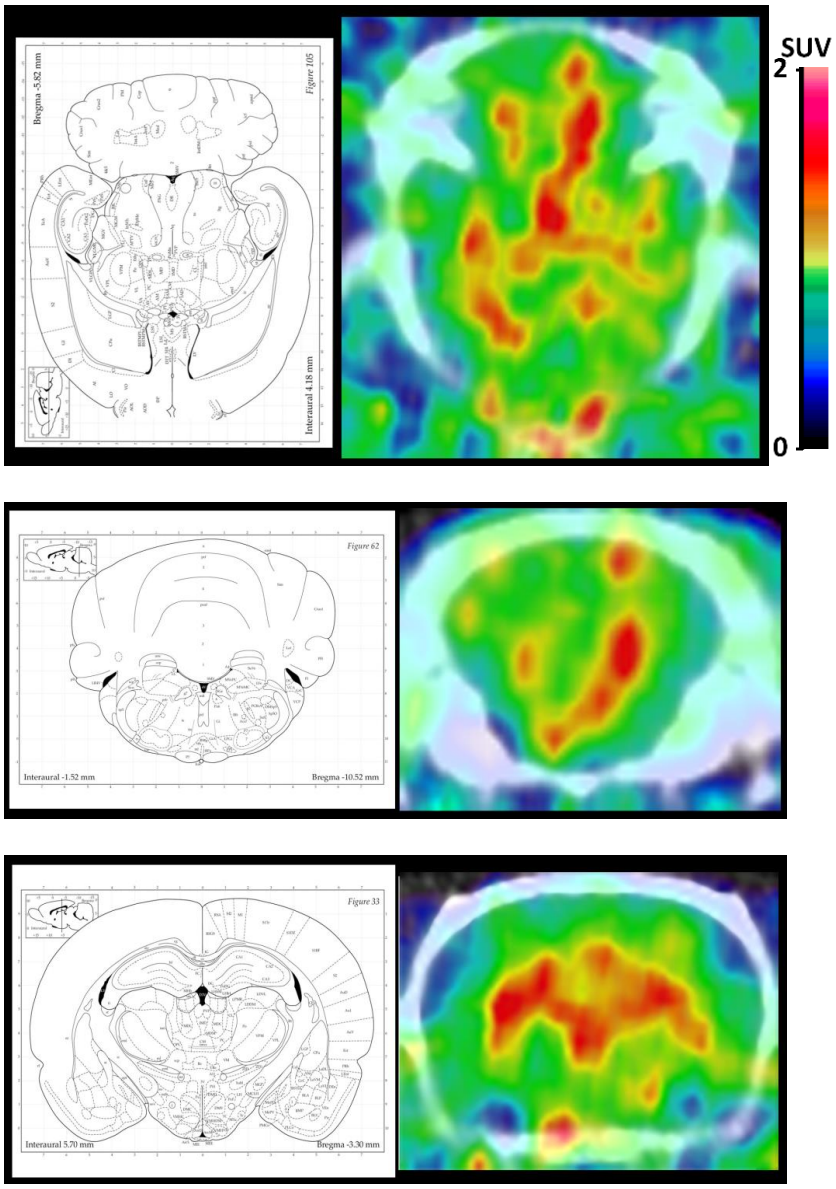

Figure 15. The corresponding map and brain image for co-localization and ROI identification.

the brain. The slope of the linear portion of the Logan plot is the distribution volume ratio (DVR). The slope of the linear portion of the lot is calculated as (**Eq. 2**). The binging potential (BP) can be calculated as **Eq. 3**. For these calculations the target ROI used is the cerebellum. The y-intercept is denoted as C' and used to accommodate for differences in the immediate tracer uptake by tissue.

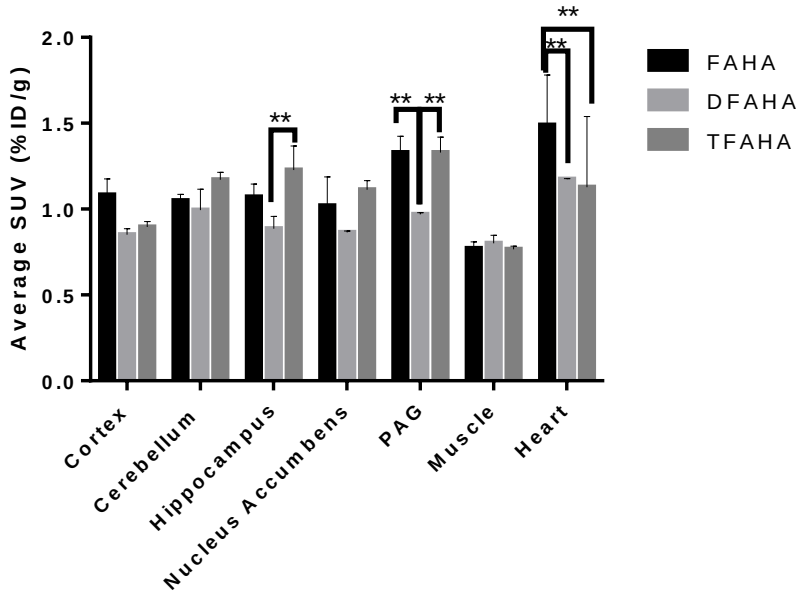

Figure 16. The average calculated SUV quantification for each of the ROI's and reference tissues for all three compounds. The error bars represent the standard deviation of the data. The stars indicate statistical significance obtained by two-way ANOVA with $P < 0.01$.

^{18}F-FAHA has non-specific interactions to many other HDAC enzymes in the brain. Therefore, it shows a higher level of accumulation. The specific interaction, however, is actually much higher for TFAHA and DFAHA because these have a very similar uptake but act on far fewer enzymes. These conclusions are supported by the biochemical results showing that FAHA is a substrate for many of the HDAC enzymes in all four classes. The plot in **Fig. 17** is the Logan plot given by **Eq. 2** show the uptake for [^{18}F]FAHA is very similar to that of [^{18}F]DFAHA, while [^{18}F]TFAHA uptake has a steeper slope and therefore higher levels of metabolite accumulation in the cerebellum.

Following PET/CT *in vivo* imaging with [^{18}F]TFAHA, quantitative autoradiography (QAR) was performed to verify the results at higher resolution. **Fig. 18** demonstrates a high degree of correlation between the areas of ^{18}F-TFAHA-derived accumulation displayed by autoradiography and the PET images in **Fig**. **15.** Higher levels of accumulation of [^{18}F]TFAHA were observed in n. accumbens, hippocampus, periaqueductal grey, and cerebellar nuclei.

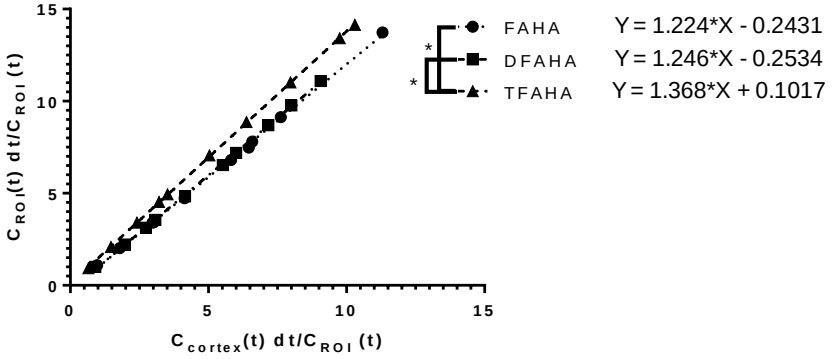

Figure 17. The Logan plot for the primary ROI, cerebellum, with the cortex used as a reference tissue. The stars represent statistical significance as determined by comparison of linear regression fit with a $P < 0.01$.

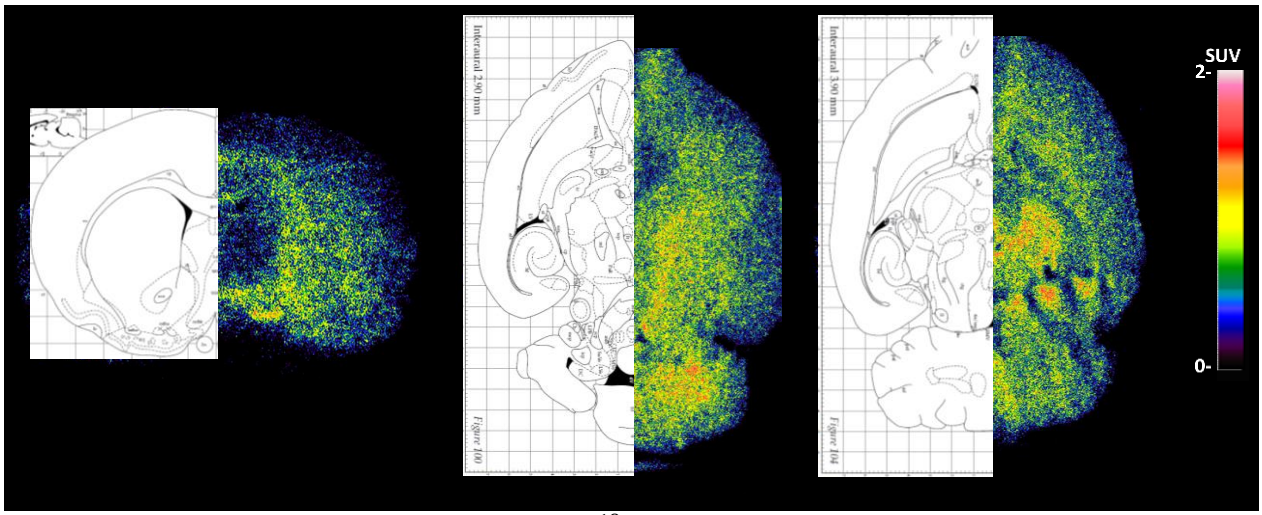

Figure 18. Quantitative autoradiography for ^{18}F-TFAHA in the rat brain following *in vivo* i.v. injection of the radiotracer and PET imaging. The rat brain atlas maps are shown with the images for co-registration.

Furthermore, our preliminary imaging studies in a rat demonstrated the feasibility of PET/CT with [^{18}F]TFAHA for monitoring pharmacologic inhibition of HDACs class IIa with SAHA. Significant inhibition of [^{18}F]TFAHA-derived radioactivity accumulation in the brain was observed when SAHA (100 mg/kg) was administered i.p. 30 min prior to i.v. administration of [^{18}F]TFAHA (**Fig. 19**). Additionally, we are currently conducting expanded studies in rats to determine the IC_{50} values for SAHA for different regions of the brain.

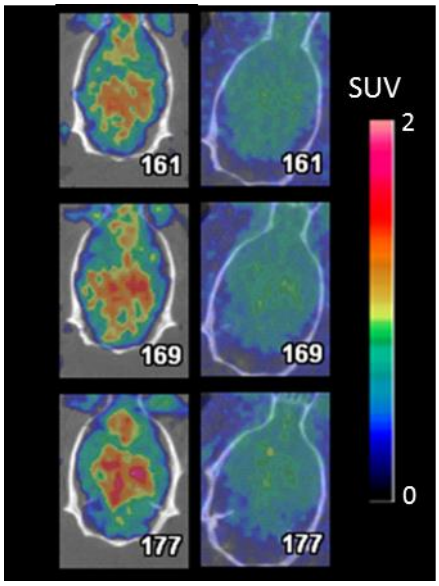

Figure 19. A normal rat imaged with ^{18}F-TFAHA before (left) and after (right) 100mg/kg injection of HDAC inhibitor, SAHA.

3b. Continuing work

Due to the prevalence of HDACs 4 and 5 in the *n. accumbens*, *hippocampus*, *amygdala*, *periaqueductal grey*, and *cerebellum* in the brain and immunohistochemistry data suggesting that HDACs class IIa enzymes are overexpressed in cases of brain trauma and stress, the disease model proposed for study is post-traumatic stress disorder (PTSD) (Kwapis and Wood, 2014; Zovkic et al., 2013). The rat model for PTSD has been well established by Dr. Perrine's group using a method termed single-prolonged stress (SPS) (Eagle et al., 2013a; Eagle et al., 2013b; Knox et al., 2010). In conjunction with Dr. Perrine's group, the efficacy of ^{18}F-TFAHA as an imaging agent for PTSD will be studied in rats. The aim is to understand the changes in relative expression of HDAC class IIa enzymes in the brain at varying time points after a traumatic event. Quantification of ^{18}F-TFAHA-derived radioactivity accumulation in areas of the brain known to express high levels of HDAC class IIa (primarily HDACs 4, 5 and 9) will be used as a method for a non-invasively monitoring changes enzymatic activity. These PET/CT images will also be compared

against IHC stained sections from sacrificed animals at each time point (24hrs, 7d, 14d post SPS) to verify imaging results. Furthermore, autoradiography will be done on some of these animals to gain higher resolution images of the radioactivity distribution within the brain. These may also be done with dual labeling to allow for comparison between C^{14}-$C_6H_{12}O_6$ and ^{18}F-TFAHA distribution. Preliminary work in this project has demonstrated significant differences as compared to baseline in ^{18}F-TFAHA-derived accumulation in areas of the brain known to have high HDAC class IIa expression-activity, especially at 24h post SPS. As this has evolved into a very large project due to promising results, the majority of the work will be presented in a separate PhD thesis of another student in BME.

Additionally, HDACs class IIa has demonstrated promise for treatment of cancers, There are many HDAC targeted drugs (HDACs class I and II) currently in clinical or pre-clinical use for treatment of lymphomas and leukemias, in particular. Recently, HDACs class IIa targeted inhibitors have also arisen and shown promise in preclinical work for inhibiting melanoma cell growth and proliferation (Venza et al., 2013). Furthermore, in identifying HDAC regulatory enzymes with upregulation in a very aggressive form of brain cancer, gliomas, HDACs 4 and 5 demonstrated significant increase in expression via immunohistochemical (IHC) staining in patient derived tissues (Protein Data Bank). Therefore, PET imaging of glioma tumor models using ^{18}F-TFAHA as an HDACs class IIa-selective imaging agent may lead to furthering the understanding of HDAC-mediated epigenetic regulation in pathophysiology of disease.

^{18}F-TFAHA has shown great promise as an imaging agent for detection of glioma cancer in the brain. In studies of both U87 and 9L rat glioma models clear detection of the tumor is differentiable from the rest of the brain and demonstrates significantly different uptake between structures in the brain and the tumor. This will be expanded upon in chapter 5. An example image

for ^{18}F-TFAHA characterization in 9L an U87 tumor models are demonstrated below in **Fig. 20-21**. Within the tumor images, large amounts of intratumoral heterogeneity is visible as demonstrated by the distribution of ^{18}F-TFAHA-derived radioactivity within the areas of tumor tissue, i.e. areas of high and low expression activity of HDACs class IIa. Also, many differences in HDACs class IIa expression between 9L and U87 tumors, both in degree of expression as well as localization, are visible within these images. The localization and expression-activity of HDACs class IIa will be compared and contrasted with SIRT1 heterogeneity in chapter 5. In summary, HDACs class IIa are upregulated within tumor tissue as demonstrated by increases in ^{18}F-TFAHA-derived radioactivity accumulation as observed via *in vivo* PET/CT imaging. This finding provides a promising opportunity for identifying treatments to slow or reverse tumor progression in this aggressive form of cancer.

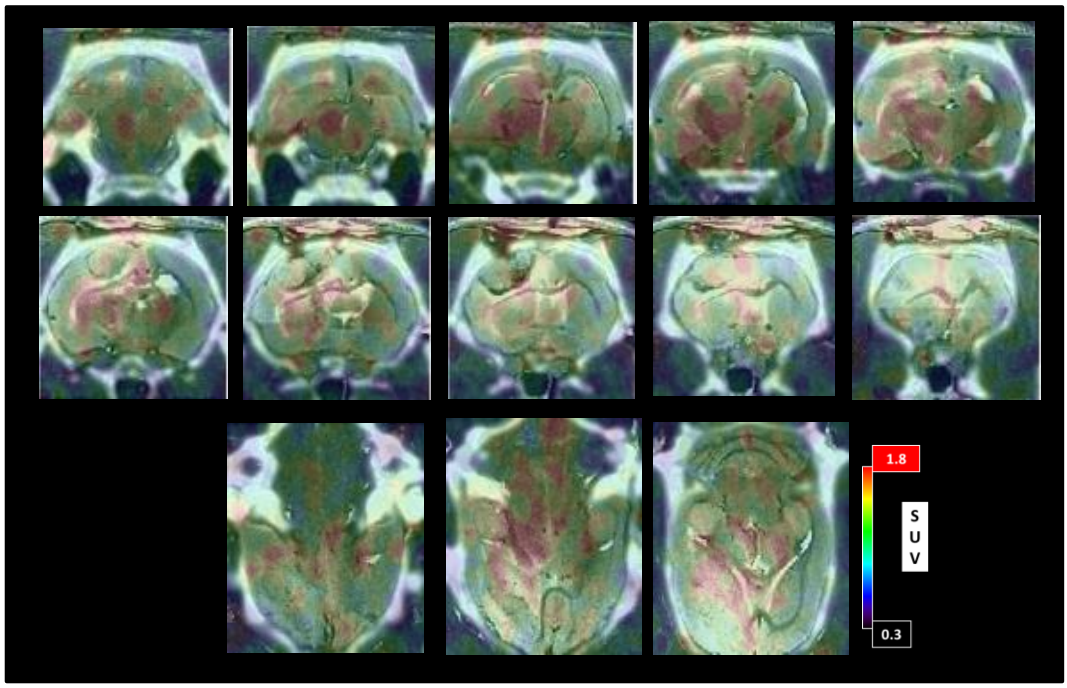

Figure 20. Dynamic PET/CT images using ^{18}F-TFAHA in a 9L tumor-bearing rat, with PET/CT images overlaid on MR. These images demonstrate increased accumulation of the radiotracer in areas of the tumor lesions with relatively higher levels of HDAC activity.

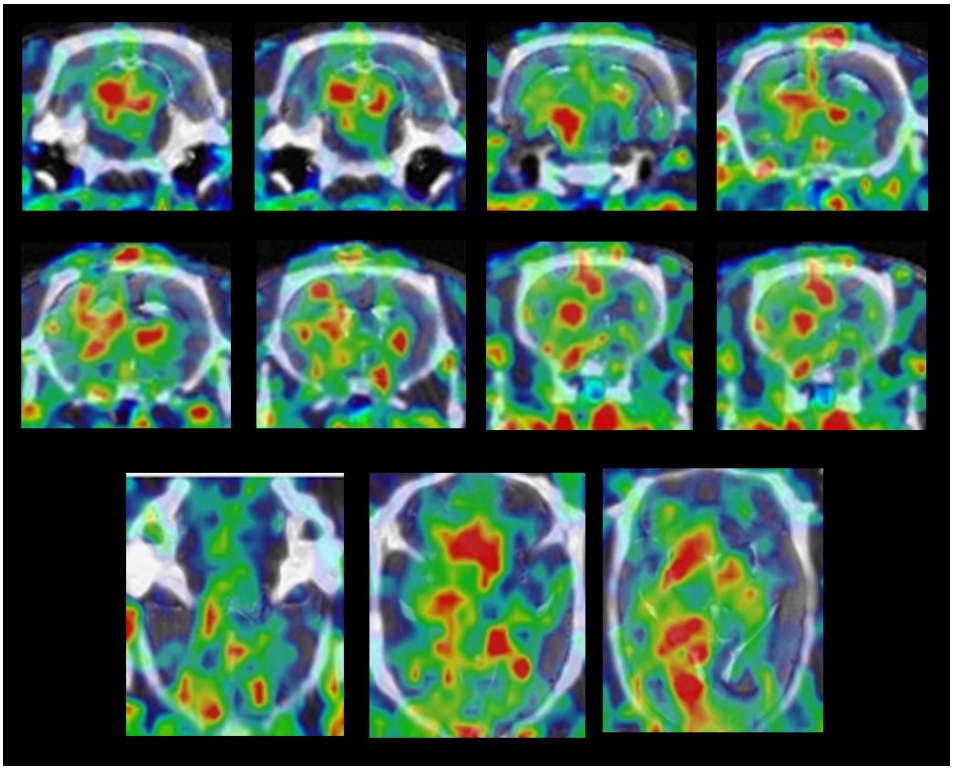

Figure 21. Dynamic PET/CT images using ^{18}F-TFAHA in a U87 tumor-bearing rat, with PET/CT images overlaid on MR. These images demonstrate increased accumulation of the radiotracer in areas of the tumor lesions with relatively higher levels of HDAC activity.

CHAPTER 4 DEVELOPMENT OF NOVEL PET IMAGING SUBSTRATES FOR SIRT2

This work has been submitted as a provisional U.S. Patent.

Towards the development of a novel radiotracer for quantitative imaging of SIRT2 expression activity with PET, a focused library of potential substrates of SIRT2 has been synthesized with tert-butyloxycarbonyl-lysine-aminomethylcoumarin (Boc-Lys-AMC) backbone derivatized on the free amino terminus of lysine with a fluoroalkyl chain varying between 3 and 16 carbons in length. Enzyme kinetic studies with recombinant SIRT2 demonstrated most efficient cleavage of the myristoyl group, followed by 12-fluorododecanoic and 10-fluorodecanoic groups (k_{cat}/k_m equals 716.5 ± 72.8, 615.4 ± 50.5, 269.5 ± 52.1 $s^{-1}M^{-1}$, respectively). Subsequently, an aminohexanoicanilide (AHA) backbone was derivatized with 12-bromo- and 12-iododecanoic groups to generate precursors for radiosynthesis of 12-[^{18}F]fluorododecanoic aminohexanoicanilide (12-[^{18}F]DDAHA). *In vitro* uptake studies demonstrated a three-fold higher accumulation of 12-[^{18}F]DDAHA in U87 glioma cells with high SIRT2 activity, as compared to MiaPaCa, MDA-MB-231, and MCF10A cells with relatively lower SIRT2 activity. Non-invasive PET imaging with 12-[^{18}F]DDAHA should enable *in vivo* studies of SIRT2-mediated epigenetic regulation in normal physiology and in different diseases, and to facilitate the development of novel SIRT2-targeted therapies.

4a. A novel substrate radiotracer for molecular imaging of SIRT2 expression and activity with positron emission tomography

Robin E. Bonomi, Vadim Popov, Aleksandr Shavrin, Philip Alther, Nashaat Turkman, Thomas Mangner, Juri G. Gelovani

Introduction

SIRT2 is primarily localized in the cytoplasm, but can translocate into the nucleus (North and Verdin, 2007a) and deacetylase of cytoplasmic alpha-tubulin and nuclear H4K16 proteins,

thereby acting as a mitotic exit and cell cycle regulator (Hiratsuka et al., 2003; Inoue et al., 2007a; Inoue et al., 2007c; Inoue et al., 2009; North and Verdin, 2007a; North and Verdin, 2007b). Several studies have revealed important roles of SIRT2 in the pathogenesis of various diseases. SIRT2 can play a neuroprotective role in neuorodegenerative diseases, such as Parkinson's, Alzheimer's (Wang et al., 2013), and Huntington's (Donmez and Outeiro, 2013). SIRT2 has been identified as having both cancer-promoting functions (i.e., through stabilization of Myc oncoproteins in breast cancer (Liu et al., 2013), (McGlynn et al., 2014)), as well as cancer suppressing functions (i.e., through tubulin regulation (Hiratsuka et al., 2003)). Therefore, SIRT2 has been identified as a potential drug target for treatment of various neurodengenerative and inflammatory diseases, and cancer. However, it is important to assess its activity during pharmacomodulation (i.e., activation or inhibition) due to pleiotropic roles of SIRT2 under normal and pathologic conditions. The development of non-invasive molecular imaging approaches for monitoring SIRT2 expression and activity *in vivo* using PET with SIRT2-selective substrate radiotracer may aid in the development of therapies targeting SIRT2.

Understanding structure-activity relationships (SAR) of SIRT2 and its endogenous substrates is important for the development of SIRT2-specific substrate-type radiotracers. The best studied endogenous substrates of SIRT2 are acetyl-α-tubulin and acetyl-H4K16. SIRT2, similar to other SIRT isoforms namely 4, 5, and 6, is able to cleave larger moieties outside of the acetyl. In particular, it has been demonstrated that SIRT2 can cleave a myristoyl group from the myristoyl-(K19 and K20)TNFα (Yao and Yang, 2011).

To explore the efficiency with which SIRT2 cleaves larger leaving groups, a focused library of potential substrates was synthesized with tert-butyloxycarbonyl-lysine-aminomethylcoumarin (Boc-Lys-AMC) backbone derivatized on the free amino terminus of lysine with a fluoroalkyl

chain varying between 3 and 16 carbons in length. Additionally, the influence of fluorine substitution on the ω-carbon in the alkyl chain on substrate affinity and specificity for SIRT2 was evaluated as well. The library of compounds was studied using a fluorogenic enzyme assay with recombinant SIRT2 to determine trends in catalytic efficiency. Furthermore, the SAR of these compounds with SIRT2 was investigated using *in silico* modeling to better understand the observed trends (**Fig. 22**). Based on these studies, the lead compound, the Boc-Lys(12-fluorododecanoyl)-AMC, was identified and its analogue with an aminohexanoicanilide (AHA) backbone was synthesized (12-fluorododecanoic-AHA; 12-FDDAHA). The AHA backbone has been used previously to generate effective HDAC class IIa specific radiotracers: [^{18}F]FAHA and [^{18}F]TFAHA(Bonomi et al., 2015; Yeh et al., 2013a)[a,19b]. Additionally, the radiolabeled analogue

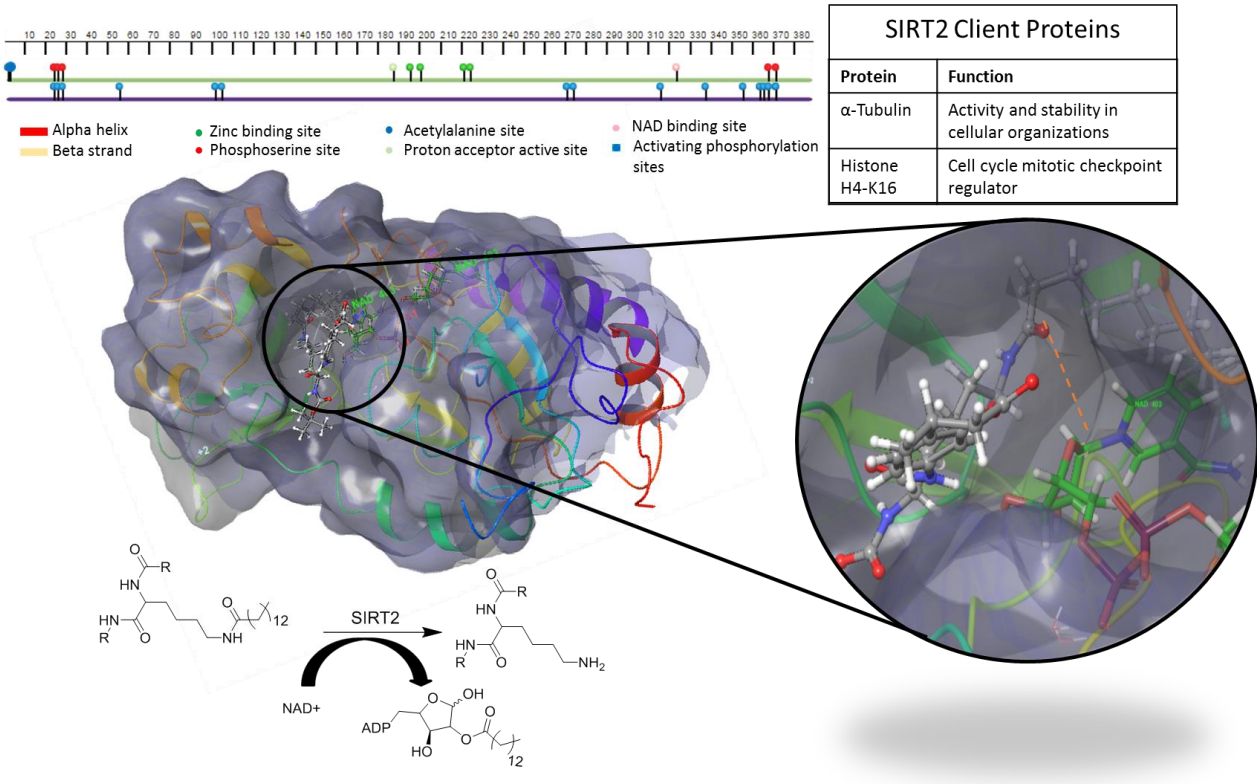

SIRT2 Client Proteins	
Protein	**Function**
α-Tubulin	Activity and stability in cellular organizations
Histone H4-K16	Cell cycle mitotic checkpoint regulator

Figure 22. The structure of SIRT2 docked with the Boc-Lys(12F-dodecanoyl)-AMC and NAD$^+$ adapted from crystal structure 4RMG. The SIRT2 sites of phosphorylation and binding highlighted on the residue chart. The SIRT2 client proteins are also listed in the table and the mechanism for NAD-dependent SIRT2 mediated cleavage of long acyl chains is depicted here.

of the lead compound, 12-[^{18}F]DDAHA, was synthesized from 12-iododododecanoic and 12-bromododecanoic precursors. Finally, the uptake of 12-[^{18}F]DDAHA was studied *in vitro* to determine the magnitude of radiotracer accumulation in cells with high versus low SIRT2 expression.

Results:

The library of compounds with terminally fluorinated acyl chains was synthesized through traditional coupling methods of the fluorinated carboxylic acid chain with the lysine amino derivative via in-situ formation of an acetyl chloride in moderate yields of 20-55%. Synthesis of the fluorinated carboxylic acid chains employed a novel approach: diethylaminosulfur trifluoride was used for non-selective fluorination of the n-hydroxycarboxylic acid forming the acetyl fluoride and fluorination of the terminal carbon. Selective hydrolysis of the acetyl fluoride was achieved using flash chromatography over silica gel to form a mono-ω-fluorinated chain due to the abrupt change in pH. The purity of final compounds in the

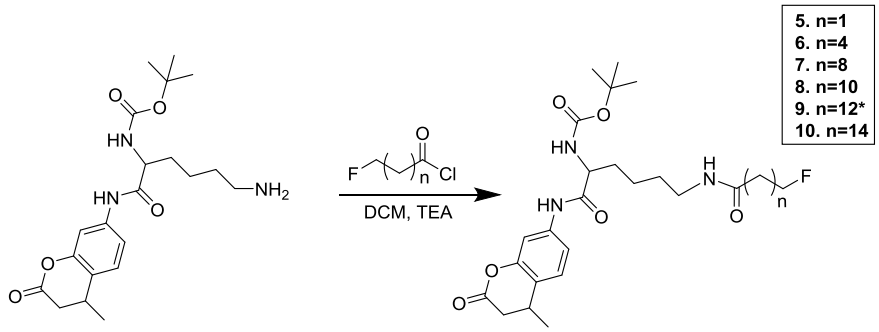

Figure 23. The focused library of compounds synthesized with fluroalkyl chain derivatized lysines. A) The backbone used *tert*-butyloxycarbonyl-L-lysine-7-amino-3-methylcoumarin (Boc-Lys-AMC) was coupled to fluoroalkyl chains, varying in length from 3 carbons to 16 carbons using acetyl chloride coupling.

library was >95%, as determined by ^{1}H-NMR, ^{13}C-NMR, ^{19}F-NMR, and HRMS (**Fig. 23**).

Compound **11** was synthesized from Cbz-Lys-OH (Bachem) and Boc-Lys-AMC (Bachem), which was derivatized to Boc-Lys(myr)-AMC. Following myristoylation, the Boc protecting group was removed and the resulting free lysine amino terminus was coupled with the Cbz-Lys-OH group. The four-step synthesis yielded **11** in a yield of 12% with >95% purity as determined by ^{1}H NMR, ^{13}C NMR, and HRMS (**Fig. 24**).

Results from *in vitro* characterization of this library of compounds using fluorogenic assay demonstrated a positive correlation between the substrate efficiency for SIRT2 and the increasing length of the leaving alkyl chain. Compound **9** containing the myristoyl group was the most efficient substrate of SIRT2 with K_{cat}/K_m = 715.6±72.8 $s^{-1}M^{-1}$followed by compound **8** (fluorododecanoyl) and compound **7** (fluorodecanoyl) with K_{cat}/K_m of 615.4±50.5 $s^{-1}M^{-1}$ and

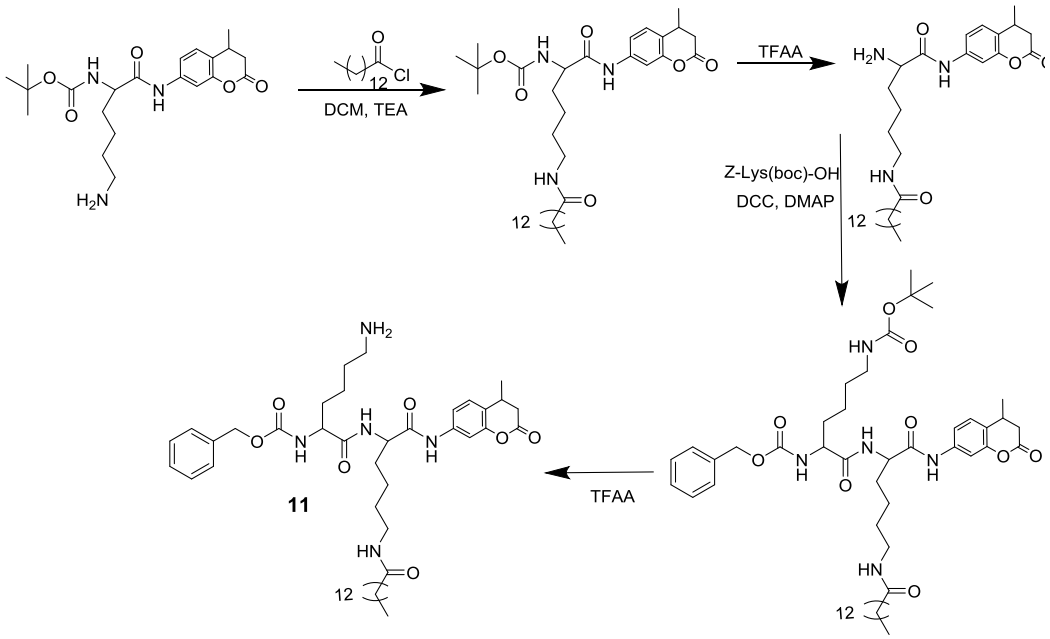

Figure 24. To experimentally determine the effect of the cap on the selectivity of a substrate for SIRT2 we developed a di-lysine substrate, with a more peptidic backbone, Cbz-lys-lys(myr)-AMC (**11**). This allows for head to head comparison between the Boc-lys(myr)-AMC (**9)**.

269.5±52.1 $s^{-1}M^{-1}$, respectively. In contrast, compound **10** containing the fluoropalmitoyl leaving

A

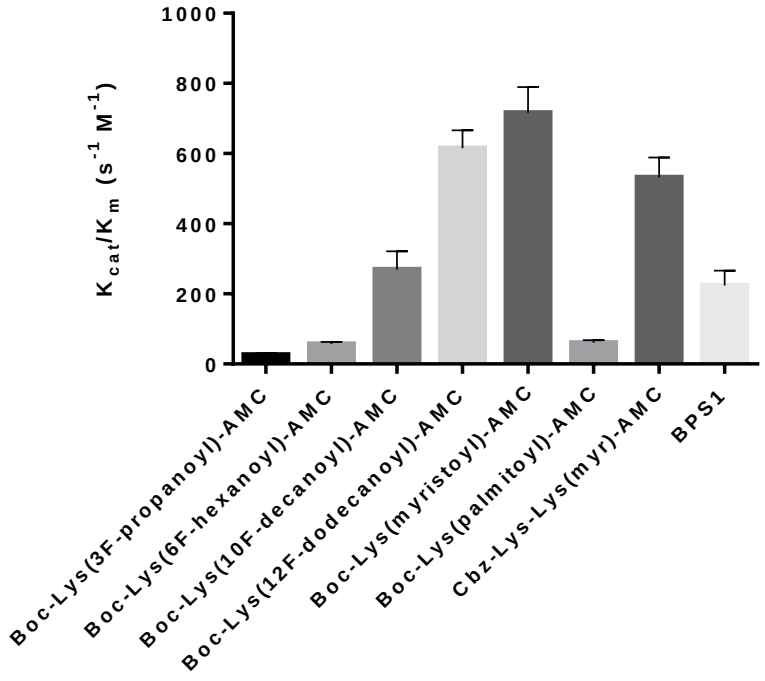

B

Compound	K_m (μM)	Stand. Dev.	V_{max} (uM/sec)	Stand. Dev.	K_{cat} (s^{-1})	Stand. Dev.	K_{cat}/k_m (s^{-1}, M^{-1})	Stand. Dev.
Boc-Lys(3F-propanoyl)-AMC (5)	53.53	11.44	0.15	0.016	1.41E-03	5.00E-04	26.3	5.07
Boc-Lys(6F-hexanoyl)-AMC (6)	44.89	4.56	0.28	0.013	2.58E-03	4.11E-04	57.4	5.22
Boc-Lys(10F-decanoyl)-AMC (7)	18.03	4.07	0.52	0.041	4.86E-03	1.29E-03	269.5	52.2
Boc-Lys(12F-dodecanoyl)-AMC (8)	8.07	0.79	0.54	0.014	4.97E-03	4.25E-04	615.4	50.5
Boc-Lys(myristoyl)-AMC (9)	2.36	0.22	0.26	0.010	2.38E-03	3.03E-04	716.5	72.9
Boc-Lys(fluoropalmitoyl)-AMC (10)	51.15	6.91	0.33	0.022	3.09E-03	6.83E-04	60.4	7.31
Cbz-Lys-Lys(myr)-AMC (11)	10.36	1.30	0.60	0.022	5.51E-03	6.88E-04	532.3	56.2
BPS1	31.73	5.57	0.95	0.022	8.78E-03	6.98E-04	275.0	42.6

Fig. 25. Biochemical assay data from fluorogenic (*Fluor de Lys*®) assay. **A)** The catalytic efficiency (k_{cat}/k_m) for SIRT2 against different length fluoroalkyl chain leaving groups to assess the structure activity relationship between these compounds and SIRT2. The error bars represent the standard deviation of N=6 experiments. **B)** The table details the effect on k_m (amount of substrate necessary for half of v_{max}), v_{max} (the maximal turnover velocity for a given substrate in SIRT2), and k_{cat} (the catalytic efficiency for a given substrate with SIRT2).

group exhibited a significant decrease in substrate efficiency for SIRT2 (30.4±7.3 $s^{-1}M^{-1}$), as compared to compounds containing shorter fluoroalkyl chains. The reference substrate, p53(379-382)K382ac-AMC (**BPS1**) exhibited K_{cat}/K_m = 275±42 $s^{-1}M^{-1}$ (**Fig. 25**).

To assess the influence of a "cap" modification on SIRT2 selectivity, compounds **4, 5** and **7** were evaluated against a panel of recombinant sirtuins (SIRT1-7). **7** was cleaved efficiently by

SIRT2, SIRT3 and, to a lesser extent, by SIRT6. In contrast, **8** and **9** were cleaved efficiently only by SIRT2 (**Fig. 26**). To validate the catalytic efficiency of SIRT2 with **8**, a competitive inhibition assay with AGK2 was performed, which yielded an IC_{50} of 28.21µM (**Fig. 27)**.

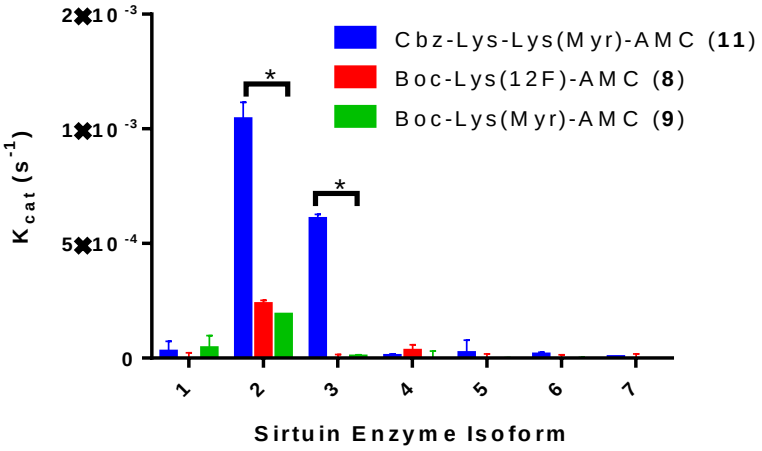

Figure 26. Compound **11** is not selective for SIRT2 whereas compounds **8** and **9** are selective for SIRT2. These results were taken from 40-minute incubation of substrate with enzyme. The error bars represent the standard deviations of the means with significance of $P<0.05$ denoted by *, as determined by two-way ANOVA.

In silico modeling studies demonstrated that positioning of compounds **8** and **9** in the SIRT2 active site resulted in a smaller distance between the carbonyl carbon and the nicotinamide-ribose ester linkage (**Fig. 28**). This may contribute to enhanced substrate efficiency of these compounds.

12-fluorododecanoyl-AHA (12-FDDAHA) and 12-[^{18}F]-dodecanoylAHA (12-[^{18}F]DDAHA) were synthesized as non-radiolabeled and radiolabeled analogues of **8** (**Fig. 29-30).** The initial radio-synthesis of 12-[^{18}F]DDAHA (**15**) was performed using a brominated precursor, 12Br-DDAHA (**13**), however due to low radiochemical yield, the iodinated precursor, 12I-DDAHA (**14**), was used for

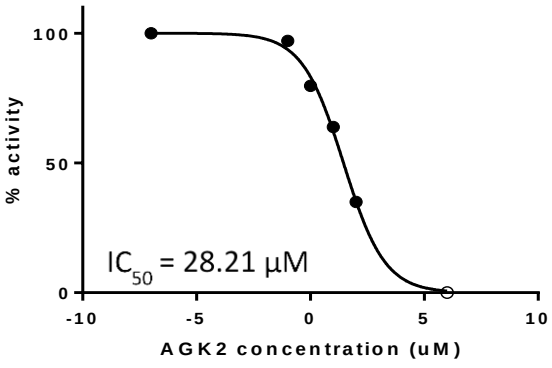

Figure 27. Boc-Lys(12F-dodecanoyl)-AMC (**8**) was used to experimentally determine the IC_{50} value for a known inhibitor AGK2.

optimization of the radiolabeling procedure and improve radio-synthetic yield. The iodinated precursor (**14**) was synthesized from the brominated precursor in a high yield of 73% using literature procedure(Belanger et al., 2011). The radiochemical yield achieved with precursor **14** was 5-fold higher than that with precursor **13**. The highest radiofluorination yields were achieved

A

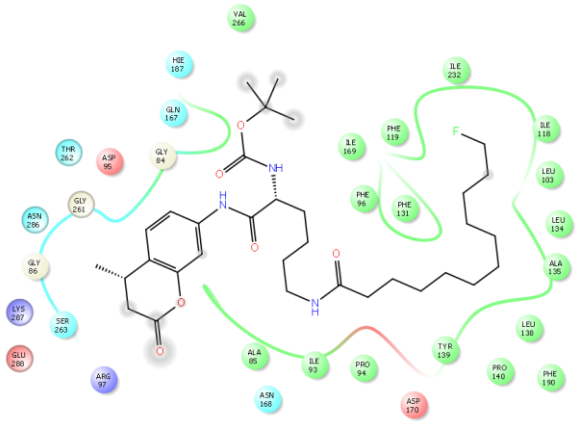

B

Compound Name	MW (g/mol)	Docking Score	Distance ADP–carbonyl (Å)	Distance after closing (Å)
Boc-lys(12F)-AMC	619	-8.925	4.30	3.6
Boc-lys(myr)-AMC	630	-7.977	5.52	3.8
Boc-lys(10F)-AMC	592	-9.304	5.50	3.8
Boc-lys(6F)-AMC	522	-8.524	5.97	4.2
12-DDFAHA	405	-9.070	7.22	5.5

Figure 28. A) The 2D representation of the interactions between SIRT2 and the substrate, Boc-Lys(12F-dodecanyl)-AMC. The 12-fluoro dodecanyl leaving group has similar interactions to those in literature, evidence that the leaving group is fitting in the correct position. **B)** The table of results from our compound docking study. The compound name, MW, docking score (where more negative is a better fit), and most importantly, the distance between the 1' postion of the ADP ring and the carbonyl of the leaving group. This distance is also shown after the 1.7Å correction for catalytic conformational change.

using precursor **14** in acetonitrile at 85-90°C. 12-[^{18}F]DDAHA was obtained with purity of >95%

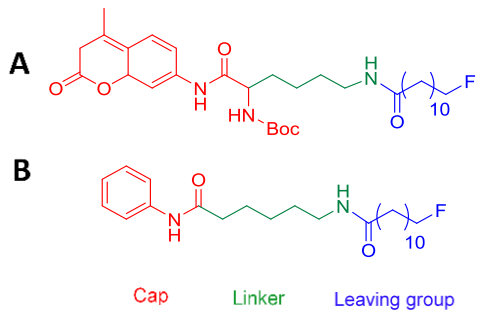

Figure 29. A) The backbone used for enzymatic *in vitro* biochemical assays- Boc-Lys-AMC. **B)** The backbone developed for improved systemic viability of a small molecule radiotracer.

(**Fig. 30**) and a decay corrected radiochemical yield of 12% (total preparation time: 66 min) with specific activity of 259 Gbq/mmol.

The level of uptake of 12-[^{18}F]DDAHA in cell cultures after 30 minutes of incubation *in vitro* was significantly above the cells-to-culture medium equilibrium and was 3-fold higher in U87-NesTG cells, expressing higher levels of SIRT2, as compared to MiaPaCa, MDA231, MCF10A, expressing relatively lower levels of SIRT2 (**Fig. 31**).

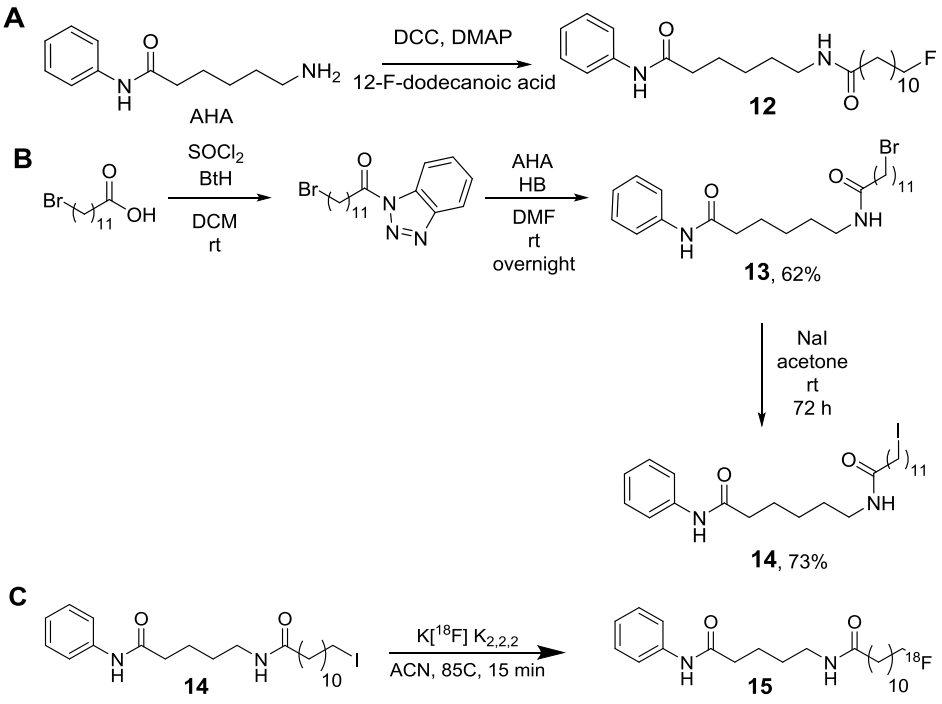

Figure 30. A) The synthesis of both the cold (non-radiolabeled) analogue (**13**) and **B)** precursors for 12-[^{18}F]DDAHA, 12-BrDDAHA (**13**) and 12-IDDAHA (**14**). The 12-[^{18}F]DDAHA (**15**) radiotracer was synthesized from the iodinated precursor and the in dry acetonitrile in 85°C for 15 minutes.

Discussion

Understanding structure-activity relationships of SIRT2 with various natural and synthetic substrates to develop novel ^{18}F-labeled radiotracers for quantitative molecular imaging of SIRT2 expression and activity, it is important to. Previously it has been reported that in addition to an acetyl group, SIRT2 can also cleave long acyl chains from lysine residues, including a myristoyl moiety (He et al., 2014). Other HDAC class III enzymes, such as SIRT3 and SIRT6, have also been reported to cleave a myristoylated lysines of the H3K9 peptide (Feldman et al., 2013; Feldman et al., 2015) and K19-20TNF-α (He et al., 2014). However, there are no data on the effects of fluorine substitution on the ω-carbon in alkyl chains on different lengths on SIRT2 catalytic efficiency.

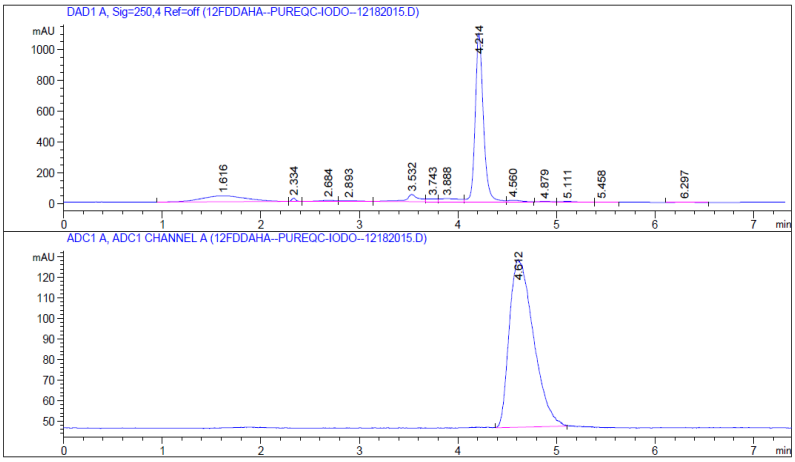

Figure 31. The quality control chromatogram of the 12-[^{18}F]DDAHA **(15)** radiotracer as analyzed by HPLC demonstrates high radiochemical purity and very small amount of UV impurities. **A)** The UV non-radiolabeled standard chromatogram (**12**) **B)** The radio-HPLC chromatogram for the labeled 12-[^{18}F]DDAHA, (**15**).

Our current studies demonstrated that the catalytic efficiency of SIRT2 gradually increases with the elongation of fluoroalkyl chain from 3 to 12 carbons. The catalytic efficiency of SIRT2 for fluorododecanoyl chain (K_{cat}/K_m = 615.4±50.5 $s^{-1}M^{-1}$) is comparable (difference is not statistically significant) with that of the non-fluorinated myristoyl chain (reference compound), which is cleaved most efficiently (K_{cat}/K_m = 716.5±72.8 $s^{-1}M^{-1}$). In contrast, the catalytic efficiency of SIRT2 was significantly lower for the fluoropalmitoyl group (K_{cat}/K_m = 60.4±7.3 $s^{-1}M^{-1}$) (**Fig.**

25). These observations are in agreement with previous reports, demonstrating a similar trend in SIRT2 catalytic efficiency for the H3K9 peptide backbone derivatized with hexanoyl, octanoyl, decanoyl, dodecanoyl, and myristoyl groups, but significantly less efficiently the palmitoyl and lipoyl-derivatized H3K9 peptide (Feldman et al., 2013; Feldman et al., 2015). Similarly, using TNF-α peptide backbone with varying chain lengths to a fluorophore or quencher moiety the longer chain length (11 carbons) resulted in much improved catalytic efficiency over the shorter (6 or 8 carbons) or very long (13 carbons) chain lengths(Schuster et al., 2016). However, despite the similarities in trends, the absolute K_{cat}/K_m values obtained in the current study for different alkyl chains with Boc-Lys-AMC backbone are significantly lower than those reported previously using a H3K9 or TNF-α peptide (Feldman et al., 2013; Feldman et al., 2015; Schuster et al., 2016), which can be explained, at least in part, by the higher efficiency of a peptide "cap" group, as compared to Boc-Lys-AMC. Similarly, reports of a "cap" group containing either p53 or TNF-α peptide residues on one side and an AMC group on the other demonstrate reduced K_{cat}/K_m as compared to compounds with a full peptide cap (Chiang and Lin, 2016; Feldman et al., 2015; Schuster et al., 2016). Also, the observed differences may be due to the presence of electronegative ω–terminal fluorine. In the current study, the K_{cat}/K_m values were determined by measuring the rate of the

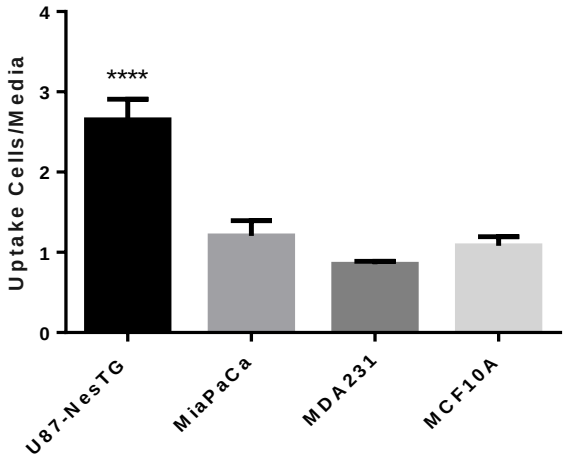

Figure 32. The radiotracer 12-[^{18}F]DDAHA (**15)** was used in cellular uptake studies for four tumor cell lines. The error bars represent the standard deviation for N=4 for each cell line. Where **** represents P<0.05 as determined by One-Way ANOVA and Tukey's multiple comparisons test this value is significantly larger than the other three values.

AMC cleavage product formation, whereas in some of the previously reported data K_{cat}/K_m values were determined by measuring the rate of NAD^+ consumption, which may also explain the differences in absolute K_{cat}/K_m values between studies.

Furthermore, results of current *in silico* modeling studies demonstrate that the distance between the carbonyl-carbon to the ADPR-nicotinamide ester linkage is smaller for longer chain leaving groups, such as the fluorododecanoyl derivatized Boc-Lys-AMC and AHA backbones (**Fig. 29**). These *in silico* docking studies were conducted using currently available crystal structures of SIRT2, which depict the enzyme in either the "closed" or "open" confirmation (i.e. before or after enzymatic reaction with a substrate). Because there are no crystal structures available for SIRT2 in the transition state with bound NAD^+, we chose the structure of SIRT2 co-crystallized with SirReal2 (SIRT2 inhibitor) and NAD^+(Rumpf et al., 2015) (PDB: 4RMG). This crystal structure with full NAD^+ intact, rather than post cleavage with only ADPR present (Moniot et al., 2013), is indicative of an enzyme in the open confirmation when a substrate initially docks inside the enzyme active site. This step is especially important for the SIRT enzymes, as the close proximity and accurate positioning between nicotinamide and the substrate carbonyl moiety is crucial for the reaction to occur. The root mean square deviation (r.m.s.d) for the central carbon during the transition from the "open" to "closed" conformation has been characterized in the literature (Rumpf et al., 2015), allowing estimation of the changes in key interaction distances. The r.m.s.d of the open versus closed configuration is about 1.7Å in PDB 4RMG. Using this correction factor, the distances between a leaving group carbonyl and a nicotinamide of NAD^+ ring fall into an acceptable range for reaction to occur. Other studies have explored the structural activity in 5 ns molecular dynamic simulations and noted similar findings for the structural changes in the SIRT2 active site (Sakkiah et al., 2013). Therefore, we hypothesize that the distance between

the amide bond carbonyl carbon and the nicotinamide cleavage site of NAD^+ plays an important role in substrate catalytic efficiency of SIRT enzymes. The mechanism of SIRT2 mediated cleavage of acylated lysine moieties involves simultaneous cleavage of nicotinamide and activation and subsequent cleavage of the acyl carbonyl carbon amide bond. Therefore, the selection of site for with substitution fluorine atom (strongly electronegative and electron withdrawing) is crucial for preservation of catalytic activity of SIRT2. For example, if a fluorine atom (or another electron withdrawing group) were to be placed in close proximity to the α-carbon, catalytic efficiency would decrease, as reported by us previously for fluro- and trifluoro-acetamidohexanoicanilide (Bonomi et al., 2015; Yeh et al., 2013a).

To examine the selectivity of compounds for SIRT2 among all SIRT enzymes, three of the most efficient substrates, **8, 9,** and **11** were screened against a panel of recombinant SIRT enzymes (SIRT 1-7). The aim was to elucidate the differences in SIRT selectivity that may occur as a result of altering the cap (mono- vs. di-lysine cap), the leaving group (12- vs 14-carbon chain) and last the terminal fluorine atom (12F-carbon vs 14-carbon). Our results indicate that compound **11,** with a di-lysine cap, was cleaved more effectively by SIRT3 and SIRT6 than compound **5,** with a mono-lysine cap. Therefore, **9** is more selective to SIRT2 as it shows very little cleavage by other SIRT enzymes. Both **8** (12F-carbon chain) and **9** (14-carbon chain) are cleaved effectively by SIRT2 and not by any other SIRT enzymes, indicating that both leaving groups are selective for SIRT2. These findings are consistent with other reports in the literature (Feldman et al., 2013; He et al., 2014; Pan et al., 2011b) and demonstrate that leaving group specificity may not entirely define the selectivity of a substrate to a certain SIRT enzyme. Altering the cap group can have a significant impact on the efficiency with which the SIRT enzyme cleaves a substrate.

Also, we assessed the effectiveness of the lead substrate **8** against a potent selective SIRT2 inhibitor AGK2 (Cui et al., 2014). A competitive inhibition study (Cui et al., 2014) was performed using increasing concentrations of AGK2 with **8** at its apparent k_m concentration (8 μM) for SIRT2. The observed inhibition of SIRT2 by AGK2 at IC_{50} of 28.21 μM (**Fig. 27**) using **8** as substrate was comparable to previously reported IC_{50} values of 3-5 μM obtained with myristoylated or acetylated substrates of SIRT2(Hoffmann et al., 2014; Lain et al., 2008). As demonstrated by the comparable catalytic efficiencies of **8** and **BPS1** (p53 (379-382)K382ac-AMC) this data further confirm that **8** is an efficient substrate of SIRT2.

Based on the results of biochemical and *in silico* modeling studies, we have chosen the dodecanoyl chain fluorinated on the ω-position for coupling to an AHA backbone to generate the SIRT2-specific ^{18}F-labeled radiotracer termed 12-[^{18}F]DDAHA. We did not study the 14-fluoromyristoyl-Boc-Lys-AMC and 14-[^{18}F]fluoromyristoyl-AHA, because Boc-Lys(12-fluorododecanoyl)-AMC exhibits 2/3 efficiency of Boc-Lys(myristoyl)-AMC as selective substrate for SIRT2, and because radiotracers with smaller molecular weight have pharmacokinetic advantages over radiotracers with larger molecular weight. Nevertheless, the synthesis and evaluation of these compounds are currently underway and will be reported separately. For synthesis of 12-[^{18}F]DDAHA, we adapted methods for radiolabeling of ω-[^{18}F]substituted long chain fatty acids (Belanger et al., 2011), that are used for PET imaging of cardiac metabolism (Pandey et al., 2012) (**Fig. 30-31**). Our studies confirmed previous reports that ω-iodinated dodecanoyl precursor provides a 3-fold higher radiosynthetic yield than the ω-brominated precursor (Belanger et al., 2011). The radiosynthetic yield for 12-[^{18}F]DDAHA could be optimized further by using microwave assisted heating (Belanger et al., 2011).

The mechanism of substrate cleavage by SIRT enzymes allows for a radioactive leaving group to be transiently entrapped in the cell in a similar manner to other radiotracers such as ^{18}F-FDG and ^{18}F-FLT, by converting or coupling a tracer into a more polar molecule. In this case, an ester linkage between a leaving group and O-ADPR (**Fig. 22**) forms, thereby preventing the leaving group from crossing a cell membrane because ^{18}F-fluoroalkyl-O-ADPR is quite large and polar. Therefore, SIRT2-mediated cleavage of ^{18}F-fluoroalkyl group from 12-[^{18}F]DDAHA with formation of ^{18}F-fluoroalkyl-O-ADPR complex represents the rate-limiting step in the cellular entrapment of 12-[^{18}F]DDAHA-derived radioactivity. The removal of the acetyl or longer acyl chain moieties from O-ADPR group has been hypothesized to occur by way of ARH3 cleavage or possible methanolysis to form 1'O-methyl'ADPR (Fahie et al., 2009; Mashimo et al., 2014). Additionally, a nucleophilic attack from lysine side chains of other proteins in close proximity may also de-acetylate the O-AADPR. Further studies are needed to fully characterize the half-life of O-12-[^{18}F]DD-ADPR and residence time for the 12-[^{18}F]dodecanoyl moiety within the cell. Although this entrapment may be transient, it should provide a long enough residence time within the cell for adequate PET imaging and quantification of SIRT2 expression-activity product.

In vitro radiotracer uptake studies in cell lines with varying degrees of SIRT2 expression provided initial evidence for the efficacy of 12-[^{18}F]DDAHA as a radiotracer for quantification of SIRT2 expression-activity. The level of 12-[^{18}F]DDAHA derived radioactivity accumulation was increased three fold in U87 glioma cells over other cells with relatively lower SIRT2 expression (i.e. MiaPaCa, MDA-MB-231, and MCF10A) (**Fig. 32**). Previous studies demonstrated downregulation of SIRT2 expression in about 70% of gliomas (Hiratsuka et al., 2003; Inoue et al., 2007b). In contrast, more recent studies demonstrated that the labeling index of nuclear-localized SIRT2 is significantly higher in glioblastomas (grade IV), as compared to astrocytomas (grade II)

and normal brain tissue and strongly correlated with malignant progression and the overall survival of patients with glioblastomas (Imaoka et al., 2012). The immunohistochemical staining of many tissues in the Human Protein Atlas displays intense staining of SIRT2 protein in all glioma tissues with greater magnitude than in breast or pancreatic cancer patient derived tissue samples (http://www.proteinatlas.org/search/sirt2). Higher levels of expression and higher labeling index for SIRT2 is also associated with progression and poor prognosis in patients with non-small cell lung cancer (NSCLC) (Grbesa et al., 2015) and cervical carcinoma(Singh et al., 2015). Some tumors (i.e., melanomas), may harbor mutations in SIRT2 gene resulting in reduction of enzymatic activity by 80–90% compared to the wild-type protein, however consequences to tumor progression and overall prognosis are yet unknown (Lennerz et al., 2005). Therefore, molecular imaging with PET using SIRT2-specific radiotracers should provide information about the location and magnitude of SIRT2 expression and activity in tumors non-invasively and in real time. This may help to determine the mechanistic, therapeutic, and prognostic roles of SIRT2 in different cancers. Also, SIRT2 is an emerging target for therapy of various neurologic diseases, including neurodegeneration (Donmez and Outeiro, 2013), as well as cardiac (Matsushima and Sadoshima, 2015) and metabolic diseases (Houtkooper et al., 2012; Matsushima and Sadoshima, 2015).

The translation of 12-[^{18}F]DDAHA to *in vivo* PET imaging may further the field of epigenetic regulation in both norm and disease and facilitate development and clinical translation of SIRT2-targeted drugs. PET imaging with a substrate type radiotracer such as 12-[^{18}F]DDAHA, will allow for *in vivo* visualization and quantification of the enzyme expression-activity product. Accumulation of 12-[^{18}F]DDAHA-derived radioactivity is directly proportional to the amount of active enzyme in a tissue. The current approach to imaging SIRT2 activity using substrate-type radiotracers complements other methodologies for PET imaging of enzymes, including

radiolabeled inhibitors. PET imaging with radiolabeled enzyme inhibitors is essentially similar to a receptor-ligand based imaging approach, where the amount of radiotracer-derived radioactivity accumulation is proportional to the amount of free (unoccupied) receptor or enzyme in a given tissue (J, 2000). Visualization of receptor or enzyme occupancy is especially important for determining the pharmacokinetics and bio-distribution of an inhibitor (i.e. drug or therapeutic agent). Successful inhibitor-type radiotracers have been developed specifically for HDAC class I, in the form of ^{11}C-Martinostat (Kim et al., 2013; Reid et al., 2009a; Wey et al., 2015). However, imaging with an inhibitor does not provide information about the enzyme activity. In contrast, substrate-type radiotracers allow for assessment of the enzyme expression-activity and monitoring the pharmacodynamics of inhibitor at the target (enzyme) level.

Although several previous studies have reported significant defluorination of ω-[^{18}F]substituted fatty acids in rodents following intravenous injection (Pandey et al., 2012), it occurs at a much lower magnitude in higher mammals (i.e. pigs and dogs) and in humans, due to a decrease in level of expression of defluorinating enzymes (Pandey et al., 2012). The AHA backbone was selected based on our previous success with the development of HDAC class IIa specific radiotracers ^{18}F-FAHA and ^{18}F-TFAHA(Bonomi et al., 2015; Yeh et al., 2013a) and because the use of peptide-based backbones will prevent (or significantly reduce) the ability of radiotracers to cross cellular membranes by non-facilitated diffusion. Although it is still possible that 12-[^{18}F]DDAHA may exhibit unacceptable levels of defluorination *in vivo*, an alternative site for radiofluorination may be explored in the ω-3 position of dodecanoyl chain. Alternatively, carbon-11 labeling of the dodecanoyl chain could be accomplished similar to ^{11}C-palmitate (Mock et al., 2011; Runkle et al., 2011).

Conclusions

In summary, guided by the results of biochemical and *in silico* modeling studies of structure-activity relationships between SIRT2 and a non-peptide type lysine mimicking substrate backbone derivatized with fluoroalkyl chains of different length, we have developed and validated *in vitro* a novel SIRT2-selective substrate-type radiotracer termed 12-[^{18}F]DDAHA. 12-[^{18}F]DDAHA is suitable for assessment of SIRT2 expression-activity using *in vitro* radiotracer uptake assays in cell cultures and potentially for *in vivo* PET imaging of SIRT2 expression-activity in normal and/or diseased organs and tissues. Molecular imaging with PET using SIRT2-specific radiotracers, such as 12-[^{18}F]DDAHA, should provide information about the location and magnitude of SIRT2 expression and activity in tumors non-invasively and in real time, which should help to determine the mechanistic, therapeutic, and prognostic roles of SIRT2 in different diseases.

Experimental Methods

All solvents were purchased from Sigma-Aldrich Chemicals (Milwaukee, WI) and used without further purification. Boc-Lys(Ac)-AMC and Cbz-Lys-OH were purchased from Bachem (Bubendorf, Switzerland) and used without further purification. Preparation of 6-amino-1-hexanoicanilide *(*Mukhopadhyay et al., 2006*)* was synthesized using a previously published procedure (Mukhopadhyay U, 2006b). Thin layer chromatography (TLC) was performed on pre-coated Dynamic Absorbance F-254 silica gel, aluminum backed plates (Norcross, Georgia); flash chromatography was performed using silica gel pore size 60 Å, 230-400 mesh particle size (Sigma-Aldrich, Milwaukee, WI).

NMR spectra including ^{1}H, ^{13}C and ^{19}F were performed on Mercury 400 MHz, Varian 500 MHz or Agilent 600 MHz spectrometers. High-resolution mass spectra (HRMS) were obtained using Waters LCT Premier/XE spectrometer (Milford, MA) with an electrospray ionization (ESI) technique. The analytical high performance liquid chromatography (HPLC) system included:

Ascentis RP-Amide 4.4x150 mm column (Supelco, Bellefonte, PA) connected to the 1100 series pump and UV detector (Agilent Technologies, Stuttgart, Germany), operated at 254 nm, and a radioactivity detector FC3200 (Eckert and Ziegler Radiopharma, Inc, Berlin, Germany). The semi-preparative HPLC system included: the Alltima 250x10mm C18 column (Fisher Scientific, Waltham, MA) connected to the P4.1S pump, Azura 2.1S UV detector (Knauer, Berlin, Germany), operated at 254 nm, and a radioactivity detector FC-3500 (Eckert and Ziegler Radiopharma, Inc, Berlin, Germany).

SIRT Enzyme Assay: Recombinant SIRT1-7 enzymes and BPS1 reference substrate for SIRT2, an oligopeptide corresponding to 379-382 of p53 (Arg-His-Lys-Lys(Ac)-AMC) (Huhtiniemi et al., 2011; Marcotte et al., 2004) were purchased from BPS Bioscience (San Diego, CA). 10 mM solutions of all newly synthesized compounds were prepared in pure DMSO and then diluted to 100 μM aliquots in DMSO for further use. Enzyme assay reactions were performed in black, low binding 96-well microtiter plates (Nagle Nunc International, Rochester, NY). End point assays were performed by incubation of the appropriate substrate, NAD, a SIRT enzyme, and inhibitor (if applicable) in enzyme assay buffer (50 μL final volume). Control wells without enzyme were included in each plate. After 40 min at 37 °C, a developer mixture (50 μL) containing nicotinamide (2 mM) and trypsin (0.4 mg mL^{-1}) was added, and the mixtures incubated for 30 min at 22°C. The intensity of cleaved 7-amino-4-methylcoumarin (AMC) fluorescence was measured using Synergy H1 microplate reader (Biotek, Winooski, VT) at 360 nm excitation and 450 nm emission wave lengths. Experiments for determination of enzyme kinetic parameters were performed by incubation of test compounds or BPS1 reference substrate at different concentrations with NAD^+ and individual SIRT enzymes in an assay buffer (100 μL final volume) at 37°C for different periods of time (5, 10, 20, 30, and 60 min), followed by *in situ* fluorophore cleavage by

addition of a developer mixture (50 μL) containing nicotinamide (2 mM) and trypsin (0.4 mg mL^{-1}). Fluorescence was measured as relative fluorescence units (RFU) at 22°C to determine the initial linear rate V_0 (RFU min^{-1}) for each concentration. The data were analyzed using GraphPad Prism v6.02 (GraphPad, La Jolla, CA) to afford k_m (μM) and V_{max} (RFU min^{-1}) values. The k_{cat} values were calculated based on the RFU vs AMC concentration standard curve and the enzyme purities and concentrations provided by the manufacturer.

Computational Docking Studies: Schrodinger Suite (New York, NY) with the Glide(Zhu et al., 2014) docking program was used for simulating ligand-protein interactions *in silico.* The ligands were prepared using LigPrep (Sastry et al., 2013) in Maestro v10.3 and the lowest 5 energy states were used for covalent docking interactions. Epik was used to generate the tautomeric states and choosing the lowest Epic (Shelley et al., 2007) ionization state. The protein, SIRT2 (PDB: 4RMG) was prepared with the Protein Preparation Wizard (Sastry et al., 2013). A Cartesian coordinate receptor grid was generated on SIRT2 by positioning the prereaction form of the ligand in the binding site close to the NAD^+. The affinity score is given as a Glide score based on the binding mode of the ligand with the protein where the optimal interactions are represented by a low Glide score (Friesner et al., 2004). The distance between the NAD^+ and the carbonyl-carbon of the leaving group cleavage site was calculated manually using the Measure Distance functionality.

Cell cultures and in vitro Radiotracer Uptake Studies: The U87MG, MiaPaca, and MDA-MB-231 cell lines were obtained from the American Type Tissue Culture Collection (ATCC); the MCF10A cell line was obtained from the cell culture repository of the Karmanos Cancer Institute (Detroit, MI). Tumor cells were propagated in DMEM supplemented with 10% fetal calf serum (FCS), penicillin and streptomycin, at 37°C in a humidified atmosphere with 5% CO_2. In vitro

radiotracer uptake studies were performed as previously described (Yeh et al., 2013c). Briefly, prior to in vitro radiotracer uptake experiment, the cells were inspected for confluency and viability. Each of the four cell plates for a given cell line had the media removed by pipette aspiration, and fresh media (15mL) containing the radiotracer (1-2uCi/mL) was added to cells in the culture plates. The tumor cell monolayers were incubated with the radioactivity-containing medium for 30 minutes. The cells were then harvested by gentle unidirectional scraping and the suspensions of cells in the media were transferred into 15mL conical centrifuge tubes and pelleted by centrifugation (3000 rpm for 2 min). 50uL samples of supernatant and cell pellets flash-frozen on dry ice were placed in pre-weighed scintillation vials, weighed, and the radioactivity was measured using Pakard 5500 gamma counter (Perkin Elmer, CA). The background-corrected and decay-corrected radioactivity concentrations in individual cell pellets (cpm/g) was divided by corresponding cell culture media samples (cpm/g) to determine the fold increase of radiotracer accumulation in cells versus the cell culture media.

Chemical Synthesis:

Synthesis of ω-fluorinated acyl chains: 3-fluoropropionic acid was purchased from Santa Cruz Biotechnology (Dallas, TX) and used without further purification. 10-hydroxydecanoic acid, 12-hydroxydodecanoic acid, and 16-hexadecanoichydroxyhexadecanoic acid were purchased from Sigma Aldrich (Milwaukee, WI) and used for synthesis of ω-fluorinated carboxylic acid chains. The n-hydroxycarboxylic acids were treated with molar excess of diethylaminosulfur trifluoride (DAST) at 0°C for 5-10 minutes. Immediately following, the reaction mixture was transferred dropwise to 5 ml of hexane resting on a small plug of silica gel primed with hexane to selectively hydrolyze the acetyl fluoride formed during the DAST reaction. The compounds were

eluted from the silica using 50:50 ethyl acetate/hexane and they were used without further purification for formation of acetyl chloride and coupling to the lysine derivative.

***tert*-Butyl (7-(3-fluoropropanamido)-1-((4-methyl-2-oxochroman-7-yl)amino)-1-oxoheptan-2-yl)carbamate (5)**: 3-Fluoropropionic acid (61.7 mg, 0.66 mmol) was dissolved in acetonitrile with 1 equivalent of *N,N'*-dicyclohexylcarbodiimide (DCC) (155 mg) and a catalyst amount of 4-dimethylaminopyridine (DMAP) (few crystals). The mixture was stirred at 22°C under argon for 10 minutes. Subsequently, Boc-Lys-AMC (188 mg, 0.46 mmol) was dissolved in 7 mL of dichloromethane (DCM) with 1 equivalent of triethylamine (TEA) and added dropwise to the reaction mixture. The reaction was stirred continuously at 22°C, under argon, for 12 hours. Following completion of the reaction, the solvent was evaporated and the compound was purified by column chromatography using a gradient of 0.5-2% methanol/dichloromethane for elution. The product was obtained in 85% yield as an off white powder. ^{1}H NMR (400 MHz, $CDCl_3$) δ 9.42 (s, 1H), 7.68 (s, 1H), 7.47 (s, 1H), 7.38 (s, 1H), 7.26 (s, 1H), 6.20 (s, 1H), 6.14 (s, 1H), 5.54 (s, 1H), 5.29 (s, 1H), 4.79 (t, J = 5.6 Hz, 1H), 4.67 (t, J = 5.6 Hz, 1H), 4.30 (s, 1H), 3.51 – 3.37 (m, 1H), 3.35 – 3.16 (m, 1H), 2.60 (dd, J = 15.3, 9.7 Hz, 1H), 2.54 (t, J = 5.6 Hz, 1H), 2.38 (s, 2H), 1.45 (s, H), 1.94 – 1.88 (m, 2H), 1.82 – 1.62 (m, 2H), 1.57 (dd, J = 16.4, 11.8 Hz, 2H), 1.30 (dt, J = 17.4, 13.0 Hz, 2H), 1.20 – 0.99 (m, 2H). ^{19}F NMR (376 MHz, $CDCl_3$) δ -217.96 (tt, J = 47.0, 27.5 Hz). HRMS (+ESI-TOF) m/z for $C_{25}H_{35}N_3O_6$ $[M+Na]^+$ calculated: 493.5802; found: 493.2097

***tert*-Butyl (7-(6-fluorohexanamido)-1-((4-methyl-2-oxochroman-7-yl)amino)-1-oxoheptan-2-yl)carbamate (6):** 6-Bromoethylhexanoate (1 g) was dissolved in 10 mL of TBAF and stirred at 80°C for 3 hours. The resulting mixture was evaporated and purified by column chromatography using 10% ethyl acetate in hexane as the eluent. The ethyl protecting group was hydrolyzed by 100ul of 15wt% sodium methoxide in methanol. The following mixture was

evaporated and 2 mL of thionyl chloride ($SOCl_2$) was added to the residue. The resulting mixture was stirred at 60°C, under reflux, for 3 hours. Following the reaction, all $SOCl_2$ was evaporated and the product was washed with toluene before being evaporated once more. Boc-Lys-AMC (Bachem (92 mg, 0.24 mmol) was dissolved in 10 mL of dichloromethane with 1 equivalent of TEA. The mixture was added dropwise to the flask containing the acetyl chloride residue, and the reaction was stirred continuously at 22°C, under argon, for 12 hours. Following completion of the reaction, the solvent was evaporated and the compound was purified by column chromatography using a gradient of 3-5% methanol/dichloromethane for elution. The product was obtained in 20% yield as an off white powder. ^{1}H NMR (600 MHz, $CDCl_3$) δ 11.20 (s, 1H), 9.40 (s, 1H), 7.68 (s, 1H), 7.45 (s, 2H), 7.42 (s, 2H), 7.25 (d, 2H), 6.13 (s, 1H), 5.95 (s, 1H), 5.50 (s, 1H), 4.45 (t, J = 5.9 Hz, 1H), 4.37 (t, J = 5.7 Hz, 1H), 4.28, 3.33 – 3.26 (m, 1H), 3.23 (dd, J = 13.3, 6.7 Hz, 1H), 2.99 (d, J = 4.3 Hz, 1H), 2.55 (s, 2H), 2.37 (s, 2H), 2.18 (t, J = 7.4 Hz, 2H), 1.77 – 1.62 (m, 7H), 1.57 (dd, J = 13.8, 6.9 Hz, 3H), 1.50 – 1.40 (m, 14H), 0.95 (t, J = 7.1 Hz, 2H). ^{13}C NMR (151 MHz, $CDCl_3$) δ 173.2, 171.4, 161.1, 154.5, 152.3, 141.5, 125.0, 123.6, 115.8, 115.6, 113.2, 107.1, 83.9 (d, J = 164.4 Hz), 80.4, 77.0 76.8, 60.0, 55.0, 52.2, 48.6, 38.3, 36.5, 31.2, 30.1 (d, J = 19.5 Hz), 28.8, 28.3, 25.3, 25.1, 25.0, 24.9, 22.5, 20.1, 18.5, 13.5. ^{19}F NMR (376 MHz, $CDCl_3$) δ -175.21 – -184.59 (m). HRMS (+ESI-TOF) m/z for $C_{28}H_{41}N_3O_6$ $[M+Na]^+$ calculated: 535.66; found: 535.2642

***tert*-Butyl (7-(10-fluorodecanamido)-1-((4-methyl-2-oxochroman-7-yl)amino)-1-oxoheptan-2-yl)carbamate (7)**: 10-Fluorodecanoic acid (45 mg, 0.24 mmol) was dissolved in excess $SOCl_2$ (1 mL, 1.3 mmol) and stirred at 60°C, under reflux, for 3 hours. Following the reaction, all $SOCl_2$ was evaporated and the product was washed with toluene before being evaporated once more. Boc-Lys-AMC (96 mg, 0.24 mmol) was dissolved in 7 mL of

dichloromethane with 1 equivalent of TEA. The mixture was added dropwise to the flask containing the acetyl chloride residue, and the reaction was stirred continuously at 22°C, under argon, for 12 hours. Following completion of the reaction, the solvent was evaporated and the compound purified by column chromatography using a gradient of 3-5% methanol/dichloromethane for elution. The product was obtained in 55% yield as an off white powder. ^{1}H NMR (499 MHz, $CDCl_3$) δ: 9.55 (s, 1H), 7.70 (s, 1H), 7.45 (s, 2H), 7.33 (s, 1H), 6.13 (s, 1H), 5.94 (s, 1H), 5.59 (s, 1H), 4.47 (d, J = 12.1 Hz, 1H), 4.39 – 4.34 (m, 1H), 4.02 (s, 1H), 2.38 (s, 2H), 1.95 (s, 2H), 2.28 (t, J = 7.5 Hz, 1H), 2.16 (t, J = 7.6 Hz, 2H), 1.79 – 1.52 (m, 9H), 1.46 (s, 9H), 1.26 (s, 10H). ^{13}C NMR (126 MHz, $CDCl_3$) δ 173.6, 171.6, 161.2, 156.5, 154.0, 152.5, 141.6, 125.0, 115.7, 115.6, 113.1, 107.1, 84.2 (d, J = 163.9 Hz), 80.4, 64.3, 55.1, 38.5, 36.7, 34.4, 31.6, 30.4, 30.3, 29.4, 29.31, 29.26, 29.2, 29.1, 29.0, 28.6, 28.4, 25.8, 25.7, 25.13, 25.08, 25.0, 22.7, 18.5. ^{19}F NMR (376 MHz, $CDCl_3$) δ -217.73 – -218.25 (m). HRMS (+ESI-TOF) m/z for $C_{32}H_{49}N_3O_6$ $[M+Na]^+$ calculated: 614.3519, found M+Na: 614.3581

***tert*-Butyl (7-(12-fluorododecanamido)-1-((4-methyl-2-oxochroman-7-yl)amino)-1-oxoheptan-2-yl)carbamate (8):** 12-Fluorododecanoic acid (21 mg, 0.027 mmol) was dissolved in excess $SOCl_2$ (1 mL, 1.3 mmol) and stirred at 60°C, under reflux, for 3 hours. Following the reaction, all $SOCl_2$ was evaporated and the product was washed with toluene before being evaporated once more. Boc-Lys-AMC (36 mg, 0.09mmol) was dissolved in 7 mL of dichloromethane with 1 equivalent of triethylamine (TEA). The mixture was added dropwise to the flask containing the acetyl chloride residue, and the reaction was stirred continuously at 22°C, under argon, for 12 hours. Following completion of the reaction, the solvent was evaporated and the compound was purified by column chromatography using a gradient of 3-8% methanol/dichloromethane for elution. The product was obtained in 20% yield as an off white

powder. ^{1}H NMR (500 MHz, $CDCl_3$) δ: 9.55 (s, 1H), 7.70 (s, 1H), 7.43 (d, J = 8.4 Hz, 1H), 7.32 (d, J = 7.5 Hz, 1H), 6.12 (s, 1H), 5.95 (s, 1H), 5.62 (d, J = 6.5 Hz, 1H), 4.41 (dt, J = 47.4, 6.2 Hz, 2H), 3.34 – 3.16 (m, 2H), 2.36 (s, 3H), 2.15 (t, J = 7.7 Hz, 2H), 1.99 – 1.88 (m, 2H), 1.81 – 1.71 (m, 2H), 1.72 – 1.51 (m, 8H), 1.44 (s, 9H), 1.39 – 1.32 (m, 4H), 1.23 (d, J = 5.6 Hz, 14H). ^{13}C NMR (126 MHz, $CDCl_3$) δ: 173.8, 171.8, 161.3, 156.6, 154.1, 152.6, 141.7, 125.1, 115.8, 115.7, 113.2, 107.2, 84.3 (d, J = 163.8 Hz). 80.5, 55.3, 38.7, 36.9, 31.7, 30.6, 30.4, 29.6, 29.4, 29.3, 29.1, 28.5, 25.9, 25.3, 25.2, 25.0, 22.8, 18.6. ^{19}F NMR (376 MHz, $CDCL_3$) δ -217.99 (dq, *J* = 47.4, 25.0 Hz). HRMS (+ESI-TOF) m/z for $C_{34}H_{53}N_3O_6$ $[M+Na]^+$ calculated: 626.3415 found: 626.3395

***tert*-Butyl (7-(14-decanamido)-1-((4-methyl-2-oxochroman-7-yl)amino)-1-oxoheptan-2-yl)carbamate (9):** Boc-Lys-AMC (100 mg, 0.25 mmol) was dissolved in 5 mL of dimethylformamide (DMF) with excess of *N*,*N*-diisopropylethylamine (DIPEA) (0.5 mL). Myristoyl chloride (92 mg, 0.37 mmol Sigma-Aldrich, Milwaukee, WI) was added dropwise to reaction at 0°C and subsequently stirred at 22°C under argon for 12 hours. The resulting mixture was evaporated and the residue was dissolved into ethyl acetate (EtOAc) and was washed 2 times with 2N aqueous hydrochloric acid solution. The organic layer was separated and dried for 2 hours on sodium sulfate, evaporated, and purified by using flash chromatography in an Alltech 900 mg silica cartridge (Fisher Scientific, Waltham, MA) with EtOAc as an eluent. The compound was isolated as a white powder in 64% yield. ^{1}H NMR (600 MHz, $CDCl_3$) δ 9.62 (s, 1H), 7.71 (s, 1H), 7.42 (d, *J* = 8.3 Hz, 1H), 7.29 (d, *J* = 7.7 Hz, 1H), 6.14 (s, 1H), 6.10 (s, 1H), 5.67 (d, *J* = 7.0 Hz, 1H), 4.34 (d, *J* = 4.0 Hz, 1H), 3.33 – 3.15 (m, 2H), 2.35 (s, 3H), 2.16 (t, *J* = 7.6 Hz, 2H), 1.95 – 1.87 (m, 1H), 1.79 – 1.69 (m, 1H), 1.61 – 1.53 (m, 4H), 1.44 (s, 9H), 1.31 – 1.15 (m, 26H), 0.85 (t, *J* = 7.0 Hz, 3H). ^{13}C NMR (151 MHz, $CDCl_3$) δ 174.0, 171.8, 161.3, 156.6, 154.0, 152.7, 141.7, 125.1, 115.8, 115.7, 113.2, 107.2, 80.5, 55.3, 38.8, 36.8, 32.0, 31.8, 29.8, 29.8, 29.7, 29.6, 29.5,

29.5, 29.1, 28.5, 26.0, 22.9, 22.8, 18.6, 14.2. HRMS (+ESI-TOF) m/z for $C_{36}H_{57}N_3O_6$ [M-CH_3+Na]$^+$ calculated: 636.3890 found: 636.3795.

***tert*-Butyl (7-(16-fluorohexadecanamido)-1-((4-methyl-2-oxochroman-7-yl)amino)-1-oxoheptan-2-yl)carbamate (10)**: 16-Fluorohexadecanoic acid (100 mg, 0.38 mmol) was dissolved in excess $SOCl_2$ (1 mL, 1.3 mmol) and stirred at 60°C, under reflux, for 3 hours. Following the reaction, all $SOCl_2$ was evaporated and the product was washed with toluene before being evaporated once more. Boc-Lys-AMC (100 mg, 0.25 mmol) was dissolved in 10 mL of dichloromethane with 1 equivalent of triethylamine (TEA). The mixture was added dropwise to the flask containing the acetyl chloride residue, and the reaction was stirred continuously at 22°C, under argon, for 12 hours. Following completion of the reaction, the solvent was evaporated and the compound was purified by column chromatography using a gradient of 3-8% methanol/dichloromethane for elution and isolated as a white powder in 20% yield. ^{1}H NMR (500 MHz, $CDCl_3$) δ 9.27 (s, 1H), 7.69 (s, 1H), 7.50 (s, 2H), 6.19 (s, 1H), 5.76 – 5.67 (m, 1H), 5.40 (d, J = 7.7 Hz, 1H), 5.31 (s, 1H), 4.49 (t, J = 6.2 Hz, 1H), 4.39 (t, J = 6.2 Hz, 1H), 4.06 (t, J = 6.7 Hz, 3H), 3.67 (d, J = 4.8 Hz, 3H), 3.65 (d, J = 4.7 Hz, 1H), 2.41 (s, 2H), 2.30 (dd, J = 15.0, 7.5 Hz, 5H), 2.21 – 2.17 (m, 1H), 1.66 – 1.60 (m, 9H), 1.47 (s, 9H), 1.28 (d, J = 16.1 Hz, 28H). ^{19}F NMR (376 MHz, $CDCl_3$) δ -217.83 – -218.35 (m). HRMS (+ESI-TOF) m/z for $C_{38}H_{61}N_3O_6$ [M+Na]$^+$ calculated: 698.4500, found: 698.4520

Benzyl (6-amino-1-((1-((4-methyl-2-oxochroman-7-yl)amino)-1-oxo-6-propionamidohexan-2-yl)amino)-1-oxohexan-2-yl)carbamate (11): Boc-Lys-AMC (232 mg, 0.45mmol) was dissolved in trifluoroacetic acid (TFA) to remove the boc protecting group. The mixture was stirred for 30 minutes at 22°C and the TFA (2.5 mL) was evaporated. The resulting residue was dissolved in dichloromethane (DCM) and 1eq of TEA was added to neutralize the

product. The mixture was evaporated and the product was washed with water and dried to remove salts. The intermediate product was obtained as 138 mg of white powder. This product was dissolved in DCM and 0.8 equivalents (85 mg) of Cbz-Lys-OH was added along with 1.5 eq. 1-Ethyl-3-(3-dimethylaminopropyl)carbodiimide (EDC) (67 mg) and Hydroxybenzotriazole **(**HOBT) (50 mg) and 3 eq. of DIPEA (0.12 mL). The mixture was stirred for 12 hours at 22°C under argon. The mixture was evaporated and dissolved in ethyl acetate and washed with saturated sodium carbonate solution. The organic layer dried over magnesium sulfate and evaporated. The residue was purified by column chromatography and the product was eluted with a gradient of 3-5% MeOH/DCM. The product was obtained as an off white powder in 12% yield (40 mg). ^{1}H NMR (600 MHz, DMSO-d_6) δ 10.41 (s, 1H), 8.08 (d, J = 7.4 Hz, 1H), 7.75 (s, 1H), 7.68 (dd, J = 10.8, 7.3 Hz, 2H), 7.46 (d, J = 8.5 Hz, 1H), 7.37 (d, J = 7.7 Hz, 1H), 7.32(s, 3H), 7.28 (dd, J = 7.3, 2.8 Hz, 1H), 6.72 (t, J = 5.5 Hz, 1H), 6.24 (s, 1H), 5.00 (s, 2H), 4.34 (dd, J = 13.7, 7.7 Hz, 1H), 3.98 (dd, J = 12.8, 8.3 Hz, 1H), 3.02 – 2.95 (m, 2H), 2.84 (dt, J = 12.7, 6.5 Hz, 2H), 2.37 (s, 3H), 1.96 (t, J = 7.4 Hz, 2H), 1.75 – 1.65 (m, 1H), 1.65 – 1.53 (m, 2H), 1.48 (d, J = 9.4 Hz, 1H), 1.42 – 1.34 (m, 3H), 1.33 (12H), 1.18 (s, 22H), 0.81 (t, J = 7.0 Hz, 3H). ^{13}C NMR (126 MHz, $CDCl_3$) δ: 174.2, 173.3, 170.9, 161.4, 157.0, 156.7, 154.1, 152.6, 141.7, 136.2, 128.6, 128.3, 128.1, 125.0, 116.0, 113.3, 107.4, 79.4, 67.2, 55.7, 54.1, 50.8, 38.5, 36.9, 32.0, 30.9, 29.8, 29.7, 29.6, 29.5, 29.4, 29.1, 28.5, 26.0, 25.4, 22.8, 22.6, 18.6, 14.2. HRMS (+ESI-TOF) m/z for $C_{49}H_{75}N_5O_9$ $[M+Na]^+$ calculated: 776.3913, found: 776.3911

6-(12-Fluorododecanamido)-*N*-phenylhexanamide (12): 6-Amino-*N*-phenylhexanamide (AHA(Mukhopadhyay et al., 2006)) (0.10 g, 0.48 mmol) was dissolved in acetonitrile with 12-fluorododecanoic acid, a catalyst amount of DMAP (few crystals), and 1 equivalent of DCC (275 mg). The mixture was stirred under argon at 22°C for 12 hours. The solvent was evaporated and

the residue was purified by column chromatography. The product was eluted with 3% MeOH in DCM and subsequently purified by semi-preparative HPLC to improve the purity, eluted as a single peak at 8 minutes with 50% acetonitrile/water. The final compound was isolated in 10% yield. ^{1}H NMR (400 MHz, DMSO-d_6) δ 9.85 (s, 1H), 7.72 (s, 1H), 7.56 (d, J = 7.85Hz, 2H), 7.25 (d, J = 1.8 Hz, 2H), 6.99 (t, J = 7.3 Hz, 1H), 4.44 (dt, J = 47.6 Hz, 2H), 2.99 (s, 2H), 2.25 (m, 2H), 1.98 (m, 2H), 1.54 (m, 4H), 1.37 (m, 4H), 1.20 (s, 10H).^{19}F NMR (376 MHz, DMSO-d_6) δ -216.36 – -216.88 (m). HRMS (+ESI-TOF) m/z for $C_{24}H_{40}FN_2O_2$ $[M+Na]^+$ calculated 407.3074, found 407.3083.

6-(12-Bromododecanamido)-*N*-phenylhexanamide (13): DIPEA (0.13 mL, 0.73 mmol) was added to the mixture of 6-amino-*N*-phenylhexanamide (AHA) (prepared using previously published method(Mukhopadhyay et al., 2006)) (0.10 g, 0.48 mmol) and bromoundecanoic acid benzotriazole (0.21 g, 0.58 mmol) dissolved in DMF (5 mL), and left to stir at 22°C for 6 h. The solvent was then evaporated under reduced pressure; the crude was dissolved in DCM and washed with 2N hydrochloric acid. The organic layer was dried over sodium sulfate. Evaporation and purification with column chromatography (eluent - EtOAc) gave the desired precursor in 62% yield. ^{1}H NMR (400 MHz, $CDCl_3$) δ 8.25 (s, 1H), 7.55 (d, *J* = 7.9 Hz, 2H), 7.27 (t, *J* = 7.9 Hz, 2H), 7.06 (t, *J* = 7.4 Hz, 1H), 5.96 (t, *J* = 5.2 Hz, 1H), 3.38 (t, *J* = 6.9 Hz, 2H), 3.22 (dd, *J* = 13.2, 6.8 Hz, 2H), 2.35 (t, *J* = 7.4 Hz, 2H), 2.13 (t, *J* = 7.6 Hz, 2H), 1.88 – 1.77 (m, 2H), 1.76 – 1.66 (m, 2H), 1.61 – 1.45 (m, 4H), 1.43 – 1.31 (m, 4H), 1.24 (s, 10H). ^{13}C NMR (101 MHz, $CDCl_3$) δ 173.6, 171.8, 138.4, 128.9, 124.1, 119.9, 39.2, 37.3, 36.9, 34.2, 32.9, 29.6, 29.5, 29.5, 29.4, 29.4, 29.3, 28.8, 28.2, 26.4, 25.9, 25.0. HRMS (+ESI-TOF) m/z for $C_{24}H_{40}BrN_2O_2$ $[M+Na]^+$ calculated 467.2273, found 467.2283.

6-(12-Iododododecanamido)-*N*-phenylhexanamide (14): 6-(12-Bromododecanamido)-*N*-phenylhexanamide (100 mg) was dissolved in acetone and 4 equivalents of NaI was added at 22°C and the mixture was stirred for 80 hours. The solution was evaporated and purified with column chromatography (eluent – EtOAc) to give the desired product in 73% yield (80 mg). ^{1}H NMR (600 MHz, $CDCl_3$) δ 7.54 (d, *J* = 7.6 Hz, 3H), 7.31 (t, *J* = 7.8 Hz, 2H), 7.09 (t, *J* = 7.4 Hz, 1H), 5.63 (s, 1H), 3.26 (dd, *J* = 13.2, 6.7 Hz, 2H), 3.18 (t, *J* = 7.0 Hz, 2H), 2.37 (t, *J* = 7.3 Hz, 2H), 2.14 (t, *J* = 7.6, 2H), 1.85 – 1.72 (m, 4H), 1.63 – 1.57 (m, 2H), 1.57 – 1.51 (m, 2H), 1.44 – 1.34 (m, 4H), 1.26 (m, 12H). HRMS (+ESI-TOF) m/z for $C_{24}H_{40}IN_2O_2$ $[M+Na]^+$ calculated 515.2135, found 515.2131.

6-^{18}F-(12-fluorododecanamido)-*N*-phenylhexanamide (15): The F-18 was obtained in kryptofix/K[^{18}F] complex in acetonitrile/water (1 mL) from the PET/Cyclotron Facility, Wayne State University (Detroit, MI) and transferred into a crimped 2 mL V-vial for azeotropic drying. Acetonitrile (0.4 mL) was added to the mixture, which was dried under a stream of argon at 90-100°C. A solution of **14** (2-3 mg) in dry acetonitrile (0.4 mL) was added to the dried kryptofix/ K[^{18}F] and heated to 85-90°C under argon with stirring for 20 minutes. After cooling, the reaction mixture was passed through a 900 mg Altech silica gel cartridge (Fisher Scientific, Waltham, MA) and eluted with 2 mL of 10% methanol in dichloromethane (DCM). The solvent was evaporated under a stream of argon to remove DCM and to reduce the volume to 0.5 mL. The **15** was purified by semipreparative HPLC (40% ACN in water) by collecting the peak at 9 min. The decay corrected radiochemical yield was 12% and the compound purity was >95%, as assessed by analytical HPLC and co-elution with the non-radiolabeled reference standard **12**.

4b. Continuing work

Preliminary dynamic PET/CT images acquired after i.v. administration of 12-[^{18}F]-DDAHA in normal and 9L tumor bearing rats have been done however significant defluorination is visible as soon as 5-10 minutes after injection of the radiotracer and increases with time post injection (**Fig. 33**). This is indicated by the abnormally high uptake of ^{18}F into the bones of the animal and is increasing with time. As noted previously, this has been hypothesized based on studies performed with 16-[^{18}F]-palmitic acid substrates, which demonstrated high rates of

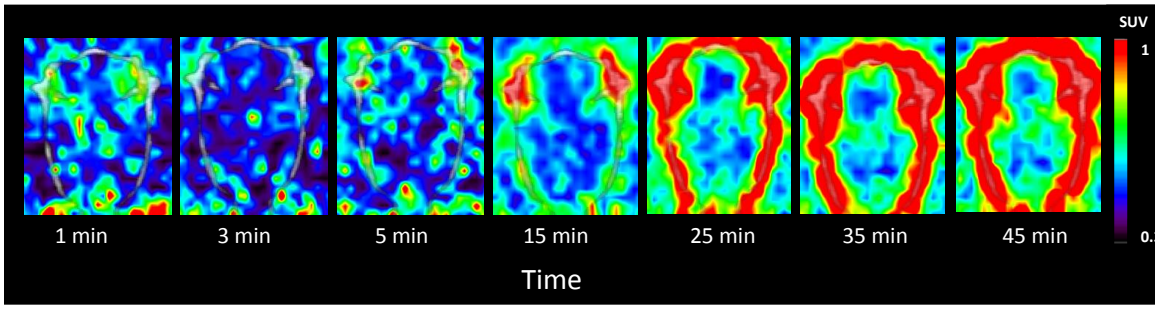

Figure 33. PET/CT images from a rat bearing a 9L brain tumor with 12[^{18}F]-DDAHA demonstrating significant defluorination, as indicated by F-18 accumulation in the bone especially with increasing time post i.v. injection of the radiotracer.

defluorination in rodents. It is possible that this problem would not persist in higher mammals and humans due to significantly lower circulating concentrations of enzymes, we have also begun work on a second generation of compounds aimed at reducing the likelihood of defluorination.

It has been suggested that positioning the fluorine atom on the ω-3 position rather than on the terminal, ω-carbon, may reduce defluorination (Pandey et al., 2012). We have hypothesized that other midchain substitutions of a fluorine-18 atom may also prevent defluorination. From preliminary *in silico* studies it is plausible that these compounds would retain SIRT2 selectivity. In light of these observations, we have designed synthesis schemes for generating a second set of SIRT2 selective radiotracers based upon mid-chain fluorination of dodecanoyl or myristoyl acyl chains (**Fig. 34)**. These synthesis schemes may provide means for constructing a more robust

SIRT2-selective radiotracer to prevent against defluorination in rodents as well as higher mammals. These schemes cover the chains fluorinated at the ɣ-position, generating 4-fluorododecanoyl and 4-flurotetradecanoyl, as well as 5-position to make 5-fluorododecanoyl and 5-flurotetradecanoyl leaving groups which would be radiolabeled from the brominated-precursors. While these compounds place the fluorine atom in closer proximity to the carbonyl carbon, it should be far enough to limit interference with enzymatic activation and cleavage site. Additionally, we have developed schemes for radiolabeling the more terminal fluorines at ω-3 and ω-4 sites to generate 9-fluorododecanoyl or 11-fluorotetradecanoyl (ω-3) substituted chains and 8-fluorododecanoyl or 10-fluorotetradecanoyl (ω-4) substituted chains with possible radiofluorination from the brominated precursors.

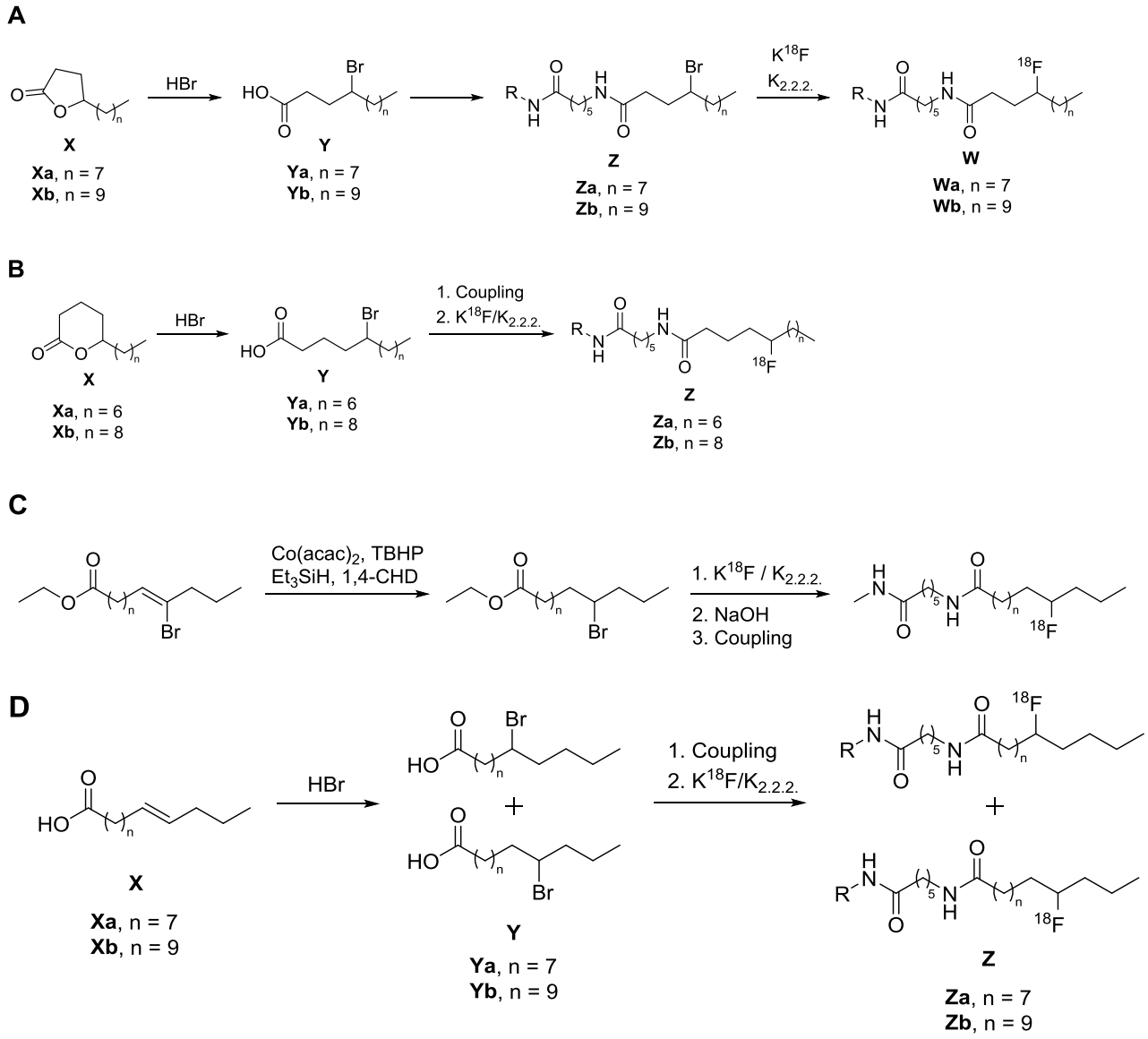

Fig. 34. Possible schemes for synthesis of alternative SIRT2-selective radiotracers that may be less susceptible to defluorination. **A)** Sample synthesis for 4-fluorododecanoyl or 4-fluorotetradecanoyl compounds with radiofluorination from the brominated precursor. **B)** Sample synthesis scheme for construction of 5-fluorododeconyl or 5-fluorotetradecanoyl compounds with radiofluorination from the brominated precursor. **C)** Sample synthesis for the ω-3 compounds, 9-fluorododecanoyl or 11-fluorotetradecanoyl substituted chains. **D)** Synthesis of ω-4 compounds 8-fluorododecanoyl or 10-fluorotetradecanoyl substituted chains with possible radiofluorination from the brominated precursors.

CHAPTER 5 DEVELOPMENT OF NOVEL PET IMAGING SUBSTRATES FOR SIRT1

5a. Development of a novel substrate-type radiotracer, 2-[^{18}F]PhAHA, for PET imaging of SIRT1-mediated epigenetic regulation

Robin Bonomi, Vadim Popov, Maxwell Laws, David Gelovani, Anjoy Majhi, Amer M. Najjar, Aleksander Shavrin, Tong William Ping-Yiu, Nashaat Turkman, Xin Lu, Thomas Mangner, Juri G. Gelovani*

Introduction

Seven sub-types of SIRTs (SIRT 1-7) have been identified in humans (Haberland et al., 2009) and play a role in gene silencing, cell cycle regulation, metabolism, apoptosis, lifespan and circadian rhythms (Pan et al., 2011a). In particular, SIRT1 has been recognized for involvement in diabetes, cardiovascular disease and neurodegeneration (Haigis, 2010) through cleavage of an acetyl moiety from lysine residues of various proteins including PPARϒ, and NF-Kβ, and members of the p53 family. Furthermore, increased expression of SIRT1 has been correlated with poor prognosis in a variety of cancers such as pancreatic (Wauters et al., 2013), non-small cell lung carcinoma (Grbesa et al., 2015) and leukemias (Li et al., 2012)

Due to the biological importance of SIRT1 (further reviewed in chapter two), many targeted therapies have been developed using small molecule therapeutics for activation or inhibition of SIRT1. Because of the notable link between resveratrol and SIRT1, clinical trials were conducted using resveratrol or a synthetic small molecule activator (i.e. SRT2104) to activate SIRT1-mediated pathways for treatment of diabetes and obesity (Hoffmann et al., 2014; Poulsen et al., 2013; Pulla et al., 2012). Additionally, the observation of SIRT1 overexpression in proliferative cancer cells has prompted investigation of the effects of SIRT1 inhibitors on progression of various cancers (Liu et al., 2009).

Several SIRT1 selective inhibitors have been developed and reported in literature, such as Selisistat (EX-527) (Napper et al., 2005; Solomon et al., 2006), Sirtinol (Grozinger et al., 2001), and Tenovin-6 (Lain et al., 2008). These compounds are gaining recognition for treatment of diseases through SIRT1-targeted pharmacomodulation. *In vitro* evidence has demonstrated a reduction in growth and proliferation of colon cancer and uveal melanoma cancer stem cells after treatment with SIRT1-selective inhibitors EX-527 and tenovin-6 (Dai et al., 2016; Suzuki et al., 2009). Though these SIRT1 inhibitors have shown promise as anticancer drugs *in vitro* and in preliminary *in vivo* studies, few have been evaluated or approved for clinical trials (Park et al., 2004).

As noted, SIRT1 plays a pivotal role in many important cellular processes, however, the up- and downstream effects of SIRT1 are not fully understood. Therefore, the development of non-invasive imaging approaches to monitoring SIRT1 expression and activity *in vivo* via PET imaging with a SIRT1-selective substrate radiotracer may aid in understanding disease progression and the development of novel SIRT1-targeted therapeutics.

Recently, studies have demonstrated that SIRT1 is able to cleave other leaving groups outside of the acetyl moiety (Yao and Yang, 2011). In particular, Hirsch et al. demonstrated that SIRT1 can dephenylacetylate a lysine residue (Hirsch and Zheng, 2011) (**Fig. 35**). Additionally, it has been implicated that other SIRT enzymes, namely SIRT2 and SIRT6, may contain the ability to cleave long acyl chains but may not be able to cleave an aromatic ring (Yao and Yang, 2011). Towards the development of a SIRT1-selective substrate radiotracer we developed a library of compounds investigating the relationship of substituted aromatic rings as leaving groups on SIRT1 catalytic efficiency. *In vitro* assessment of these compounds using a fluorogenic assay indicated that the fluorinated phenyl ring leaving groups were cleaved more efficiently by SIRT1 than the

substituted benzyl ring leaving groups or aromatic rings with iodinated substitutions. For purposes of high-throughput screening, this library was developed with the carbazol-lysine-aminomethylcoumarin backbone, however, this peptide mimetic is not well suited for use as an *in vivo* imaging agent, due to its high lipophilicity. Through fluoromeric screening, 2-fluorophenyl (2FPh) was identified as the lead leaving group to use for further development into a systemically viable radiotracer. Following this, 2-fluorophenylhexanoicanilide was developed using the aminohexanoicanilide backbone to form an analogous compound to the tested one, Cbz-Lys(2FPh)-AMC, using providing increased systemic viability as seen in [^{18}F]-TFAHA (Bonomi et al., 2015) and [^{18}F]-FAHA (Yeh et al., 2013a). The resulting compound, 2-fluorophenylaminohexanoicanilide (2-FPhAHA) was synthesized in the radiolabeled version [^{18}F]-2-fluorophenylaminohexanoicanilide ([^{18}F]-2FPhAHA) from the 2-nitrophenyl precursor. [^{18}F]-2FPhAHA demonstrated efficacy as a viable imaging agent for SIRT1 expression-activity through *in vitro* and *in vivo* assessment. PET/CT images with [^{18}F]-2FPhAHA in the rat model resulted in [^{18}F]-2FPhAHA-derived accumulation in areas of the brain with higher SIRT1 activity were validated by the IHC and ISH data in literature (Ramadori et al., 2008; Zakhary et al., 2010) as well as by our own IHC and autoradiography data. Quantification of PET/CT images was performed using Logan plot analysis for specific regions of the brain to validate the differential washout of [^{18}F]-2FPhAHA within the brain.

The development of [^{18}F]-2FPhAHA as a BBB permeable SIRT1-selective substrate type radiotracer with and subsequent characterization of SIRT1 expression-activity *in vivo* in the

absence of disease may further the study of SIRT1-mediated epigenetic regulation in various neuropathologies.

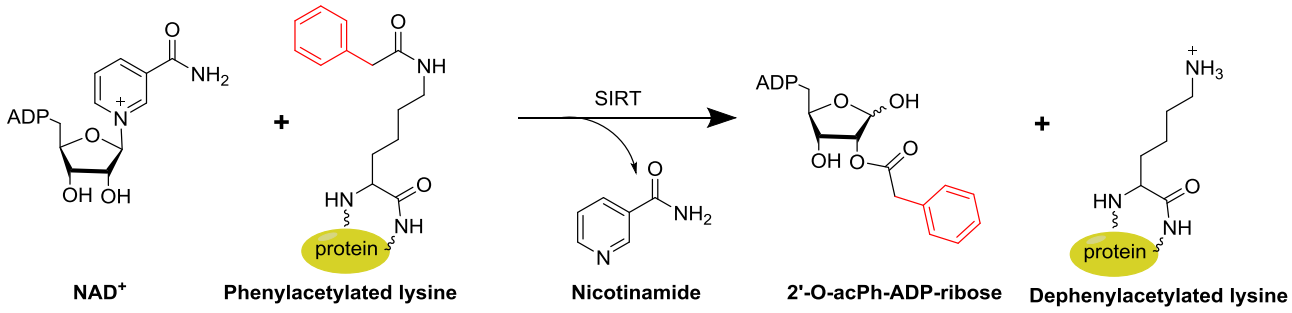

Figure 35. The unique SIRT1 mechanism for cleavage of a benzyl moiety (highlighted in red) from a lysine residue of a protein using NAD^+ as a cofactor.

Results:

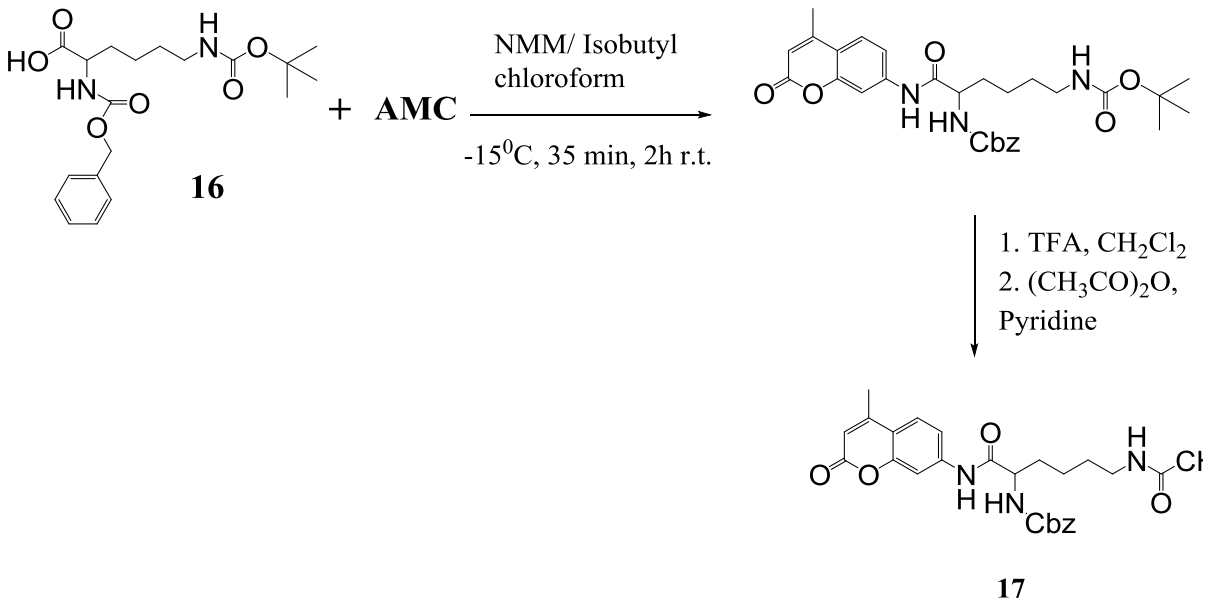

Figure 36. Synthesis of control compound **17,** Cbz-Lys(ac)-AMC.

The library of compounds developed for *in vitro* assessment of SIRT1 catalytic activity utilized the carbazol-Lysine-aminomethylcoumarin backbone (Cbz-Lys-AMC) dervatized with fluorinated and iodinated phenyl and benzyl substituents (**Fig. 36-37**). The compounds (**17-27**)

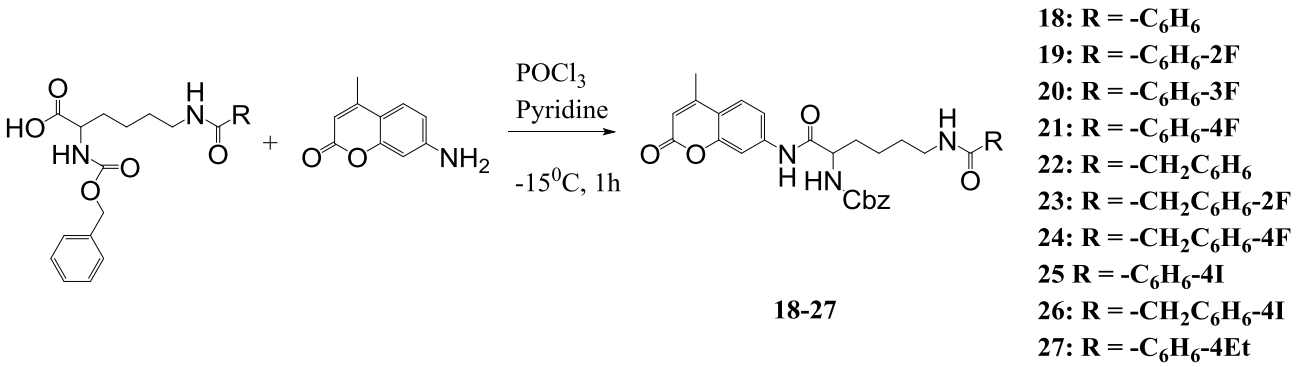

Figure 37. Synthesis of the focused library of SIRT1 substrates

were primarily synthesized from variations of existing methodologies for peptide mimetic synthesis, including acetyl-chloride coupling, in yields of 50-80% with >95% chemical purity as assessed by TLC, ^{1}H, ^{13}C, and ^{19}F NMR and HRMS.

The synthesis of 4-Fluorophenylaminohexanoicanilide (**28**) was accomplished through DCC-catalyzed coupling of the 4-fluorobenzoic acid with compound **1** in a yield of 77% and >95% purity **(Fig. 38**). The synthesis of small molecule compounds including, 2-[^{18}F]ethyl benzoate (**30**), 2-[^{18}F]benzoic acid (**31**), and 2-[^{18}F]benzaldehyde (**34**) with decay corrected radiochemical yields of 25% and 15%, respectively, was accomplished through radiofluorination of commercially available *ortho*-nitro compounds (**29, 32**) with high radiochemical purity (>95%) (**Fig. 39**). These compounds were assessed by analytical radio-HPLC for purity and verification of compound identification.

Synthesis of non-radiolabeled 2-fluorophenylaminohexanoicanilide (**35**) was performed using *in situ* acetyl chloride formation to couple the commercially available 2-fluorobenzoic acid with N-aminophenylhexamide (prepared by previous methodology (Mukhopadhyay et al., 2006)) in a 30% yield and high chemical purity, >95%, as

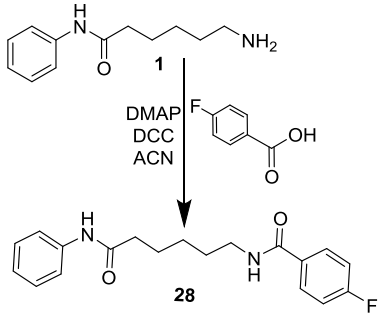

Figure 38. Synthesis of 4-fluorophenylaminohexanoic anilide (**28**).

assessed by TLC, ^{1}H, ^{13}C, and ^{19}F NMR and HRMS. The synthesis of 2-nitrophenylaminohexanoicanilide (**36**) was accomplished through coupling 2-nitrophenyl acetyl chloride with N-phenylhexamide in 70% yield with >95% chemical purity, as assessed by TLC, ^{1}H, ^{13}C, and ^{19}F NMR and HRMS. This compound was used for subsequent radiofluorination to produce [^{18}F]-2FPhAHA (**37**) under novel radiofluorination conditions of 135°C in dry DMSO to produce the compound with high radiochemical purity >99% and a decay corrected RCY of 15% as assessed by radio-analytical HPLC (**Fig. 40**).

Fluorogenic assay results screening compounds **18-27** from library in **Fig. 37** indicate leaving groups containing a phenyl ring are cleaved more rapidly by SIRT1 than those with a benzyl moiety (**Fig. 41**). The aromatic ring leaving groups containing fluorine atoms are cleaved more rapidly than iodine-substituted rings. In particular, the fluorinated phenyl groups, especially in *ortho*- or *meta*-position, are the most efficiently cleaved substrates, with k_{cat}/k_m values of 26.02 (**19**) and 63.39 M^{-1}, s^{-1} (**20**), respectively (**Fig. 42**). The *ortho*-fluorophenyl leaving group is cleaved 5-fold more efficiently by SIRT1 than any other SIRT or HDAC enzyme (**Fig. 43**). A reference, control, compound, **BPS1**, a p53 fragment (Arg-His-Lys-Lys(ac)-AMC) was also analyzed for comparison purposes.

The IC_{50} for the Cbz-Lys(2FPh)-AMC is 12.60 uM as assessed by competitive

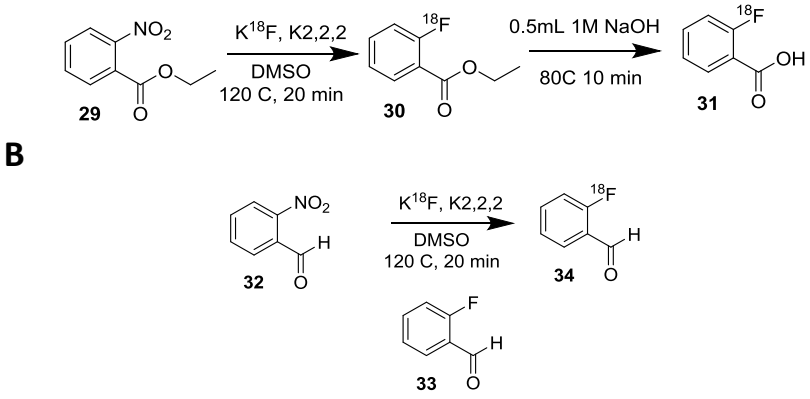

Figure 39. A) Synthesis of 2-[^{18}F]-ethylbenzoate (**30)** and corresponding benzoic acid (**31**) from the commercially available 2-nitro-ethylbenzoate (**29**). **B)** Synthesis of 2-[^{18}F]benzaldehyde (**34**) from 2-nitrobenzaldehyde (**32**).

inhibition assay with commercial SIRT1 inhibitor, EX-527 (**Fig. 44**).

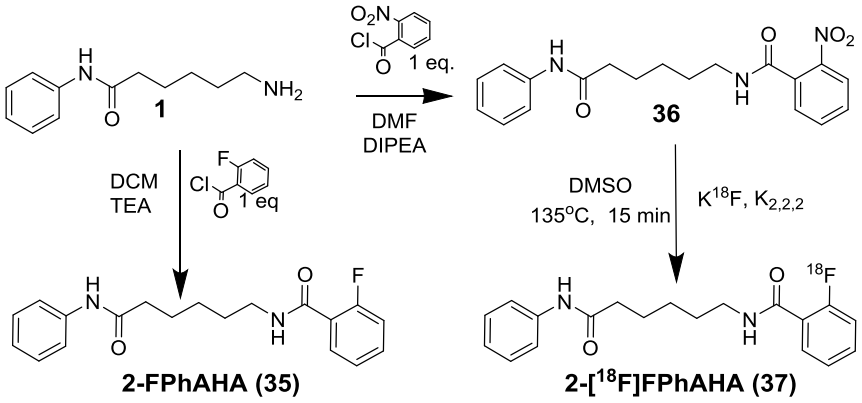

Figure 40. Synthesis of 2-nitrophenylaminohexanoicanilide (**36**) to be used as a precursor for radiolabeling with F-18 to form 2-[^{18}F]phenylaminohexanoicanilide (**37**). The non-radiolabeled standard 2-fluorophenylaminohexanoicanilide (**35**) was

In vivo assessment of 2-[^{18}F]PhAHA via dynamic PET/CT/MRI imaging in the normal rat displayed significant accumulation of 2-[^{18}F]PhAHA-derived radioactivity in specific areas of the brain, i.e. *n.accumbens, dentate gyrus, hippocampus, lateral septal nucleus, caudate putamen* and *amygdala* (**Fig. 45-46**). These areas of the brain correlate well with reported IHC data for SIRT1 expression within rodent brain (**Fig. 47**). Autoradiography preformed from these images demonstrated accumulated radioactivity in these areas of the brain as determined by alignment with brain atlas maps (**Fig. 48**).

In vivo inhibitor studies demonstrate significant decrease in accumulation of 2-[^{18}F]PhAHA-derived radioactivity in areas of the brain after i.p. administration of EX-527 (5mg/kg), SIRT1-selective inhibitor, 30 min prior to PET/CT imaging (**Fig. 49**).

Assessment of radiolabeled 2-[^{18}F]PhAHA metabolites by *in vivo* PET/CT imaging with i.v. administered 2-[^{18}F]Ethylbenzoate (further metabolized to 2-[^{18}F]Benzoic acid) and 2-[^{18}F]benzaldehyde was conducted to establish the potential contribution of metabolites to regional

uptake of 2-[^{18}F]PhAHA (**Fig. 50)**. Furthermore, it is interesting to analyze the differences in radiotracer derived accumulation in each of these three compounds.

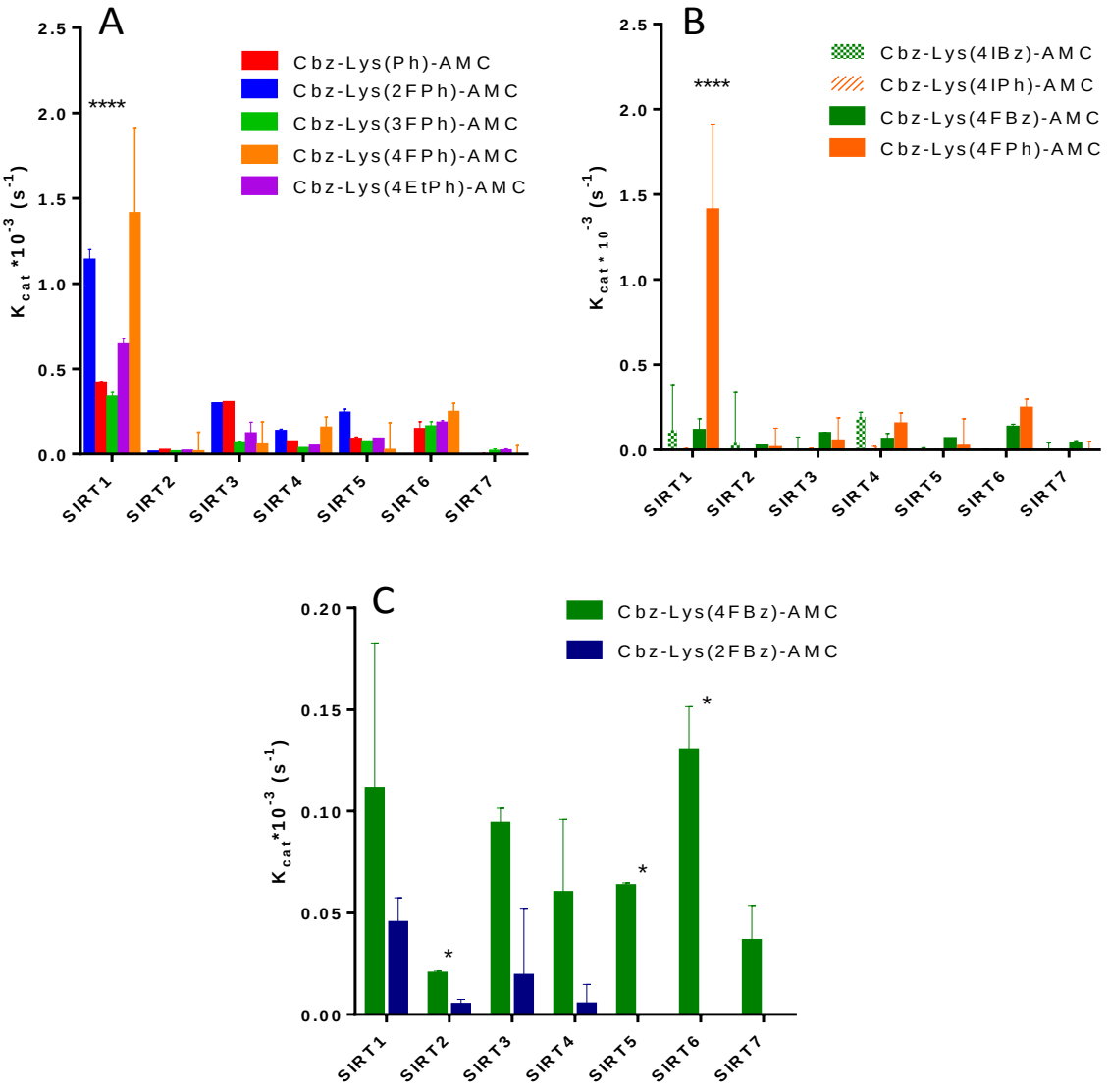

Figure 41. The catalytic efficiencies (k_{cat}) for the library of compounds synthesized assayed against a panel of recombinant SIRT enzymes. **A**) Demonstrates the catalytic cleavage rat to be greatest for the 4FPh leaving group and the 2FPh leaving group. Statistical significance is denoted by stars as tested by ANOVA. **B**) Comparing the iodine vs fluorine substitutions on a phenyl or benzyl ring, 4IPh is cleaved significantly faster than the iodinated compounds, especially for SIRT1. **C**) Comparison of 2FBz vs 4FBz leaving groups, the 4FBz is cleaved more efficiently by SIRT1.

Discussion:

Towards the development of a novel substrate-type radiotracer for quantitative molecular imaging of SIRT1 expression and activity, we developed a focused library of substrates comprised of the Cbz-Lys-AMC backbone and various phenyl or benzyl leaving groups. This cap group has been widely used for SIRT substrates and is especially useful for preliminary screening due to the presence of a fluorescent moiety, 7-amino-4-methylcoumarin (AMC), with which high throughput fluorogenic assays can be used. Previously, it has been reported that in addition to the acetyl group, SIRT1 can also cleave a phenylacetylated lysine with 56% of the natural catalytic efficiency (Hirsch and Zheng, 2011) (**Fig. 29**). Similarly, other class III HDAC enzymes have been reported to cleave long acyl chains (myristoyl), glutaryl or succinyl moieties (Du et al., 2011; He et al., 2014; Heltweg et al., 2004; Hirsch and Zheng, 2011). However, there are no data on the effects of aromatic ring fluorine substitution or phenyl vs. benzyl moieties on SIRT1 catalytic efficiency.

Current studies demonstrate that SIRT1 catalytic rate of cleavage (k_{cat}) is greatest with either the 2FPh (**19**) leaving group or the 4FPh (**21**) leaving group (**Fig. 36**). Furthermore, these compounds display much greater rates of catalytic cleavage by SIRT1 than any of the other sirtuins. In testing the catalytic rate of cleavage for other types of leaving groups, including iodinated substrates (**25, 26**) and phenyl (**18-21**) and benzyl (**22-24**) moieties, it is clear that 2FPh (**19**), 3FPh (**20**), and 4FPh (**21**) are the strongest candidates for SIRT1 (**Fig. 42**). However, the rates of catalytic cleavage (k_{cat}) are not always proportional to the catalytic efficiency (k_{cat}/k_m), therefore further analysis was done to ensure the most efficient substrate leaving group was used for radiotracer development. Taking this into account, a full kinetic analysis was performed for a subset of the original library of compounds, to include only compounds **18-24**. These results confirm that SIRT1 catalytic efficiency (k_{cat}/k_m) is greatest with a phenyl ring leaving group as

opposed to a benzyl (phenylacetyl) moiety (**Fig. 42**). Interestingly, **21** was cleaved with a greater

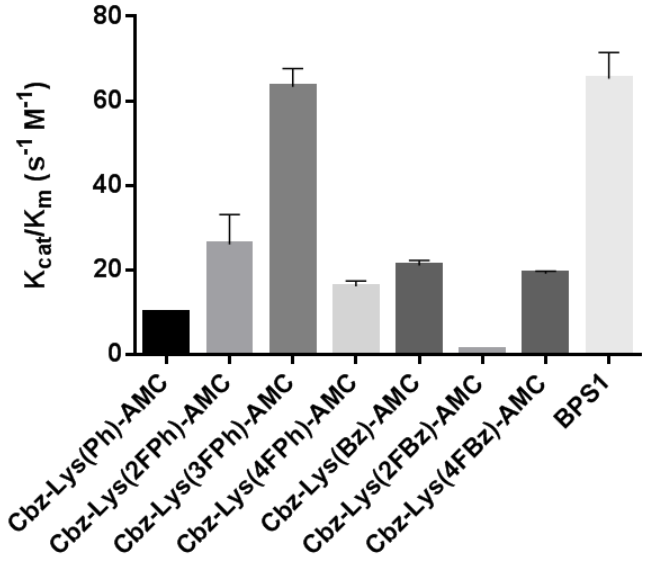

	Ph	2FPh	3FPh	4FPh	Bz	4FBz	BPS1
Vmax (uM/sec)	0.015	0.102	0.373	0.028	0.051	0.294	0.536
Stand. Dev.	4.32E-04	3.53E-02	1.81E-02	3.33E-03	5.27E-03	6.36E-03	2.83E-01
km(uM)	91.99	239.16	358.95	104.84	147.96	940.38	500.34
Stand. Dev.	2.70	82.71	17.41	12.61	15.32	20.34	264.45
kcat (per sec)	0.0009	0.0062	0.0228	0.0017	0.0031	0.0179	0.0327
Stand. Dev.	2.56E-05	2.09E-03	1.07E-03	1.97E-04	3.12E-04	3.76E-04	1.68E-02
kcat/km (per sec, M)	9.75	26.02	63.39	16.08	21.00	19.06	65.29
Stand. Dev.	0.37	7.07	4.32	1.32	1.22	0.58	6.21

Figure 42. Evaluation of fluorine substituent positioning on both the phenyl and benzyl leaving groups on SIRT1 catalytic efficiency, as determined by fluorogenic (*Fluor de Lys*®) assay. The catalytic efficiency of SIRT1 is demonstrated by k_{cat}/k_m and the error bars represent the standard deviation of the mean from N=3 experiments. The full kinetic parameters for SIRT1 with selected substrates are detailed in this table. The data represents the apparent Michelis-Menton kinetics as derived from initial steady-state reaction velocity.

rate than **20** but is cleaved less efficiently when k_m is taken into account, making compounds **19** and **20** the most efficient substrates for SIRT1(k_{cat}/k_m = 26.02 and 63.39 M^{-1}, s^{-1}) (**Fig. 36**).

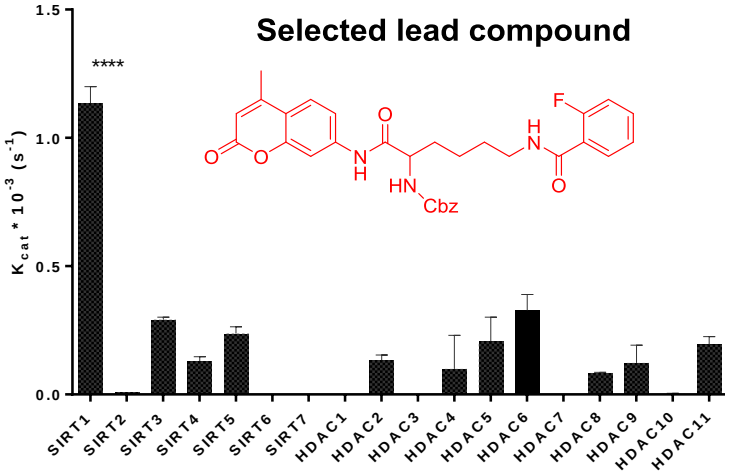

Figure 43. The catalytic efficiency for the lead compound Cbz-Lys (2FPh)-AMC (19) was assessed in a panel of recombinant HDACs for relative selectivity for SIRT1. The data were analyzed by one way ANOVA; statistically significant differences with P<0.05 were denoted by ****.

Previously, SIRT1 has been reported to cleave a benzyl leaving group at 50% of its natural deacetylation rate, which is confirmed here, comparing **22** (21 M^{-1}, s^{-1}) to **BPS1** (65 M^{-1}, s^{-1}) (**Fig. 42**), however, a fluorine substitution on the benzyl leaving group decreases the catalytic efficiency. Whereas, with a phenyl moiety, fluorine substitution actually increases catalytic efficiency. Compound **20**, containing 3-fluorophenyl leaving group, is cleaved equally as efficiently as the acetylated standard, p53Lys^{382}(ac) analogue (Arg-His-Lys-Lys(ac)-AMC, **BPS1**). (k_{cat}/k_m = 65.29 M^{-1}, s^{-1}) and compound **19** cleaved at 25% of the rate.

Although, the 3-fluorophenyl (**20**) leaving group is cleaved moderately more efficiently by SIRT1 than the 2-fluorophenyl leaving group, compound **19** was chosen as the lead substrate for further development as an imaging agent. This decision was influenced by a significant increase in difficulty for radiofluorination and opportunity for *in vivo* defluorination by various esterase enzymes with a *meta*-fluorophenyl ring. However, current work is focused on development of 3-[^{18}F]fluorophenyl derived radiotracer for a SIRT1-selective imaging agent, as well.

To establish selectivity of **19** for SIRT1 among other SIRT and HDAC proteins, compound **19** was screened against a panel of recombinant proteins including HDACs1-11 and SIRT1-7. Compound **19** demonstrated at least 3-fold increase in relative rates of cleavage by SIRT1 over all HDACs based upon k_{cat} values. HDAC 6 expressed the closest catalytic activity to SIRT1 of any other HDAC enzymes, with a relative k_{cat} of 30% of SIRT1 (**Fig. 44**), however HDAC6 has much lower expression in the brain, effectively increasing the SIRT1 selectivity within the brain (Ramadori et al., 2008). Furthermore, to assess the effectiveness of lead substrate **19** against a potent, SIRT1-selective inhibitor, a competitive inhibition assay with EX-527 (Selisistat) (Cui et al., 2014; Napper et al., 2005) was performed using increasing concentrations of EX-527 and apparent k_m concentration of **19** for SIRT1 (239 µM). The observed inhibition for SIRT1 cleavage of compound **19** with increasing concentrations of EX-527 can be used to

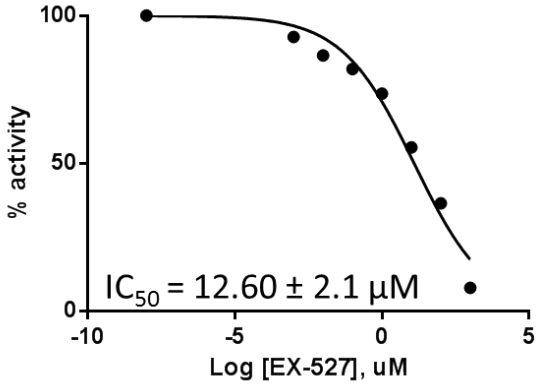

Figure 44. IC_{50} curve for SIRT1 with **19** at its apparent *km* value obtained by competition assay with known potent SIRT1 selective inhibitor, EX-527 at increasing concentrations on the log scale.

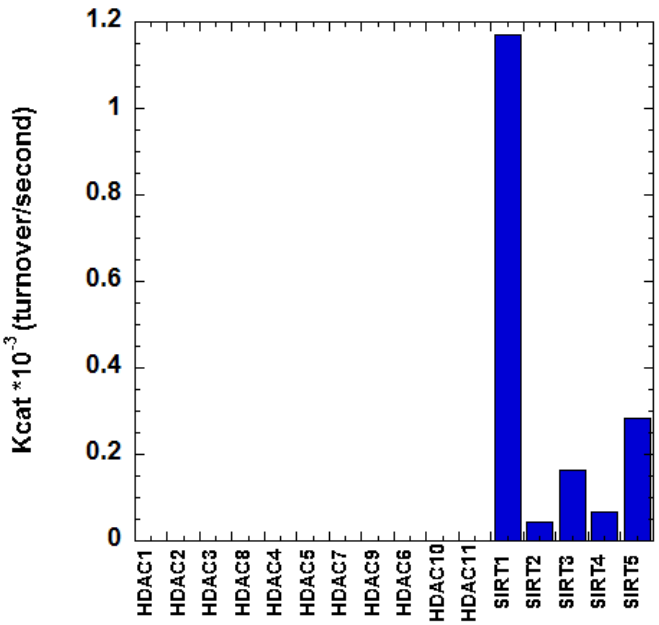

Figure 45. HPLC analysis for catalytic rates of cleavage of 4-FPhAHA (**28**) with a panel of recombinant HDAC enzymes (HDACs 1-11 and SIRT1-5) demonstrating selective cleavage by SIRT1.

calculate an IC_{50} value of 12.6 +/- 2.1 μM (**Fig. 44**). This value is significantly higher than previously reported IC_{50} value of 0.098 μM obtained using fluorogenic oligo peptide-acylated substrates of p53-Lys^{382} (**BPS1**) (Napper et al., 2005). Using our system, we independently found a comparable IC_{50} of 0.0103 +/- 0.0025 μM for **BPS1** and SIRT1 with inhibitor EX-527. While the experimental IC_{50} values for **BPS1** and **19** vary significantly, the catalytic efficiency (k_{cat}/k_m) differ much less and may be explainable, at least in part, due to the differences in cap groups (peptide vs blocking group).

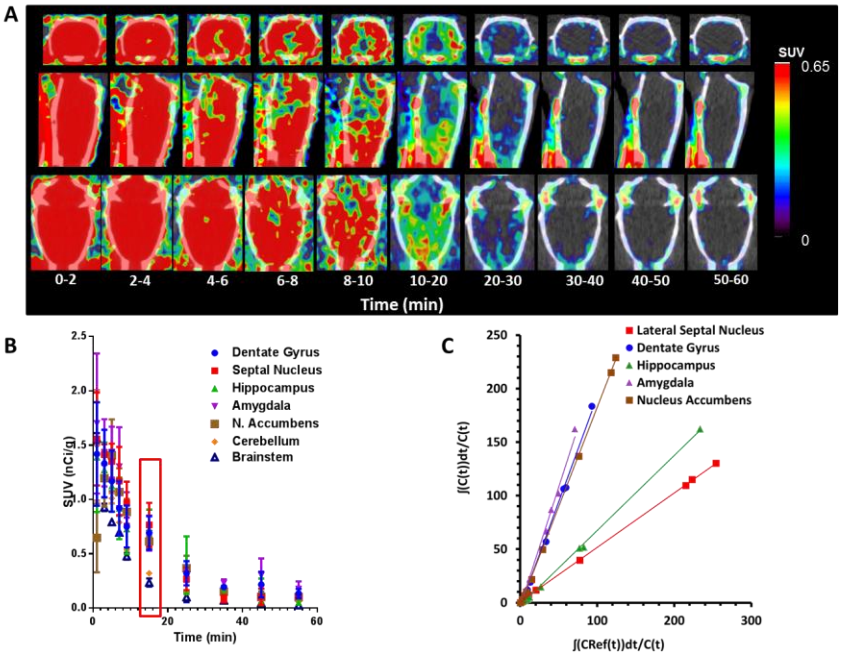

Figure 46. Dynamic PET/CT images acquired using 2-[^{18}F]PhAHA demonstrating differential washout over time normalized to peak SUV values at 20 min.

To create a more pharmacologically viable substrate radiotracer, compound **19** has been converted to an analogue using aminohexanoicanilide (AHA) backbone rather than the larger Cbz-Lys-AMC group. The resulting radiotracer, 2-[^{18}F]fluorophenylacetamidohexanoicanilide (2-[^{18}F]PhAHA, **37**), was developed in both F-18 and F-19 versions (**Fig. 40**). Towards synthesis of this radiolabeled compound, there are no established methods for radiofluorination on a phenyl ring in the *ortho* position, thus we developed new methodology for radiosynthesis of 2-[^{18}F]PhAHA. Originally, both 2-nitrophenylaminohexanoicanilide (2-NO_2PhAHA, **36**) and 2-

trimethylamoniumsalt-phenylaminohexanoicanilide precursors were developed, however after testing radiofluorination conditions, only 2-NO_2PhAHA proved to be successful. This finding contradicts the data for *para*- radiofluorination on a phenyl ring where the trimethylammonium salt precursor produces higher yields than the nitro leaving group.

In vitro HPLC analysis of 4-FPhAHA demonstrates comparable cleavage rates (k_{cat}) as compared to *in vitro* fluorogenic studies of **21** for SIRTs 1-5 (**Fig. 45**). This study confirms the

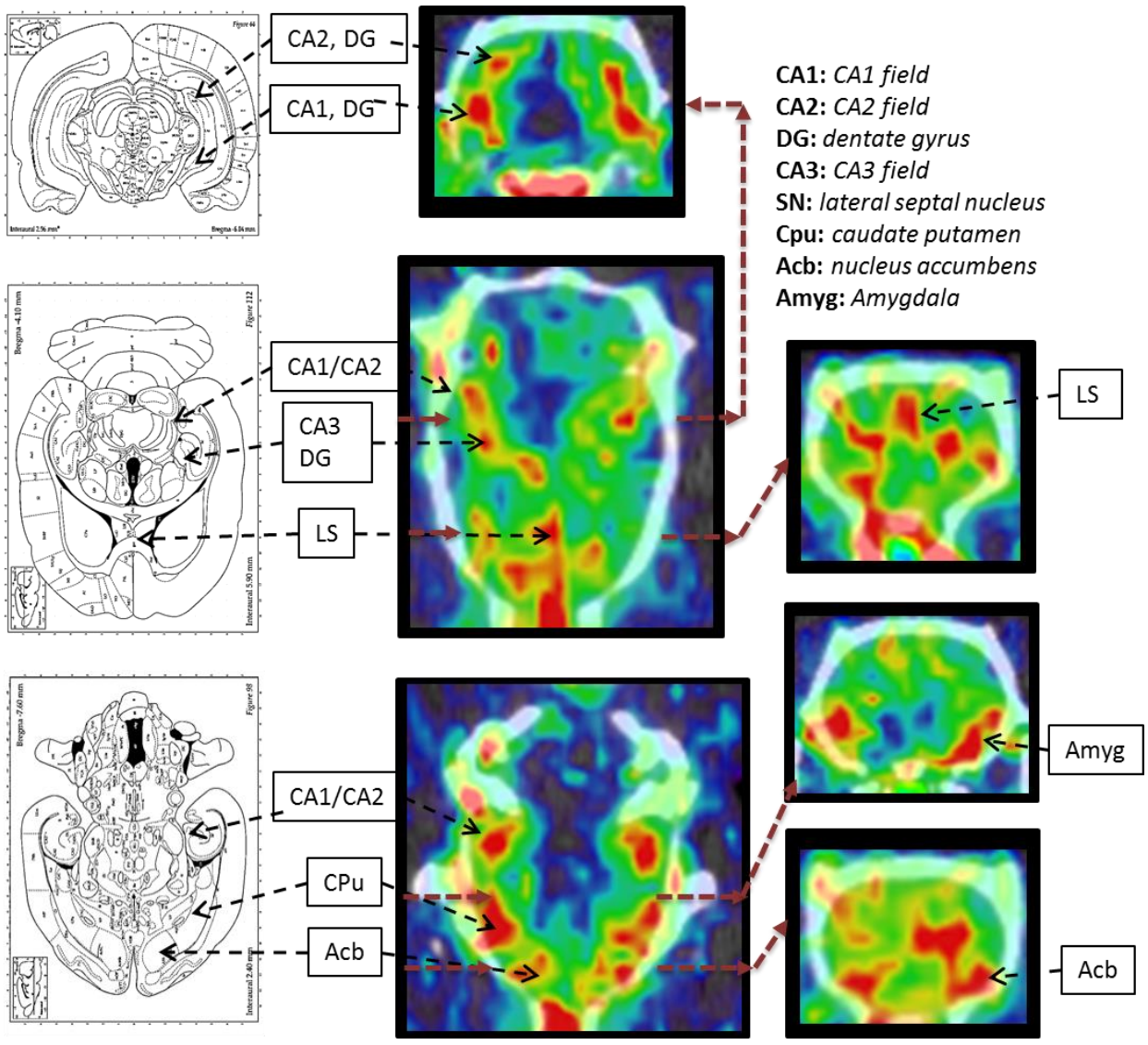

Figure 47. Representative PET/CT images using 2-[^{18}F]PhAHA aligned with rat brain atlas maps demonstrating the areas of high accumulation that align with areas of the brain such as *hippocampus (CA1, CA2, CA3), dentate gyrus(DG), n. accumbens (Acb), caudate putamen (Cpu),* and *amygdala (amyg).*

AHA backbone is sufficiently recognized and attached leaving group is cleaved by SIRT1 without appreciable loss in efficacy.

The mechanism of substrate cleavage by SIRT enzymes allows for the radioactive leaving group to be transiently entrapped in a cell in a similar manner to other radiotracers such as ^{18}F-FDG and ^{18}F-FLT, by conversion of a tracer into a more polar molecule. Theoretically, as the result of ester linkage between the leaving group with O-ADPR (**Fig. 35**), the leaving group is trapped inside the cell in form of the ^{18}F-fluorophenyl-O-ADPR product. Therefore, SIRT1-mediated cleavage of ^{18}F-fluorophenyl group from 2-[^{18}F]PhAHA with formation of 2-^{18}F-fluorophenyl-O-ADPR complex represents the rate-limiting step in the cellular entrapment of 2-[^{18}F]PhAHA -derived radioactivity. The removal of an acetyl (or other) moiety from the O-ADPR group has been investigated and hypothesized that enzymes such as ARH3 may cleave an acetyl moiety from the O-AADPR (O-acetyl-ADP-ribose) ring or possible methanolysis of acetyl into 1'O-methyl'ADPR may occur. Additionally, a nucleophilic attack from lysine side chains of other proteins in close proximity may

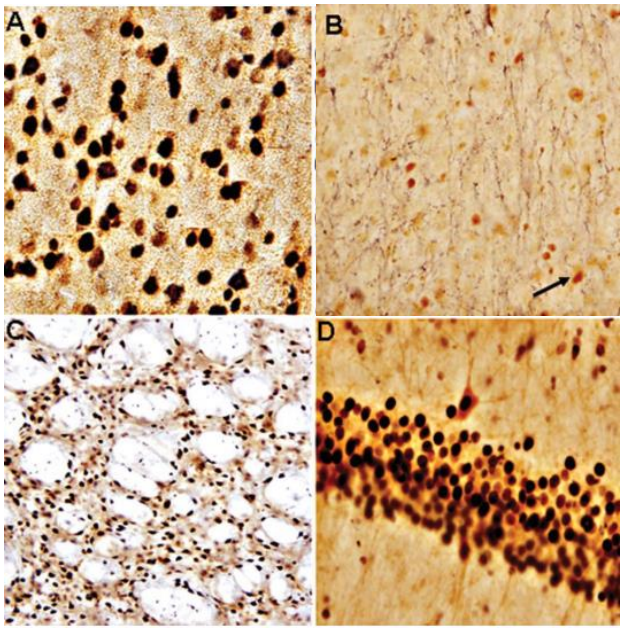

Figure 48. IHC results demonstrating increased SIRT1-expression in the rat. A) Rat prefrontal cortex; B) Rat nucleus accumbens; C) Rat striatum; D) rat hippocampus. Data is from literature (Zakhary et al., 2010). The arrow indicates nuclear localization of the stain within neuronal fibers.

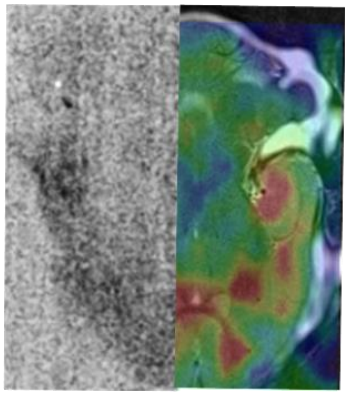

Figure 49. Autoradiography (left) aligned with corresponding PET/CT/MR image (right) for 2-[^{18}F]PhAHA.

also de-acetylate the O-AADPR. However, little is known about the removal of a larger group such as a phenyl ring from ADP moiety, therefore further studies are needed to fully characterize the half-life of O-2-[^{18}F]Ph-ADPR, and determine whether this intermediate is in fact stabile. These factors will contribute to the residence time for the possible radiotracer-derived metabolite, 2-[^{18}F]benzoic acid, within the cell. Characterizing the nature of this entrapment is important because this represents k_4 in the molecular imaging equation and determines whether the circulating metabolite may contribute to radiotracer volume of distribution.

Additionally, altered SIRT1 expression levels have been noted in many neurodegenerative diseases, such as Huntington's, and have led to exploratory clinical trials with SIRT1 selective inhibitors, such as Selisistat (EX-527) (Smith et al., 2014), for treatment of the disease (Sussmuth et al., 2015). Though there is some debate in literature regarding the effectiveness of SIRT1 activators vs. inhibitors for treatment of neurodegeneration (Naia and Rego, 2015). In fact, both SIRT1-activators and inhibitors are currently in clinical trials for treatments of different pathologic conditions. Therefore, non-invasive molecular imaging with PET using SIRT1-specific substrate-type radiotracers may provide information about both location and magnitude for SIRT1-expression and activity, which could help to determine the mechanistic, therapeutic and prognostic roles of SIRT1 in different pathological states. One area where this may be especially useful, is within the brain, where biopsies are not possible and SIRT1 plays very pleiotropic roles in both norm and neuropathological conditions.

Dynamic PET/CT images of the brain, acquired in normal rats, using 2-[^{18}F]PhAHA, have demonstrated significant differential tracer washout in areas of the brain with relatively higher SIRT1 expression, as correlated with ISH and IHC results in literature (Ramadori et al., 2008; Zakhary et al., 2010) (**Fig. 46-48)**. The accumulation of 2-[^{18}F]PhAHA- derived radioactivity in

areas of the brain is most predominant at 15-30 minutes post administration of the tracer. This is verified by both Logan plots and time activity curve quantification of PET/CT images with 2-[^{18}F]PhAHA (**Fig. 46**). Alignment of the brain regions to the corresponding brain atlas regions demonstrates high activity in *hippocampus, caudate putamen, dentate gyrus, amygdala and n. accumbens* (**Fig. 47**). While there is very little tracer-derived radioactivity accumulation in the brainstem region or the cerebellum. This observation, coupled with literature findings of little SIRT1 activity in these areas, allow us to use the brainstem as a reference tissue for quantification.

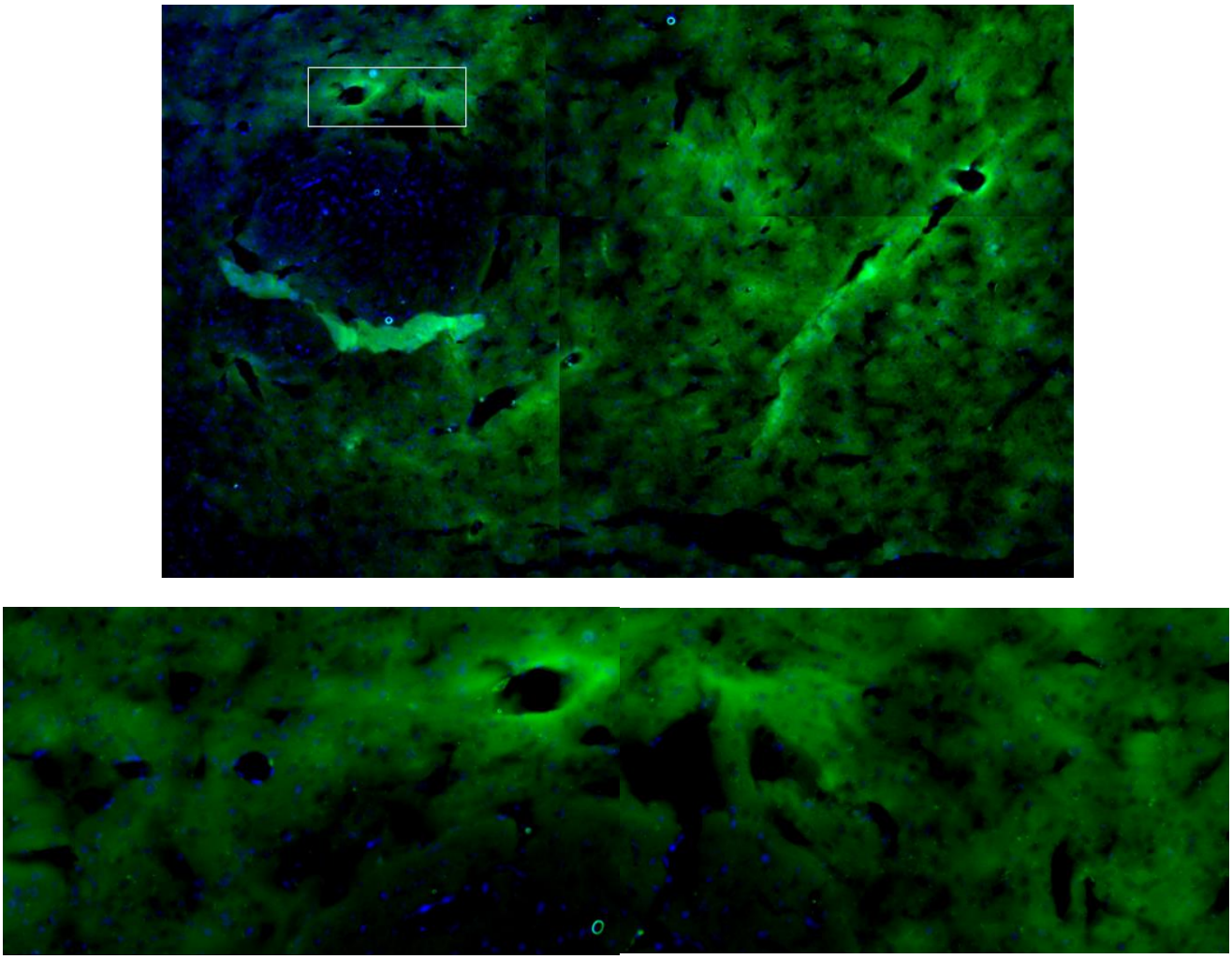

Figure 50. Fluorescent microscopy staining for SIRT1 with an alexa-fluor 488 primary conjugated antibody (green), counter stained with DAPI as a nuclear marker (blue) at 10x magnification. The white box is magnified at 20x on bottom.

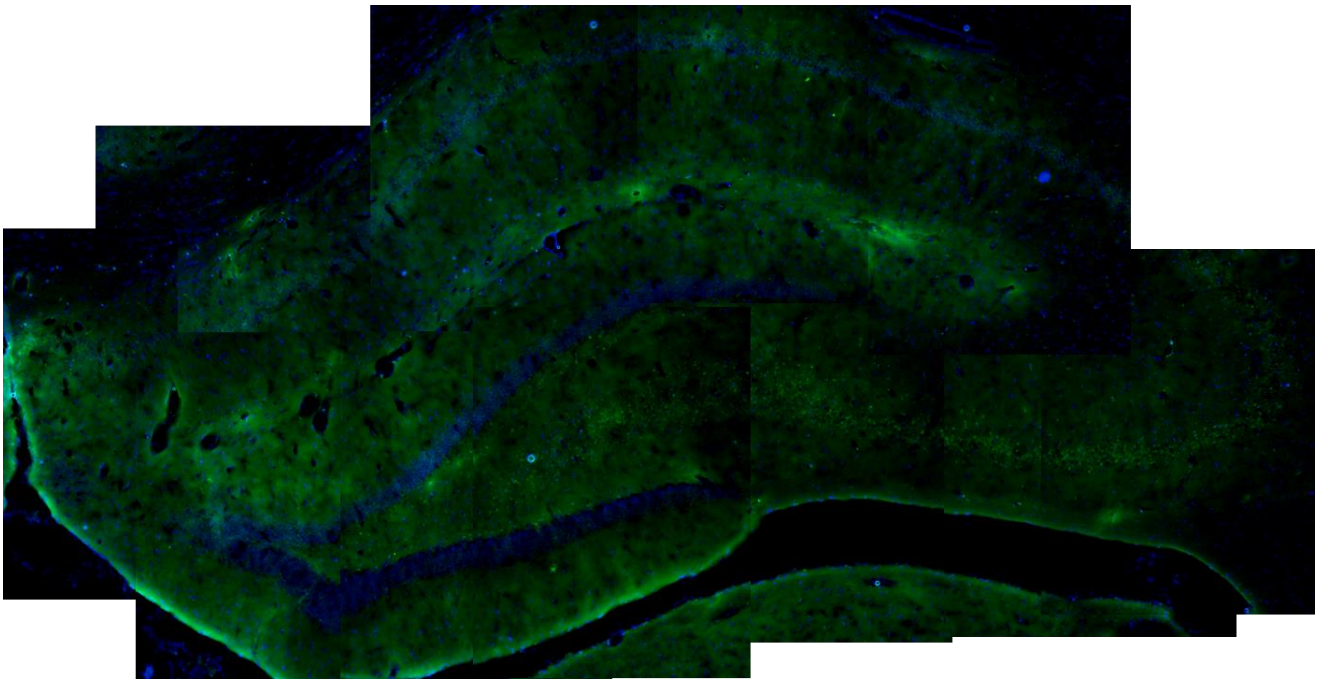

Figure 51. Fluorescent staining of SIRT1 expression in the hippocampus of a rat brain (green) counter stained with DAPI nuclear marker (blue).

Furthermore, autoradiography was performed at 20 minutes post i.v. administration of 2-[^{18}F]PhAHA to capture the radioactivity accumulated at this time point, corresponding to the highest point of differential washout on the time activity curves (**Fig. 49**). The axial autoradiography images acquired with 2-[^{18}F]PhAHA correlate well to the axial PET/CT images of the corresponding brain region.

Fluorescent microscopy of brain slices stained for SIRT1 with DAPI counter stains demonstrates increased SIRT1 expression in hippocampal regions,

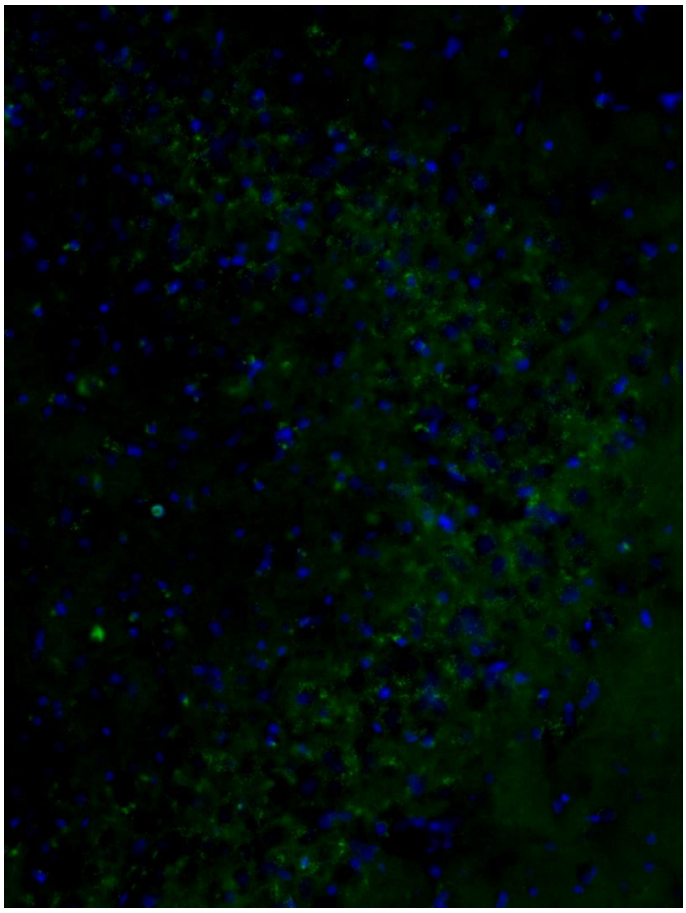

Figure 52. 20x magnification of hippocampal CA2 region with SIRT1 fluorescent stain in green and DAPI, nuclear marker, in blue.

specifically in the CA2 region and *nucleus accumbens* (**Fig. 50-52**). The ventral and ventral-medial sides of the *n. accumbens* demonstrate the highest increase in SIRT1 expression. From the magnified image, it is possible to depict both nuclear and cytoplasmic localization for SIRT1. The hippocampal region also demonstrates significant increases in SIRT1 expression as seen on fluorescent images of the CA1, CA2 and CA3 region (**Fig. 51**). This correlates well with what is seen on PET/CT images with 2-[^{18}F]PhAHA. It is evident from this image that the CA2 (lateral aspect of hippocampus) region has higher SIRT1 expression than CA1 (medial aspect of hippocampus). The magnified view of CA2 shows heterogenous localization for SIRT1, both cytoplasmic as well as nuclear. Interestingly, the corpus collosum has no SIRT1 expression and only shows nuclear stains. Another key factor to note is the strong axonal staining evident within the hippocampus indicating strong SIRT1 localization and presence within the axonal cytoplasm. Within some cells of the image, it is possible to define the distinct axon radiating from the nucleus. The staining of SIRT1 in the hippocampus matches the more lateral accumulation of 2-[^{18}F]PhAHA within the hippocampus and lack of accumulation in the middle of the hippocampal region on coronal sections. Furthermore, these data correspond well to the published IHC and ISH data for SIRT1 in both mouse and rat brains (Ramadori et al., 2008; Zakhary et al., 2010).

To further test the responsiveness of novel SIRT1-selective radiotracer 2-[^{18}F]PhAHA to an inhibitor *in vivo*, EX-527 was used at 5mg/kg dose i.p. 30 min prior to imaging to demonstrate differences in 2-[^{18}F]PhAHA-derived radioactivity accumulation before and after inhibitor administration in the same animal, 24 hours apart. The significant decreases in 2-[^{18}F]PhAHA-derived radioactivity accumulation evident in dynamic PET/CT images after administration of inhibitor, specifically in regions of the brain of previously high radioactivity accumulation, validates the *in vivo* selectivity of this radiotracer for SIRT1. Quantitatively, these differences are demonstrated as differences in SUV at 22 min post radiotracer injection, for many regions of the brain, as well as muscle for reference (**Fig. 53**). As previously noted, the brainstem demonstrates little SIRT1 activity and accumulation of 2-[^{18}F]PhAHA-derived radioactivity product, this is further validated through the lack of differences seen with and without inhibitor (**Fig. 53**). However, it should be noted that EX-527 may have limited BBB penetrability, thereby dampening the effects of the inhibitor within the brain. This is evidenced by other ongoing studies in rats

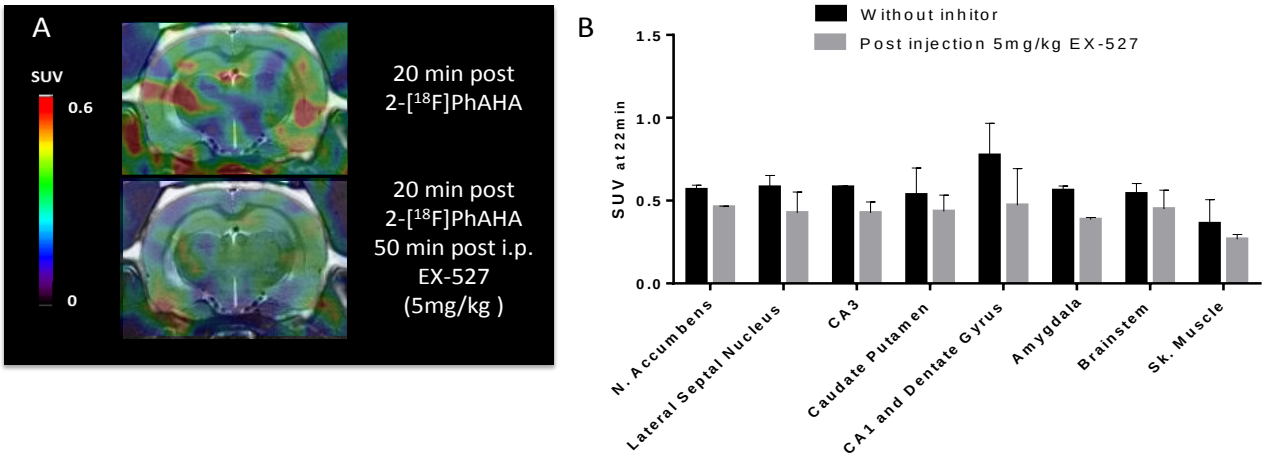

Figure 53. **A)** PET/CT images acquired with 2-[^{18}F]PhAHA (at 20 min post i.v. bolus injection) and without administration of SIRT1 selective inhibitor EX-527 (5 mg/kg) given 30 min prior to radiotracer i.p.. **B)** Quantification of dynamic PET/CT images demonstrating a decrease in uptake of 2-[^{18}F]PhAHA in areas of high SIRT1-specific accumulation within the brain.

bearing brain tumors, with a broken BBB, where much greater differences in 2-[^{18}F]PhAHA-derived radioactivity accumulation are seen before and after inhibitor administration.

Additional PET/CT images were acquired using radiolabeled metabolites of 2-[^{18}F]PhAHA (**37**), including 2-[^{18}F]Ethylbenzoate (**30**), 2-[^{18}F]benzoic acid (**31**) and 2-[^{18}F]benzaldehyde (**34**) in both normal mice and rats (**Fig. 54-55**). It is possible that when 2-[^{18}F]PhAHA is cleaved the phenyl ring leaving group may be attached to the -OADPR ring only briefly due to increased steric hindrance of a phenyl ring as compared to an acetyl moiety. While more *in vitro* studies are needed to understand this mechanism in full, imaging animals with possible radiolabeled metabolites provides information regarding the potential contribution of metabolites to the images acquired with 2-[^{18}F]PhAHA. This study also helps to identify whether SIRT1 mediated cleavage is the primary source of cleavage for the parent compound or whether peripheral cleavage is occurring, leading to an increased fraction of free metabolites.

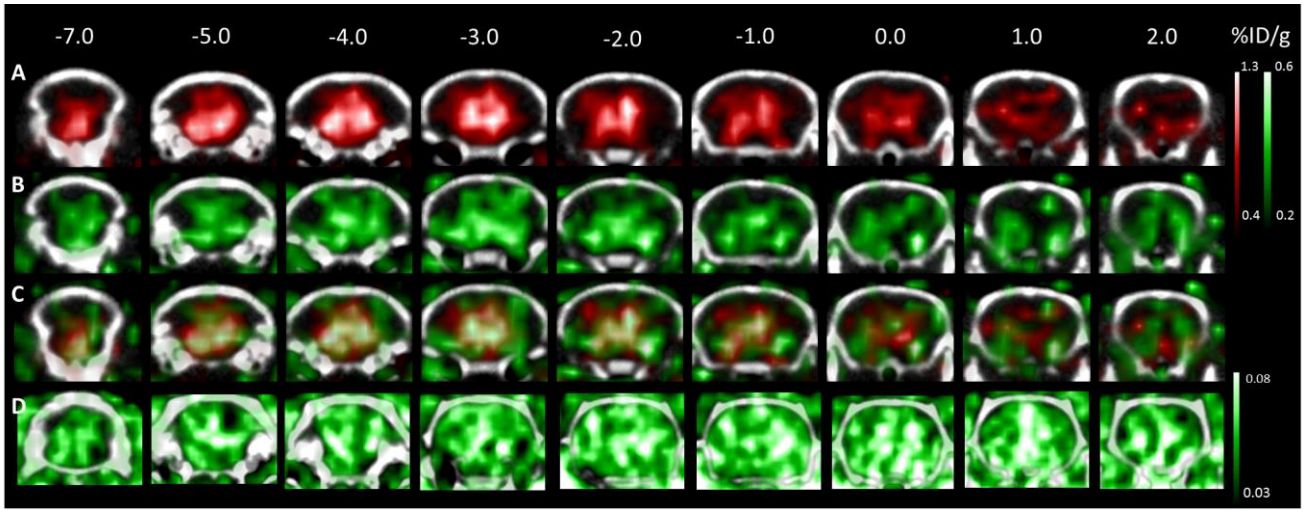

Figure 54. A) PET/CT images of a mouse post i.v. administration of 2-[^{18}F]Benzoic acid (**31**) **B)**: PET/CT images of a mouse post i.v. administration of 2-[^{18}F]ethylbenzoate (**30**) **C)** Overlay of **A** and **B D)** PET/CT images of a rat post i.v. administration of 2-[^{18}F]Ethylbenzoate. All images taken at 25 min. post radiotracer injection.

2-[^{18}F]Ethylbenzoate was chosen as an attempt to create a more BBB permeable metabolite that would be cleaved to 2-[^{18}F]benzoic acid (**31**) upon entering the brain by the abundant brain esterases. However, PET/CT images in mice at 20 min. post i.v. administration of **30** and **31** demonstrated an increased BBB penetration of **31** over **30**, which was surprising given the nature of the compounds' polarity (**Fig. 54**). Furthermore, once inside the brain both of these compounds exhibited remarkable differences in accumulation patterns. Compound **31** accumulates preferentially in the median reticular nucleus (-2.0- -4.0), where as compound **30** accumulates much more in the hypothalamic and amygdala regions (-2.0) (**Fig. 53-54**). Also, interesting to note that imaging with compound **30** in a rat (**Fig. 54D, Fig 55**) does not demonstrate the same patterns as in a mouse and exhibits even lower BBB permeability. One possible reason for these differences could be due to changes in esterase activity between species. The reasoning behind reduced BBB penetrance with compound **30** is still yet unknown and warrants further investigation.

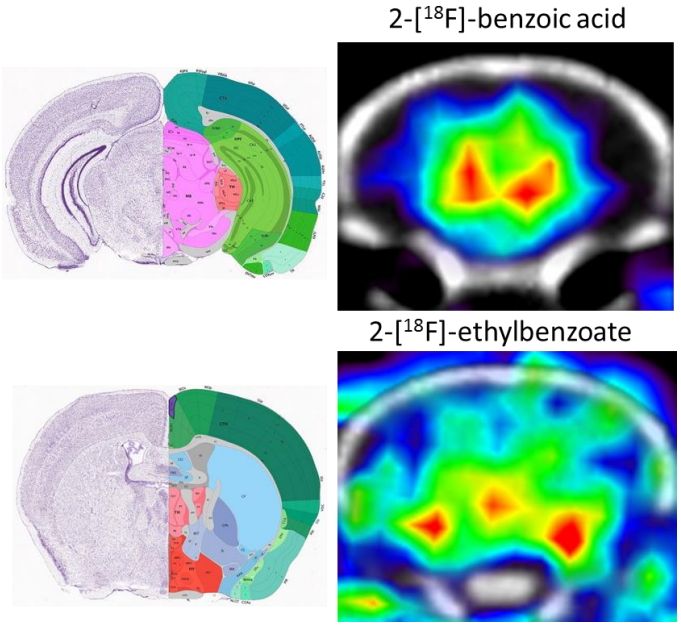

Figure 55. PET/CT images with compound **30** (bottom) and **31** (top) and corresponding brain histology and maps.

In a rat, compounds **30** and **34** were studied with the parent compound **37**. Compound **34** demonstrated significantly increased BBB permeability over compound **30** and strong accumulation in the brainstem (**Fig. 54**). 2-[^{18}F]benzaldehyde exhibits remarkably different patterns of radioactivity accumulation within the

brain as compared to the parent compound, 2-[^{18}F]PhAHA. The biggest difference between the two is a great increase in accumulation of 2-[^{18}F]benzaldehyde-derived radioactivity within the brainstem, whereas 2-[^{18}F]PhAHA-derived radioactivity accumulation in this area is minimal. There are some regions within the brain of overlap, such as *nucleus accumbens*. The large variation in patterns of radioactivity accumulation between these three radiotracers within the brain highlights the results of using a substrate-type radiotracer. Within the brain, SIRT1-mediated cleavage of the parent compound causes cellular entrapment of the radiolabeled leaving group. Administration of the "pre-cleaved" metabolite (i.e. fluorobenzoic acid or fluorobenzaldehyde) does not allow enzyme-mediated entrapment to occur.

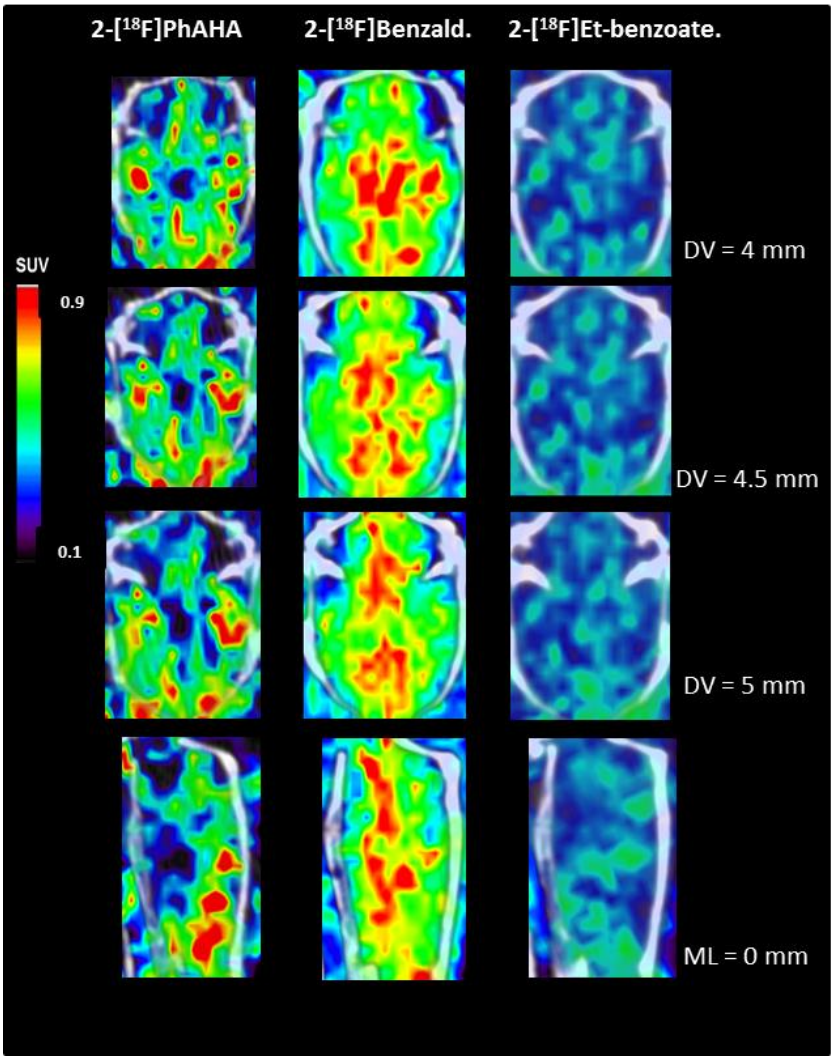

Figure 56. Comparison between PET/CT images acquired 20 min. post i.v. administration of three tracers, the parent compound 2-[^{18}F]PhAHA (**37**), and two possible metabolites: 2-[^{18}F]benzaldehyde (**34**) and 2-[^{18}F]Ethylbenzoate (**30**) metabolized to 2-[^{18}F]benzoic acid (**31**).

The pattern of accumulation of 2-[^{18}F]-benzaldehyde (**34**) within specific regions of the brain has not yet been fully explained. However, it is known that benzaldehyde acts as a potent inhibitor of glutathione peroxidase (GSH-PX) (Tabatabaie and Floyd, 1996). Reportedly, 250 μM of benzaldehyde is sufficient to completely remove all residual GSH-PX activity and 2-bromobenzaldehyde or 2-hydroxybenzaldehyde reduce GSH-PX activity by 80% at 250 μM (Tabatabaie and Floyd, 1996). These two compounds have similar chemical properties and size to 2-fluorobenzaldehyde. Furthermore, areas within the brain demonstrating high levels of GSH-PX include structures within the brainstem (i.e. *pons*, *medulla*, *mesencephalon*) (Nisticò et al., 1992). These structures have almost a 2 fold increase in levels of active GSH-PX over other structures within the brain such as the *cortex* and *hippocampus*, particularly in adult rats (Nisticò et al., 1992). These findings may provide an explanation to the perceived selectivity for 2-[^{18}F]-benzaldehyde (**34**) accumulation within structures of the brain, though more studies are needed for conclusive results.

At this point, we can conclude that the metabolites may not be having a large influence on the distribution of 2-[^{18}F]PhAHA seen in the brain. Even more importantly, there is a difference between SIRT1-mediated cleavage of 2-[^{18}F]PhAHA and administering the pre-cleaved product, thus indirectly supporting the theory to the degree of radiolabeled metabolite entrapment within the cell. Further studies are also necessary to understand why the stark difference in BBB permeability between **30** and **31**.

The translation of 2-[^{18}F]PhAHA to *in vivo* PET imaging may further the field of epigenetic regulation in both norm and disease and facilitate the development and clinical translation of SIRT1-targeted drugs. PET imaging with a substrate type radiotracer such as 2-[^{18}F]PhAHA will allow for in vivo visualization and quantification of the enzyme expression-activity product.

Therefore, the accumulation of 2-[^{18}F]PhAHA derived radioactivity is directly proportional to the amount of active enzyme in a tissue. The current approach to imaging SIRT1 activity using substrate-type radiotracers complements other methodologies for PET imaging of enzymes, including radiolabeled inhibitors. PET imaging with radiolabeled enzyme inhibitors is essentially similar to a receptor-ligand based imaging approach, where the amount of radiotracer-derived radioactivity accumulation is proportional to the amount of free (unoccupied) receptor or enzyme in a given tissue (J, 2000). The visualization of receptor or enzyme occupancy is especially important for determining the pharmacokinetics and bio-distribution of an inhibitor (i.e. drug or therapeutic agent). Successful inhibitor-type radiotracers have been developed specifically for HDAC class I, in the form of ^{11}C-Martinostat (Hooker et al., 2009). However, imaging with an inhibitor does not provide information about the enzyme activity. In contrast, substrate-type radiotracers allow for assessment of the enzyme expression-activity and monitoring the pharmacodynamics of inhibitor at the target (enzyme) level.

Conclusions

Visualization and quantification of SIRT1 expression-activity non-invasively *in vivo* via PET imaging may help elucidate the role of SIRT1 in both norm and disease. This work includes the first ever PET/CT imaging with and characterization of SIRT1-selective radiotracer, 2-[^{18}F]PhAHA, in the brain and can be applied to many future studies of larger animals and pathologies such as cancers and neurodegenerative disorders. Additionally, this novel understanding of SIRT1 structure activity relationships may help in development of BBB permeable pharmacologic modulators. In summary, the development of a novel method for imaging SIRT1 expression-activity in the brain should help further the field of epigenetics and treatment of untreatable diseases.

Experimental Section

All solvents were purchased from Sigma-Aldrich Chemicals (Milwaukee, WI) and used without further purification. Boc-Lys(Ac)-AMC and Cbz-Lys-OH were purchased from Bachem (Bubendorf, Switzerland) and used without further purification. Preparation of 6-amino-1hexanoicanilide (Mukhopadhyay et al., 2006) was synthesized using a previously published procedure (Yeh et al., 2013a). Thin layer chromatography (TLC) was performed on pre-coated Dynamic Absorbance F-254 silica gel, aluminum backed plates (Norcross, Georgia); flash chromatography was performed using silica gel pore size 60 Å, 230-400 mesh particle size (Sigma-Aldrich, Milwaukee, WI). NMR spectra including ^{1}H, ^{13}C and ^{19}F were performed on Mercury 400 MHz, Varian 500 MHz or Agilent 600 MHz spectrometers. High-resolution mass spectra (HRMS) were obtained using Waters LCT Premier/XE spectrometer (Milford, MA) with an electrospray ionization (ESI) technique. The analytical high performance liquid chromatography (HPLC) system included: Ascentis RP-Amide 4.4x150 mm column (Supelco, Bellefonte, PA) connected to the 1100 series pump and UV detector (Agilent Technologies, Stuttgart, Germany), operated at 254 nm, and a radioactivity detector FC3200 (Eckert and Ziegler Radiopharma, Inc, Berlin, Germany). The semi-preparative HPLC system included: the Alltima 250x10mm C18 column (Fisher Scientific, Waltham, MA) connected to the P4.1S pump, Azura 2.1S UV detector (Knauer, Berlin, Germany), operated at 254 nm, and a radioactivity detector FC-3500 (Eckert and Ziegler Radiopharma, Inc, Berlin, Germany).

SIRT Enzyme Assay: Recombinant SIRT1-7 enzymes and BPS1 reference substrate for SIRT2, an oligopeptide corresponding to 379-382 of p53 (Arg-His-Lys-Lys(Ac)-AMC) were purchased from BPS Bioscience (San Diego, CA). 10 mM solutions of all newly synthesized compounds were prepared in pure DMSO and then diluted to 100 µM aliquots in DMSO for further

use. Enzyme assay reactions were performed in black, low binding 96-well microtiter plates (Nagle Nunc International, Rochester, NY). Endpoint assays were performed by incubation of the appropriate substrate, NAD, a SIRT enzyme, and inhibitor (if applicable) in enzyme assay buffer (50 µL final volume). Control wells without enzyme were included in each plate. After 40 min at 37 °C, a developer mixture (50 µL) containing nicotinamide (2 mM) and trypsin (0.4 mg mL−1) was added, and the mixtures incubated for 30 min at 22°C. The intensity of cleaved 7-amino-4methylcoumarin (AMC) fluorescence was measured using Synergy H1 microplate reader (Biotek, Winooski, VT) at 360 nm excitation and 450 nm emission wave lengths. Experiments for determination of enzyme kinetic parameters were performed by incubation of test compounds or BPS1 reference substrate at different concentrations with NAD+ and individual SIRT enzymes in an assay buffer (100 µL final volume) at 37°C for different periods of time (5, 10, 20, 30, and 60 min), followed by in situ fluorophore cleavage by addition of a developer mixture (50 µL) containing nicotinamide (2 mM) and trypsin (0.4 mg mL−1). Fluorescence was measured as relative fluorescence units (RFU) at 22°C to determine the initial linear rate V0 (RFU min^{-1}) for each concentration. The data were analyzed using GraphPad Prism v6.02 (GraphPad, La Jolla, CA) to afford km (µM) and Vmax (RFU min^{-1}) values. The kcat values were calculated based on the RFU vs AMC concentration standard curve and the enzyme purities and concentrations provided by the manufacturer.

Fluorescent Staining: Perfused and fixed rat brains were sliced into 20 µm thick slices on a microtome for staining. The slices were mounted onto slides and stained with fluorescently conjugated primary SIRT1 antibody (Abcam) using 1:200 dilution. Following staining the slides were cover slipped using Vecashield mounting medium with DAPI included by placing 25 µL

drops of mounting media on each tissue slice. Images were taken using EVOS FL Auto Imaging System microscope (Thermo Fisher Scientific).

MRI Procedure: Animals initially anesthetized with 5% isoflurane, and maintained between 2-3% for the remainder of the experiment. During the procedure each animal was placed on a heated re-circulating water platform in order to maintain body temperature. The animals were held in position using a bite bar and a receive-only surface coil 2-element phased array for the rat brain) was placed dorsal to the head. Scans were acquired using a 7T ClinScan system (Bruker, UK) controlled by the Syngo software (Siemens, Knoxville, TN). A localizing scan was performed and adjustments to head position were made accordingly. T_2 images were obtained (repetition time [TR] 3530 ms echo time, [TE] 38 ms, FOV 3.2 cm x 3.2 cm x 2.4 cm, resolution 125 µm x 125 µm x 1 mm). Images were processed using ImageJ software (Bethesda, MD).

PET Imaging Procedures in Animals: All studies performed under a protocol approved by the Institutional Animal Care and Use Committee of Wayne State University. Sprague-Dawley rats (200-250 g, N=3) were anesthetized with 3% isoflurane in oxygen and maintained at 2% isoflurane in oxygen throughout the imaging studies. The body temperature was maintained using electronically controlled heating pad (M2M Imaging, Cleveland, OH) set at 37^{o}C. Anesthetized rats placed in the microPET R4 scanner (Siemens, Knoxville, TN) in the supine position with the long axis of the animal parallel to the long axis of the scanner with the brain positioned in the center of the field of view. Each radiotracer (300-500 µCi/animal) was administered in saline via the tail-vein injection in a total volume ≤1.25 ml. Dynamic PET images were obtained over 60 minutes, followed by 2 overlapping frames (5 min each) acquired to obtain a whole body images of radiotracer biodistribution in other organs and tissues. After PET imaging, the positioning bed with the affixed anesthetized animal was transferred to the Inveon SPECT/CT scanner (Siemens,

Knoxville, TN) and CT images and 4 overlapping frames (2 min each) were acquired covering the whole body using X-ray tube settings of 80 kV and 500 μA.

Image Analysis and Quantification: PET images were reconstructed using ordered subset expectation–maximization (OSEM) method. PET image analysis was accomplished using the AMIDE software. Digital Rat Brain Atlas was used for alignment and identification of specific anatomical markers in the brain (Watson, 2006). GraphPad Prism 6 (Graph Pad Software La Jolla, CA) and Excel 2010 (Microsoft, Redmond, WA) were used for image data analysis. Levels of accumulation of individual radiotracers in tissues were expressed as standard uptake values (SUV) that were calculated for the regions of interest (Ron S. Broide and Floyd E. Bloom) using the AMIDE software. The SUV is defined as the ratio of the tissue radioactivity concentration C (e.g. expressed as Bq/g tissue) at given time point post injection T, and the injected dose (e.g. in Bq, decay-corrected to the same time T), and normalized by the body weight in grams. Calculations for Logan plot analysis were performed as previously noted (Logan J, 1996).

Autoradiography: After PET imaging (or at certain time point after 300-500 μCi radiotracer injection i.v.), the animals were sacrificed, the brain was rapidly extracted, frozen, and embedded in the mounting medium M1 (Shandon-Lipshaw, Pittsburg, PA). Serial 20 μm thick coronal sections of frozen brain tissue were obtained at -13°C using a cryo-microtome CM3050S (Leica, Germany). Tissue sections were thaw-mounted on poly-A lysine coated glass slides and heat-fixed for 5 min at 65°C on a slide warmer (Fischer Scientific, PA). Tissue sections, mounted on slides, exposed to single-emulsion Carestream Kodak BioMax MR film (8”x10”, Sigma, Milwaukee, WI), without exposure to light, in cassettes for 12 hours. After tissue exposure, processing of the film used an automated system (Kodak X-Omat, Center for Molecular Medicine and Genetics, Wayne State University).

Chemical Synthesis:

Method 1: For new substrate analogues, we primarily modified the protecting group on α-nitrogen and the acyl substituent on the ε-amino group. Benzyloxy carbonyl (*Z*, Cbz) was investigated as a protecting group within the cap moiety. Compounds were prepared following previously published methods (Heltweg et al., 2004; Heltweg et al., 2003) as shown in the synthetic **Fig. 29-30** with minor modifications. Compounds **17-27** were synthesized from commercially available Cbz-Lys-OH with formation of corresponding acetyl chloride following the published methods (Heltweg et al., 2004) which upon reaction with AMC (**19**) in presence of $POCl_3$ and pyridine provide desired product in moderate to good yields.

Synthesis of compound **16**: Cbz-Lys (1 equiv.) was dissolved in a mixture of THF (5 mL) and water (5 mL). To this sodium bicarbonate (2 equiv.) and a solution of Boc_2O (2.3 equiv.) in THF (5 mL). After stirring at room temperature overnight, the THF was removed under reduced pressure and the resulting aqueous solution was neutralized with 2N HCl. This was extracted with ethyl acetate and the combined organic layers were washed with brine. The organic layer was dried with sodium sulfate and concentrated to clear. The clear oil was used for further reaction without any purification with **2** in presence of NMM/isobutyl chloroformate (Fig 2).

Benzyl (6-acetamido-1-((4-methyl-2-oxo-2*H*-chromen-7-yl)amino-1oxohexan-2-yl)carbamate (17): Compound **17** was prepared following previously published method 1, (Heltweg et al., 2004) as described in the synthetic Scheme 1 (Figure 1 and 2). Here we report MS (EI) and HRMS of the compound. MS (EI): *m*/*z* 478.4 [M-H]. High-resolution MS: Calculated for $C_{26}H_{29}N_3O_6$ (M+Na) 502.1954, found 502.1953.

Benzyl (6-benzamido-1-((4-methyl-2-oxo-2H-chromen-7-yl)amino)-1-oxohexan-2-yl)carbamate (18): Compound **18** was synthesized by method 1 (Heltweg et al., 2004). The

resulting product was chromatograph with 5% methanol in dichloromethane. Yield: 63%, ^{1}H NMR ($CDCl_3$, 600 MHz): δ 9.38 (s, 1H), 7.76 (d, 2H, J = 7.8 Hz), 7.68 (s, 1H), 7.602-7.46 (m, 3H), 7.39-7.34 (m, 7H), 6.18 (s, 1H), 595 (d, 1H, J = 7.2 Hz), 5.11 (m, 2H), 4.41 (s, 1H), 3.49 (m, 1H), 2.40 (s, 3H), 2.07-2.05 (m, 1H), 1.88-1.80 (m, 1H), 1.70-1.64 (m, 2H), 1.56-1.50 (m, 2H). ^{13}C NMR ($CDCl_3$, 600 MHz): δ 171.00, 168.24, 161.26, 156.92, 154.07, 152.46, 141.47, 136.08, 134.25, 134.23, 131.61, 128.61 (2C), 128.25, 128.02, 126.92 (2C), 125.10, 116.04, 115.84, 11.31, 107.30, 67.28, 55.41, 38.73, 38.60, 31.24, 29.71, 28.75, 22.26, 18.56. MS (EI): *m*/*z* 542.6 [M+H]. High-resolution MS: Calculated for $C_{31}H_{31}N_3O_6$ (M+Na) 564.2111, found 564.2105.

Benzyl (6-(2-fluorobenzamido)-1-((4-methyl-2-oxo-2*H*-chromen-7-yl)amino)-1-oxohexan-2-yl)carbamate (19). Compound **19** was synthesized by method 1 (Heltweg et al., 2004). The resulting product was chromatograph with 3% methanol/dichloromethane and purified by combiflash with 5% methanol/dichloromethane. Yield: 69%, ^{1}H NMR (DMSO-d_6, 600 MHz): δ 10.51 (s, 1H), 8.29 (s, 1H), 7.77 (brs, 1H), 7.71 (d, 1H, J = 8.4 Hz), 7.65 (d, 1H, J = 7.8 Hz), 7.54 (t, 1H, J = 7.2 Hz), 7.50-7.47 (m, 2H), 7.38-7.31 (m, 4H), 7.24-7.17 (m, 2H), 6.27 (s, 1H), 5.03 (s, 2H), 4.16 (m, 1H), 3.24 (q, 2H, J = 6.6 Hz), 2.40 (s, 3H), 1.72-1.66 (m, 2H), 1.56-1.38 (m, 4H). ^{13}C NMR (DMSO-d_6, 600 MHz): δ 172.49, 164.15, 160.59, 160.28, 158.63, 156.65, 154.09, 153.68, 142.67, 137.39, 132.66, 130.42, 128.84 (2C), 128.32 (2C), 126.41, 124.85, 116.55, 116.40, 115.77, 115.56, 112.75, 106.19, 65.98, 56.05, 39.33, 31.74, 29.04, 23.39, 18.45.^{19}F (DMSO-d_6, 300 MHz): δ -114.49. MS (EI): *m*/*z* 560.6 [M+H]. High-resolution MS: Calculated for $C_{31}H_{30}FN_3O_6$ (M+Na) 582.2016, found 582.1989.

Benzyl (6-(3-fluorobenzamido)-1-((4-methyl-2-oxo-2*H*-chromen-7-yl)amino)-1-oxohexan-2-yl)carbamate (20). Compound **20** was synthesized by method 1 (Heltweg et al., 2004). The resulting product was chromatograph with 3% methanol in dichloromethane and

purified by combiflash with 5% methanol/dichloromethane. Yield: 66%, ^{1}H NMR ($CDCl_3$): δ 9.19 (brs, 1H), 7.67 (s, 1H), 7.55-7.49 (m, 4H), 7.46-7.351 (m, 6H), 7.20 (t, 1H, J = 7.8 Hz), 6.56 (brs, 1H), 6.22 (s, 1H), 5.85 (brs, 1H), 5.14 (m, 2H), 4.40 (s, 1H), 3.51 (m, 2H), 2.43 (s, 3H), 2.07-2.06 (m, 1H), 1.88-1.80 (m, 1H), 1.72-1.60 (m, 2H), 1.56-1.52 (m, 2H). ^{13}C NMR ($CDCl_3$): δ 170.56, 166.86, 163.54, 161.18, 154.11, 152.21, 141.10, 136.00, 130.32, 128.59 (2C), 128.31, 128.06 (2C), 125.14, 122.43, 118.66, 118.52, 116.15, 115.80, 114.41, 114.27, 113.41, 107.31, 67.36, 55.34, 38.73, 30.95, 28.61, 22.16, 18.59. ^{19}F ($CDCl_3$, 300 MHz): δ -111.60. MS (EI): *m*/*z* 560.6 [M+H]. High-resolution MS: Calculated for $C_{31}H_{30}FN_3O_6$ (M+Na) 582.2016, found 582.1986.

Benzyl (6-(4-fluorobenzamido)-1-((4-methyl-2-oxo-2*H*-chromen-7-yl)amino)-1-oxohexan-2-yl)carbamate (21). Compound **21** was synthesized by method 1 (Heltweg et al., 2004). The resulting product was chromatograph with 5% methanol in dichloromethane and purified by combiflash with 5% methanol/dichloromethane. Yield: 72%, ^{1}H NMR ($CDCl_3$): δ 9.38 (s, 1H), 7.78 (m, 2H), 7.66 (s, 1H), 7.51-7.45 (m, 2H), 7.39-7.33 (m, 5H), 6.99 (t, 2H, 6*J*), 6.65 (t, 1H, *J* = 6 Hz)), 6.15 (s, 1H), 6.02 (d, 1H, *J* = 8 Hz)), 5.11 (s, 2H), 4.45 (brs, 1H), 3.49-3.46 (m, 2H), 2.39 (s, 3H), 2.01-1.88 (m, 2H), 1.71-1.67 (m, 2H), 1.55-1.50 (m, 2H). ^{13}C NMR ($CDCl_3$): δ 170.91, 167.16, 165.59, 161.17, 154.1, 152.36, 141.37, 136.00, 130.38 (2C), 129.31 (2C), 129.25, 128.60 (2C), 128.32, 128.06, 125.13, 116.12, 115.80, 115.69, 115.54, 113.40, 107.30, 67.37, 55.38, 38.66, 30.93, 28.69, 22.17, 18.57. ^{19}F ($CDCl_3$, 300 MHz): δ -107.70. MS (EI): *m*/*z* 560.6 [M+H]. High-resolution MS: Calculated for $C_{31}H_{30}FN_3O_6$ (M+Na) 582.2016, found 582.1985.

Benzyl (1-((4-methyl-2-oxo-2H-chromen-7-yl)amino-1-oxo-6-(2-phenylacetamido)hexan-2-yl)carbamate (22). Compound **22** was prepared following previously published method 1 (Heltweg et al., 2004) as described in the synthetic Scheme 1. The resulting product was chromatograph with 3% methanol in dichloromethane and purified by combiflash

with 5% methanol/dichloromethane. Yield: 59%, This is known compound, so here we report MS (EI): *m*/*z* 554.6 [M-H]. High-resolution MS: Calculated for $C_{32}H_{33}N_3O_6$ (M+Na) 578.2267, found 578.2269.

Benzyl (6-(2-(2-fluorophenyl)acetamido)-1-((4-methyl-2-oxo-2H-chromen-7-yl)amino)-1-oxohexan-2-yl)carbamate (23). Compound **23** was synthesized by method 1 (Heltweg et al., 2004). The resulting product was chromatograph with 3% methanol in dichloromethane and purified by combiflash with 5% methanol/dichloromethane. Yield: 57%, ^{1}H NMR (DMSO-d_6): δ 10.52 (s, 1H), 8.06 (t, 1H, J = 5.4 Hz), 7.78 (s, 1H),7.73-7.64 (m, 2H), 7.51 (s, 1H), 7.37-7.24 (m, 7H), 7.12-7.09 (m, 2H), 6.27 (s, 1H), 5.04 (s, 2H), 4.13 (m, 1H), 3.04 (m, 2H), 2.40 (s, 3H), 1.68-1.33 (m, 6H). ^{13}C NMR (DMSO-d_6): δ 172.10, 169.51, 167.22, 160.38, 156.18, 154.00, 153.68, 142.69, 137.39, 132.19, 129.14, 129.01 (2C), 128.96, 128.85 (2C), 126.45, 124.60, 122.62, 115.79, 115.57, 115.48, 112.76, 106.19, 65.99, 55.33, 38.98, 35.74, 31.17, 28.81, 22.85, 18.45. ^{19}F (DMSO-d_6, 300 MHz): δ -117.40. MS (EI): *m*/*z* 572.6 [M-H]. High-resolution MS: Calculated for $C_{32}H_{32}FN_3O_6$ (M+Na) 596.2173, found 596.2180.

Benzyl (6-(2-(4-fluorophenyl)acetamido)-1-((4-methyl-2-oxo-2H-chromen-7-yl)amino)-1-oxohexan-2-yl)carbamate (24). Compound **24** was synthesized by method 1 (Heltweg et al., 2004). The resulting product was chromatograph with 3% methanol in dichloromethane and purified by combiflash with 5% methanol/dichloromethane. Yield: 60%, ^{1}H NMR (MeOD): δ 7.78 (s, 1H), 7.67 (d, 1H, *J* = 8.2 Hz), 7.46 (d, 1H, *J* = 2 Hz), 7.39-7.25 (m, 7H), 7.00-6.97 (m, 2H), 6.22 (s, 1H), 5.12-5.11 (m, 2H), 4.26 (t, 1H, J = 5.3 Hz), 3.45 (s, 2H), 3.19 (t, 2H, *J* = 6.6 Hz), 2.45 (s, 3H), 1.86-1.74 (m, 2H), 1.56-1.40 (m, 4H). ^{13}C NMR (MeOD): δ 172.44, 172.36, 162.70, 161.81, 161.08, 157.23, 153.91, 153.82, 141.94, 136.74, 131.58, 130.61, 130.40, 130.35, 128.09, 127.66, 127.48, 125.27, 115.82, 115.79, 114.81, 114.76, 112.22, 106.66, 66.40, 55.83, 42.37,

38.79, 31.46, 28.58, 22.82, 17.12. ^{19}F (MeOD, 300 MHz): δ -118.40. MS (EI): *m*/*z* 574.7 [M+H]. High-resolution MS: Calculated for $C_{32}H_{32}FN_3O_6$ (M+Na) 596.2173, found 596.2173.

Benzyl (6-(4-iodobenzamido)-1-((4-methyl-2-oxo-2*H*-chromen-7-yl)amino)-1-oxohexan-2-yl)carbamate (25). Compound **25** was synthesized by method 1 (Heltweg et al., 2004). The resulting product was chromatograph with 5% methanol in dichloromethane and purified by combiflash with 5% methanol/dichloromethane. Yield: 60%, 1H NMR (CDCl3): δ 9.17 (s, 1H), 7.69-7.66 (m, 3H), 7.54-7.46 (m, 4H), 7.42-7.34 (m, 5H), 6.21 (s, 1H), 5.86 (brs, 1H), 5.12 (s, 2H), 4.38 (brs, 1H), 3.55-3.44 (m, 2H), 2.43 (s, 3H), 2.10-2.06 (m, 1H), 1.89-1.84 (m, 1H), 1.71-1.68 (m, 2H), 1.57-1.50 (m, 2H). 13C NMR (MeOD): δ 171.50, 166.21, 160.30, 155.42, 152.20, 135.86, 132.30 (2C), 126.97, 126.58 (2C), 126.15, 125.96, 123.76, 122.76, 120.18, 119.09, 118.70, 116.95, 114.96, 114.32, 110.82, 105.17, 96.01, 64.87, 54.25, 37.45, 29.90, 27.00, 21.10, 15.70. MS (EI): m/z 667.5 [M+]. High-resolution MS: Calculated for $C_{31}H_{30}IN_3O_6$ (M+Na) 690.1077, found 690.1075.

Benzyl (6-(2-(4-iodophenyl)acetamido)-1-((4-methyl-2-oxo-2H-chromen-7-yl)amino)-1-oxohexan-2-yl)carbamate (26). Compound **26** was synthesized by method 1 (Heltweg et al., 2004). The resulting product was chromatograph with 3% methanol in dichloromethane and purified by combiflash with 5% methanol/dichloromethane. Yield: 72%, ^{1}H NMR (MeOD): δ 8.11 (brs, 1H), 7.88 (d, 1H, J = 8.4 Hz), 7.82 (s, 1H), 7.76-7.73 (m, 2H), 7.67 (d, 1H, J = 8.4 Hz), 7.61 (d, 1H, J = 7.8 Hz), 7.54-7.48 (m, 2H), 7.40-7.31 (m, 2H), 7.09 (d, 1H, J = 7.8 Hz), 7.04 (d, 1H, J = 8.4 Hz), 6.26 (s, 1H), 5.13 (m, 2H), 4.25 (m, 1H), 3.43 (s, 2H), 3.21 (m, 2H), 2.48 (s, 3H), 1.89-1.74 (m, 2H), 1.56-1.48 (m, 4H). 13C NMR (MeOD): δ 172.04, 171.92, 161.87, 154.00, 153.89, 137.31 (2C), 137.23, 135.45, 131.20, 130.80 (2C), 128.09, 127.67, 127.50, 126.50, 125.35, 115.91, 115.86, 112.26, 106.72, 91.30, 66.41, 55.80, 41.83, 38.53, 31.45, 28.53, 22.78, 17.15. MS (EI):

m/z 680.4 [M-H]. High-resolution MS: Calculated for C32H32IN3O6 (M+Na) 704.1233, found 704.1231.

Benzyl (6-(4-ethylbenzamido)-1-((4-methyl-2-oxo-2H-chromen-7-yl)amino)-1-oxohexan-2-yl)carbamate (27). Compound **27** was synthesized by method 1 (Heltweg et al., 2004). The resulting product was chromatograph with 5% methanol in dichloromethane and purified by combiflash with 5% methanol/dichloromethane. Yield: 77%, ^{1}H NMR ($CDCl_3$): δ 9.71 (s, 1H), 7.68 (m, 3H), 7.44-7.39 (m, 2H), 7.38-7.30 (m, 4H), 7.12 (d, 2H, J = 7.8 Hz), 6.87 (s, 1H), 6.26 (d, 1H, J = 7.8 Hz), 6.11 (s, 1H), 5.07 (s, 2H), 4.45 (brs, 1H), 3.42 (m, 2H), 2.62 (q, 2H, J = 7.2 Hz), 2.44 (s, 3H), 1.98-1.82 (m, 2H), 1.67-1.48 (m, 4H), 1.19 (t, 3H, J = 7.2 Hz). ^{13}C NMR ($CDCl_3$): δ 171.55, 168.20, 161.40, 156.88, 153.89, 152.75, 148.11, 141.63, 136.17, 131.90, 128.51 (2C), 128.13, 127.97 (2C), 127.89, 127.10 (3C), 125.05, 115.93, 115.84, 113.52, 107.21, 67.14, 55.65, 39.09, 31.78, 28.89, 28.70, 22.55, 18.51, 15.27. MS (EI): *m*/*z* 570.7 [M+H]. High-resolution MS: Calculated for $C_{33}H_{35}N_3O_6$ (M+Na) 592.2424, found 592.2433.

Synthesis of 4-fluoro-phenylhexanoicanilide (28): 0.64 mmol of 4-fluorophenylacetic acid (purchased from Alfa-Aesar) was dissolved in ACN and 1 equivalent of DMAP was added with a catalyst amount of DCC. The mixture was stirred under argon for 10 minutes. Subsequently the amine, compound R1, (0.48 mmol) was dissolved in ACN and added to the mixture dropwise. The reaction was stirred under argon, at room temperature, overnight. The compound was purified using flash chromatography on a silica column and eluted with 3% MeOH in DCM. The compound was dried as white crystals in a yield of 77%. ^{1}H NMR (499 MHz, $CDCl_3$) δ 8.19(s, 1H), 8.12 (d, *J* = 7.9 Hz, 1H), 7.90 (t, J = 7.9 Hz, 1H), 7.85 (dd, *J* = 8.5, 5.4 Hz, 2H), 7.79 (dd, *J* = 8.4, 5.4 Hz, 1H), 7.69 (t, *J* = 7.3 Hz, 1H), 7.59 (t, *J* = 8.7 Hz, 3H), 6.27 (s, 1H), 4.20 (s,3H), 4.10 (s, 1H), 3.99 (t,2H, *J* =), 3.82 (dd, *J* = 13.2, 6.8 Hz, 1H), 2.92 (t, *J* = 7.3 Hz, 1H), 2.50 (dd, *J* = 12.6, 3.2 Hz,

3H), 2.36 – 2.24 (m, 4H), 2.11 – 2.01 (m, 2H), 1.90 (d, *J* = 12.5, 8.9 Hz, 4H), 1.77 – 1.66 (m, 4H). ^{13}C NMR (126 MHz, $CDCl_3$) δ 175.42, 171.36, 130.95, 128.95, 124.19, 119.80, 115.83 (d, *J* = 21.3 Hz), 115.36 (d, *J* = 21.5 Hz), 77.27, 77.02, 76.76, 49.38, 42.80, 40.45, 39.29, 37.17, 33.70, 28.87, 25.96, 25.51, 24.84, 24.68. ^{19}F NMR (376 MHz, CDCl3) δ -115.86 (m).

Radiosynthesis of 4-^{18}F-phenylhexanoicanilide (28a): A solution of kryptofix/ K[^{18}F] was received from the cyclotron and transferred into a crimped V-vial for drying. Acetonitrile (0.4 mL) was added to the mixture and it was dried under a stream of argon at 80°C. 4 mg of 4-nitro benzaldehyde in 0.4mL of DMF was added and stirred for 20 min at 120°C under Argon. 0.2mL of $CHCl_3$ was then added to the mixture with 0.2mL of KOH/MeOH and stirred at -78°C for 10 min. The reaction mixture was evaporated under argon at room temperature to the DMF base. The resulting mixture was eluted through a cartridge with 10% MeOH/DCM and evaporated to dryness. Subsequently, 0.4mL of t-Bu-OH was added with concentrated, 5M, NaOH and stirred for 5 min at room temperature. Borohydride (10mg) was added to the reaction mixture and stirred for 10 minutes at 50°C. The resulting mixture was filtered and injected into semi-prep HPLC and purified with 35% ACN in H_2O. The eluted mixture was coupled with compound **1** (10mg) using DCC and DMAP. This was then purified for a yield of 180 uCi of pure compound (0.2% yield not decay corrected).

2-Nitro-ethylbenzoate (29): Purchased from Alfa Aesar and used without further purification.

2-F-ethylbenzoate (30a): Purchased from Alfa Aesar and used without further purification.

2-^{18}F-ethylbenzoate (30b): The F-18 was obtained in kryptofix/K[^{18}F] complex in acetonitrile/water (1 mL) from the PET/Cyclotron Facility, Wayne State University (Detroit, MI) and transferred into a crimped 2 mL V-vial for azeotropic drying. Acetonitrile (0.4 mL) was added

to the mixture, which was dried under a stream of argon at 90-100°C. A solution of **29** (~2 mg) in dry DMSO (0.4 mL) was added to the dried kryptofix/ K[^{18}F] and heated to 120°C under argon with stirring for 15 minutes. After cooling, the reaction mixture was passed through a 900 mg Altech silica gel cartridge (Fisher Scientific, Waltham, MA) and eluted with 2 mL of 10% methanol in dichloromethane (DCM). The solvent was evaporated under a stream of argon to remove DCM and to reduce the volume to 0.5 mL. **31** was purified by semipreparative HPLC (50% ACN in water) by collecting the peak at 15 min. The decay corrected radiochemical yield was 25% and the compound purity was >95%, as assessed by analytical HPLC and co-elution with the non-radiolabeled reference standard **32**.

2-^{18}F-benzoic acid (31): Compound **30** was treated with 0.5mL of 1M NaOH at 80°C for 10 minutes for hydrolysis of the ester group and form **31**. Completion of the reaction was assessed by analytical HPLC. Subsequently, the solution was neutralized to pH of 7.5 with 0.5 mL of 1M HCl and the mixture was evaporated to dryness under a stream of argon. Compound **31** was redissolved in saline and prepared for animal injection.

2-Nitro-benzaldehyde (32): Purchased from Alfa Aesar and used without further purification.

2-Fluoro-benzaldehyde (33): Purchased from Sigma and used without further purification.

2-^{18}F-benzaldehyde (34): The F-18 was obtained in kryptofix/K[^{18}F] complex in acetonitrile/water (1 mL) from the PET/Cyclotron Facility, Wayne State University (Detroit, MI) and transferred into a crimped 2 mL V-vial for azeotropic drying. Acetonitrile (0.4 mL) was added to the mixture, which was dried under a stream of argon at 90-100°C. A solution of **32** (~2 mg) in dry DMSO (0.4 mL) was added to the dried kryptofix/ K[^{18}F] and heated to 130-140°C under argon with stirring for 12 minutes. After cooling, the reaction mixture was passed through a 900

mg Altech silica gel cartridge (Fisher Scientific, Waltham, MA) and eluted with 2 mL of 10% methanol in dichloromethane (DCM). The solvent was evaporated under a stream of argon to remove DCM and to reduce the volume to 0.5 mL. **34** was purified by semipreparative HPLC (50% ACN in water) by collecting the peak at 15 min. The decay corrected radiochemical yield was 15% and the compound purity was >95%, as assessed by analytical HPLC and co-elution with the non-radiolabeled reference standard **33**.

2-fluoro-phenylhexanoicanilide, 2-FPhAHA (35): Compound 1 (0.240g, 1.163 mmol) was dissolved in 5mL of dichloromethane and 0.5mL triethylamine. The 2-fluoro benzoylchloride (0.2 mL, 1.696 mmol) was added dropwise at 0°C. The reaction was stirred at 0°C for 30 minutes then gradually warmed to RT and stirred under argon for 3 hours. The mixture was washed with ethylacetate and 4N HCl solution. The organic layer was dried over magnesium sulfate and then evaporated to dryness. The resulting crude mixture was re-crystallized with diethyl-ether overnight and then filtered with vacuum filtration before being dried under high-vacuum. Product **35** (110mg) was made as a white solid in 28% yield. 1H NMR (400 MHz, cdcl3) δ 8.13 – 7.97 (m, 1H), 7.81 (s, 1H), 7.53 (d, J = 7.8 Hz, 2H), 7.45 – 7.41 (m, 1H), 7.35 – 7.16 (m, 3H), 7.16 – 6.99 (m, 2H), 6.80 (s, 1H), 3.46 (d, J = 5.9 Hz, 2H), 2.35 (t, *J* = 7.3 Hz, 2H), 1.82 – 1.69 (m, 2H), 1.69 – 1.58 (m, 2H), 1.44 (d, *J* = 6.5 Hz, 2H). 13C NMR (101 MHz, cdcl3) δ 171.33, 163.47, 161.73, 159.28, 138.18, 133.15 (d, *J* = 9.3 Hz), 131.82, 128.86, 124.75 (d, *J* = 3.1 Hz), 124.00, 121.21 (d, *J* = 11.3 Hz), 119.82, 115.98 (d, *J* = 24.8 Hz), 77.35, 77.03, 76.71, 39.74, 37.32, 29.17, 26.36, 25.02. M/Z calculated: 329.1665; M/Z found : 329.1654

2-Nitro-*N*-(6-oxo-6-(phenylamino)hexyl)benzamide: The solution of 2-nitrobenzoyl chloride (0.12 g, 0.62 mmol) in 0.5 mL of DCM was added dropwise to the mixture of phenylhexanamide (0.10 g, 0.48 mmol) and Hunig's base (0.13 mL, 0.73 mmol) in DMF (5 mL)

at 0°C and then left to stir at room temperature for 12 h. The solvent was then evaporated under reduced pressure; the crude was dissolved in EtOAc and washed with water. The organic layer was dried over sodium sulfate. Evaporation and purification with column chromatography (eluent - EtOAc) gave the desired precursor in 70-72% yield. ^{1}H NMR (600 MHz, DMSO-d_6) δ 9.87 (s, 1H), 8.66 (t, *J* = 5.5 Hz, 1H), 8.02 (d, *J* = 8.1 Hz, 1H), 7.75 (t, *J* = 7.5 Hz, 1H), 7.67 (t, *J* = 7.8 Hz, 1H), 7.60 (d, *J* = 8.2 Hz, 2H), 7.57 (d, *J* = 7.5 Hz, 1H), 7.28 (t, *J* = 7.8 Hz, 2H), 7.01 (t, *J* = 7.3 Hz, 1H), 3.22 (dd, *J* = 12.9, 6.6 Hz, 2H), 2.32 (t, *J* = 7.4 Hz, 2H), 1.67 – 1.59 (m, 2H), 1.58 – 1.50 (m, 2H), 1.42 – 1.33 (m, 2H). ^{13}C NMR (151 MHz, DMSO-d_6) δ 171.2, 165.3, 147.0, 139.4, 133.5, 132.8, 130.5, 129.0, 128.6, 124.0, 122.9, 119.0, 39.0, 36.4, 28.6, 26.1, 24.8. HRMS (+ESI-TOF) m/z for $C_{19}H_{21}N_3O_4$ $[M+Na]^+$ 356.1600; M/Z found : 356.1598

Radiosynthesis of 2-^{18}F-phenylhexanoicanilide 2-[^{18}F]PhAHA (37): The F-18 was obtained in kryptofix/K[^{18}F] complex in acetonitrile/water (1 mL) from the PET/Cyclotron Facility, Wayne State University (Detroit, MI) and transferred into a crimped 2 mL V-vial for azeotropic drying. Acetonitrile (0.4 mL) was added to the mixture, which was dried under a stream of argon at 90-100°C. A solution of **36** (~2 mg) in dry DMSO (0.4 mL) was added to the dried kryptofix/ K[^{18}F] and heated to 130-140°C under argon with stirring for 12 minutes. After cooling, the reaction mixture was passed through a 900 mg Altech silica gel cartridge (Fisher Scientific, Waltham, MA) and eluted with 2 mL of 10% methanol in dichloromethane (DCM). The solvent was evaporated under a stream of argon to remove DCM and to reduce the volume to 0.5 mL. **37** was purified by semi-preparative HPLC (65% ACN in water) by collecting the peak at 6 min. The decay corrected radiochemical yield was 10% and the compound purity was >95%, as assessed by analytical HPLC and co-elution with the non-radiolabeled reference standard **35**.

5b. Continuing work

The most aggressive and common form of brain cancer, gliomas, can originate from any glial cell within the brain but most commonly derive from astrocytes (astrocytoma, 70% of the cases) or oligodendrocytes (oligodendroglioma, 20-25% of the cases), while the remaining tumor types are formed from a mixture of astrocytes, oligodendrocytes and ependymal cells (Lino and Merlo, 2009). Glioblastomas or glioblastoma multiforme (GBM) tumors are generally termed as grade IV astrocytomas, based on the World Health Organization (WHO) classification scale. Glioblastomas are the most common, making up 50% of functional brain tissue tumors and 20% of intracranial tumors, as well as the most aggressive brain tumor type (median survival is 14.6 months, 30% 2 year survival). While substantial progress has been made towards improving diagnosis of this disease, very little progress has been made in regards to treatment over the last decade.

Currently, GBM is treated primarily with surgery, when possible, followed by radiation and temozolomide (TMZ) treatment (Dubrow et al., 2013). Approval and increased usage of TMZ during the last decade has improved patient survival but there continues to be an unmet need for effective treatments of GBM. The standard of care therapy, even when successful, leaves patients with an average of only 6.9 months before recurrence (Stupp et al., 2005). Therefore, extensive research into biological mechanisms behind glioma tumor formation has been a primary area of focus for many researchers. Subsequently, the field of epigenetics and epigenetic regulators, have arisen as promising possible treatment targets for of this deadly disease. Epigenetic modifiers, such as HDAC enzymes, are responsible for manipulating gene transcription and may play a pivotal role in changing cellular phenotype from benign to malignant. In particular, SIRT1 (class III

HDAC) has emerged from the group of HDACs as a promising target within epigenetics for cancer therapy.

SIRT1, as previously mentioned, plays a large role in metabolic regulation and oxidative stress. One primary complication for SIRT1 targeted therapy, is the pleiotropic role of SIRT1 in pathologic states and the role of SIRT1 as a strict tumor suppressor or promoter has yet to be fully uncovered and remains unclear at this time. For example, SIRT1 upregulation is correlated with disease progression and poor prognosis in breast and pancreatic cancers however the opposite has been observed in bladder and ovarian cancers (Mvunta et al., 2016; Sanchez-Carbayo et al., 2006). SIRT1-targeted small molecule activators (i.e. Resveratrol and SRT501) are currently in use in clinical trials for treatment of colon cancer and hepatocellular carcinoma (NCT00256334, NCT00920803), in these varieties of cancer, SIRT1 upregulation has been demonstrated to be beneficial. However, SIRT1 expression within one cancer type at different stages does not remain constant, implicating SIRT1 as a possible regulator of cancer prognosis.

One possible innovation for GBM that has been identified are SIRT1-targeted therapies due to its role in apoptotic pathways. Knockdown of SIRT1 in glioma cell lines demonstrated growth inhibition and increased apoptosis as compared to the wild type cancer cells, indicating that SIRT1 may play a role in the progression of GBM via PTEN/PI3K/AKT pathway (Qu et al., 2012); a pathway which is commonly over-activated in GBM (Narayan et al., 2013). Additional indications of SIRT1 in GBM pathology include glioblastoma cell lines with further adaptation to glucose dependence (Warburg effect) had increased levels NAD^+ and SIRT1 expression .

Due to the key regulatory role of SIRT1 in stress, apoptotic and metabolic responses within cells, SIRT1-directed therapies may provide a new route for treatment of gliomas. However, much is still unknown about the exact role of SIRT1 within cancers and especially gliomas. This work

should provide more evidence for treatment of glioma with SIRT1-directed therapies based on *in vivo*, *non-invasive* imaging studies with a SIRT1-selective imaging agent.

To establish overexpression of SIRT1 in specific glioma cell lines, *in vitro* cellular uptake studies were performed using SRIT1-selective PET imaging agent termed 2-[^{18}F]PhAHA. This study demonstrated increased radio-metabolite accumulation in U87 and C6 cells, expressing relatively higher expression of SIRT1, and decreased radio-metabolite accumulation in cells with relatively lower levels of expression of SIRT1 (i.e. MiaPaCa, MD-MB-231, MCF10DCIS). This work translated into *in vivo* imaging where glioma and gliosarcoma rat models were developed by intracranial injection of both U87 and 9L glioma cells. It should be noted that 9L and C6 cell lines represent a subset of grade IV astrocytomas, known as gliosarcomas, and are rat-derived tumor lines (Han et al., 2010). Many similarities between human glioma and rat derived gliosarcoma tumor types exist but there are also differences in the pathogenicity of the cells (Barth and Kaur, 2009). Imaging both U87 as well as 9L derived tumors *in vivo* with 2-[^{18}F]PhAHA will provide a better understanding and comparisons for the expression-activity of SIRT1 in two types of tumor.

Using 2-[^{18}F]PhAHA for PET imaging it is possible to quantify and visualize changes in SIRT1 expression-activity as well as regional localization over time and tumor growth. For adequate tumor-co-registration and identification of brain regions, the PET/CT images were co-aligned with T_2 weighted MRI. Quantification of images was performed using Logan analysis for further understanding of changes in radiotracer accumulation in the tumor and other areas of the brain with high SIRT1 activity. For further proof that 2-[^{18}F]PhAHA is SIRT1-selective in tumor models, imaging studies using known SIRT1 inhibitor, EX-527, were performed. As expected, the accumulation of 2-[^{18}F]PhAHA-derived radioactivity in the tumor and other areas of the brain with high SIRT1 expression was markedly decreased after administration of inhibitor.

These preliminary studies provide evidence that SIRT1 may play a role in progression of GBM and may be a possible undiscovered target for therapy. Furthermore, this new technology provides a route for non-invasive monitoring of therapy as well as designing individualized treatments based on enzyme expression levels within the tumor, which may vary patient to patient and even within a tumor of one patient.

Results and Discussion:

Towards improving treatments and diagnosis for patients with GBM, characterization of SIRT1-selective radiotracer, 2-[^{18}F]PhAHA, was performed both *in vitro* and *in vivo* glioma and gliosarcoma tumor models. Development of PET imaging with 2-[^{18}F]PhAHA in an animal glioma model is aimed at laying the foundation for future work to monitor the effects of SIRT1-targeted pharmacomodulation on tumor growth and progression. These studies demonstrate significant differences in SIRT1 expression-activity in tumor vs. normal brain tissue based on increased radioactive accumulation of 2-[^{18}F]PhAHA-derived products.

For this study, two different types of glioma models, human-derived glioblastoma and rat-derived gliosarcoma, were developed in two types of rats, nude and Sprague Dawley (SD). Using the U87 lineage, a human-derived glioblastoma cell line in nude rats (Pontén, 1975), allowed for characterization in a more clinically relevant tumor as glioblastomas make up the majority of brain tumors. However, to better understand the fundamental role of SIRT1 in brain tumors, a Fischer rat-derived gliosarcoma SD rat model was also developed using 9L cell lines (Benda et al., 1971). Though gliosarcoma tumors make up a smaller percentage of clinically seen brain tumors, they represent a very severe and poorly understood group (Han et al., 2010). The 9L gliosarcoma is a well-established and widely used model for understanding tumor growth and biology (Stojiljkovic et al.). This model is especially appealing due to its immunogenicity in syngeneic hosts, such as

Fischer or SD rats, increasing success rates for tumor cell acceptance, post-injection. Additionally, the 9L cell line is a rapidly growing and more severe form of cancer than the U87 (Barth and Kaur, 2009).

The noted increase in 9L tumor severity of may be due in part to a missense mutation in the DNA binding region of a key tumor suppressor protein, p53 (Asai et al., 1994). This mutation may disrupt the p53 interaction s-Myc and cause further progression of cell pathology (Asai et al., 1994). However, the U87 cell line expresses wildtype p53 protein, but instead contains a pathogenic mutation in PTEN tumor suppressor gene (Haas-Kogan et al., 1998). These mutated proteins contribute significantly to the pathogenicity of the tumor but the effect on SIRT1 is involvement is yet unknown. Further study of the *in vivo* tumor models with SIRT1-selective radiotracer may help further this understanding.

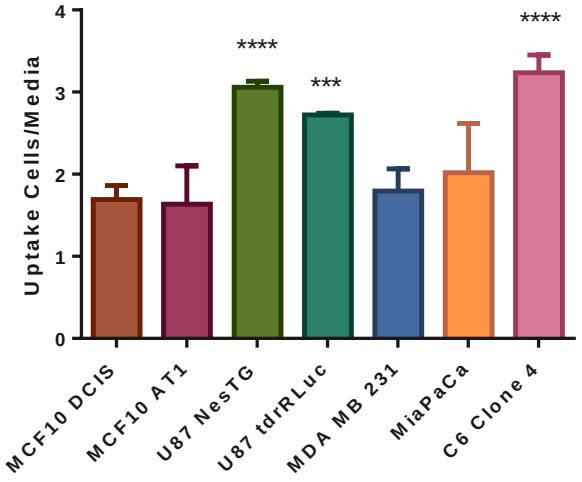

Figure 57. Of the cell lines tested, U87 and C6 glioma lines demonstrate the highest uptake of SIRT1-selective radiotracer 2-[^{18}F]PhAHA derived radioactivity ($P>0.05$, One Way ANOVA).

As indicated by *in vitro* cell uptake studies performed with 2-[^{18}F]PhAHA, U87 and 9L cell lines accumulate increased levels of radioactivity as opposed to other cell lines (i.e. MiaPaCa, MDA MB-231, MCF10AT1, and MCF10DCIS) (**Fig. 57**). This correlates well with previous literature demonstrating an increase in levels of SIRT1 protein in glioma tissue using immunohistochemistry (IHC) with a staining intensity index for quantification (http://www.proteinatlas.org/ENSG0000009671-SIRT1/cancer/tissue/glioma). An example of literature SIRT1 IHC results in glioma tissue is

displayed in **Fig. 55** (Ma et al., 2013). These panels indicate an increase in SIRT1 staining intensity in glioma tumor tissue as compared to normal brain tissue.

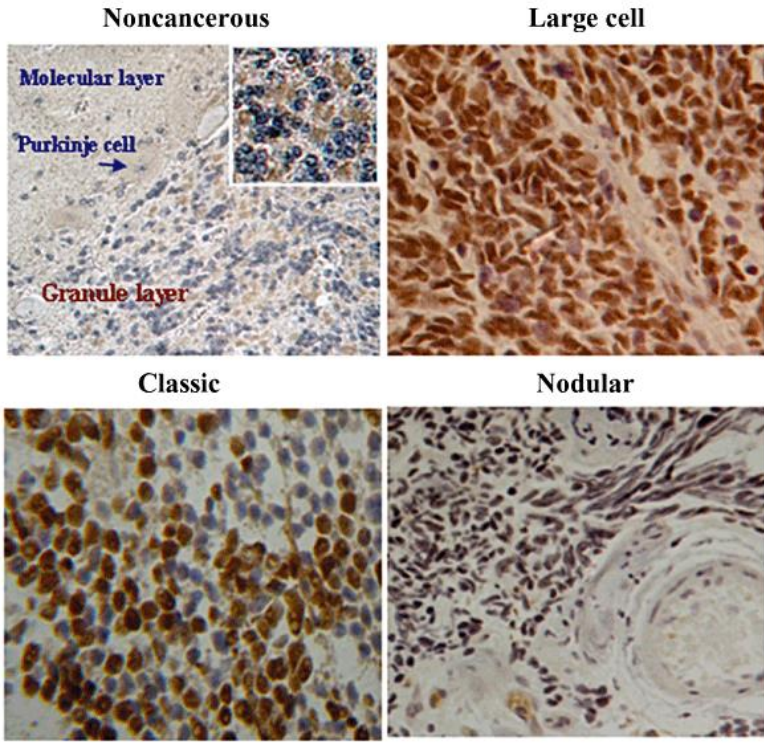

Figure 58: IHC results for SIRT1 staining in different types of medulloblastoma cells. (Ma et al., 2013).

Following *in vitro* characterization, tumors were grown in rats from i.c. injections of either 9L or U87 cell suspensions. For verification of tumor growth and location, T_2-weighted MR images of each animal were acquired between 10 and 14 days post i.c. tumor cell implantation. The SD rats developed 9L tumors successfully and underwent PET/CT and MR imaging sessions. The U87 cells, transfected with GFP, tumors were grown in nude rats and bioluminescence imaging was performed in addition to PET/CT and MRI. PET/CT imaging with 2-[^{18}F]PhAHA were acquired shortly after the MR images to allow for accurate co-registration and overlays of these images. From the dynamic PET/CT images, peak times for differential washout between areas of high levels and relatively lower

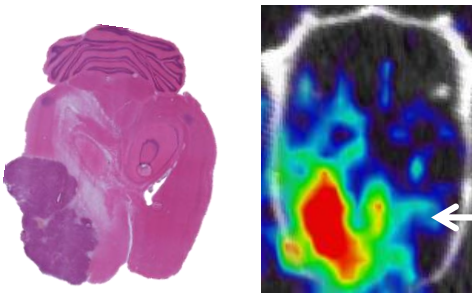

Figure 59. H&E staining of axial section from brain of 9L tumor bearing rat aligned with corresponding PET/CT image at 30 min post administration of 2-[^{18}F]PhAHA. Arrow indicates bregma (site of injection).

levels of SIRT1 expression-activity within the brain, remained about 20 minutes as was the case in normal animals.

Within some tumors, excellent co-registration exists between tumor and 2-[^{18}F]PhAHA-derived radioactivity accumulation, however, in others the areas of highest accumulation are in surrounding tumor tissue rather than centered within of the tumor itself. **Fig. 59-60** displays a 9L tumor bearing rat with increased levels of 2-[^{18}F]PhAHA-derived radioactivity accumulation in the tumor tissue. However, **Fig. 61** displays PET/CT imaging using 2-[^{18}F]PhAHA in a U87 tumor-bearing rat and there is greater per-tumoral accumulation than central tumor accumulation. Yet, even in this animal, there are certain lesions with increased accumulation in the tumor. Both tumor types, 9L and U87, display great heterogeneity within the tumor tissue. Sample images of 2-[^{18}F]PhAHA-derived radioactivity accumulation in both 9L and U87 tumor bearing rats are displayed centered on the injection site at bregma (**Fig. 59-60**).

To assess the effectiveness and growth localization of tumor tissue within the brain as well as confirmation that the cells are being expressed properly, bioluminescence imaging was performed with animals bearing U87 tumors. This is only possible with the

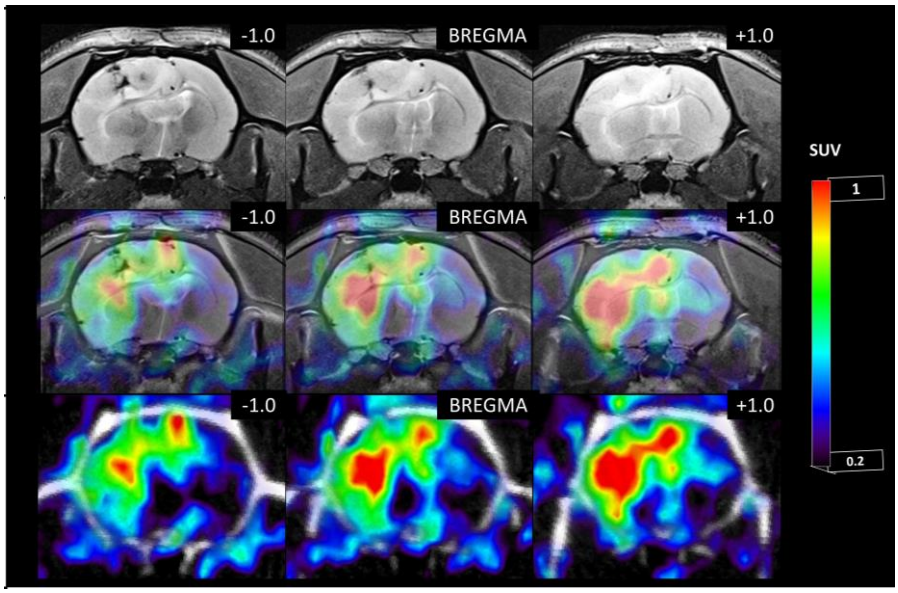

Figure 60. Coronal slices from dynamic PET/CT/MRI images of 9L tumor bearing rat at 30 min post 2-[^{18}F]PhAHA administration centered at bregma. **Top**: MRI only; **Middle**: MRI/PET overlay; **Bottom**: PET/CT

U87 cell line, as it has been transfected with luciferase (**Fig. 62**).

Following characterization of 2-[^{18}F]PhAHA in both tumor models, U87 and 9L, it was interesting to compare the expression-activity of SIRT1 with HDACs class IIA, using ^{18}F-TFAHA as a radiotracer for PET imaging. **Figures 63-64** display each tracer separately as well as the two overlaid in panels for U87 and 9L tumor models demonstrating the similarities and differences between HDAC and SIRT1 expression within one animal, 24 hours apart. These overlays effectively demonstrate the localization and differences in activity between HDACs class IIa and SIRT1 within regions of tumor and brain tissue.

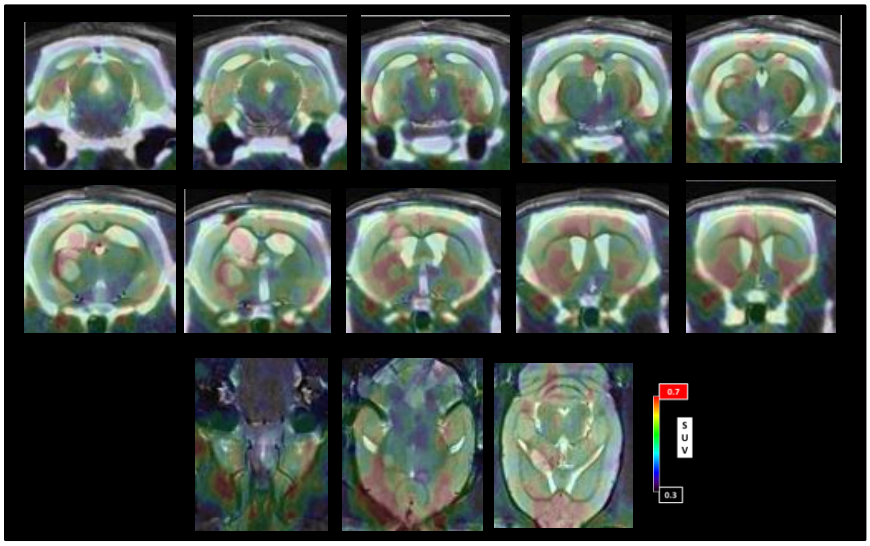

Figure 61. Coronal and axial slices from dynamic PET/CT/MRI images of U87 tumor bearing rat at 30 min post 2-[^{18}F]PhAHA administration centered at bregma. **Top**: MRI only; **Middle**: MRI/PET overlay; **Bottom**: PET/CT

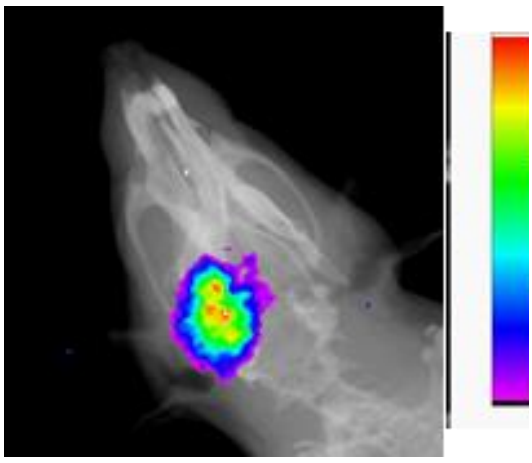

Figure 62: Bioluminescence imaging of U87TdRLuc tumor in a rat demonstrating tumor localization within the brain.

Heterogeneity within the 9L tumors is clearly defined by differences in 2-[^{18}F]PhAHA and ^{18}F-TFAHA accumulation. For example, tissue surrounding the needle track and infiltration in this area demonstrates increased accumulation of 2-[^{18}F]PhAHA but not of ^{18}F-TFAHA-derived radioactivity. Additionally, different lesions within this tumor have different levels of HDACs class IIa and SIRT1 expression-activity.

In U87 animals, one of the most striking differences is in the cerebellar lesion of the tumor at -4.0mm. This lesion demonstrates increased ^{18}F-TFAHA-derived radioactivity accumulation as opposed to this same lesion imaged with 2-[^{18}F]PhAHA, which demonstrates very little

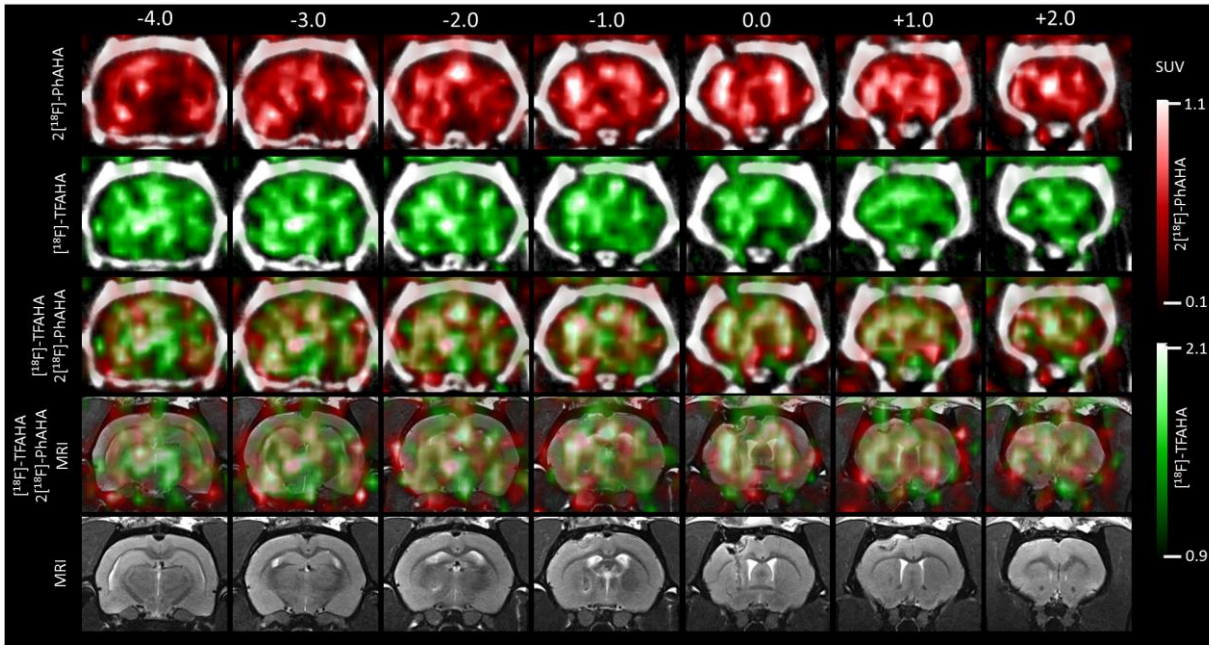

Figure 63. Coronal slices through bregma, injection site (0.0) and 1 mm steps to either side, for both tracers in the same 9L bearing tumor rat, 24 hours apart. Top, in red, are PET/CT images using 2-[^{18}F]PhAHA at 20 min post i.v. administration. In green, are PET/CT images using ^{18}F-TFAHA also at 20 min post i.v. administration of the tracer. The following line demonstrates overlay of the two tracers on CT followed by the tracer overlay on MRI. Lastly, MRI alone on bottom.

accumulation in this lesion (**Fig. 64**). In slices at -1.0 and -2.0 the accumulation of 2-[^{18}F]PhAHA-derived radioactivity is much more peripheral than that of ^{18}F-TFAHA, located more centrally. In certain areas of the brain, the two classes of HDACs appear to complement each other in their activity levels. These observations will be further confirmed by IHC staining.

Looking at the similarities and differences between 2-[^{18}F]PhAHA – derived radioactivity accumulation within the two tumor models, it may be possible to conclude that there is higher SIRT1 expression-activity within the 9L tumor tissue (N = 6 animals) than the U87 tumor tissue (N = 3 animals) (**Fig. 63**). While, this is not conclusive, or statistically significant due to unequal numbers of animals, certainly more studies are needed to understand if this is a robust observation, or not. And if so, determining the mechanism causing these differences in SIRT1 expression levels will also be important. This difference is quantified by the differences in slopes between 9L (m=2.2) and U87 (m = 1.6) Logan plots when the brainstem is used as reference tissue, where the

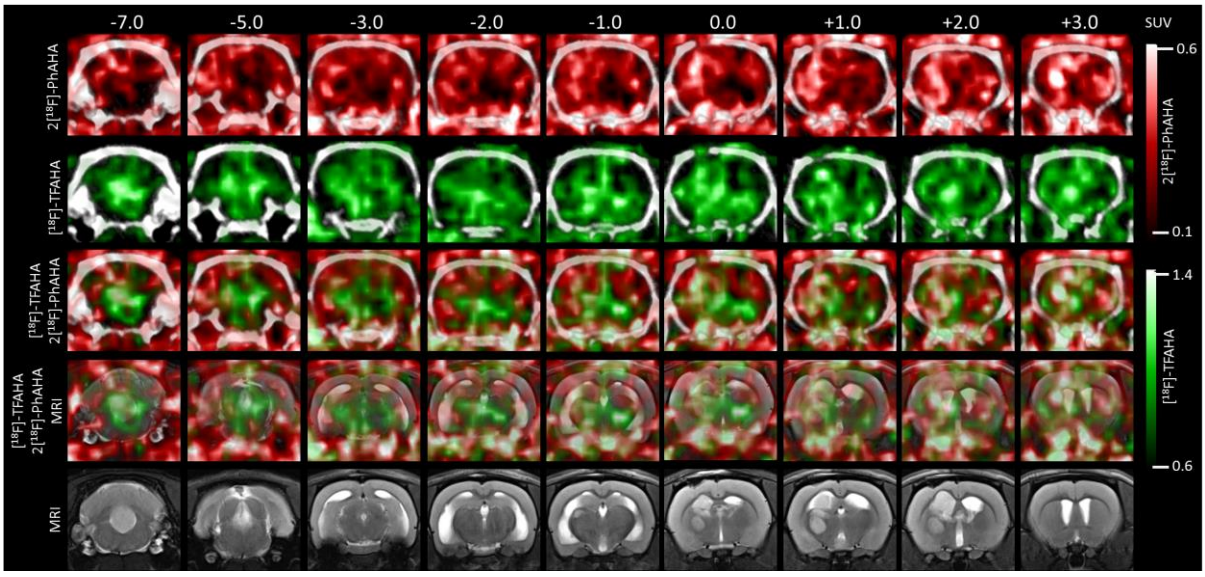

Fig. 64: Coronal slices through bregma, injection site (0.0) and 1 mm steps to either side, for both tracers in the same U87 bearing tumor rat, 24 hours apart. Top, in red, are PET/CT images using 2-[^{18}F]PhAHA at 20 min post i.v. administration. In green, are PET/CT images using ^{18}F-TFAHA also at 20 min post i.v. administration of the tracer. The following line demonstrates overlay of the two tracers on CT followed by the tracer overlay on MRI. Lastly, MRI alone on bottom.

dotted lines represent 95% confidence intervals about the lines of best fit. The increase in slope in 9L tumor animals demonstrates a higher distribution volume for the tracer in the tumor tissue relative to the U87 tumor animals. Therefore, 2-[^{18}F]PhAHA is accumulating more effectively in 9L tumors than U87 tumors (based on N = 6 for each group). Though, these results are still preliminary, as more studies are needed for full characterization of this finding. However, one possible reason for this may be due to afore mentioned p53 mutation within 9L gliosarcoma cell lines causing changes to SIRT1-p53 interactions (Asai et al., 1994). According to the current understanding, SIRT1 deacetylates p53 to promote cellular senescence and act as a co-tumor suppressor in many cases, however, this is complicated because SIRT1 does not fit the model of a true tumor suppressor (Brooks and Gu, 2011). Therefore, decreasing the effectiveness of p53 due to a mutation may or may not affect SIRT1 expression and activity within the cell.

Quantification of the animals bearing 9L gliosarcoma and U87 glioma tumors demonstrate rapid accumulation and increase in 2-[^{18}F]PhAHA-derived accumulation within the tumor almost

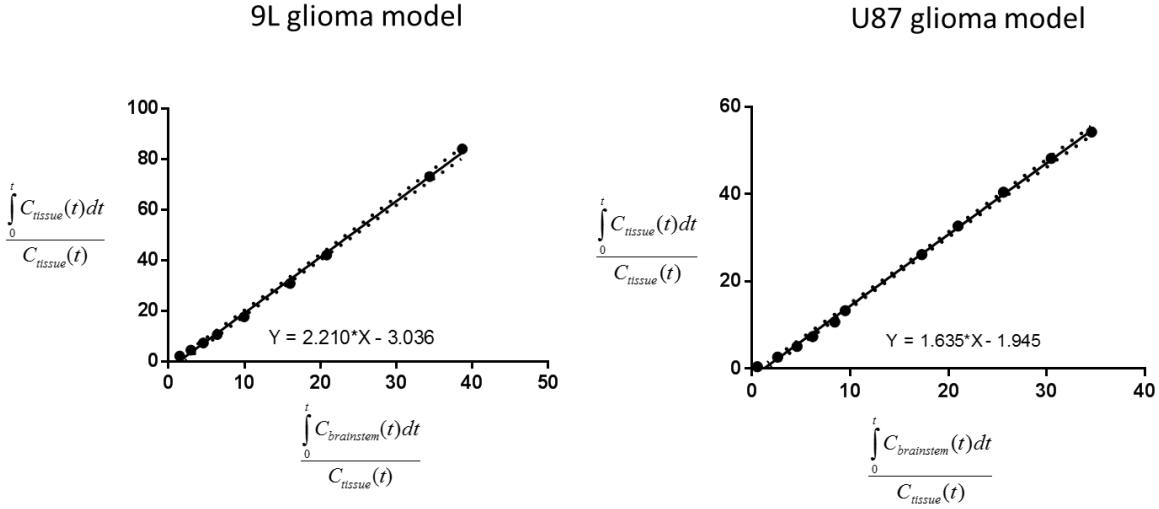

Figure. 65: Quantification of 2-[^{18}F]PhAHA-derived accumulation in tumor tissue in both U87 and 9L glioma models with brainstem as reference tissue for the Logan plot analysis. Dotted lines represent 95% confidence interval.

immediately post administration of the tracer. Additional Logan plot analysis for 9L tumor bearing

rats was performed using other areas of the brain including *cortex, caudate putamen, n. accumbens,* and *hippocampus* (**Fig. 66**) and the brainstem as reference tissue. Based on Logan analysis of the data, equilibrium was reached almost instantaneously as the y-intercept for each line (area of the brain, including tumor) was about zero. This is an important point for establishing and understanding the bio-availability of the radiotracer within the body. The Logan analysis also demonstrated significant differences, based on slopes of best-fit lines, for tumor tissue as compared to non-cancerous cortical tissue within the brain when normalized by the brainstem as a reference tissue (**Fig. 65-66**). Additionally, a significant difference in 2-[^{18}F]PhAHA-derived accumulation between ipsilateral and contralateral regions of the brain, particularly in *n. accumbens* (**Fig. 66**). Interestingly, this is not true for all areas of the brain with high radio-metabolite accumulation, *i.e. hippocampus, caudate putamen,* as these regions display little differences between ipsi-and contralateral sides for N = 6 animals, based on 95% confidence intervals (**Fig. 66**). To understand completely if this is true difference in *n. accumbens* SIRT1 activity, more studies, including ex-

vivo studies, are needed. It is possible that this an artifact due to partial volume effect as it is near the highly radioactive tumor tissue.

Furthermore, due to the non-invasive method of imaging, this technology can be used for longitudinal studies and evaluation of SIRT1-targeted pharmacomodulation on tumor progression. Use of 2-[^{18}F]PhAHA as a PET imaging agent has been successful for imaging the increase in SIRT1 expression-activity during progression of gliosarcoma (9L) tumor growth (**Fig. 67**). In this case, increases in 2-[^{18}F]PhAHA-derived radioactivity correlate with tumor growth as displayed

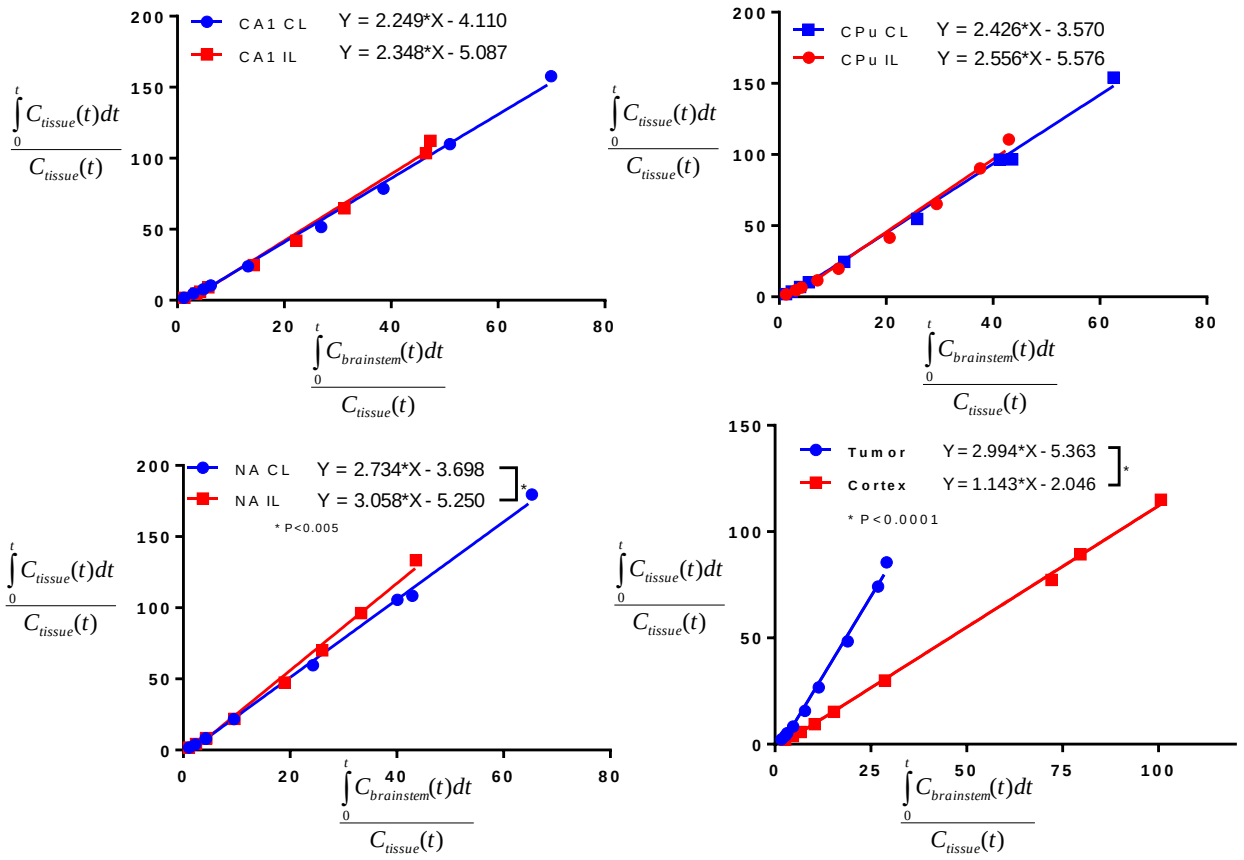

Figure 66. Logan plot quantification for areas of the brain with high SIRT1 expression-activity, including tumor lesions for animals bearing 9L tumors. All calculations were done using brainstem as reference tissue. Regression analysis was performed and demonstrated a significant difference between tumor and cortex tissue as well as a small significant difference for *n. accumbens*, i.l vs c.l. sides.

by MRI. The ability to track tumor progression *in vivo* using 2-[^{18}F]PhAHA with PET/CT imaging may become an integral part of diagnosis and treatment for cancers of the brain.

For further validation that 2-[^{18}F]PhAHA-derived accumulation is accurately displaying increases in SIRT1 expression-activity, an *in vivo* blocking study with SIRT1-selective inhibitor, EX-527 was performed. The results of the study in rats bearing a 9L gliosarcoma tumor displayed significantly decreased activity within areas of 2-[^{18}F]PhAHA-derived accumulation following intraperitoneal administration of SIRT1-selective inhibitor, EX-527 (5mg/kg 30 minutes prior to

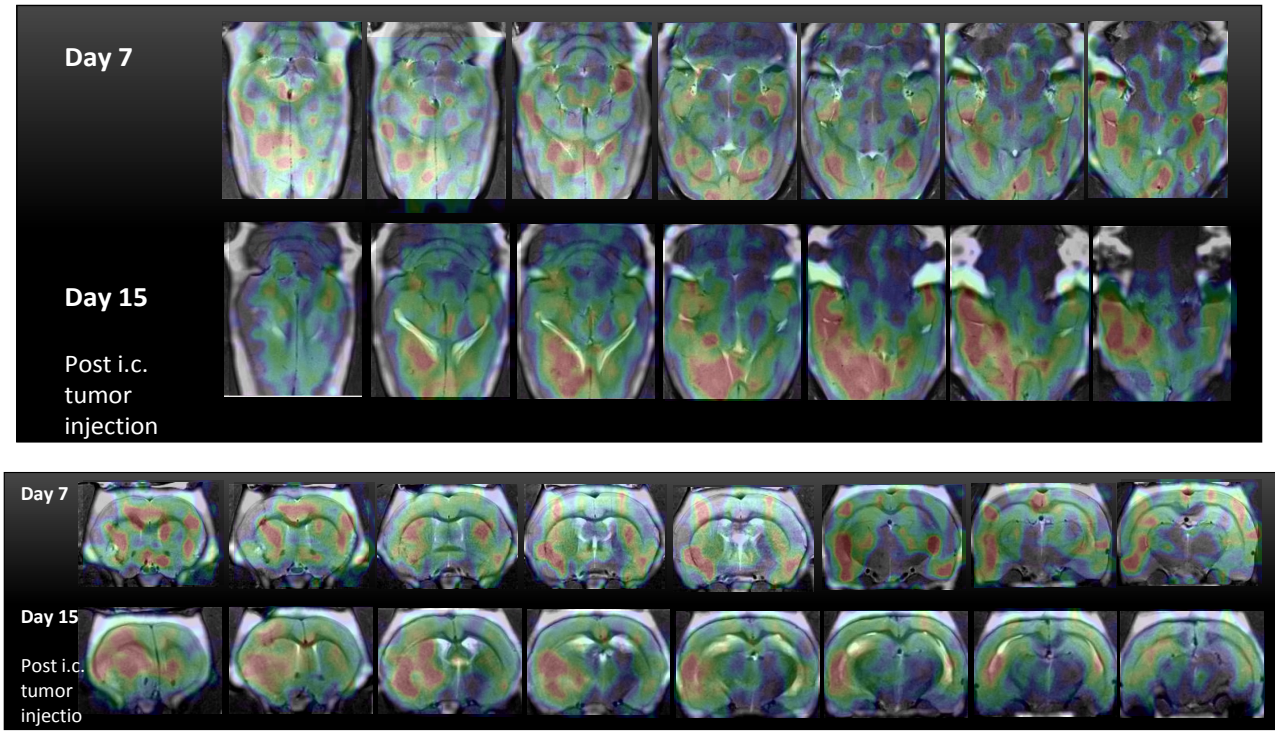

Figure 67. Coronal and axial sections in 1 mm steps through tumor of an animal at two different time points (7d and 15d) post i.c. 9L tumor cell injection. Using non-invasive SIRT1-targeted molecular imaging with 2-[^{18}F]PhAHA we are able to track the changes in tumor growth and enzyme expression over time.

administration of 2-[^{18}F]PhAHA) (**Fig. 68)** This is demonstrated both qualitatively (**Fig. 68A**) and quantitatively (**Fig. 68B**).

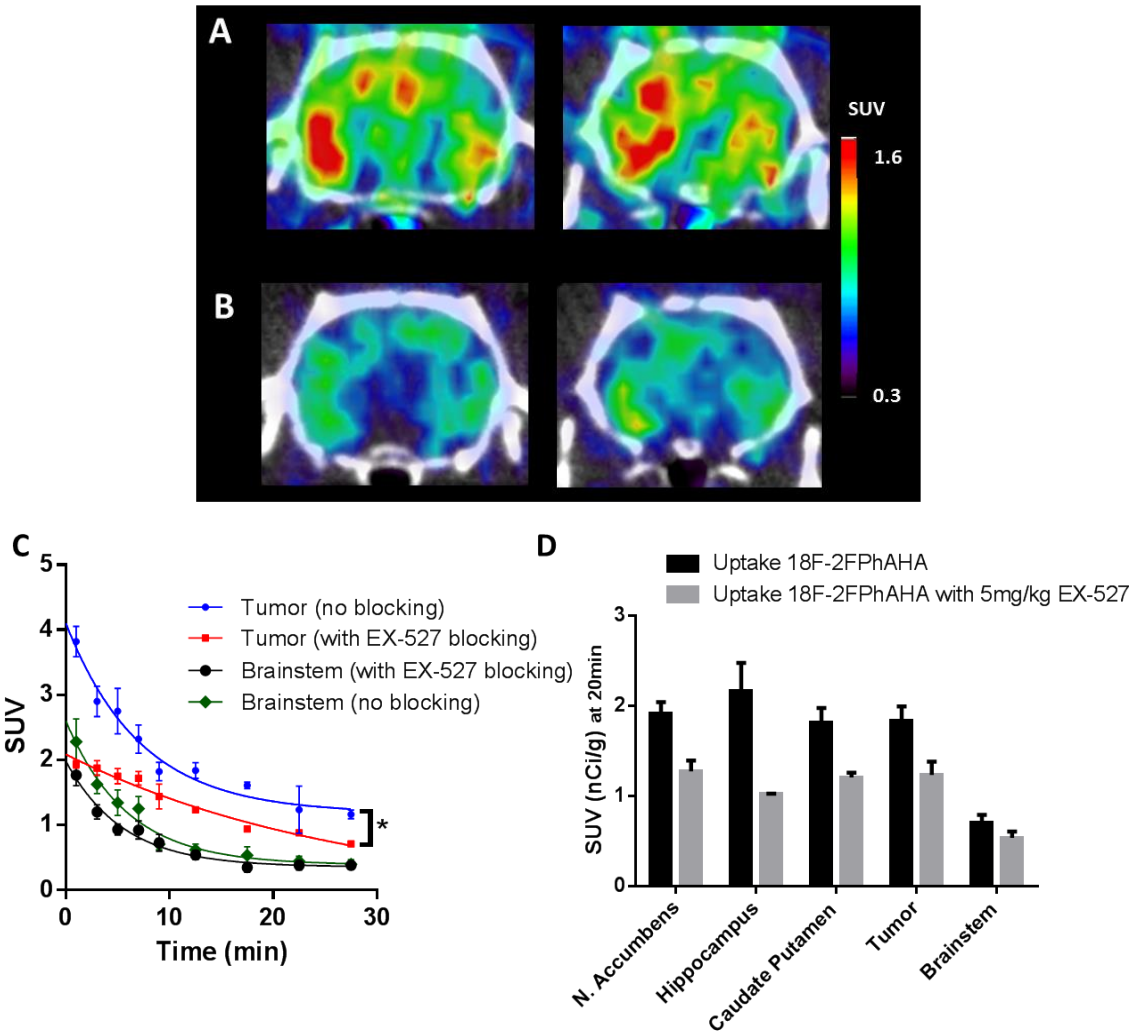

Figure 68. A) PET/CT images of a rat bearing a 9L tumor acquired at 20 minutes post i.v. administration of 2-[^{18}F]PhAHA scaled to the SUV values shown on the right. **B)** PET/CT images acquired at 20 minutes post i.v. administration of 2-[^{18}F]PhAHA and 50 minutes post i.p administration of 5 mg/kg EX-527 (SIRT1-selective inhibitor) scaled to the same SUV values as figure **A. C**) The SUV curves for the tumor with and without blocking by EX-527 as determined by ROI drawn around the tumor based on PET/MRI images. Brainstem is shown for reference tissue, with relatively lower SIRT1 expression-activity and therefore lower uptake of 2-[^{18}F]PhAHA. **D**) A quantitative representation for ROI's derived from PET images with 2-[^{18}F]PhAHA before (black) and after blocking with inhibitor (gray) for the tumor and other areas of high SIRT1 expression-activity (*i.e. N. Accumbens, Hippocampus, Caudate Putamen)*.

Conclusions:

While further validation of SIRT1 localization is needed through immunohistochemistry, these results are promising indicators for use of 2-[^{18}F]PhAHA with PET imaging in furthering the efficacy of diagnostics and therapies for GBM. In this work, it has been demonstrated that SIRT1-selective radiotracer, 2-[^{18}F]PhAHA, can be used for imaging SIRT1-expression-activity in two types of glioma models both at one time point and longitudinally. Furthermore, the imaging can be quantified to demonstrate significant differences of tracer accumulation in tissues. Most notably, this tracer can be used in complement with ^{18}F-TFAHA to demonstrate differences in HDACs class IIa expression-activity and SIRT1 expression activity in glioma models.

Methods:

Cell cultures and in vitro Radiotracer Uptake Studies: The U87MG, MiaPaca, and MDA-MB-231, 9L, and C6 cell lines were obtained from the American Type Tissue Culture Collection (ATCC); the MCF10A cell line was obtained from the cell culture repository of the Karmanos Cancer Institute (Detroit, MI). Tumor cells were propagated in DMEM supplemented with 10% fetal calf serum (FCS), penicillin and streptomycin, at 37°C in a humidified atmosphere with 5% CO_2. In vitro radiotracer uptake studies were performed as previously described (Yeh et al., 2013c). Briefly, prior to in vitro radiotracer uptake experiment, the cells were inspected for confluency and viability. Each of the four cell plates for a given cell line had the media removed by pipette aspiration, and fresh media (15 mL) containing the radiotracer (1-2 uCi/mL) was added to cells in the culture plates. The tumor cell monolayers were incubated with the radioactivity-containing medium for 30 minutes. The cells were then harvested by gentle unidirectional scraping and the suspensions of cells in the media were transferred into 15mL conical centrifuge tubes and pelleted by centrifugation (3000 rpm for 2 min). 50uL samples of supernatant and cell pellets flash-frozen on dry ice were placed in pre-weighed scintillation vials, weighed, and the radioactivity

was measured using Pakard 5500 gamma counter (Perkin Elmer, CA). The background-corrected and decay-corrected radioactivity concentrations in individual cell pellets (cpm/g) was divided by corresponding cell culture media samples (cpm/g) to determine the fold increase of radiotracer accumulation in cells versus the cell culture media.

Bioluminescence Images: Animals were anesthetized using 2-3% isofluorane mixed with air and imaging was performed while animals were under anesthesia. Bioluminescence images (BLI) of gliomas were obtained after administration of luciferin (10 µl/g i.p.) using an InVivo Xtreme system (Bruker, UK) at 10 to 14 days post U87 cell implantation.

MR Imaging: Animals initially anesthetized with 5% isoflurane, and maintained between 2-3% for the remainder of the experiment. During the procedure each animal was placed on a heated re-circulating water platform in order to maintain body temperature. The animals were held in position using a bite bar and a receive-only surface coil 2-element phased array for the rat brain) was placed dorsal to the head. Scans were acquired using a 7T ClinScan system (Bruker, UK) controlled by the Syngo software (Siemens, Knoxville, TN). A localizing scan was performed and adjustments to head position were made accordingly. T_2 images were obtained (repetition time [TR] 3530 ms echo time, [TE] 38 ms, FOV 3.2 cm x 3.2 cm x 2.4 cm, resolution 125 µm x 125 µm x 1 mm). Images were processed using ImageJ software (Bethesda, MD).

Cell Suspension: (Maxwell Laws): The U87MG or 9L were obtained from ATCC, subsequently the U87 cells were transfected with luciferase lentiviral particles at MD Andersen Cancer Center and characterized at this location. The 9L cells were dislodged using Hank's Balanced Salt solution (HBSS, 5 mL) for 1-2 minutes, centrifuged to obtain the cellular pellet, and resuspended in growth media sufficient enough to achieve $1x10^7$ cells/mL or $1x10^4$ cells/µL.

Injection Procedure: (Maxwell Laws): Rats were anesthetized via inhalation of isoflurane (3-5% in oxygen for induction, 1-3% for maintenance via nose cone). The rat was placed into a stereotaxic apparatus. An anterior/posterior incision was made to identify bregma, at which point a short-beveled 30-ga needle loaded with the cell suspension was placed relative to bregma; AP: -1.5, LAT: -4, DV: -6. A 5 µL tumor cell suspension was then injected slowly over 10 minutes, then the needle was slowly withdrawn 2 mM and the remaining 5 µL was injected slowly over 10 minutes for a total of $1x10^5$ cells in 10 µL.

Nude rats were implanted via intracerebral injection (i.c.) with U87 glioma cells ($1x10^5$ cells in 10 µL), that had been transfected to express a GFP-luciferase fusion reporter gene. Sprague-Dawley rats were given injected via i.c. injection with 9L gliosarcoma cells ($1x10^5$ cells in 10 µL) and grown for 7-14 days before the brains were harvested for ex-vivo studies.

Radiosynthesis for 2-[^{18}F]PhAHA : See previous chapter.

Ongoing work:

Currently, this study is undergoing completion through additional imaging of U87 and 9L tumor models as well as autoradiographical studies to complement the PET/CT imaging. Additional studies with EX-527 and 2-[^{18}F]PhAHA will also be performed to increase statistical significance for the EX-527-dependent inhibition of SIRT1 as visualized by differences in 2-[^{18}F]PhAHA-derived accumulation. Lastly, IHC staining of brain slices will be performed using antibodies against both SIRT1 and phospho-SIRT1 to determine the exact localization of SIRT1 and activated SIRT1 within the brain. With the addition of these studies, these results will provide valuable knowledge regarding the role of SIRT1 within glioma and gliosarcoma tumors. This data may then be applied to monitor the effects of SIRT1-targeted pharmacomodulation on tumor growth and progression.

CHAPTER 6 CONCLUSIONS AND FUTURE DIRECTIONS

HDAC enzymes and epigenetic regulation demonstrate great potential for treatment of disease. Treating difficult diseases such as Alzheimer's, cancer, and stress-related disorders may be aided greatly by the development of HDAC selective imaging substrates. The aim of this work was to develop isoform- and class-selective imaging agents for HDACs to gain understanding and visualization of HDAC expression-activity product. The use of radiolabeled substrates in PET imaging allows for non-invasive visualization and quantification of spatial and temporal dynamics of the HDACs in different organs and tissues. Through this work, selective, radiolabeled, imaging agents for HDAC class IIa, SIRT1, and SIRT2 have been established *in vitro* and *in vivo.* Furthermore, HDAC class IIa and SIRT1 imaging agents have been evaluated in a disease model, demonstrating effectiveness for imaging enzyme-mediated epigenetic regulation changes in cancer. These imaging agents can be applied to non-invasive monitoring of treatment and disease progression via PET imaging for many difficult diseases. The ability to use two complementary tracers for cancer imaging is especially important to identify areas of target responder vs non-responder in a patient. Additionally, through the development of these tracers, many of the radiochemical syntheses developed in this work follow unprecedented steps and lay a strong foundation for future radiochemical synthesis of novel fluorinated compounds.

The future work will be aimed at finishing *in vitro* characterization of these compounds and proceeding with *in vivo* studies for norm and disease. Studying the roles of the SIRTs and HDAC class IIa enzymes in stress related disorders and cancer could provide information for novel treatments and monitoring of disease. These studies are the first of their kind to demonstrate selective radiolabeled substrates for HDAC class IIa, SIRT1 and SIRT2. The synthesis of focused substrate libraries provides unprecedented information about the structure activity relationship for

these enzymes activity both *in vitro* and *in vivo*. This information may be instrumental in the development of future class- or isoform-selective activators or inhibitors for treatment of disease.

The ability to non-invasively visualize HDAC enzyme expression-activity product *in vivo* through non-invasive imaging holds incredible promise for developing new treatments for disease. These imaging agents will enable non-invasive monitoring of pharmacodynamics of HDACs inhibitors on the target level. By opening the door to new methods of diagnosis and treatment for diseases such as cancer and stress-related disorders this research may lead to effective clinical trials and drug development. While more work is necessary to establish these compounds as imaging agents *in vivo* and in disease models, the work done and proposed lay the start to an exciting path of discovery for understanding the role of epigenetic regulation in the body.

REFERENCES

Asai, A., Miyagi, Y., Sugiyama, A., Gamanuma, M., Hong, S.H., Takamoto, S., Nomura, K., Matsutani, M., Takakura, K., Kuchino, Y., 1994. Negative effects of wild-type p53 and s-Myc on cellular growth and tumorigenicity of glioma cells. Implication of the tumor suppressor genes for gene therapy. J Neurooncol 19, 259-268.

Autiero, I., Costantini, S., Colonna, G., 2009. Human sirt-1: molecular modeling and structure-function relationships of an unordered protein. PloS one 4, e7350.

Barber, M.F., Michishita-Kioi, E., Xi, Y., Tasselli, L., Kioi, M., Moqtaderi, Z., Tennen, R.I., Paredes, S., Young, N.L., Chen, K., Struhl, K., Garcia, B.A., Gozani, O., Li, W., Chua, K.F., 2012. SIRT7 links H3K18 deacetylation to maintenance of oncogenic transformation. Nature 487, 114-118.

Barth, R.F., Kaur, B., 2009. Rat brain tumor models in experimental neuro-oncology: the C6, 9L, T9, RG2, F98, BT4C, RT-2 and CNS-1 gliomas. Journal of neuro-oncology 94, 299-312.

Beauharnois, J.M., Bolivar, B.E., Welch, J.T., 2013. Sirtuin 6: a review of biological effects and potential therapeutic properties. Molecular BioSystems 9, 1789-1806.

Belanger, A.P., Pandey, M.K., DeGrado, T.R., 2011. Microwave-Assisted Radiosynthesis of [(18)F]Fluorinated Fatty Acid Analogs. Nuclear medicine and biology 38, 435-441.

Benda, P., Someda, K., Messer, J., Sweet, W.H., 1971. Morphological and immunochemical studies of rat glial tumors and clonal strains propagated in culture. Journal of neurosurgery 34, 310-323.

Bharathi, S.S., Zhang, Y., Mohsen, A.-W., Uppala, R., Balasubramani, M., Schreiber, E., Uechi, G., Beck, M.E., Rardin, M.J., Vockley, J., Verdin, E., Gibson, B.W., Hirschey, M.D.,

Goetzman, E.S., 2013. SIRT3 Regulates Long-chain Acyl-CoA Dehydrogenase by Deacetylating Conserved Lysines Near the Active Site. Journal of Biological Chemistry.

Bheda, P., Jing, H., Wolberger, C., Lin, H., 2016. The Substrate Specificity of Sirtuins. Annu Rev Biochem.

BioSolveIT, GmbH, LeadIT2.1.7, An der Ziegelei 79, 53757 St. Augustin, Germany.

Blander, G., Guarente, L., 2004. The Sir2 family of protein deacetylases. Annual review of biochemistry 73, 417-435.

Bonomi, R., Mukhopadhyay, U., Shavrin, A., Yeh, H.-H., Majhi, A., Dewage, S.W., Najjar, A., Lu, X., Cisneros, G.A., Tong, W.P., Alauddin, M.M., Liu, R.-S., Mangner, T.J., Turkman, N., Gelovani, J.G., 2015. Novel Histone Deacetylase Class IIa Selective Substrate Radiotracers for PET Imaging of Epigenetic Regulation in the Brain. PloS one 10, e0133512.

Bordone, L., Guarente, L., 2005. Calorie restriction, SIRT1 and metabolism: understanding longevity. Nature reviews. Molecular cell biology 6, 298-305.

Bottomley, M.J., Lo Surdo, P., Di Giovine, P., Cirillo, A., Scarpelli, R., Ferrigno, F., Jones, P., Neddermann, P., De Francesco, R., Steinkuhler, C., Gallinari, P., Carfi, A., 2008. Structural and functional analysis of the human HDAC4 catalytic domain reveals a regulatory structural zinc-binding domain. The Journal of biological chemistry 283, 26694-26704.

Bouras, T., Fu, M., Sauve, A.A., Wang, F., Quong, A.A., Perkins, N.D., Hay, R.T., Gu, W., Pestell, R.G., 2005. SIRT1 deacetylation and repression of p300 involves lysine residues 1020/1024 within the cell cycle regulatory domain 1. The Journal of biological chemistry 280, 10264-10276.

Brooks, C.L., Gu, W., 2009. How does SIRT1 affect metabolism, senescence and cancer? Nat Rev Cancer 9, 123-128.

Brooks, C.L., Gu, W., 2011. The impact of acetylation and deacetylation on the p53 pathway. Protein & cell 2, 456-462.

Brownell, J., J. Zhou, T. Ranalli, R. Kobayashi, D. Edmondson, S. Roth, and, Allis, C.D., 1996. Tetrahymena histone acetyltransferase A: a homolog to yeast Gcn5p linking histone acetylation to gene activation. Cell 84, 843-851.

Chen, B., Cepko, C.L., 2009. HDAC4 regulates neuronal survival in normal and diseased retinas. Science 323, 256-259.

Chen, V.B., Davis, I.W., Richardson, D.C., 2009. KING (Kinemage, Next Generation): a versatile interactive molecular and scientific visualization program. Protein science 18, 2403-2409.

Chiang, Y.L., Lin, H., 2016. An improved fluorogenic assay for SIRT1, SIRT2, and SIRT3. Organic & biomolecular chemistry 14, 2186-2190.

Chuang, D.-M., Leng, Y., Marinova, Z., Kim, H.-J., Chiu, C.-T., 2009. Multiple roles of HDAC inhibition in neurodegenerative conditions. Trends in neurosciences 32, 591-601.

Claes, A., Idema, A.J., Wesseling, P., 2007. Diffuse glioma growth: a guerilla war. Acta neuropathologica 114, 443-458.

Cohen, H.Y., Lavu, S., Bitterman, K.J., Hekking, B., Imahiyerobo, T.A., Miller, C., Frye, R., Ploegh, H., Kessler, B.M., Sinclair, D.A., 2004. Acetylation of the C terminus of Ku70 by CBP and PCAF controls Bax-mediated apoptosis. Molecular cell 13, 627-638.

Cosgrove, M.S., Bever, K., Avalos, J.L., Muhammad, S., Zhang, X., Wolberger, C., 2006. The Structural Basis of Sirtuin Substrate Affinity†,‡. Biochemistry 45, 7511-7521.

Cui, H., Kamal, Z., Ai, T., Xu, Y., More, S.S., Wilson, D.J., Chen, L., 2014. Discovery of potent and selective sirtuin 2 (SIRT2) inhibitors using a fragment-based approach. J Med Chem 57, 8340-8357.

Dai, J.M., Wang, Z.Y., Sun, D.C., Lin, R.X., Wang, S.Q., 2007. SIRT1 interacts with p73 and suppresses p73-dependent transcriptional activity. Journal of cellular physiology 210, 161-166.

Dai, W., Zhou, J., Jin, B., Pan, J., 2016. Class III-specific HDAC inhibitor Tenovin-6 induces apoptosis, suppresses migration and eliminates cancer stem cells in uveal melanoma. Scientific Reports 6, 22622.

de Ruijter, A.J., van Gennip, A.H., Caron, H.N., Kemp, S., van Kuilenburg, A.B., 2003. Histone deacetylases (HDACs): characterization of the classical HDAC family. Biochem J 370, 737-749.

Dhordain, P., Lin, R.J., Quief, S., Lantoine, D., Kerckaert, J.P., Evans, R.M., Albagli, O., 1998. The LAZ3(BCL-6) oncoprotein recruits a SMRT/mSIN3A/histone deacetylase containing complex to mediate transcriptional repression. Nucleic acids research 26, 4645-4651.

Di Giovanni, S., Knights, C.D., Rao, M., Yakovlev, A., Beers, J., Catania, J., Avantaggiati, M.L., Faden, A.I., 2006. The tumor suppressor protein p53 is required for neurite outgrowth and axon regeneration. The EMBO journal 25, 4084-4096.

Dillin, A., Kelly, J.W., 2007. Medicine. The yin-yang of sirtuins. Science (New York, N.Y 317, 461-462.

Donmez, G., Outeiro, T.F., 2013. SIRT1 and SIRT2: emerging targets in neurodegeneration. EMBO Molecular Medicine 5, 344-352.

Dryden, S.C., Nahhas, F.A., Nowak, J.E., Goustin, A.S., Tainsky, M.A., 2003. Role for human SIRT2 NAD-dependent deacetylase activity in control of mitotic exit in the cell cycle. Molecular and cellular biology 23, 3173-3185.

Du, J., Zhou, Y., Su, X., Yu, J.J., Khan, S., Jiang, H., Kim, J., Woo, J., Kim, J.H., Choi, B.H., He, B., Chen, W., Zhang, S., Cerione, R.A., Auwerx, J., Hao, Q., Lin, H., 2011. Sirt5 is a NAD-dependent protein lysine demalonylase and desuccinylase. Science (New York, N.Y.) 334, 806-809.

Dubrow, R., Darefsky, A.S., Jacobs, D.I., Park, L.S., Rose, M.G., Laurans, M.S., King, J.T., Jr., 2013. Time trends in glioblastoma multiforme survival: the role of temozolomide. Neuro-oncology 15, 1750-1761.

Eagle, A.L., Fitzpatrick, C.J., Perrine, S.A., 2013a. Single prolonged stress impairs social and object novelty recognition in rats. Behavioural brain research 256, 10.1016/j.bbr.2013.1009.1014.

Eagle, A.L., Knox, D., Roberts, M.M., Mulo, K., Liberzon, I., Galloway, M.P., Perrine, S.A., 2013b. Single prolonged stress enhances hippocampal glucocorticoid receptor and phosphorylated protein kinase B levels. Neuroscience research 75, 130-137.

Fahie, K., Hu, P., Swatkoski, S., Cotter, R.J., Zhang, Y., Wolberger, C., 2009. Side chain specificity of ADP-ribosylation by a sirtuin. The FEBS journal 276, 7159-7176.

Feldman, J.L., Baeza, J., Denu, J.M., 2013. Activation of the protein deacetylase SIRT6 by long-chain fatty acids and widespread deacylation by mammalian sirtuins. The Journal of biological chemistry 288, 31350-31356.

Feldman, J.L., Dittenhafer-Reed, K.E., Kudo, N., Thelen, J.N., Ito, A., Yoshida, M., Denu, J.M., 2015. Kinetic and Structural Basis for Acyl-Group Selectivity and NAD(+) Dependence in Sirtuin-Catalyzed Deacylation. Biochemistry 54, 3037-3050.

Finnin, M.S., Donigian, J.R., Pavletich, N.P., 2001. Structure of the histone deacetylase SIRT2. Nature structural biology 8, 621-625.

Ford, J., Ahmed, S., Allison, S., Jiang, M., Milner, J., 2008. JNK2-dependent regulation of SIRT1 protein stability. Cell Cycle 7, 3091-3097.

Friesner, R.A., Banks, J.L., Murphy, R.B., Halgren, T.A., Klicic, J.J., Mainz, D.T., Repasky, M.P., Knoll, E.H., Shelley, M., Perry, J.K., Shaw, D.E., Francis, P., Shenkin, P.S., 2004. Glide: A New Approach for Rapid, Accurate Docking and Scoring. 1. Method and Assessment of Docking Accuracy. Journal of Medicinal Chemistry 47, 1739-1749.

Gao, L., Cueto, M.A., Asselbergs, F., Atadja, P., 2002. Cloning and Functional Characterization of HDAC11, a Novel Member of the Human Histone Deacetylase Family. Journal of Biological Chemistry 277, 25748-25755.

Gao, Z., Zhang, J., Kheterpal, I., Kennedy, N., Davis, R.J., Ye, J., 2011. Sirtuin 1 (SIRT1) protein degradation in response to persistent c-Jun N-terminal kinase 1 (JNK1) activation contributes to hepatic steatosis in obesity. Journal of Biological Chemistry 286, 22227-22234.

Geng, Y.-Q., Li, T.-T., Liu, X.-Y., Li, Z.-H., Fu, Y.-C., 2011. SIRT1 and SIRT5 activity expression and behavioral responses to calorie restriction. Journal of Cellular Biochemistry 112, 3755-3761.

Gerhart-Hines, Z., Dominy, J.E., Blättler, S.M., Jedrychowski, M.P., Banks, A.S., Lim, J.-H., Chim, H., Gygi, S.P., Puigserver, P., 2011. The cAMP/PKA pathway rapidly activates SIRT1 to promote fatty acid oxidation independently of changes in NAD+. Molecular cell 44, 851-863.

Grbesa, I., Pajares, M.J., Martinez-Terroba, E., Agorreta, J., Mikecin, A.M., Larrayoz, M., Idoate, M.A., Gall-Troselj, K., Pio, R., Montuenga, L.M., 2015. Expression of sirtuin 1 and 2 is associated with poor prognosis in non-small cell lung cancer patients. PloS one 10, e0124670.

Gregoretti, I.V., Lee, Y.M., Goodson, H.V., 2004. Molecular evolution of the histone deacetylase family: functional implications of phylogenetic analysis. J Mol Biol 338, 17-31.

Grozinger, C.M., Chao, E.D., Blackwell, H.E., Moazed, D., Schreiber, S.L., 2001. Identification of a class of small molecule inhibitors of the sirtuin family of NAD-dependent deacetylases by phenotypic screening. The Journal of biological chemistry 276, 38837-38843.

Guo, H., Renaut, R.A., Chen, K., 2007. An input function estimation method for FDG-PET human brain studies.(Author abstract). Nuclear medicine and biology, 483.

Guo, X., Williams, J.G., Schug, T.T., Li, X., 2010. DYRK1A and DYRK3 promote cell survival through phosphorylation and activation of SIRT1. Journal of Biological Chemistry 285, 13223-13232.

Haas-Kogan, D., Shalev, N., Wong, M., Mills, G., Yount, G., Stokoe, D., 1998. Protein kinase B (PKB/Akt) activity is elevated in glioblastoma cells due to mutation of the tumor suppressor PTEN/MMAC. Current Biology 8, 1195-S1191.

Haberkorn U, B.B., Altmann A, Eisenhut M, Gelovani J, Mier W., 2007. Uptake and biodistribution of the histone deacetylase inhibitor SAHA in tumor bearing animals. European Journal of Nuclear Medicine and Molecular Imaging 34, S395-S395.

Haberland, M., Montgomery, R.L., Olson, E.N., 2009. The many roles of histone deacetylases in development and physiology: implications for disease and therapy. Nat Rev Genet 10, 32-42.

Haigis, M.C., Mostoslavsky, R., Haigis, K.M., Fahie, K., Christodoulou, D.C., Murphy, A.J., Valenzuela, D.M., Yancopoulos, G.D., Karow, M., Blander, G., Wolberger, C., Prolla, T.A., Weindruch, R., Alt, F.W., Guarente, L., 2006. SIRT4 inhibits glutamate dehydrogenase and opposes the effects of calorie restriction in pancreatic beta cells. Cell 126, 941-954.

Haigis, M.C.S., D. A. , 2010. Mammalian sirtuins: biological insights and disease relevance. Annu. Rev. Pathol 5, 253-295.

Han, S.J., Yang, I., Tihan, T., Prados, M.D., Parsa, A.T., 2010. Primary gliosarcoma: key clinical and pathologic distinctions from glioblastoma with implications as a unique oncologic entity. Journal of Neuro-Oncology 96, 313-320.

He, B., Hu, J., Zhang, X., Lin, H., 2014. Thiomyristoyl peptides as cell-permeable Sirt6 inhibitors. Organic & biomolecular chemistry 12, 7498-7502.

Heltweg, B., Brauch, C., Jung, M., Dequiedt, F., Marshall, B.L., Verdin, E., Yoshida, M., Nishino, N., 2004. Subtype selective substrates for histone deacetylases. Journal of Medicinal Chemistry 47, 5235-5243.

Heltweg, B., Dequiedt, F., Verdin, E., Jung, M., 2003. Nonisotopic substrate for assaying both human zinc and NAD+-dependent histone deacetylases. Analytical biochemistry 319, 42-48.

Hendricks, J.A., Keliher, E.J., Marinelli, B., Reiner, T., Weissleder, R., Mazitschek, R., 2011a. In vivo PET imaging of histone deacetylases by 18F- suberoylanilide hydroxamic acid (18F-SAHA). Journal of Medicinal Chemistry 54, 5576-5582.

Hendricks, J.A., Keliher, E.J., Marinelli, B., Reiner, T., Weissleder, R., Mazitschek, R., 2011b. In vivo PET imaging of histone deacetylases by 18F-suberoylanilide hydroxamic acid (18F-SAHA). J Med Chem 54, 5576-5582.

Hiratsuka, M., Inoue, T., Toda, T., Kimura, N., Shirayoshi, Y., Kamitani, H., Watanabe, T., Ohama, E., Tahimic, C.G., Kurimasa, A., Oshimura, M., 2003. Proteomics-based identification of differentially expressed genes in human gliomas: down-regulation of SIRT2 gene. Biochemical and biophysical research communications 309, 558-566.

Hirsch, B.M., Zheng, W., 2011. Sirtuin mechanism and inhibition: explored with N(epsilon)-acetyl-lysine analogs. Mol Biosyst 7, 16-28.

Hoffmann, G., Breitenbücher, F., Schuler, M., Ehrenhofer-Murray, A.E., 2014. A novel sirtuin 2 (SIRT2) inhibitor with p53-dependent pro-apoptotic activity in non-small cell lung cancer. Journal of Biological Chemistry 289, 5208-5216.

Hooker, J.M., Kim, S.W., Alexoff, D., Xu, Y., Shea, C., Reid, A., Volkow, N., Fowler, J.S., 2009. Histone Deacetylase Inhibitor MS-275 Exhibits Poor Brain Penetration: Pharmacokinetic Studies of [11C]MS-275 using Positron Emission Tomography. ACS Chemical Neuroscience 1, 65-73.

Houtkooper, R.H., Pirinen, E., Auwerx, J., 2012. Sirtuins as regulators of metabolism and healthspan.(Report). Nature Reviews Molecular Cell Biology, 225.

Hu, J., He, B., Bhargava, S., Lin, H., 2013. A fluorogenic assay for screening Sirt6 modulators. Organic & biomolecular chemistry 11, 5213-5216.

Huhtiniemi, T., Salo, H.S., Suuronen, T., Poso, A., Salminen, A., Leppanen, J., Jarho, E., Lahtela-Kakkonen, M., 2011. Structure-based design of pseudopeptidic inhibitors for SIRT1 and SIRT2. J Med Chem 54, 6456-6468.

Imai, S., Armstrong, C.M., Kaeberlein, M., Guarente, L., 2000. Transcriptional silencing and longevity protein Sir2 is an NAD-dependent histone deacetylase. Nature 403, 795-800.

Imaoka, N., Hiratsuka, M., Osaki, M., Kamitani, H., Kambe, A., Fukuoka, J., Kurimoto, M., Nagai, S., Okada, F., Watanabe, T., Ohama, E., Kato, S., Oshimura, M., 2012. Prognostic significance of sirtuin 2 protein nuclear localization in glioma: an immunohistochemical study. Oncology reports 28, 923-930.

Inoue, T., Hiratsuka, M., Osaki, M., Oshimura, M., 2007a. The molecular biology of mammalian SIRT proteins: SIRT2 in cell cycle regulation. Cell cycle (Georgetown, Tex 6, 1011-1018.

Inoue, T., Hiratsuka, M., Osaki, M., Yamada, H., Kishimoto, I., Yamaguchi, S., Nakano, S., Katoh, M., Ito, H., Oshimura, M., 2007b. SIRT2, a tubulin deacetylase, acts to block the entry to chromosome condensation in response to mitotic stress. Oncogene 26, 945-957.

Inoue, T., Hiratsuka, M., Osaki, M., Yamada, H., Kishimoto, I., Yamaguchi, S., Nakano, S., Katoh, M., Ito, H., Oshimura, M., 2007c. SIRT2, a tubulin deacetylase, acts to block the entry to chromosome condensation in response to mitotic stress. Oncogene 26, 945-957.

Inoue, T., Nakayama, Y., Yamada, H., Li, Y.C., Yamaguchi, S., Osaki, M., Kurimasa, A., Hiratsuka, M., Katoh, M., Oshimura, M., 2009. SIRT2 downregulation confers resistance to microtubule inhibitors by prolonging chronic mitotic arrest. Cell cycle (Georgetown, Tex 8, 1279-1291.

J, L., 2000. Graphical analysis of PET data applied to reversible and irreversible tracers. Nuclear medicine and biology 27, 661-670.

Jamonnak, N., Hirsch, B.M., Pang, Y., Zheng, W., 2010. Substrate specificity of SIRT1-catalyzed lysine Nepsilon-deacetylation reaction probed with the side chain modified Nepsilon-acetyl-lysine analogs. Bioorganic chemistry 38, 17-25.

Jiang, H., Khan, S., Wang, Y., Charron, G., He, B., Sebastian, C., Du, J., Kim, R., Ge, E., Mostoslavsky, R., Hang, H.C., Hao, Q., Lin, H., 2013. SIRT6 regulates TNF-alpha secretion through hydrolysis of long-chain fatty acyl lysine. Nature 496, 110-113.

Jin, L., Wei, W., Jiang, Y., Peng, H., Cai, J., Mao, C., Dai, H., Choy, W., Bemis, J.E., Jirousek, M.R., 2009. Crystal structures of human SIRT3 displaying substrate-induced conformational changes. Journal of Biological Chemistry 284, 24394-24405.

Jones, P., Altamura, S., De Francesco, R., Gallinari, P., Lahm, A., Neddermann, P., Rowley, M., Serafini, S., Steinkuhler, C., 2008. Probing the elusive catalytic activity of vertebrate class IIa histone deacetylases. Bioorg Med Chem Lett 18, 1814-1819.

Khochbin, S., Verdel, A., Lemercier, C., Seigneurin-Berny, D., 2001. Functional significance of histone deacetylase diversity. Curr Opin Genet Dev 11, 162-166.

Kim, M.S.e.a., 2012. An essential role for histone deacetylase 4 in synaptic plasticity and memory formation. Neuroscience 32, 10879-10886.

Kim, S.W., Hooker, J.M., Otto, N., Win, K., Muench, L., Shea, C., Carter, P., King, P., Reid, A.E., Volkow, N.D., Fowler, J.S., 2013. Whole-body pharmacokinetics of HDAC inhibitor drugs, butyric acid, valproic acid and 4-phenylbutyric acid measured with carbon-11 labeled analogs by PET. Nuclear medicine and biology 40, 912-918.

Knox, D., Perrine, S.A., George, S.A., Galloway, M.P., Liberzon, I., 2010. Single Prolonged Stress Decreases Glutamate, Glutamine, and Creatine Concentrations In The Rat Medial Prefrontal Cortex. Neuroscience letters 480, 16-20.

Kokkonen, P., Rahnasto-Rilla, M., Kiviranta, P.H., Huhtiniemi, T., Laitinen, T., Poso, A., Jarho, E., Lahtela-Kakkonen, M., 2012. Peptides and Pseudopeptides as SIRT6 Deacetylation Inhibitors. ACS Medicinal Chemistry Letters 3, 969-974.

Kokkonen, P., Rahnasto-Rilla, M., Mellini, P., Jarho, E., Lahtela-Kakkonen, M., Kokkola, T., 2014. Studying SIRT6 regulation using H3K56 based substrate and small molecules. European journal of pharmaceutical sciences : official journal of the European Federation for Pharmaceutical Sciences 63, 71-76.

Kwapis, J.L., Wood, M.A., 2014. Epigenetic mechanisms in fear conditioning: Implications for treating post-traumatic stress disorder. Trends in neurosciences 37, 706-720.

Laherty, C.D., Yang, W.M., Sun, J.M., Davie, J.R., Seto, E., Eisenman, R.N., 1997. Histone deacetylases associated with the mSin3 corepressor mediate mad transcriptional repression. Cell 89, 349-356.

Lahm, A., Paolini, C., Pallaoro, M., Nardi, M.C., Jones, P., Neddermann, P., Sambucini, S., Bottomley, M.J., Lo Surdo, P., Carfi, A., Koch, U., De Francesco, R., Steinkuhler, C., Gallinari, P., 2007. Unraveling the hidden catalytic activity of vertebrate class IIa histone deacetylases. Proc Natl Acad Sci U S A 104, 17335-17340.

Lain, S., Hollick, J.J., Campbell, J., Staples, O.D., Higgins, M., Aoubala, M., McCarthy, A., Appleyard, V., Murray, K.E., Baker, L., 2008. Discovery, in vivo activity, and mechanism of action of a small-molecule p53 activator. Cancer cell 13, 454-463.

Lakshmaiah, K.C., Jacob, L.A., Aparna, S., Lokanatha, D., Saldanha, S.C., 2014. Epigenetic therapy of cancer with histone deacetylase inhibitors. Journal of cancer research and therapeutics 10, 469-478.

Lange, G., Klein, R., Albrecht, J., Rarey, M., Reulecke, I., 2010.

Lei Liu, C.P., Jessica Ginsberg, Jennifer Shih, Siddharth Arun, Gizem Donmez, 2015. Protective role of SIRT5 against motor deficit and dopaminergic degeneration in MPTP-induced mice model of Parkinson's disease. Behavioural Brain Research 281, 215-221.

Lennerz, V., Fatho, M., Gentilini, C., Frye, R.A., Lifke, A., Ferel, D., Wolfel, C., Huber, C., Wolfel, T., 2005. The response of autologous T cells to a human melanoma is dominated by mutated neoantigens. Proc Natl Acad Sci U S A 102, 16013-16018.

Leskovac, V., 2003. Comprehensive enzyme kinetics. Kluwer Academic / Plenum Publishers, New York.

Li, L., Wang, L., Li, L., Wang, Z., Ho, Y., McDonald, T., Holyoake, Tessa L., Chen, W., Bhatia, R., 2012. Activation of p53 by SIRT1 Inhibition Enhances Elimination of CML Leukemia Stem Cells in Combination with Imatinib. Cancer cell 21, 266-281.

Li, X., Zhang, S., Blander, G., Tse, J.G., Krieger, M., Guarente, L., 2007. SIRT1 deacetylates and positively regulates the nuclear receptor LXR. Molecular cell 28, 91-106.

Lim, J.-H., Gerhart-Hines, Z., Dominy, J.E., Lee, Y., Kim, S., Tabata, M., Xiang, Y.K., Puigserver, P., 2013. Oleic acid stimulates complete oxidation of fatty acids through protein kinase A-dependent activation of SIRT1-PGC1α complex. Journal of Biological Chemistry 288, 7117-7126.

Lin, Z.F., Xu, H.B., Wang, J.Y., Lin, Q., Ruan, Z., Liu, F.B., Jin, W., Huang, H.H., Chen, X., 2013. SIRT5 desuccinylates and activates SOD1 to eliminate ROS. Biochemical and biophysical research communications 441, 191-195.

Lino, M., Merlo, A., 2009. Translating biology into clinic: the case of glioblastoma. Curr Opin Cell Biol 21.

Liu, P.Y., Xu, N., Malyukova, A., Scarlett, C.J., Sun, Y.T., Zhang, X.D., Ling, D., Su, S.P., Nelson, C., Chang, D.K., Koach, J., Tee, A.E., Haber, M., Norris, M.D., Toon, C., Rooman, I., Xue, C., Cheung, B.B., Kumar, S., Marshall, G.M., Biankin, A.V., Liu, T., 2013. The histone deacetylase SIRT2 stabilizes Myc oncoproteins. Cell death and differentiation 20, 503-514.

Liu, T., Liu, P.Y., Marshall, G.M., 2009. The Critical Role of the Class III Histone Deacetylase SIRT1 in Cancer. Cancer research 69, 1702-1705.

Logan J, F.J., Volkow ND, Wang GJ, Ding YS, Alexoff DL, 1996. Distribution volume ratios without blood sampling from graphical analysis of PET data. J Cereb Blood Flow Metab 16, 834-840.

Logan J, F.J., Volkow ND, Wolf AP, Dewey SL, Schlyer DJ, MacGregor RR, Hitzemann R, Bendriem B, Gatley SJ, Christman DR, Graphical analysis of reversible radioligand binding from time-activity measurements applied to [N-11C-methyl]-(-)-cocaine PET studies in human subjects. J Cereb Blood Flow Metab 10, 740-747.

Lombardi, P.M., Cole, K.E., Dowling, D.P., Christianson, D.W., 2011. Structure, mechanism, and inhibition of histone deacetylases and related metalloenzymes. Current opinion in structural biology 21, 735-743.

Luo, J., Nikolaev, A.Y., Imai, S., Chen, D., Su, F., Shiloh, A., Guarente, L., Gu, W., 2001. Negative control of p53 by Sir2alpha promotes cell survival under stress. Cell 107, 137-148.

Ma, J.-X., Li, H., Chen, X.-M., Yang, X.-H., Wang, Q., Wu, M.-L., Kong, Q.-Y., Li, Z.-X., Liu, J., 2013. Expression patterns and potential roles of SIRT1 in human medulloblastoma cells in vivo and in vitro. Neuropathology 33, 7-16.

Majdzadeh, N., Morrison, B.E., D'Mello, S.R., 2008. Class IIA HDACs in the regulation of neurodegeneration. Front Biosci 13, 1072-1082.

Marcotte, P.A., Richardson, P.R., Guo, J., Barrett, L.W., Xu, N., Gunasekera, A., Glaser, K.B., 2004. Fluorescence assay of SIRT protein deacetylases using an acetylated peptide substrate and a secondary trypsin reaction. Analytical biochemistry 332, 90-99.

Mashimo, M., Kato, J., Moss, J., 2014. Structure and function of the ARH family of ADP-ribose-acceptor hydrolases. DNA repair 0, 88-94.

Mathias, R.A., Greco, T.M., Oberstein, A., Budayeva, H.G., Chakrabarti, R., Rowland, E.A., Kang, Y., Shenk, T., Cristea, I.M., 2014. Sirtuin 4 Is a Lipoamidase Regulating Pyruvate Dehydrogenase Complex Activity. Cell 159, 1615-1625.

Matsushima, S., Sadoshima, J., 2015. The role of sirtuins in cardiac disease. American journal of physiology. Heart and circulatory physiology 309, H1375-1389.

McGlynn, L.M., Zino, S., MacDonald, A.I., Curle, J., Reilly, J.E., Mohammed, Z.M., McMillan, D.C., Mallon, E., Payne, A.P., Edwards, J., Shiels, P.G., 2014. SIRT2: tumour suppressor or tumour promoter in operable breast cancer? European journal of cancer (Oxford, England : 1990) 50, 290-301.

Meng, Q., Li, F., Jiang, S., Li, Z., 2013. Novel (64)Cu-Labeled CUDC-101 for in Vivo PET Imaging of Histone Deacetylases. ACS Med Chem Lett 4, 858-862.

Michan, S., Sinclair, D., 2007. Sirtuins in mammals: insights into their biological function. The Biochemical journal 404, 1-13.

Mock, B.H., Brown-Proctor, C., Green, M.A., Steele, B., Glick-Wilson, B.E., Zheng, Q.-H., 2011. An automated SPE-based high-yield synthesis of [11C]acetate and [11C]palmitate: no liquid–liquid extraction, solvent evaporation or distillation required. Nuclear medicine and biology 38, 1135-1142.

Moniot, S., Steegborn, C., Schutkowski, M., 2013. Crystal structure analysis of human Sirt2 and its ADP-ribose complex. Journal of Structural Biology 182, 136-143.

Morris, M.J., Monteggia, L.M., 2013. Unique functional roles for class I and class II histone deacetylases in central nervous system development and function. Int J Dev Neurosci 31, 370-381.

Mukhopadhyay, U., Tong, W.P., Gelovani, J.G., Alauddin, M.M., 2006. Radiosynthesis of 6-([18F]fluoroacetamido)-1-hexanoicanilide ([18F]FAHA) for PET imaging of histone deacetylase (HDAC). Journal of Labelled Compounds and Radiopharmaceuticals 49, 997-1006.

Mukhopadhyay U, T.W., Gelovani J, Alauddin M., 2006a. Radiosynthesis of 6-([18F]fluoroacetamido)-1-hexanoicanilide ([18F]FAHA) for PET imaging of histone deacetylase (HDAC). J Label Comp Radiopharm. 49, 997–1006.

Mukhopadhyay U, T.W., **Gelovani J**, Alauddin MM, 2006b. Radiosynthesis of 6-(^{18}F-fluoroacetamido)-1-hexanoicanilide (^{18}F-FAHA) for PET Imaging of histone deacetylase (HDAC). *J Labelled Comp Radiopharm* 49, 997-1006.

Muth, V., Nadaud, S., Grummt, I., Voit, R., 2001. Acetylation of TAF(I)68, a subunit of TIF-IB/SL1, activates RNA polymerase I transcription. The EMBO journal 20, 1353-1362.

Mvunta, D.H., Miyamoto, T., Asaka, R., Yamada, Y., Ando, H., Higuchi, S., Ida, K., Kashima, H., Shiozawa, T., 2016. Overexpression of SIRT1 is Associated With Poor Outcomes in Patients With Ovarian Carcinoma. Applied immunohistochemistry & molecular morphology : AIMM / official publication of the Society for Applied Immunohistochemistry.

Naia, L., Rego, A.C., 2015. Sirtuins: double players in Huntington's disease. Biochimica et biophysica acta 1852, 2183-2194.

Napper, A.D., Hixon, J., McDonagh, T., Keavey, K., Pons, J.-F., Barker, J., Yau, W.T., Amouzegh, P., Flegg, A., Hamelin, E., Thomas, R.J., Kates, M., Jones, S., Navia, M.A., Saunders, J.O., DiStefano, P.S., Curtis, R., 2005. Discovery of Indoles as Potent and Selective Inhibitors of the Deacetylase SIRT1. Journal of Medicinal Chemistry 48, 8045-8054.

Narayan, R.S., Fedrigo, C.A., Stalpers, L.J., Baumert, B.G., Sminia, P., 2013. Targeting the Akt-pathway to improve radiosensitivity in glioblastoma. Curr Pharm Des 19, 951-957.

Nishii R, M.U., Yeh H, Sohomonyan S, Volgin A, Alauddin M, Tong W, Gelovani J., 2007. PET imaging of histone deacetylase activity in rat brain using 6-([18F]fluoroacetamide)-1-hexanoicanilide ([18F]FAHA). J Nucl Med 48, 336.

Nishina, S., Kosaki, R., Yagihashi, T., Azuma, N., Okamoto, N., Hatsukawa, Y., Kurosawa, K., Yamane, T., Mizuno, S., Tsuzuki, K., Kosaki, K., 2012. Ophthalmic features of CHARGE syndrome with CHD7 mutations. Am J Med Genet A 158a, 514-518.

Nisticò, G., Ciriolo, M.R., Fiskin, K., Iannone, M., de Martino, A., Rotilio, G., 1992. NGF restores decrease in catalase activity and increases superoxide dismutase and glutathione peroxidase activity in the brain of aged rats. Free Radical Biology and Medicine 12, 177-181.

North, B.J., Verdin, E., 2004. Sirtuins: Sir2-related NAD-dependent protein deacetylases. Genome Biol 5, 224.

North, B.J., Verdin, E., 2007a. Interphase Nucleo-Cytoplasmic Shuttling and Localization of SIRT2 during Mitosis. PloS one 2, e784.

North, B.J., Verdin, E., 2007b. Mitotic regulation of SIRT2 by cyclin-dependent kinase 1-dependent phosphorylation. J Biol Chem 282, 19546-19555.

Oberdoerffer, P., Michan, S., McVay, M., Mostoslavsky, R., Vann, J., Park, S.K., Hartlerode, A., Stegmuller, J., Hafner, A., Loerch, P., Wright, S.M., Mills, K.D., Bonni, A., Yankner, B.A., Scully, R., Prolla, T.A., Alt, F.W., Sinclair, D.A., 2008. SIRT1 redistribution on chromatin promotes genomic stability but alters gene expression during aging. Cell 135, 907-918.

Outeiro, T.F., Kontopoulos, E., Altmann, S.M., Kufareva, I., Strathearn, K.E., Amore, A.M., Volk, C.B., Maxwell, M.M., Rochet, J.C., McLean, P.J., Young, A.B., Abagyan, R., Feany, M.B., Hyman, B.T., Kazantsev, A.G., 2007. Sirtuin 2 inhibitors rescue alpha-synuclein-mediated toxicity in models of Parkinson's disease. Science (New York, N.Y 317, 516-519.

Outeiro, T.F., Marques, O., Kazantsev, A., 2008. Therapeutic role of sirtuins in neurodegenerative disease. Biochimica et biophysica acta 1782, 363-369.

Ozden, O., Park, S.-H., Wagner, B.A., Song, H.Y., Zhu, Y., Vassilopoulos, A., Jung, B., Buettner, G.R., Gius, D., 2014. SIRT3 deacetylates and increases pyruvate dehydrogenase activity in cancer cells. Free Radical Biology and Medicine 76, 163-172.

Pan, P.W., Feldman, J.L., Devries, M.K., Dong, A., Edwards, A.M., Denu, J.M., 2011a. Structure and biochemical functions of SIRT6. Journal of Biological Chemistry 286, 14575-14587.

Pan, P.W., Feldman, J.L., Devries, M.K., Dong, A., Edwards, A.M., Denu, J.M., 2011b. Structure and biochemical functions of SIRT6. The Journal of biological chemistry 286, 14575-14587.

Pandey, M.K., Belanger, A.P., Wang, S., DeGrado, T.R., 2012. Structure Dependence of Long-Chain [(18)F]Fluorothia Fatty Acids as Myocardial Fatty Acid Oxidation Probes. Journal of medicinal chemistry 55, 10674-10684.

Pandithage, R., Lilischkis, R., Harting, K., Wolf, A., Jedamzik, B., Luscher-Firzlaff, J., Vervoorts, J., Lasonder, E., Kremmer, E., Knoll, B., Luscher, B., 2008. The regulation of SIRT2 function by cyclin-dependent kinases affects cell motility. The Journal of cell biology 180, 915-929.

Paredes, S., Villanova, L., Chua, K.F., 2014. Molecular Pathways: Emerging Roles of Mammalian Sirtuin SIRT7 in Cancer. Clinical Cancer Research 20, 1741-1746.

Park, J.H., Jung, Y., Kim, T.Y., Kim, S.G., Jong, H.S., Lee, J.W., Kim, D.K., Lee, J.S., Kim, N.K., Kim, T.Y., Bang, Y.J., 2004. Class I histone deacetylase-selective novel synthetic inhibitors potently inhibit human tumor proliferation. Clinical cancer research : an official journal of the American Association for Cancer Research 10, 5271-5281.

Paxinos, G., and Charles Watson, 2006. The rat brain in stereotaxic coordinates.

Peng, C., Lu, Z., Xie, Z., Cheng, Z., Chen, Y., Tan, M., Luo, H., Zhang, Y., He, W., Yang, K., Zwaans, B.M., Tishkoff, D., Ho, L., Lombard, D., He, T.C., Dai, J., Verdin, E., Ye, Y., Zhao,

Y., 2011. The first identification of lysine malonylation substrates and its regulatory enzyme. Molecular & cellular proteomics : MCP 10, M111.012658.

Pettersen, E.F., Goddard, T.D., Huang, C.C., Couch, G.S., Greenblatt, D.M., Meng, E.C., Ferrin, T.E., 2004. UCSF Chimera--a visualization system for exploratory research and analysis. Journal of computational chemistry 25, 1605-1612.

Picard, F., Kurtev, M., Chung, N., Topark-Ngarm, A., Senawong, T., Machado De Oliveira, R., Leid, M., McBurney, M.W., Guarente, L., 2004. Sirt1 promotes fat mobilization in white adipocytes by repressing PPAR-gamma. Nature 429, 771-776.

Pontén, J., 1975. Neoplastic human glia cells in culture, Human tumor cells in vitro. Springer, pp. 175-206.

Poulsen, M.M., Vestergaard, P.F., Clasen, B.F., Radko, Y., Christensen, L.P., Stødkilde-Jørgensen, H., Møller, N., Jessen, N., Pedersen, S.B., Jørgensen, J.O.L., 2013. High-Dose Resveratrol Supplementation in Obese Men: An Investigator-Initiated, Randomized, Placebo-Controlled Clinical Trial of Substrate Metabolism, Insulin Sensitivity, and Body Composition. Diabetes 62, 1186-1195.

Price, V., Wang, L., D'Mello, S.R., 2013. Conditional deletion of histone deacetylase-4 in the central nervous system has no major effect on brain architecture or neuronal viability. J Neurosci Res 91, 407-415.

Pulla, V.K., Battu, M.B., Alvala, M., Sriram, D., Yogeeswari, P., 2012. Can targeting SIRT-1 to treat type 2 diabetes be a good strategy? A review. Expert Opinion on Therapeutic Targets 16, 819-832.

Qu, Y., Zhang, J., Wu, S., Li, B., Liu, S., Cheng, J., 2012. SIRT1 promotes proliferation and inhibits apoptosis of human malignant glioma cell lines. Neuroscience letters 525, 168-172.

Rahman, S., Islam, R., 2011. Mammalian Sirt1: insights on its biological functions. Cell Communication and Signaling.

Ramadori, G., Lee, C.E., Bookout, A.L., Lee, S., Williams, K.W., Anderson, J., Elmquist, J.K., Coppari, R., 2008. Brain SIRT1: anatomical distribution and regulation by energy availability. The Journal of Neuroscience 28, 9989-9996.

Rarey, M., Kramer, B., Lengauer, T., Klebe, G., 1996. A Fast Flexible Docking Method using an Incremental Construction Algorithm. Journal of Molecular Biology 261, 470-489.

Reid, A.E., Hooker, J., Shumay, E., Logan, J., Shea, C., Kim, S.W., Collins, S., Xu, Y., Volkow, N., Fowler, J.S., 2009a. Evaluation of 6-([18F]fluoroacetamido)-1-hexanoicanilide for PET imaging of histone deacetylase in the baboon brain. Nuclear medicine and biology 36, 247-258.

Reid, A.E., Hooker, J., Shumay, E., Logan, J., Shea, C., Kim, S.W., Collins, S., Xu, Y., Volkow, N., Fowler, J.S., 2009b. Evaluation of 6-([(18)F]fluoroacetamido)-1-hexanoicanilide for PET imaging of histone deacetylase in the baboon brain. Nucl Med Biol 36, 247-258.

Renthal, W., Maze, I., Krishnan, V., Covington, H.E., 3rd, Xiao, G., Kumar, A., Russo, S.J., Graham, A., Tsankova, N., Kippin, T.E., Kerstetter, K.A., Neve, R.L., Haggarty, S.J., McKinsey, T.A., Bassel-Duby, R., Olson, E.N., Nestler, E.J., 2007. Histone deacetylase 5 epigenetically controls behavioral adaptations to chronic emotional stimuli. Neuron 56, 517-529.

Riester, D., Hildmann, C., Grunewald, S., Beckers, T., Schwienhorst, A., 2007. Factors affecting the substrate specificity of histone deacetylases. Biochem Biophys Res Commun 357, 439-445.

Riester, D., Wegener, D., Hildmann, C., Schwienhorst, A., 2004. Members of the histone deacetylase superfamily differ in substrate specificity towards small synthetic substrates. Biochemical and biophysical research communications 324, 1116-1123.

Roessler, C., Nowak, T., Pannek, M., Gertz, M., Nguyen, G.T., Scharfe, M., Born, I., Sippl, W., Steegborn, C., Schutkowski, M., 2014. Chemical probing of the human sirtuin 5 active site reveals its substrate acyl specificity and Peptide-based inhibitors. Angewandte Chemie (International ed. in English) 53, 10728-10732.

Ron S. Broide, J.M.R., Najla Aftahi, Warren Young,, Floyd E. Bloom, a.C.J.W., 2006. Distribution of Histone Deacetylases 1–11 in the Rat Brain. Journal of Molecular Neuroscience 07, 47-58.

Rumpf, T., Schiedel, M., Karaman, B., Roessler, C., North, B.J., Lehotzky, A., Oláh, J., Ladwein, K.I., Schmidtkunz, K., Gajer, M., Pannek, M., Steegborn, C., Sinclair, D.A., Gerhardt, S., Ovádi, J., Schutkowski, M., Sippl, W., Einsle, O., Jung, M., 2015. Selective Sirt2 inhibition by ligand-induced rearrangement of the active site. Nat Commun 6.

Runkle, A.C., Shao, X., Tluczek, L.J., Henderson, B.D., Hockley, B.G., Scott, P.J., 2011. Automated production of [11C]acetate and [11C]palmitate using a modified GE Tracerlab FX(C-Pro). Applied radiation and isotopes : including data, instrumentation and methods for use in agriculture, industry and medicine 69, 691-698.

Sakkiah, S., Arooj, M., Cao, G.P., Lee, K.W., 2013. Insight the C-Site Pocket Conformational Changes Responsible for Sirtuin 2 Activity Using Molecular Dynamics Simulations. PloS one 8, e59278.

Sali, A., Blundell, T.L., 1993. Comparative protein modelling by satisfaction of spatial restraints. J Mol Biol 234, 779-815.

Sanabria S, F.H., Riffel K, Williams M, Gibson R, Gelovani JG, Cook J, Hostetler E., 2008. Quantification of HDAC inhibition by F-SAHA in rhesus monkey brain using the PET tracer [18F]FAHA. NeuroImage 41, T15.

Sanchez-Carbayo, M., Socci, N.D., Lozano, J., Saint, F., Cordon-Cardo, C., 2006. Defining molecular profiles of poor outcome in patients with invasive bladder cancer using oligonucleotide microarrays. J Clin Oncol 24, 778-789.

Sankaranarayanapillai, M., Tong, W.P., Maxwell, D.S., Pal, A., Pang, J., Bornmann, W.G., Gelovani, J.G., Ronen, S.M., 2006. Detection of histone deacetylase inhibition by noninvasive magnetic resonance spectroscopy. Molecular cancer therapeutics 5, 1325-1334.

Sankaranarayanapillai, M., Tong, W.P., Yuan, Q., Bankson, J.A., Dafni, H., Bornmann, W.G., Soghomonyan, S., Pal, A., Ramirez, M.S., Webb, D., Kaluarachchi, K., Gelovani, J.G., Ronen, S.M., 2008. Monitoring histone deacetylase inhibition in vivo: noninvasive magnetic resonance spectroscopy method. Mol Imaging 7, 92-100.

Sastry, G.M., Adzhigirey, M., Day, T., Annabhimoju, R., Sherman, W., 2013. Protein and ligand preparation: parameters, protocols, and influence on virtual screening enrichments. J Comput Aided Mol Des 27, 221-234.

Sauve, A.A., 2010. Sirtuin chemical mechanisms. Biochimica et biophysica acta 1804, 1591-1603.

Sauve, A.A., Wolberger, C., Schramm, V.L., Boeke, J.D., 2006. The Biochemistry of Sirtuins. Annual Review of Biochemistry 75, 435-465.

Schlicker, C., Gertz, M., Papatheodorou, P., Kachholz, B., Becker, C.F., Steegborn, C., 2008a. Substrates and regulation mechanisms for the human mitochondrial sirtuins Sirt3 and Sirt5. Journal of molecular biology 382, 790-801.

Schlicker, C., Gertz, M., Papatheodorou, P., Kachholz, B., Becker, C.F., Steegborn, C., 2008b. Substrates and regulation mechanisms for the human mitochondrial sirtuins Sirt3 and Sirt5. J Mol Biol 382, 790-801.

Schneider, N., Lange, G., Hindle, S., Klein, R., Rarey, M., 2013. A consistent description of Hydrogen bond and Dehydration energies in protein–ligand complexes: methods behind the HYDE scoring function. J Comput Aided Mol Des 27, 15-29.

Schuster, S., Roessler, C., Meleshin, M., Zimmermann, P., Simic, Z., Kambach, C., Schiene-Fischer, C., Steegborn, C., Hottiger, M.O., Schutkowski, M., 2016. A continuous sirtuin activity assay without any coupling to enzymatic or chemical reactions. Sci Rep 6, 22643.

Schwer, B., Verdin, E., 2008. Conserved metabolic regulatory functions of sirtuins. Cell metabolism 7, 104-112.

Seo, Y.J., Muench, L., Reid, A., Chen, J., Kang, Y., Hooker, J.M., Volkow, N.D., Fowler, J.S., Kim, S.W., 2013. Radionuclide labeling and evaluation of candidate radioligands for PET imaging of histone deacetylase in the brain. Bioorganic & medicinal chemistry letters 23, 6700-6705.

Shelley, J.C., Cholleti, A., Frye, L.L., Greenwood, J.R., Timlin, M.R., Uchimaya, M., 2007. Epik: a software program for pK a prediction and protonation state generation for drug-like molecules. J Comput Aided Mol Des 21, 681-691.

Singh, S., Kumar, P.U., Thakur, S., Kiran, S., Sen, B., Sharma, S., Rao, V.V., Poongothai, A.R., Ramakrishna, G., 2015. Expression/localization patterns of sirtuins (SIRT1, SIRT2, and SIRT7) during progression of cervical cancer and effects of sirtuin inhibitors on growth of cervical cancer cells. Tumour biology : the journal of the International Society for Oncodevelopmental Biology and Medicine 36, 6159-6171.

Smith, B.C., Settles, B., Hallows, W.C., Craven, M.W., Denu, J.M., 2011. SIRT3 Substrate Specificity Determined by Peptide Arrays and Machine Learning. ACS chemical biology 6, 146-157.

Smith, M.R., Syed, A., Lukacsovich, T., Purcell, J., Barbaro, B.A., Worthge, S.A., Wei, S.R., Pollio, G., Magnoni, L., Scali, C., Massai, L., Franceschini, D., Camarri, M., Gianfriddo, M., Diodato, E., Thomas, R., Gokce, O., Tabrizi, S.J., Caricasole, A., Landwehrmeyer, B., Menalled, L., Murphy, C., Ramboz, S., Luthi-Carter, R., Westerberg, G., Marsh, J.L., 2014. A potent and selective Sirtuin 1 inhibitor alleviates pathology in multiple animal and cell models of Huntington's disease. Human molecular genetics 23, 2995-3007.

Solomon, J.M., Pasupuleti, R., Xu, L., McDonagh, T., Curtis, R., DiStefano, P.S., Huber, L.J., 2006. Inhibition of SIRT1 Catalytic Activity Increases p53 Acetylation but Does Not Alter Cell Survival following DNA Damage. Molecular and Cellular Biology 26, 28-38.

Stojiljkovic, M., Piperski, V., Dacevic, M., Rakic, L., Ruzdijic, S., Kanazir, S., Characterization of 9L Glioma Model of the Wistar Rat. Journal of Neuro-Oncology 63, 1-7.

Stupp, R., Mason, W.P., van den Bent, M.J., Weller, M., Fisher, B., Taphoorn, M.J., Belanger, K., Brandes, A.A., Marosi, C., Bogdahn, U., Curschmann, J., Janzer, R.C., Ludwin, S.K., Gorlia, T., Allgeier, A., Lacombe, D., Cairncross, J.G., Eisenhauer, E., Mirimanoff, R.O., 2005. Radiotherapy plus concomitant and adjuvant temozolomide for glioblastoma. The New England journal of medicine 352, 987-996.

Sussmuth, S.D., Haider, S., Landwehrmeyer, G.B., Farmer, R., Frost, C., Tripepi, G., Andersen, C.A., Di Bacco, M., Lamanna, C., Diodato, E., Massai, L., Diamanti, D., Mori, E., Magnoni, L., Dreyhaupt, J., Schiefele, K., Craufurd, D., Saft, C., Rudzinska, M., Ryglewicz, D., Orth, M., Brzozy, S., Baran, A., Pollio, G., Andre, R., Tabrizi, S.J., Darpo, B., Westerberg, G.,

2015. An exploratory double-blind, randomized clinical trial with selisistat, a SirT1 inhibitor, in patients with Huntington's disease. British journal of clinical pharmacology 79, 465-476.

Suzuki, K., Koike, T., 2007. Mammalian Sir2-related protein (SIRT) 2-mediated modulation of resistance to axonal degeneration in slow Wallerian degeneration mice: a crucial role of tubulin deacetylation. Neuroscience 147, 599-612.

Suzuki, T., Asaba, T., Imai, E., Tsumoto, H., Nakagawa, H., Miyata, N., 2009. Identification of a cell-active non-peptide sirtuin inhibitor containing N-thioacetyl lysine. Bioorganic & medicinal chemistry letters 19, 5670-5672.

Tabatabaie, T., Floyd, R.A., 1996. Inactivation of Glutathione Peroxidase by Benzaldehyde. Toxicology and Applied Pharmacology 141, 389-393.

Tan, M., Peng, C., Anderson, Kristin A., Chhoy, P., Xie, Z., Dai, L., Park, J., Chen, Y., Huang, H., Zhang, Y., Ro, J., Wagner, Gregory R., Green, Michelle F., Madsen, Andreas S., Schmiesing, J., Peterson, Brett S., Xu, G., Ilkayeva, Olga R., Muehlbauer, Michael J., Braulke, T., Mühlhausen, C., Backos, Donald S., Olsen, Christian A., McGuire, Peter J., Pletcher, Scott D., Lombard, David B., Hirschey, Matthew D., Zhao, Y., 2014. Lysine Glutarylation Is a Protein Posttranslational Modification Regulated by SIRT5. Cell metabolism 19, 605-617.

Tang, B.L., Chua, C.E., 2008. SIRT2, tubulin deacetylation, and oligodendroglia differentiation. Cell motility and the cytoskeleton 65, 179-182.

Tang, W., Kuruvilla, S.A., Galitovskiy, V., Pan, M.L., Grando, S.A., Mukherjee, J., 2014. Targeting histone deacetylase in lung cancer for early diagnosis: (18)F-FAHA PET/CT imaging of NNK-treated A/J mice model. Am J Nucl Med Mol Imaging 4, 324-332.

Tarantino, G., Finelli, C., Scopacasa, F., Pasanisi, F., Contaldo, F., Capone, D., Savastano, S., 2014. Circulating Levels of Sirtuin 4, a Potential Marker of Oxidative Metabolism, Related to Coronary Artery Disease in Obese Patients Suffering from NAFLD, with Normal or Slightly Increased Liver Enzymes. Oxidative medicine and cellular longevity 2014, 10.

Taunton, J., C. A. Hassig, and S. L. Schreiber, 1996. A mammalian histone deacetylase related to the yeast transcriptional regulator Rpd3p. Science (New York, N.Y.) 272, 408-411.

Taylor, D.M., Maxwell, M.M., Luthi-Carter, R., Kazantsev, A.G., 2008. Biological and potential therapeutic roles of sirtuin deacetylases. Cell Mol Life Sci 65, 4000-4018.

Tedeschi, A., Di Giovanni, S., 2009. The non-apoptotic role of p53 in neuronal biology: enlightening the dark side of the moon. EMBO reports 10, 576-583.

Thomas, E.A., 2009. Focal nature of neurological disorders necessitates isotype-selective histone deacetylase (HDAC) inhibitors. Mol Neurobiol 40, 33-45.

Vaquero, A., Scher, M., Lee, D., Erdjument-Bromage, H., Tempst, P., Reinberg, D., 2004a. Human SirT1 interacts with histone H1 and promotes formation of facultative heterochromatin. Molecular cell 16, 93-105.

Vaquero, A., Scher, M., Lee, D., Erdjument-Bromage, H., Tempst, P., Reinberg, D., 2004b. Human SirT1 Interacts with Histone H1 and Promotes Formation of Facultative Heterochromatin. Molecular cell 16, 93-105.

Vaziri, H., Dessain, S.K., Ng Eaton, E., Imai, S.I., Frye, R.A., Pandita, T.K., Guarente, L., Weinberg, R.A., 2001. hSIR2(SIRT1) functions as an NAD-dependent p53 deacetylase. Cell 107, 149-159.

Venza, I., Visalli, M., Oteri, R., Cucinotta, M., Teti, D., Venza, M., 2013. Class II-specific histone deacetylase inhibitors MC1568 and MC1575 suppress IL-8 expression in human melanoma cells. Pigment cell & melanoma research 26, 193-204.

Volmar, C.-H., Wahlestedt, C., 2015. Histone deacetylases (HDACs) and brain function. Neuroepigenetics 1, 20-27.

Wang, C., Schroeder, F.A., Wey, H.Y., Borra, R., Wagner, F.F., Reis, S., Kim, S.W., Holson, E.B., Haggarty, S.J., Hooker, J.M., 2014. In vivo imaging of histone deacetylases (HDACs) in the central nervous system and major peripheral organs. J Med Chem 57, 7999-8009.

Wang, F., Nguyen, M., Qin, F.X., Tong, Q., 2007. SIRT2 deacetylates FOXO3a in response to oxidative stress and caloric restriction. Aging cell 6, 505-514.

Wang, F., Tong, Q., 2009. SIRT2 suppresses adipocyte differentiation by deacetylating FOXO1 and enhancing FOXO1's repressive interaction with PPARgamma. Molecular biology of the cell 20, 801-808.

Wang, J., Yu, J.-T., Tan, M.-S., Jiang, T., Tan, L., 2013. Epigenetic mechanisms in Alzheimer's disease: Implications for pathogenesis and therapy. Ageing Research Reviews 12, 1024-1041.

Wang, R.H., Sengupta, K., Li, C., Kim, H.S., Cao, L., Xiao, C., Kim, S., Xu, X., Zheng, Y., Chilton, B., Jia, R., Zheng, Z.M., Appella, E., Wang, X.W., Ried, T., Deng, C.X., 2008. Impaired DNA damage response, genome instability, and tumorigenesis in SIRT1 mutant mice. Cancer cell 14, 312-323.

Watson, G.P.C., 2006. The Rat Brain in Stereotaxic Coordinates. Academic Press.

Wauters, E., Lobo, V.J.S.-A., Pinho, A.V., Mawson, A., Herranz, D., Wu, J., Cowley, M.J., Colvin, E.K., Njicop, E.N., Sutherland, R.L., 2013. Sirtuin-1 regulates acinar-to-ductal metaplasia and supports cancer cell viability in pancreatic cancer. Cancer research 73, 2357-2367.

Wey, H.Y., Wang, C., Schroeder, F.A., Logan, J., Price, J.C., Hooker, J.M., 2015. Kinetic Analysis and Quantification of [(1)(1)C]Martinostat for in Vivo HDAC Imaging of the Brain. ACS Chem Neurosci 6, 708-715.

Williams, S.R.e.a., 2010. Haploinsufficiency of HDAC4 causes brachydactyly mental retardation syndrome, with brachydactyly type E, developmental delays, and behavioral problems. American Journal of Human Genetics 87.

Wolffe, A.P., and D. Pruss, 1996. Targeting chromatin disruption: transcription regulators that acetylate histones. Cell 84, 817-819.

Yang, X.-J., Grégoire, S., 2005. Class II Histone Deacetylases: from Sequence to Function, Regulation, and Clinical Implication. Molecular and Cellular Biology 25, 2873-2884.

Yang, X., Seto, E., 2007. HATs and HDACs: from structure, function and regulation to novel strategies for therapy and prevention. Oncogene 26, 5310-5318.

Yao, Y.-L., Yang, W.-M., 2011. Beyond Histone and Deacetylase: An Overview of Cytoplasmic Histone Deacetylases and Their Nonhistone Substrates. Journal of Biomedicine and Biotechnology 2011, 146493.

Yeh, H.-H., Tian, M., Hinz, R., Young, D., Shavrin, A., Mukhapadhyay, U., Flores, L.G., Balatoni, J., Soghomonyan, S., Jeong, H.J., Pal, A., Uthamanthil, R., Jackson, J.N., Nishii, R., Mizuma, H., Onoe, H., Kagawa, S., Higashi, T., Fukumitsu, N., Alauddin, M., Tong, W., Herholz, K., Gelovani, J.G., 2013a. Imaging epigenetic regulation by histone deacetylases in the brain using PET/MRI with 18F-FAHA. NeuroImage 64, 630-639.

Yeh, H.H., Young, D., Gelovani, J.G., Robinson, A., Davidson, Y., Herholz, K., Mann, D.M., 2013b. Histone deacetylase class II and acetylated core histone immunohistochemistry in human brains with Huntington's disease. Brain Res 1504, 16-24.

Yeh, S.H.-H., Lin, C.-F., Kong, F.-L., Wang, H.-E., Hsieh, Y.-J., Gelovani, J.G., Liu, R.-S., 2013c. Molecular Imaging of Nonsmall Cell Lung Carcinomas Expressing Active Mutant EGFR Kinase Using PET with [(124)I]-Morpholino-IPQA. BioMed Research International 2013, 549359.

Zakhary, S.M., Ayubcha, D., Dileo, J.N., Jose, R., Leheste, J.R., Horowitz, J.M., Torres, G., 2010. Distribution analysis of deacetylase SIRT1 in rodent and human nervous systems. The Anatomical Record 293, 1024-1032.

Zeglis, B.M., Pillarsetty, N., Divilov, V., Blasberg, R.A., Lewis, J.S., 2011. The synthesis and evaluation of N1-(4-(2-[18F]-fluoroethyl)phenyl)-N8-hydroxyoctanediamide ([18F]-FESAHA), a PET radiotracer designed for the delineation of histone deacetylase expression in cancer. Nucl Med Biol 38, 683-696.

Zhang, J., Chen, X., 2007. DeltaNp73 modulates nerve growth factor-mediated neuronal differentiation through repression of TrkA. Molecular and cellular biology 27, 3868-3880.

Zhao, K., Harshaw, R., Chai, X., Marmorstein, R., 2004. Structural basis for nicotinamide cleavage and ADP-ribose transfer by NAD(+)-dependent Sir2 histone/protein deacetylases. Proc Natl Acad Sci U S A 101, 8563-8568.

Zhu, K., Borrelli, K.W., Greenwood, J.R., Day, T., Abel, R., Farid, R.S., Harder, E., 2014. Docking Covalent Inhibitors: A Parameter Free Approach To Pose Prediction and Scoring. Journal of Chemical Information and Modeling 54, 1932-1940.

Zovkic, I.B., Meadows, J.P., Kaas, G.A., Sweatt, J.D., 2013. Interindividual variability in stress susceptibility: A role for epigenetic mechanisms in PTSD. Frontiers in Psychiatry 4.

ABSTRACT

DEVELOPMENT OF NOVEL RADIOTRACERS FOR PET IMAGING OF HDAC-MEDIATED EPIGENETIC REGULATION

by

ROBIN E. BONOMI

August 2016

Advisor: Dr. Juri Gelovani

Major: Biomedical Engineering

Degree: Doctor of Philosophy

Over the past two decades, epigenetic regulation has become a rapidly growing, highly innovative and influential field of biology and medicine. Protein acetylation and deacetylation, two key epigenetic regulatory mechanisms, are mediated by histone acetylase transferases (HATs) and histone deacetylases (HDACs), respectively. To date, the vast majority of studies on epigenetic regulation have been conducted in cell cultures and tissue samples using conventional methodologies of molecular and cellular biology, which contain inherent limitations for monitoring therapy and disease. Therefore, there is a growing need for novel, advanced methodologies that allow for non-invasive detection and monitoring of HDAC–mediated epigenetic regulatory processes in different organs and tissues. One such methodology is molecular imaging with positron emission tomography (PET), which allows for non-invasive visualization and quantification of spatial and temporal dynamics of expression-activity of various receptors and enzymes in different organs and tissues in norm and disease. The availability of selective substrates to various classes and isoforms of HDACs would enable the development of radiolabeled imaging agents for non-invasive *in vivo* PET imaging. Therefore, the aim of this work

is to develop class- and/or isoform-selective radiolabeled substrates of HDACs, with particular emphasis on class III (sirtuins, SIRTs).

Herein, HDAC class IIa, SIRT1 and SIRT2-selective radiotracers have been developed and validated through *in vitro* and *in vivo* characterization. Two of these tracers, ^{18}F-TFAHA for HDAC class IIa and and 2-[^{18}F]PhAHA for SIRT1, have also been validated in a disease model demonstrating their utility in understanding epigenetic regulation in an aggressive form of brain cancer. The development of these targeted imaging agents may help develop new therapies for disease as well as methodologies for monitoring treatment effectiveness and disease progression.

AUTOBIOGRAPHICAL STATEMENT

Robin majored in physics with chemistry and math minors at Connecticut College in New London, CT. With an ultimate goal of pursuing medical school, after graduation Robin worked in chemical engineering research for 2 years, and not only learned a tremendous amount but also thoroughly enjoyed the work. After stumbling across the field of Biomedical Engineering, Robin enrolled in graduate school at Wayne State, as it seemed to be a perfect combination of her many interests. Continuing with her original dream, she is also currently enrolled in Wayne State School of Medicine to pursue her medical doctorate degree. As an avid competitive runner, when not in the lab or studying, she can often be found out exploring and running on the roads.

EDUCATION

2011 B.A. Connecticut College, New London, CT

PROFESSIONAL APPOINTMENTS

2011 Research Assistant, Chemical Engineering, Massachusetts Institute of Technology

2012 Research Assistant, Center for Aero-Thermodynamics, Aerodyne Research, Inc.

AWARDS

2014 2nd Place Student Presentation, WSU Biomedical Eng. 75th Anniversary Symposium

2014 RUMBLE Fellow, College of Engineering, Wayne State University

2015 Kales Scholar Award, College of Engineering, Wayne State University

2015 Student Fellow Award, World Pre-Clinical Congress Conference, Boston, MA

2015 2nd Place Student Presentation, KCI Molecular Imaging Retreat

2015 Chemistry Biology Initiative Award

2016 Honorable Mention for Oral Presentation, WSU Medical School Research Symposium

PUBLICATIONS & PRESENTATIONS

Bonomi R, *et al.* Dosimetry studies of novel imaging agent for Galectin-3 expression. Poster presentation at KCI Molecular Imaging Retreat 2015.

Bonomi R, *et al.* Imaging Galectin-3 expression in Breast Cancer. Poster presentation *American Association for Cancer Research*, New Orleans, LA. April 2016.

Bonomi R, *et al* Novel structure-activity relationship profile and SIRT2-selective imaging agent. Poster presentation at KCI Molecular Imaging Retreat and *American Association for Cancer Research*, New Orleans, LA. April 2016.

Bonomi R, *et al* Novel SIRT1-selective radiotracer substrate [18F]-2FPhAHA for PET imaging of epigenetic regulation. Presented orally at *World PreClinical Congress*, Boston, MA June 2015; Presented in poster presentation at *World Molecular Imaging Conference* in Sept 2015; Poster presentation at *American Association for Cancer Research*, New Orleans, LA. April 2016

Bonomi R, *et al.* (2015) Novel Histone Deacetylase Class IIa Selective Substrate Radiotracers for PET Imaging of Epigenetic Regulation in the Brain. *PloS one* 10(8):e0133512.

Gao, C.W., Vandeputte, A.G., Yee, N.W., **Bonomi, R.E.,** *et al.*., JP-10 combustion studied with shock tube experiments and modeled with automatic reaction mechanism generation, *Combustion and Flame* **162**(8) , 3115-3129 (2015)

Wong, H-W, Peck, J.J., **Bonomi, R.E.** *et al* (2015) Quantitative determination of species production from phenol-formaldehyde resin pyrolysis. *Polymer Degradation and Stability* 112(0):122-131

Patwardhan, P.R., Timko, M.T., **Bonomi, R.E.,** Kida, Y., Hernandez, H.H., Tester, J.W., Green, W.H., *Supercritical Water Desulfurization of Organic Sulfides Is Consistent with Free-Radical Kinetics.* Energy & Fuels, 2013. **27**(10): p. 6108-6117.